frontiers | Research Topics

Advances in bioelectronics and stimulation strategies for next generation neuroprosthetics

Edited by
Liming Li, Socrates Dokos, Luming Li, Tianruo Guo and Yao-Chuan Chang

Published in
Frontiers in Neuroscience

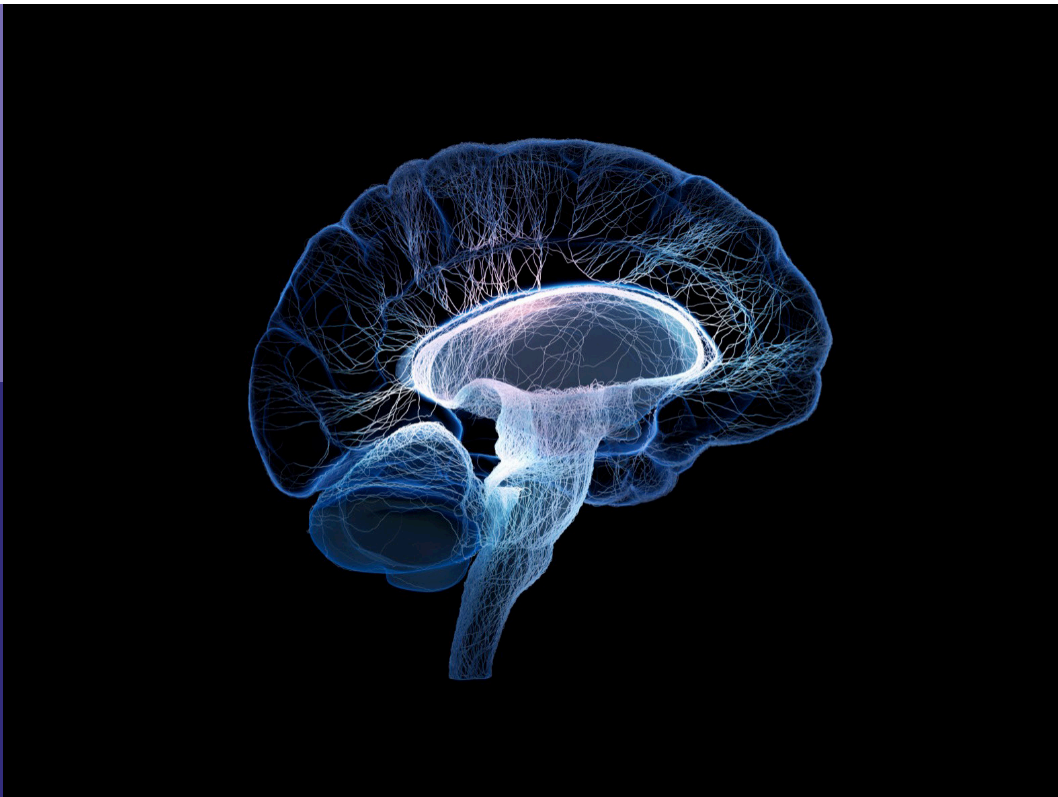

ISSN 1664-8714
ISBN 978-2-83251-429-0
DOI 10.3389/978-2-83251-429-0

About Frontiers

Frontiers is more than just an open access publisher of scholarly articles: it is a pioneering approach to the world of academia, radically improving the way scholarly research is managed. The grand vision of Frontiers is a world where all people have an equal opportunity to seek, share and generate knowledge. Frontiers provides immediate and permanent online open access to all its publications, but this alone is not enough to realize our grand goals.

Frontiers journal series

The Frontiers journal series is a multi-tier and interdisciplinary set of open-access, online journals, promising a paradigm shift from the current review, selection and dissemination processes in academic publishing. All Frontiers journals are driven by researchers for researchers; therefore, they constitute a service to the scholarly community. At the same time, the *Frontiers journal series* operates on a revolutionary invention, the tiered publishing system, initially addressing specific communities of scholars, and gradually climbing up to broader public understanding, thus serving the interests of the lay society, too.

Dedication to quality

Each Frontiers article is a landmark of the highest quality, thanks to genuinely collaborative interactions between authors and review editors, who include some of the world's best academicians. Research must be certified by peers before entering a stream of knowledge that may eventually reach the public - and shape society; therefore, Frontiers only applies the most rigorous and unbiased reviews. Frontiers revolutionizes research publishing by freely delivering the most outstanding research, evaluated with no bias from both the academic and social point of view. By applying the most advanced information technologies, Frontiers is catapulting scholarly publishing into a new generation.

What are Frontiers Research Topics?

Frontiers Research Topics are very popular trademarks of the *Frontiers journals series*: they are collections of at least ten articles, all centered on a particular subject. With their unique mix of varied contributions from Original Research to Review Articles, Frontiers Research Topics unify the most influential researchers, the latest key findings and historical advances in a hot research area.

Find out more on how to host your own Frontiers Research Topic or contribute to one as an author by contacting the Frontiers editorial office: frontiersin.org/about/contact

Advances in bioelectronics and stimulation strategies for next generation neuroprosthetics

Topic editors
Liming Li — Shanghai Jiao Tong University, China
Socrates Dokos — University of New South Wales, Australia
Luming Li — Tsinghua University, China
Tianruo Guo — University of New South Wales, Australia
Yao-Chuan Chang — Feinstein Institute for Medical Research, United States

Citation
Li, L., Dokos, S., Li, L., Guo, T., Chang, Y.-C., eds. (2023). *Advances in bioelectronics and stimulation strategies for next generation neuroprosthetics*.
Lausanne: Frontiers Media SA. doi: 10.3389/978-2-83251-429-0

Table of contents

frontiers | Frontiers in Neuroscience

TYPE Editorial
PUBLISHED 10 January 2023
DOI 10.3389/fnins.2022.1116900

Editorial: Advances in bioelectronics and stimulation strategies for next generation neuroprosthetics

Tianruo Guo[1], Yao-chuan Chang[2,3], Luming Li[4,5,6], Socrates Dokos[1] and Liming Li[7]*

[1]Graduate School of Biomedical Engineering, The University of New South Wales Sydney, Sydney, NSW, Australia, [2]Institute of Bioelectronic Medicine, Feinstein Institutes for Medical Research, Manhasset, NY, United States, [3]Medtronic PLC, Minneapolis, MN, United States, [4]National Engineering Research Center of Neuromodulation, School of Aerospace Engineering, Tsinghua University, Beijing, China, [5]Precision Medicine and Healthcare Research Center, Tsinghua-Berkeley Shenzhen Institute, Tsinghua University, Shenzhen, China, [6]IDG/McGovern Institute for Brain Research, Tsinghua University, Beijing, China, [7]School of Biomedical Engineering, Shanghai Jiao Tong University, Shanghai, China

OPEN ACCESS

EDITED AND REVIEWED BY
Laura Ballerini,
International School for Advanced Studies (SISSA), Italy

*CORRESPONDENCE
Liming Li
✉ lilm@sjtu.edu.cn

SPECIALTY SECTION
This article was submitted to Neural Technology, a section of the journal Frontiers in Neuroscience

RECEIVED 05 December 2022
ACCEPTED 13 December 2022
PUBLISHED 10 January 2023

CITATION
Guo T, Chang Y-c, Li L, Dokos S and Li L (2023) Editorial: Advances in bioelectronics and stimulation strategies for next generation neuroprosthetics.
Front. Neurosci. 16:1116900.
doi: 10.3389/fnins.2022.1116900

KEYWORDS

non-invasive stimulation, optimal implantation location, stimulus parameter identification, neural ultrastructure, neuromodulation

Editorial on the Research Topic
Advances in bioelectronics and stimulation strategies for next generation neuroprosthetics

Recent technological advances have expanded our understanding of how artificial stimulation interacts with the living nervous system (Riva and Micera, 2021; Saha et al., 2021; Walter, 2021; Ahmed et al., 2022; Chen et al., 2022; Yao et al., 2022). This Research Topic, contributed to by electrophysiologists, biomedical engineers, computational neuroscientists, and neuropsychologists, provides a state-of-the-art overview of advances in neural stimulation technologies, ranging from recent progress in functional electrical stimulation (FES) to new understanding of how weak electric field (EF) stimulation affects cellular properties. The submissions to this Research Topic can be grouped into four key areas: (A) non-invasive stimulation, (B) optimal implantation location, (C) advances in stimulus parameter identification, and (D) the influence of neural ultrastructures under EF. It is helpful to provide four quotes from Sun Tzu's *The Art of War*[1] to represent the theme of each section:

---

[1] *The Art of War* is an ancient Chinese military treatise written in 5th century BC. It remains the most influential strategy text used in military thinking, business tactics, legal strategy, politics, sports, lifestyles and beyond.

"The greatest victory requires no bleeding" — Chapter. Strategic attack 《孙子兵法 · 谋攻篇》

Significant research efforts have focused largely on developing non-invasive or minimally invasive stimulation techniques (Boes et al., 2018; Sun et al., 2018; Guo et al., 2020; Su et al., 2021, 2022; Lu et al., 2022; Ren et al., 2022). For example, transcranial direct current stimulation (tDCS) allows reversible region-specific modulation (Filmer et al., 2014). Liu S. et al. offer valuable insights into how prefrontal tDCS affects the attention bias by detecting electroencephalographic characteristics in response to rest and emotional oddball tasks. In this clinical study, tDCS caused increased brain neural activities related to emotion regulation and distinguished electrical signatures following positive targets and negative distracters, indicating great potential for tDCS in the treatment of depression. Another non-invasive neuromodulatory technique is that of trans-spinal direct current stimulation (tsDCS). Song and Martin found that cathodal tsDCS can selectively target voltage-dependent calcium channels to modulate motoneuron activity, informing therapeutic treatment strategies to achieve rehabilitation goals after injury; in particular, to increase muscle force.

In addition, motor imaginary (MI)-based brain-computer interface (BCI) must overcome multiple issues to be commercially usable, especially related to signal quality and subject-variation (Singh et al., 2021). Sensory threshold somatosensory electrical stimulation (st-SES) has been recently used to guide participants in motor imaginary tasks (Corbet et al., 2018; Vidaurre et al., 2019; Zhang et al., 2022). Chen et al. suggest that st-SES can only improve brain-switch BCI performance in those subjects with higher classification accuracy (high performers) in discriminating the MI condition from rest. Moreover, they showed that st-SES influences functional connectivity of the fronto-parietal network, but through different frequency bands for different subjects. These findings can potentially help to optimize guidance strategies to adapt to different types of MI-BCI users.

"Choose the favorable terrain before the war starts" — Chapter. Terrain 《孙子兵法 · 地形篇》

An optimal implantation region improves not only stimulation performance but also the long-term stability of implantable microelectrodes, as well as reducing side effects (Wang et al., 2020; Song et al., 2022; Zhao et al., 2022). Urdaneta et al. describe a somatosensory cortex layer-dependent long-term stability in intracortical microstimulation. Their results suggest a more consistent stimulation efficiency and less foreign body response when the electrodes were implanted in L4 and L5 of the somatosensory cortex, indicating the critical role of interface depth in the design of chronic implants. Another example of optimizing electrode placement is for electroconvulsive therapy (ECT) for severe treatment-resistant depression. Steele et al. proposed a fronto-medial ECT electrode placement that would maximize the EF in specific sagittal brain regions, whilst minimizing EF in sub-regions of the bilateral hippocampi. Such outcomes suggest electrode location can significantly reduce cognitive and non-cognitive side-effects.

"Fight smarter not harder" — Chapter. Military dispositions 《孙子兵法 · 军形篇》

Programming nerve stimulation setting is challenging and time consuming due to the huge number of possible stimulus parameter combinations (O'Doherty et al., 2011; Li et al., 2013; Yan et al., 2016; Jia et al., 2018; Guo et al., 2019; Muralidharan et al., 2020; Song et al., 2020; Zhang et al., 2020; Chang et al., 2022). In terms of FES, several "smart" strategies have been used to improve its effectiveness and acceptability. Xu et al. have introduced a control strategy for FES parameter selection, based on a direct transfer function using surface electromyography (sEMG) features and joint angles as inputs. A similar idea has been used historically in other neuromodulation fields since various stimulation parameters have been shown to evoke distinct neurological and physiological responses. Conversely, elicited physiological effects, both for targeted and untargeted neurons, can guide stimulus parameter tuning for many neural systems, including the brain (Qian et al., 2016; Chen et al., 2020, 2022), spinal cord (Verrills et al., 2016), vagus nerve (Chang et al., 2020), and the retina (Guo et al., 2018). In another example, Dong et al. have proposed a walking assistance system with adaptive algorithm to support FES therapy. As the stimulation sequence is tailored to the individual need based on real-time gait phase, healthy subjects are able to achieve better treadmill performance for various speed conditions. A similar adaptive idea has also been successfully adopted in clinical neuromodulation therapies to improve effectiveness, such as deep brain stimulation (Bocci et al., 2021) and spinal cord stimulation (Schultz et al., 2012), utilizing chosen physiological indices.

"Know the enemy, know yourself" — Chapter. Strategic attack 《孙子兵法 · 谋攻篇》

Electrical stimulation performance cannot be significantly improved by only optimizing the device in isolation without considering the biophysical complexity of the target nerve system (Abbasi and Rizzo, 2021; Ahmed et al., 2022; Italiano et al., 2022). Sophisticated computational models have been widely used in predicting the role of tissue or neural or ultra-structures under EF (Guo et al., 2014, 2016; Yang et al., 2018;

Bai et al., 2019a; Dokos and Guo, 2020). Liu(a) et al. have proposed a new biophysical model of myelin ultra-structures by simulating cytoplasmic channels in the myelin sheath as a low-impedance route, while previous models approximate the myelin sheath as an insulation layer (Schwarz and Reid, 1995; Bean, 2007; Ge et al., 2020). Using this model, Liu(b) et al. further investigated how cytoplasmic channels affect EF across the myelin sheaths, concluding that the externally applied EF can control myelin growth. These new findings indicate the possibility of using electrical modulation to treat degenerative neural diseases. Neurodegenerative progression can affect the neuroprosthetic performance (Rattay et al., 2001; Hilker et al., 2005; Loizos et al., 2018; Ly et al., 2022). Croner et al. have investigated the differential performance of cochlear stimulation in a cochlea with intact and degenerating spiral ganglion neurons (SGNs) using a biophysically detailed computational model of the human cochlea (Bai et al., 2019b). Their study identified the increased activation of neurons in unintended areas, and an insensitive neural response to various apical electrode settings when degenerating SGNs were stimulated. This study also suggested that stimulation thresholds are unlikely to be a good indicator of neural health, since degenerating SGNs showed both an increase and decrease in current threshold depending on the initial stimulation site.

Author's note

The Chinese characters shown in the Editorial refer to the origin of each subtitle in the ancient literature The Art of War by Sun Tzu.

Author contributions

All authors listed have made a substantial, direct, and intellectual contribution to the work and approved it for publication.

Funding

This work was supported by the National Natural Science Foundation of China (61971280 and 61671300), Tsinghua University Initiative Scientific Research Program (20191080597), University of Toronto-Tsinghua Joint Research Fund (20193080065), Tsinghua Precision Medicine Foundation (LC201906), and the National Key Research and Development Program of China (2021YFC2400200).

Acknowledgments

The editorial team would like to thank Dr. Chen Zhang from Tsinghua University, China, for her excellent work in communication and coordination during compilation of this Research Topic.

Conflict of interest

Y-cC was employed by Medtronic PLC.

The remaining authors declare that the research was conducted in the absence of any commercial or financial relationships that could be construed as a potential conflict of interest.

Publisher's note

References

Abbasi, B., and Rizzo, J. F. (2021). Advances in neuroscience, not devices, will determine the effectiveness of visual prostheses. *Semin Ophthalmol.* 36, 168–175. doi: 10.1080/08820538.2021.1887902

Ahmed, U., Chang, Y.-C., Zafeiropoulos, S., Nassrallah, Z., and Miller, L., et al. (2022). Strategies for precision vagus neuromodulation. *Bioelectron. Med.* 8, 9. doi: 10.1186/s42234-022-00091-1

Bai, S., Encke, J., Obando-Leitón, M., Wei,ß, R., Schäfer, F., Eberharter, J., et al. (2019b). Electrical stimulation in the human cochlea: A computational study based on high-resolution micro-CT scans. *Front. Neurosci.* 13, 1312. doi: 10.3389/fnins.2019.01312

Bai, S., Martin, D., Guo, T., Dokos, S., and Loo, C. (2019a). Computational comparison of conventional and novel electroconvulsive therapy electrode placements for the treatment of depression. *Eur. Psychiat.* 60, 71–78. doi: 10.1016/j.eurpsy.2019.05.006

Bean, B. P. (2007). The action potential in mammalian central neurons. *Nat. Rev. Neurosci.* 8, 451–465. doi: 10.1038/nrn2148

Bocci, T., Prenassi, M., Arlotti, M., Cogiamanian, F. M., Borellini, L., Moro, E., et al. (2021). Eight-hours conventional versus adaptive deebrain stimulation of the subthalamic nucleus in Parkinson's disease. *NPJ Parkinsons Dis* 7, 88. doi: 10.1038/s41531-021-00229-z

Boes, A. D., Kelly, M. S., Trapp, N. T., Stern, A. P., Press, D. Z., and Pascual-Leone, A. (2018). Noninvasive brain stimulation: challenges and opportunities for a new clinical specialty. *J Neuropsychiat. Clin. Neurosci.* 30, 173–179. doi: 10.1176/appi.neuropsych.17110262

Chang, Y.-C., Ahmed, U., Jayaprakash, N., Mughrabi, I., Lin, Q., Wu, et al. (2022). kHz-frequency electrical stimulation selectively activates small, unmyelinated vagus afferents. *Brain Stimul.* 15, 1389–1404. doi: 10.1016/j.brs.2022.09.015

Chang, Y.-C., Cracchiolo, M., Ahmed, U., Mughrabi, I., and Gabalski, A., et al. (2020). Quantitative estimation of nerve fiber engagement by vagus nerve stimulation using physiological markers. *Brain Stimul.* 13, 1617–1630. doi: 10.1016/j.brs.2020.09.002

Chen, Y., Gong, C., Tian, Y., Orlov, N., Zhang, J., Guo, Y., et al. (2020). Neuromodulation effects of deebrain stimulation on beta rhythm: A longitudinal local field potential study. *Brain Stimul.* 13, 1784–1792. doi: 10.1016/j.brs.2020.09.027

Chen, Y., Zhang, G., Guan, L., Gong, C., Ma, B., Hao, H., et al. (2022). Progress in the development of a fully implantable brain-computer interface: the potential of sensing-enabled neurostimulators. *Nat. Sci. Rev.* 9, 99. doi: 10.1093/nsr/nwac099

Corbet, T., Iturrate, I., Pereira, M., Perdikis, S., and Millán, J. D. R. (2018). Sensory threshold neuromuscular electrical stimulation fosters motor imagery performance. *Neuroimage* 176, 268–276. doi: 10.1016/j.neuroimage.2018.04.005

Dokos, S., and Guo, T. (2020). Computational models of neural retina. In *Encyclopedia of Computational Neuroscience,* eds. D. Jaeger and R. Jung (Berlin: Springer). doi: 10.1007/978-1-4614-7320-6_652-2

Filmer, H. L., Dux, P. E., and Mattingley, J. B. (2014). Applications of transcranial direct current stimulation for understanding brain function. *Trends Neurosci.* 37, 742–753. doi: 10.1016/j.tins.2014.08.003

Ge, Y., Ye, S., Zhu, K., Guo, T., Su, D., Zhang, D., et al. (2020). Mediating different-diameter A beta nerve fibers using a biomimetic 3D TENS computational model. *J. Neurosci. Methods* 346, 108891. doi: 10.1016/j.jneumeth.2020.108891

Guo, T., Shivdasani, M. N., Tsai, D., Ayton, L. N., and Rathbun, D. L. (2020). Visual prostheses: neuroengineering handbook. in *Handbook of Neuroengineering*, eds. N. V. Thakor (Singapore: Springer Singapore). doi: 10.1007/978-981-15-2848-4_31-2

Guo, T., Tsai, D., Bai, S., Morley, J. W., Suaning, G. J., Lovell, N. H., et al. (2014). Understanding the retina: a review of computational models of the retina from the single cell to the network level. *Crit. Rev. Biomed. Eng.* 42, 419–436. doi: 10.1615/CritRevBiomedEng.2014011732

Guo, T., Tsai, D., Morley, J. W., Suaning, G. J., Kameneva, T., Lovell, N. H., et al. (2016). Electrical activity of ON and OFF retinal ganglion cells: a modelling study. *J. Neural. Eng.* 13, 025005. doi: 10.1088/1741-2560/13/2/025005

Guo, T., Tsai, D., Yang, C. Y., Abed, A. A., Twyford, P., Fried, S. I., et al. (2019). Mediating retinal ganglion cell spike rates using high-frequency electrical stimulation. *Front. Neurosci* 13, 413. doi: 10.3389/fnins.2019.00413

Guo, T., Yang, C. Y., Tsai, D., Muralidharan, M., Suaning, G. J., Morley, J. W., et al. (2018). Closed-looefficient searching of optimal electrical stimulation parameters for preferential excitation of retinal ganglion cells. *Front. Neurosci.* 12, 168. doi: 10.3389/fnins.2018.00168

Hilker, R., Portman, A. T., Voges, J., Staal, M. J., Burghaus, L., van Laar, T., et al. (2005). Disease progression continues in patients with advanced Parkinson's disease and effective subthalamic nucleus stimulation. *J. Neurol. Neurosurg. Psychiat.* 76, 1217–1221. doi: 10.1136/jnnp.2004.057893

Italiano, M. L., Guo, T., and Lovell, N. H. (2022). Improving the spatial resolution of artificial vision using midget retinal ganglion cell populations modeled at the human fovea. *J. Neur. Eng.* 19, 035002. doi: 10.1088/1741-2552/ac72c2

Jia, F., Shukla, A. W., Hu, W., Almeida, L., Holanda, V., Zhang, J., et al. (2018). DeeBrain stimulation at variable frequency to improve motor outcomes in parkinson's disease. *Movem. Diso. Clin. Pract.* 5, 538–541. doi: 10.1002/mdc3.12658

Li, M., Yan, Y., Wang, Q., Zhao, H., Chai, X., Sui, X., et al. (2013). A simulation of current focusing and steering with penetrating optic nerve electrodes. *J. Neural. Eng.* 10, 066007. doi: 10.1088/1741-2560/10/6/066007

Loizos, K., Marc, R., Humayun, M., Anderson, J. R., Jones, B. W., Lazzi, G., et al. (2018). Increasing electrical stimulation efficacy in degenerated retina: stimulus waveform design in a multiscale computational model. *IEEE Trans. Neur. Syst. Rehabil. Eng.* 26, 1111–1120. doi: 10.1109/TNSRE.2018.2832055

Lu, Z., Zhou, M., Guo, T., Liang, J., Wu, W., Gao, Q., et al. (2022). An in-silico analysis of retinal electric field distribution induced by different electrode design of trans-corneal electrical stimulation. *J. Neural Eng.* 19, 055004. doi: 10.1088/1741-2552/ac8e32

Ly, K., Guo, T., Tsai, D., Muralidharan, M., Shivdasani, M. N., Lovell, N. H., et al. (2022). Simulating the impact of photoreceptor loss and inner retinal network changes on electrical activity of the retina. *J. Neur. Eng.* 19, 065002. doi: 10.1088/1741-2552/aca221

Muralidharan, M., Guo, T., Shivdasani, M. N., Tsai, D., Fried, S., Li, L., et al. (2020). Neural activity of functionally different retinal ganglion cells can be robustly modulated by high-rate electrical pulse trains. *J. Neur. Eng.* 17, 045013. doi: 10.1088/1741-2552/ab9a97

O'Doherty, J. E., Lebedev, M. A., Ifft, P. J., Zhuang, K. Z., Shokur, S., Bleuler, H., et al. (2011). Active tactile exploration using a brain-machine-brain interface. *Nature* 479, 228–231. doi: 10.1038/nature10489

Qian, X., Chen, Y., Ma, B., and Hao, H. (2016). Chronically monitoring the deebrain rhythms: from stimulation to recording. *Sci. Bull.* 61, 1522–1524. doi: 10.1007/s11434-016-1159-y

Rattay, F., Leao, R. N., and Felix, H. A. (2001). model of the electrically excited human cochlear neuron. I. Contribution of neural substructures to the generation and propagation of spikes. *Hear. Res.* 153, 43–63. doi: 10.1016/S0378-5955(00)00256-2

Ren, J., Chi, Q., Hubbard, C. S., Cui, W., Wang, D., Li, L., et al. (2022). Personalized functional imaging identifies brain stimulation target for a patient with trauma-induced functional disruption. *Brain Stimul.* 15, 53–56. doi: 10.1016/j.brs.2021.11.005

Riva, E. R., and Micera, S. (2021). Progress and challenges of implantable neural interfaces based on nature-derived materials. *Bioelectron. Med.* 7, 6. doi: 10.1186/s42234-021-00067-7

Saha, S., Mamun, K. A., Ahmed, K., Mostafa, R., Naik, G. R., Darvishi, S., et al. (2021). Progress in brain computer interface: challenges and opportunities. *Front. Syst. Neurosci.* 15. doi: 10.3389/fnsys.2021.578875

Schultz, D. M., Webster, L., Kosek, P., Dar, U., Tan, Y., Sun, M., et al. (2012). Sensor-driven position-adaptive spinal cord stimulation for chronic pain. *Pain Phys.* 15, 1–12. doi: 10.36076/ppj.2012/15/1

Schwarz, J. R., and Reid, G. (1995). Action potentials and membrane currents in the human node of Ranvier. *Pflügers Archiv.* 430, 283–292. doi: 10.1007/BF00374660

Singh, A., Hussain, A. A., and Lal, S. (2021). A comprehensive review on critical issues and possible solutions of motor imagery based electroencephalography brain-computer interface. *Sensors* 21, 2173. doi: 10.3390/s21062173

Song, X., Guo, T., Shivdasani, M. N., Dokos, S., Lovell, N. H., Li, X., et al. (2020). Creation of virtual channels in the retina using synchronous and asynchronous stimulation—a modelling study. *J. Neur. Eng.* 17, 065001. doi: 10.1088/1741-2552/abc3a9

Song, X., Qiu, S., Shivdasani, M. N., Zhou, F., Liu, Z., Ma, S., et al. (2022). An in-silico analysis of electrically evoked responses of midget and parasol retinal ganglion cells in different retinal regions. *J. Neur. Eng.* 19, 026018. doi: 10.1088/1741-2552/ac5b18

Su, X., Guo, J., Zhou, M., Chen, J., Li, L., Chen, Y., et al. (2021). Computational modeling of spatially selective retinal stimulation with temporally interfering electric fields. *IEEE Trans. Neural. Syst. Rehabil. Eng.* 29, 418–428. doi: 10.1109/TNSRE.2021.3055203

Su, X., Zhou, M., Di, L., Chen, J., Zhai, Z., Liang, J., et al. (2022). The visual cortical responses to sinusoidal transcorneal electrical stimulation. *Brain Res.* 1785, 147875. doi: 10.1016/j.brainres.2022.147875

Sun, P., Li, H., Lu, Z., Su, X., Ma, Z., Chen, J., et al. (2018). Comparison of cortical responses to the activation of retina by visual stimulation and transcorneal electrical stimulation. *Brain Stimul.* 11, 667–675. doi: 10.1016/j.brs.2018.02.009

Verrills, P., Sinclair, C., and Barnard, A. (2016). A review of spinal cord stimulation systems for chronic pain. *J. Pain Res.* 9, 481–492. doi: 10.2147/JPR.S108884

Vidaurre, C., Murguialday, A. R., Haufe, S., Gómez, M., Müller, K.-R., and Nikulin V. V. (2019). Enhancing sensorimotor BCI performance with assistive afferent activity: An online evaluation. *Neuroimage* 199, 375–386. doi: 10.1016/j.neuroimage.2019.05.074

Walter, P. (2021). Visual Prostheses. in *Neuroengineering Handbook*, eds. N. V. Thakor (Singapore: Springer).

Wang, Z., Cai, X., Qiu, R., Yao, C., Tian, Y., Gong, C., et al. (2020). Case report: Lateral habenula deebrain stimulation for treatment-resistant depression. *Front. Psychiat.* 11, 616501. doi: 10.3389/fpsyt.2020.616501

Yan, Y., Lu, Y., Li, M., Ma, Z., Cao, P., Chen, Y., et al. (2016). Electrically evoked responses in the rabbit cortex induced by current steering with penetrating optic nerve electrodes. *Invest. Ophthalmol. Vis. Sci.* 57, 6327–6338. doi: 10.1167/iovs.15-17543

Yang, C. Y., Tsai, D., Guo, T., Dokos, S., Suaning, G. J., Morley, J. W., et al. (2018). Differential electrical responses in retinal ganglion cell subtypes: effects of synaptic blockade and stimulating electrode location. *J. Neural. Eng.* 15, 046020. doi: 10.1088/1741-2552/aac315

Yao, X., Liu, H., Si, J., Ding, X., Zhao, Y., Zheng, Y., et al. (2022). Research status and future development of cochlear reimplantation. *Front. Neurosci.* 16, 824389. doi: 10.3389/fnins.2022.824389

Zhang, J., Hu, W., Chen, H., Meng, F., Li, L., Okun, M. S., et al. (2020). Implementation of a novel bluetooth technology for remote deebrain stimulation programming: the pre- and post-COVID-19 Beijing experience. *Movement Diso.* 35, 909–910. doi: 10.1002/mds.28098

Zhang, L., Chen, L., Wang, Z., Zhang, X., and Liu, X. (2022). "Enhancing Visual-Guided Motor Imagery Performance Via Sensory Threshold Somatosensory Electrical Stimulation Training," in *IEEE Transactions on Biomedical Engineering*. doi: 10.1109/TBME.2022.3202189

Zhao, H., Liu, R., Zhang, H., Cao, P., and Liu, Z. (2022). Research progress on the flexibility of an implantable neural microelectrode. *Micromachines* 13, 386. doi: 10.3390/mi13030386

frontiers | Frontiers in Neuroscience

ORIGINAL RESEARCH
published: 25 April 2022
doi: 10.3389/fnins.2022.856948

Trans-Spinal Direct Current Stimulation Targets Ca^{2+} Channels to Induce Persistent Motor Unit Responses

Weiguo Song[1,2]* *and John H. Martin*[1,3]*

[1] Department of Molecular, Cellular, and Biomedical Sciences, Center for Discovery and Innovation, City University of New York School of Medicine, New York, NY, United States, [2] Institute of Bioelectronic Medicine, Feinstein Institutes for Medical Research, Manhasset, NY, United States, [3] Neuroscience Program, Graduate Center of the City University of New York, New York, NY, United States

Edited by:
Liming Li,
Shanghai Jiao Tong University, China

Reviewed by:
Tommaso Bocci,
University of Milan, Italy
C. J. Heckman,
Northwestern University,
United States
Piotr Krutki,
Poznań University of Physical
Education, Poland

***Correspondence:**
John H. Martin
jmartin@ccny.cuny.edu
Weiguo Song
wsong2@northwell.edu

Specialty section:
This article was submitted to
Neural Technology,
a section of the journal
Frontiers in Neuroscience

Received: *17 January 2022*
Accepted: *04 March 2022*
Published: *25 April 2022*

Citation:
Song W and Martin JH (2022)
Trans-Spinal Direct Current
Stimulation Targets Ca^{2+} *Channels*
to Induce Persistent Motor Unit
Responses.
Front. Neurosci. 16:856948.
doi: 10.3389/fnins.2022.856948

Trans-spinal direct current stimulation (tsDCS) is a neuromodulatory approach to augment spinal cord activity to improve function after neurological disease and injury. Little is known about the mechanisms underlying tsDCS actions on the motor system. The purpose of this study is to determine the role for a persistent inward current (PIC)-like response in motoneurons in mediating tsDCS actions. We recorded single motor units from the extensor and flexor carpi radialis muscles in healthy sedated rats and measured unit activity changes produced by cervical enlargement cathodal and anodal tsDCS (c-tsDCS; a-tsDCS). Both c-tsDCS and a-tsDCS immediately increased spontaneous motor unit firing during stimulation. After c-tsDCS was stopped, spontaneous firing persisted for a substantial period (165 ± 5s), yet after a-tsDCS activity shortly returned to baseline (27 ± 7s). Administration of the L-type calcium channel blocker Nimodipine reduced spontaneous motor unit firing during c-tsDCS and blocked the persistent response. By contrast, Nimodipine did not change unit firing during a-tsDCS but the short persistent response was blocked. Computer simulation using a two-compartment neuronal model replicated the main experimental observations: larger and more persistent responses during and after c-tsDCS than a-tsDCS. Using reduced Ca^{2+} conductance to model Nimodipine action, a reduced response during c-tsDCS and elimination of the persistent response was observed. Our experimental findings, supported by computer simulation, show that c-tsDCS can target Ca^{2+} conductances to augment motoneuron activity. As tsDCS is well-tolerated in humans, this knowledge informs therapeutic treatment strategies to achieve rehabilitation goals after injury; in particular, to increase muscle force.

Keywords: motoneuron, trans-spinal direct current stimulation, persistent inward current (PIC), nimodipine, spinal cord, rat

INTRODUCTION

Spinal neuromodulation is a promising strategy to augment spinal cord activity to promote motor function after injury (for review, see Ievins and Moritz, 2017 and Jack et al., 2020). Several approaches have been implemented in animal models and humans. Non-invasive trans-spinal cord direct current stimulation (tsDCS) has the potential for promoting spinal motor function through its modulatory actions on sensory processing (Aguilar et al., 2011), reflexes (Winkler et al., 2010; Song et al., 2015; Mekhael et al., 2019), the motor cortex motor map (Ahmed, 2013a; Song et al., 2015), and enhancing spinal motor circuit function and motor output (Ahmed, 2011; Jankowska, 2017; Song and Martin, 2017). tsDCS has also been used for treating different neurological diseases and injuries (e.g., Picelli et al., 2015 and Lamy et al., 2021) and for pain control (Guidetti et al., 2021). The effects of tsDCS tend to be polarity dependent. Most studies showed cathodal (c)-tsDCS augments muscle activity driven synaptically by CNS stimulation and anodal (a)-tsDCS, either has no effect or suppresses activity (Bolzoni et al., 2013; Baczyk et al., 2014; Bolzoni and Jankowska, 2015; Knikou et al., 2015; Song et al., 2016). However, the effects are not entirely consistent with reports of anodal facilitation (Ahmed, 2016; Baczyk et al., 2019, 2020b). Many questions remain unanswered about the mechanisms underlying tsDCS neuromodulation of spinal circuits, including the neuronal targets engaged by tsDCS (synaptic vs. intrinsic; interneurons and motoneurons) and the molecular underpinnings. Modeling and experimental studies suggesting that spinal nerve roots and spinal neurons—in particular, motoneurons (Elbasiouny and Mushahwar, 2007)—play a role in augmenting motor output with polarizing spinal neuromodulation (Hernandez-Labrado et al., 2011; Jankowska, 2017). Here we focus on the spinal motoneuron, through single motor unit recording, as a potential target for tsDCS.

Spinal motoneurons are located ventrally in the gray matter, with large cell bodies and extensive dendritic arbors, especially long dorsal branches (Stifani, 2014). Motoneurons have a myriad of synaptic and intrinsic molecular mechanisms enabling flexible excitability regulation (Heckman et al., 2003; Stifani, 2014). Voltage-dependent persistent inward currents (PICs or plateau potential) are leveraged by the motor systems to modulate motoneuron activity (Heckmann et al., 2005) and, as such, may be a potential target for neuromodulatory regulation of muscle functions. PICs are long-lasting responses that are primarily mediated by an L-type Ca^{2+} conductance (Hultborn, 2002). PICs increase motoneuronal firing rate and prolong the firing duration after stimulation has ended. PICs play important motor control roles during normal motor behavior (Kiehn and Eken, 1989; Gorassini et al., 1999; Gorassini et al., 2002a,b). After spinal injury, PICs become dysregulated and contribute to hyperreflexia and spasms (Heckman et al., 2003; Murray et al., 2010; Marcantoni et al., 2020). C-tsDCS enhances motor cortex-evoked muscle responses (MEPs) during (Ahmed, 2011; Knikou et al., 2015; Song et al., 2015) and after stimulation (Ahmed, 2011; Song et al., 2016). For transcranial DC stimulation, the capacity for prolonged MEP enhancement is thought to reflect activity-dependent plasticity (e.g., LTP) (Fritsch et al., 2010; Monte-Silva et al., 2013; Lefaucheur et al., 2017). Whereas LTP-like mechanisms may be engaged under some conditions, we propose that PICs—an intrinsic membrane mechanism—are a target of tsDCS neuromodulation. We focus on PICs because modeling of the neuronal response to DC stimulation indicates that the neuronal somato-dendritic membrane polarizes within the applied electric field (Bikson et al., 2004); especially the long dendritic processes of motoneurons (Elbasiouny and Mushahwar, 2007), which is where L-type $Ca^{2}+$ channels are predominantly localized (Heckmann et al., 2005).

In this study, we examine changes in spontaneous wrist muscle single motor unit firing induced by tsDCS as a means to understand its actions on motoneurons (Gorassini et al., 1999). We hypothesize that an increase in spontaneous motoneuron activity, assessed non-invasively using single motor unit recording, will occur during and persist following c-tsDCS. Persistent motor unit firing after stimulation is consistent with an increase in PICs in motoneurons (Gorassini et al., 1999). We recorded single unit responses in the extensor/flexor carpi radialis (ECR/FCR) muscles in sedated rats before, during, and following c-tsDCS and a-tsDCS of the cervical spinal cord (Song et al., 2015). We show that both c- and a-tsDCS consistently increased motor unit firing during stimulation but only c-tsDCS produced a robust persistent response. Pharmacological blockade of L-type calcium channels using Nimodipine, an FDA-approved L-type Ca^{2+} antagonist that has been used to mitigate spasticity in an animal injury model (Marcantoni et al., 2020), eliminated the persistent response. We also provide support for the major experimental observations using a computer simulation based on a two-compartment neuron model (Booth et al., 1997; Kurian et al., 2011; Kim, 2017; Lafon et al., 2017). Our study suggests that tsDCS modulates spinal activity, in part, by differentially acting on the dendrite and soma of motoneurons, with c-tsDCS preferentially activating Ca^{2+} channels in the dendrite to produce PICs, while a-tsDCS preferentially depolarizes the soma.

MATERIALS AND METHODS

The effects of c- and a-tsDCS on single motor unit firing and Nimodipine channel blocking experiments were examined in sedated rats (Sprague-Dawley; $n = 5$; 280–320 g). Experimental design incorporated repeated testing of animals with both c-tsDCS and a-tsDCS (two sessions). We allowed for a period of at least 7 days between each experiment in the same animal for any carryover effects to dissipate. All experiments were approved by the IACUC of the City University of New York Advanced Science Research Center.

Animal Preparation

Rats were sedated with ketamine (80 mg/kg, IP) during stimulation and recording for all experiments. Animals were placed on a table in a prone position with normal body temperature maintained with a heating blanket. The forepaw was placed in a posture that extended the wrist without inducing background electromyographic (EMG) activity. The sedation level was checked by monitoring the breathing rate, spontaneous vibrissae whisking, and hindlimb withdrawal to toe pinch. Supplemental doses of ketamine (25 mg/kg) were administered as needed to maintain the required sedation during the experiment. After final testing, rats were euthanized by IP administration of a Ketamine/Xylazine overdose.

Trans-Spinal Direct Current Stimulation

Two 1.5 cm × 2 cm gel patch electrodes (StimTent Com.) were used to deliver tsDCS. First, the hair over the dorsal neck and chest of the animal was shaved and further removed with Nair. Second, electrically conductive adhesive was sprayed over the contact surface of electrodes, to optimize and stabilize electrical conduction between the skin and electrodes, and then applied to fixed locations in each animal (dorsally, over C4-T1 and the other was placed over the chest; **Figure 1A**) according to the results of prior modeling experiments (Song et al., 2015). The polarity of tsDCS stimulation was referenced to the dorsal electrode (cathode). tsDCS was generated with an analog isolated stimulator (model 2200, A-M Systems), that was controlled by an analog output channel of an experimental control and data acquisition system (CED, Inc., Cambridge, United Kingdom). Twenty seconds of c-tsDCS (-3 mA) or a-tsDCS (+3 mA) was tested with a 3s ramp for both up and down phases (**Figures 1A,B**). To avoid the effect of cathodal stimulation on the anodal response, and vice versa, we typically recorded unit activity either in response to one or the other polarity during a given day. The tsDCS intensity of ±3 mA was chosen based on our previous observation and a modeling study indicating consistent effects on MEP enhancement with c-tsDCS (Song et al., 2015). This intensity (current density: 1 mA/cm^2; total charge density: 26 mC/cm^2) could induce consistent effects, and is below the threshold value for tissue damage (Yuen et al., 1981; McCreery et al., 1990; Liebetanz et al., 2009). This current produced reddening of the skin, especially at the edges of the electrode, but no damage.

Single Motor Unit Recording

Pairs of PFA-insulated stainless steel microwire electrodes (0.002" diameter, A-M Systems) were deinsulated at the tip (about 1 mm) and were inserted into the flexor carpi radialis (FCR) and/or extensor carpi radialis (ECR) muscles. EMGs from the recorded muscles were filtered (300–5000 Hz) and amplified (×1,000), and then digitized at a sampling frequency of 10 kHz with an acquisition system (CED, Inc). Raw EMG records (**Figure 1C**) were analyzed offline for single motor units. Spikes of single motor units were sorted according to principle component analysis (PCA) or template matching from the recorded EMG signals (**Figures 1C,D**) and further manually cluster-cut with a customized script written with Spike 2 (**Figure 1A**, inset). The firing rate of each sorted single motor unit was smoothed with a 1s sliding window, and the ensemble response was constructed from the smoothed firing of all the recorded motor units during c-tsDCS and a-tsDCS. The majority of the recorded motor units were from the ECR muscle, with additional recordings from FCR (c-tsDCS: ECR, 16; FCR, 4) and 22 (a-tsDCS ECR, 17; FCR, 5). No differences were found between ECR and FCR responses; thus, we combined data from the two muscles.

Classification of Motor Unit Response Pattern

We classified two response components of motor units (**Figure 1E**). The (1) direct response corresponds to unit firing during the ramp and plateau phases of tsDCS and (2) the persistent response corresponded to firing after the tsDCS had returned to baseline. Motor units were characterized according to the following five metrics: (1) the percentage of units that showed a direct response during tsDCS; (2) the firing rate during tsDCS; (3) the percentage of units that showed persistent firing after tsDCS; (4) persistent firing duration, which is the duration of elevated firing (over baseline) after cessation of tsDCS; and (5) persistent response gain, which is the ratio of the area of the persistent unit response over area of the direct response.

Ca^{2+} Channel Blockade

Since PICs are primarily mediated by an increase in inward calcium current (Li and Bennett, 2003), we used the L-type calcium channel blocker Nimodipine (125 mg, Sigma Inc., Burlington, MA, United States, USP grade) to determine if the persistent effect of tsDCS on motor unit firing is mediated by a calcium PIC. Nimodipine is a non-selective L-type Ca^{2+} channel blocker (Carlson et al., 2020). Nimodipine was dissolved in vehicle (ethanol, DMSO, polyethylene glycol and saline in the following proportions: 1:1:8:10), and then sterilized using a syringe filter (30 μm), and stored in a sterile dark bottle at room temperature. It was injected into the tail vein over a 3–5 min period (5 mg/kg). Induction time for the drug is approximately 30 min after IP injection (Marcantoni et al., 2020). We choose to use IV administration to obtain a faster response. We examined open field behavior after Nimodipine administration and did not observe any behavioral changes at this dose (data not shown).

Two-Compartment Computational Model to Predict Effect of Trans-Spinal Direct Current Stimulation on Motor Unit Firing

Experimental observations were compared with a computer simulation using a two-compartment neuron model. With this model, PICs were previously found to be changed after spinal cord injury (Kurian et al., 2011). This model also has been used to study normal spinal motor neuron behavior (Booth et al., 1997; Kim, 2017). The motor neuron was modeled with two simplified compartments: dendritic and axosomatic. Both compartments are described by active and passive conductances following the Hodgkin-Huxley formalism. The somatic compartment contains ionic conductances that generate action potentials. The dendritic compartment contains conductances responsible for plateau potentials for generating PICs. Voltage-dependent Na and Ca^{2+} channels were modeled in the dendrite only. The model included the following dendritic conductances: Na_p (Sodium, persistent); K_{Ca} (Potassium, Ca^{2+} dependent); Ca_p (Calcium, persistent); L (maximal leakage conductance). The following somatic conductances were modeled: Na (maximal Sodium conductance); Ca_N (Calcium, N-like); L (maximal leakage conductance); K_{Ca} (Potassium, Ca^{2+}-dependent); K_{dr} (Potassium, delayed rectified). All channel dynamics and transition rates, along with conductances for the model, were set according to published values (Kurian et al., 2011). tsDCS was modeled as an external electrical field, as previously described (Lafon et al., 2017). During direct current stimulation, the neuron will polarize along the

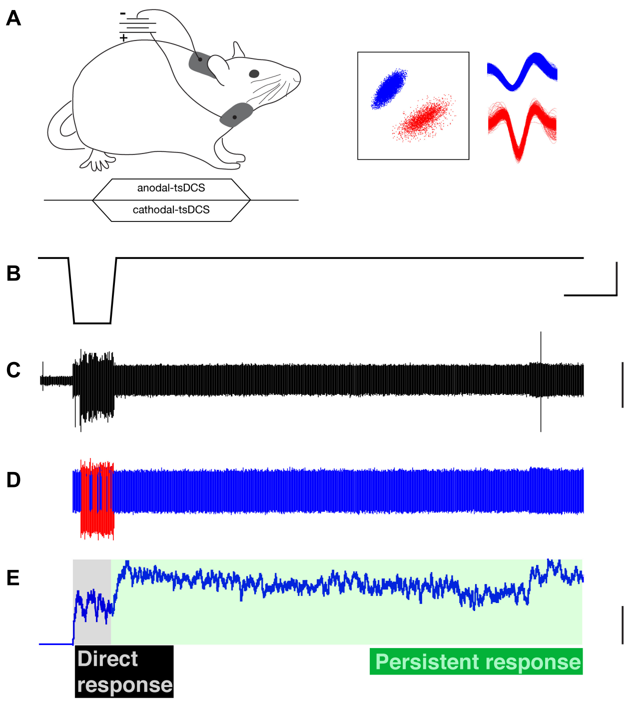

FIGURE 1 | Trans-spinal direct current stimulation (tsDCS) and single motor unit recording. **(A)** Schematic of experimental setup (top) and time-course of tsDCS (bottom). tsDCS was delivered through patch electrodes with the active electrode placed dorsally over the C4 to T1 vertebrae and the return electrode (i.e., opposite polarity) placed over chest. tsDCS was ramped over a 3s period to the maximal current, which was maintained for 20s, and ramped back to zero during a 3s period. **(B)** Cathodal-tsDCS waveform. **(C)** Raw electromyographic (EMG) recording (ECR muscle). **(D)** Raw EMG activity was sorted into single motor units using a PCA-based identification. Representative examples of two single motor units (red and blue). Their corresponding waveforms are shown in part **(A)** (right). **(E)** The firing rate was used to characterize the firing pattern; only the firing rate of the blue-colored unit is shown. The direct response is during the stimulation period (gray shading), whereas the persistent response is after tsDCS is turned off (green shading). Calibrations. **(B)** 25s, 2.5 vDC. C. 0.2 arbitrary units. **(E)** 25 Hz.

direction of the electric field. This results in opposite changes in membrane potential at the dendritic and somatic sties. The numerical solutions of the model were computed using ode15s function of Matlab (Mathworks, Inc., Nattic, MA, United States).

Statistical Analysis

The differences between two conditions (pre vs. post Nimodipine or a-tsDCS vs. c-tsDCS) within each group were assessed by parametric tests (*t*-test, MATLAB). We performed a linear regression. The non-parametric Kolmogorov–Smirnov test was used to assess differences in the distributions of two groups (K-S test, MATLAB). The significance level was set at 0.05. All data analyses were performed using MATLAB (The Math Works). In accordance with the Journal's Data Availability Declaration, for quantitative presentation of data, all values are shown.

RESULTS

Effects of Trans-Spinal Direct Current Stimulation on Motor Unit Activity

We first distinguished the effect of tsDCS during the period of stimulation (direct response) from unit firing that was changed after tsDCS ended (persistent response). A representative ECR EMG recording is shown (**Figures 2A,B**) and two units activated in response to c-tsDCS were isolated (**Figure 2C**). Motor unit activity is transformed into a continuous frequency plot (**Figure 2D**). C-tsDCS produces a robust increase in firing during stimulation for both units. Remarkably, the firing of one of the motor units (blue) is maintained for 210 seconds after stimulation ends. Whereas a-tsDCS (**Figure 2E**) also produced a direct effect, there was little or no maintenance of persistent unit firing (**Figures 2F–H**). Note, the delay in firing from stimulus onset of the red unit is due to the current ramp and the response threshold for the particular unit. In addition to showing modulatory effects on spontaneous single motor unit activity by tsDCS, we demonstrate that c-tsDCS produces a persistent response similar to the increase in motoneuronal firing observed during activation of a PIC. We also noticed for each of these units that c-tsDCS induced a stronger effect than a-tsDCS during testing (data not shown).

Direct Response Induced by Cathodal and Anodal Trans-Spinal Direct Current Stimulation

We recorded from a total of 20 motor units (ECR, 16; FCR, 4) during c-tsDCS and 22 (ECR, 17; FCR, 5) during a-tsDCS in five rats across multiple sessions with at least 7 days between any two sessions in the same animal. No differences were found between

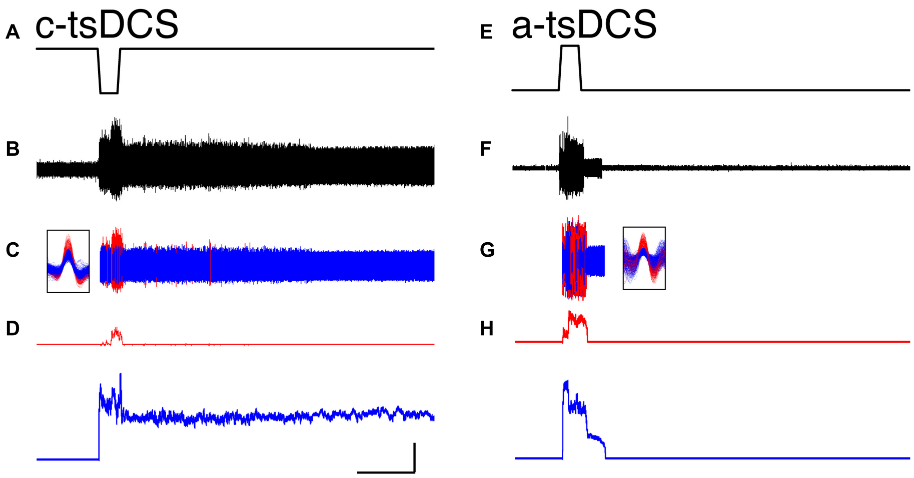

FIGURE 2 | Representative single motor unit responses during trans-spinal direct current stimulation (tsDCS) [**(A,E)**; ± 3 mA] during cathodal-tsDCS (c-tsDCS) **(A–D)** and anodal-tsDCS (a-tsDCS) **(E–H)**. Raw EMG activity **(B)**, single motor unit activity [**(C)**; red, blue for each unit], and response histograms **(D)** are shown. The unit waveforms were sorted from the raw EMG recording. Both c-tsDCS and a-tsDCS induced single motor unit responses during the stimulation period (direct response). Whereas responses persisted after stimulation stops for both polarities, c-tsDCS **(B–D)** evoked long-duration persistent responses. During a-tsDCS **(E–H)**, there was a brief persistent response. Note, the responses were truncated at 380s; the activity of the blue unit in A persisted for a total of approximately 532s. Calibration: 50s, 50 Hz.

ECR and FCR responses; thus, we combined date from the two muscles. The percentage of units that had a direct response was slightly higher in c-tsDCS (100%) than a-tsDCS (86%). The cumulative distribution function (**Figure 3A**) plots the mean firing rate during the stimulation period. There was no significant difference between c-tsDCS and a-tsDCS distributions (K&S test), nor was there a difference in mean firing rate (**Figure 3A**, inset; *t*-test, $p > 0.05$).

Cathodal Trans-Spinal Direct Current Stimulation Persistent Response Is Greater Than the Anodal Persistent Response

Similar to the direct response, most units showed some persistent response with either polarity (90% in c-tsDCS vs. 77% in a-tsDCS). However, the cumulative distribution functions of persistent firing duration were significantly different for the two polarities (**Figure 3B**; K-S test, $p < 0.05$) and show a wide range of response durations. The mean duration of the persistent increase in motor unit firing was approximately six-times longer after c-tsDCS than a-tsDCS (**Figure 3B**, inset; *t*-test, $p < 0.05$). We computed a measure of the gain of the persistent response for each unit (**Figure 3B**; persistent response area divided by direct response area) and found this was also approximately 6 times greater for cathodal than anodal stimulation (*t*-test, $p < 0.05$). Our findings suggest that c-tsDCS activates a PIC to prolong the elevated motor unit activity beyond the stimulation period.

Persistent Response Is Eliminated by Calcium Channel Blockade

To better understand the underlying mechanism of the persistent increase in motor unit firing during tsDCS, and to distinguish the mechanisms underlying the direct from the persistent responses, we administered the L-type Ca^{2+} channel blocker Nimodipine (5 mg/kg, IV; tested 15 min post-injection). We determined if Ca^{2+} channel blockade changed the properties of the direct and persistent responses. For the two units shown, the direct responses to c-tsDCS and a-tsDCS were similar (**Figures 4A,B**), whereas the persistent response was only produced by c-tsDCS. Nimodipine completely blocked the persistent response in the motor unit, with a smaller effect on the direct response (**Figure 4A**). Although there was no persistent response produced by a-tsDCS in the unit shown (**Figure 4B**) there was a small reduction in firing during the direct response. Interestingly, there was a small increase in the direct response duration but insufficient to produce a persistent effect after stimulation ceased. Ensemble responses (**Figures 4C,D**; 20 motor units in c-tsDCS and 22 in a-tsDCS) show complete elimination of the persistent response after c-tsDCS with approximately a 50% decrease in the peak of the direct response after Nimodipine (**Figure 4C**). In contrast, Nimodipine had a minimal effect on the direct response to a-tsDCS and the small persistent response that was produced, was eliminated (**Figure 4D**).

To better reveal how variable the response to Ca^{2+} channel blockade is, we plot the cumulative distribution function for the change in the direct response firing rate (**Figure 5A**; pre-Nimodipine minus post-Nimodipine). The plot shows a consistent reduction with c-tsDCS (rightward shift) and a mixture of symmetrical changes around zero for a-tsDCS. The effect of blockade on the two polarities was significant (K-S test, $p < 0.05$; **Figure 5A**). The percentage of motor units showing a direct response was significantly decreased after Nimodipine for c-tsDCS (−50%). than for a-tsDCS (−11%). The mean reduction in firing rate of the direct response after blockade was also significantly different between c-tsDCS and a-tsDCS

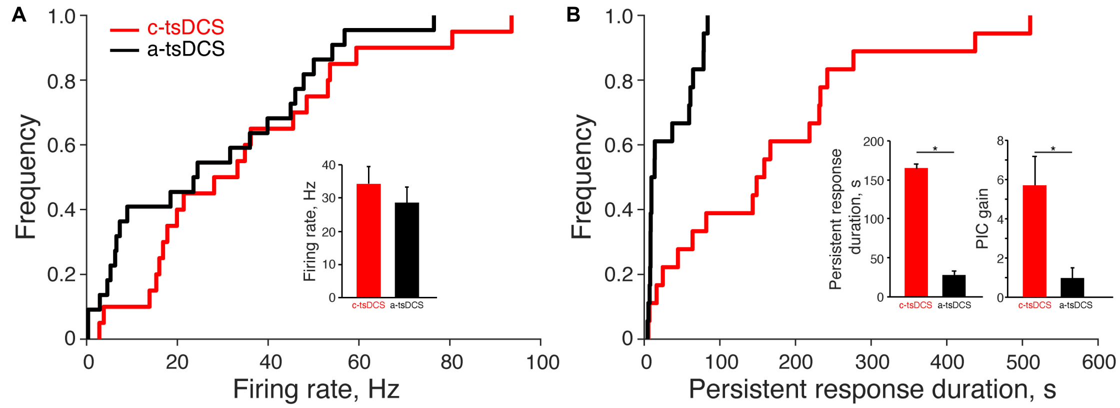

FIGURE 3 | Effect of trans-spinal direct current stimulation (tsDCS) on the motor unit direct and persistent response. **(A)** The cumulative distribution functions of the direct response for anodal-tsDCS (a-tsDCS) and cathodal-tsDCS (c-tsDCS) were not significantly different (K-S test, $p = 0.22$). Inset plots mean firing rates during both c-tsDCS and a-tsDCS, which were not significantly different (*t*-test, $p = 0.29$). **(B)** The cumulative distribution function of persistent response duration was significantly different between c-tsDCS and a-tsDCS (K-S test, $^*p = 0.0005$). The inset plots mean PIC duration, which was significantly longer for c-tsDCS (*t*-test, $^*p = 0.0002$) and PIC gain, was significantly longer and stronger during c-tsDCS than during a-tsDCS (*t*-test, $^*p = 0.006$).

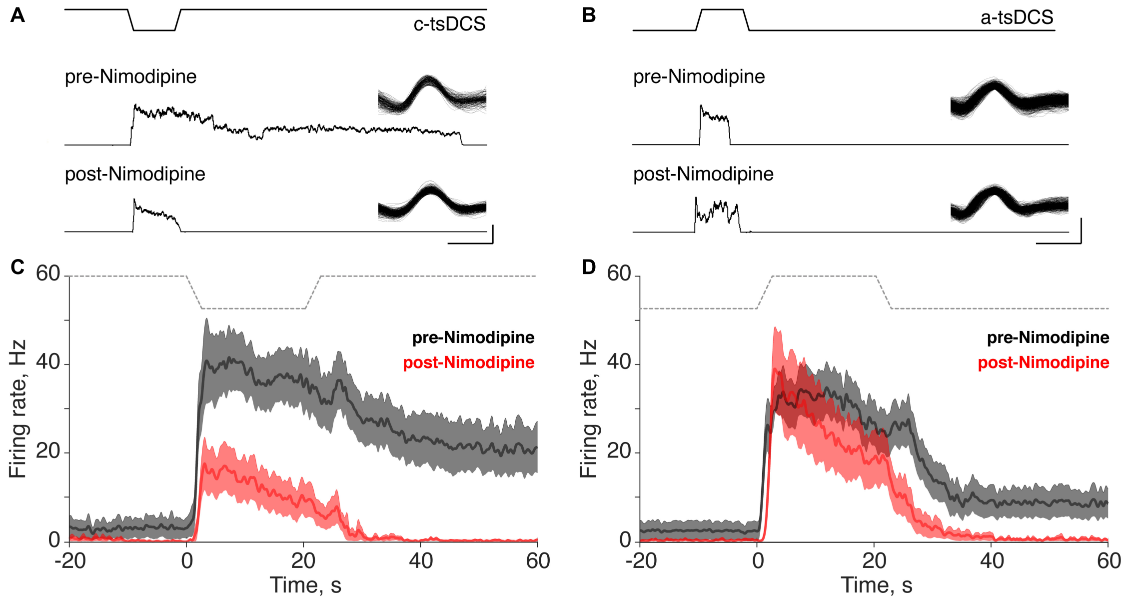

FIGURE 4 | Effect of the L-type calcium channel blocker Nimodipine on direct and persistent responses of trans-spinal direct current stimulation (tsDCS) (±3 mA). **(A,B)** Typical responses of single motor units before and after Nimodipine application during cathodal-tsDCS (c-tsDCS) **(A)** and anodal-tsDCS (a-tsDCS) **(B)**. From top to bottom, we show the tsDCS waveform, and pre- and post-Nimodipine unit histograms. The inset shows the waveform of the isolated motor unit. C-tsDCS induced both direct responses and persistent responses. For c-tsDCS, Nimodipine reduced the direct response and blocked the persistent response. Nimodipine did not change the response during a-tsDCS stimulation but did block the brief persistent response. The single unit waveforms were identified from the sorted single motor units from the raw data and the smoothed firing rate (1s window) before and after Nimodipine. **(C,D)** The ensemble response from all the recorded units shows that Nimodipine completely blocked the persistent response and also suppressed the direct response during c-tsDCS **(C)**. By contrast, a-tsDCS did not significantly affect the direct response during a-tsDCS **(D)**. The thick lines and shaded area **(C,D)** represent mean ±SE, and gray lines indicate the applied tsDCS.

(*t*-test, $p < 0.05$; **Figure 5A**, inset). The effect of calcium channel blockade on the direct response was linearly correlated with the mean firing rate of the direct response (**Figure 5B**). The larger the direct response the stronger the blockade effect for both c-tsDCS (slope: −0.70, R-sq: 0.59; $p < 0.05$) and a-tsDCS (slope: −0.62, R-sq 0.20; $p < 0.05$).

After Nimodipine administration, the duration of the persistent response showed a consistent reduction for the c-tsDCS and, not surprisingly, a negligible change for a-tsDCS (**Figure 5C**). Most of the persistent responses of motor units were blocked by Nimodipine for both c-tsDCS (−67%) and a-tsDCS (−58%). Similar to the direct response, the blockade effect was

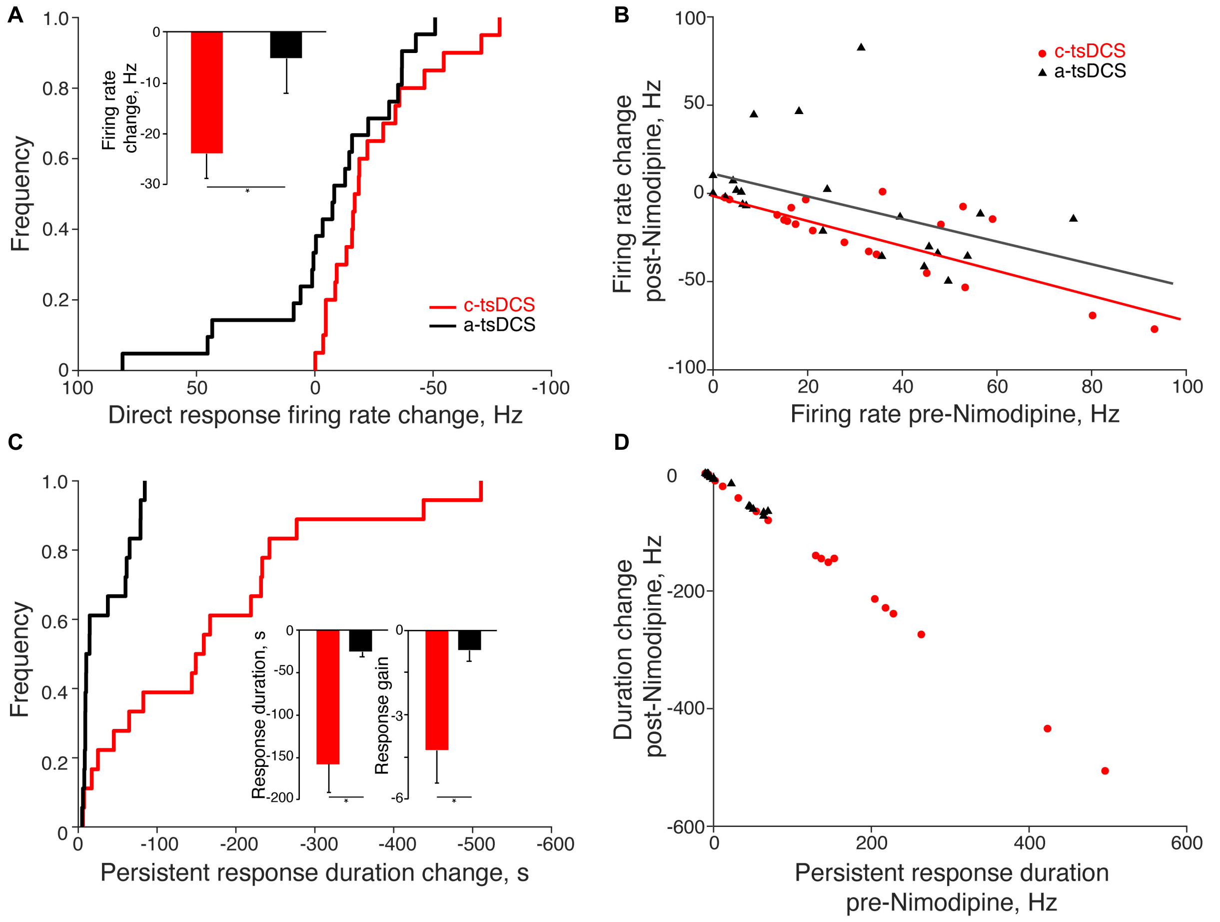

FIGURE 5 | Quantification of the effects of Nimodipine on the direct and persistent responses of single motor units. **(A)** The change of the direct response firing rate (post-Nimodipine response minus pre-Nimodipine response) was significantly larger for cathodal-tsDCS (c-tsDCS) than for anodal-tsDCS (a-tsDCS) (K-S test, $^{*}p = 0.046$) as shown in the cumulative distribution histogram. The inset plots the reduction in the firing rate during the direct response; the reduction was significantly greater for c-tsDCS than for a-tsDCS (*t*-test, $^{*}p = 0.03$). **(B)** The blockade effect of nimodipine was correlated with the direct response amplitude; each data point represents a single motor unit (c-tsDCS regression line: slope: −0.70, R-sq: 0.59, $p = 0.0001$; a-tsDCS regression line: slope −0.62, R-sq:0.20, $p = 0.04$). **(C)** The change in duration of the persistent response (post-Nimodipine response minus pre-Nimodipine response) was significantly greater for c-tsDCS than for a-tsDCS (K-S test, $^{*}p = 0.0005$). The insets plot the reduction in the duration (left), and gain (right) of the persistent response for both c- and a-tsDCS; the blockade effect of Nimodipine was significantly stronger for c-tsDCS than for a-tsDCS (*t*-test, duration $^{*}p = 0.0002$; gain $^{*}p = 0.04$). **(D)** The effect of blockade was correlated with the persistent response strength; each data point represents a single motor unit (c-tsDCS regression line: slope: −1.00, R-sq: 1.00, p = 1e-28; a-tsDCS regression line: slope −0.92, R-sq:0.98, p = 3e-18).

linearly correlated with the strength of persistent response: the larger the persistent response the stronger the blockade effect for both c-tsDCS and a-tsDCS (**Figure 5D**). The slope of this relationship is negative one (R:1, $p < 0.05$), thus affirming the strong L-type calcium channel dependence. Not surprisingly, the blockade effect was stronger for c-tsDCS than for a-tsDCS; for both persistent response duration and persistent response gain (**Figure 5C**, insets). Our findings reveal a robust effect of Nimodipine on abrogating the persistent response produced by c-tsDCS suggesting that the persistent response is mediated by a Ca^{2+} PIC.

Two-Compartment Simulation

We used a computer simulation of a two-compartment neuron model (Booth et al., 1997; Kurian et al., 2011; Kim, 2017) to inform our finding that the persistent motor unit response is mediated by a Ca^{2+} PIC. **Figure 6A** shows a schematic representation of the neuron model as well as its coupling to the external field through the extracellular potential difference V_E. Voltage-dependent sodium channels and calcium channels were modeled in the dendrite only (Heckman et al., 2003; Murray et al., 2010; Marcantoni et al., 2020). The motor neuron time constant and conductance parameters used in our simulation were chosen from a published paper (Kurian et al., 2011; Mekhael et al., 2019). The strength of the external applied direct current stimulation (DCS) was modeled according to our published data (Song et al., 2015), and the effect of calcium channel blockade produced by Nimodipine was modeled by a partial Ca^{2+} conductance block. We used a 10% reduction (from 0.35 to 0.315); however, progressive Ca^{2+}

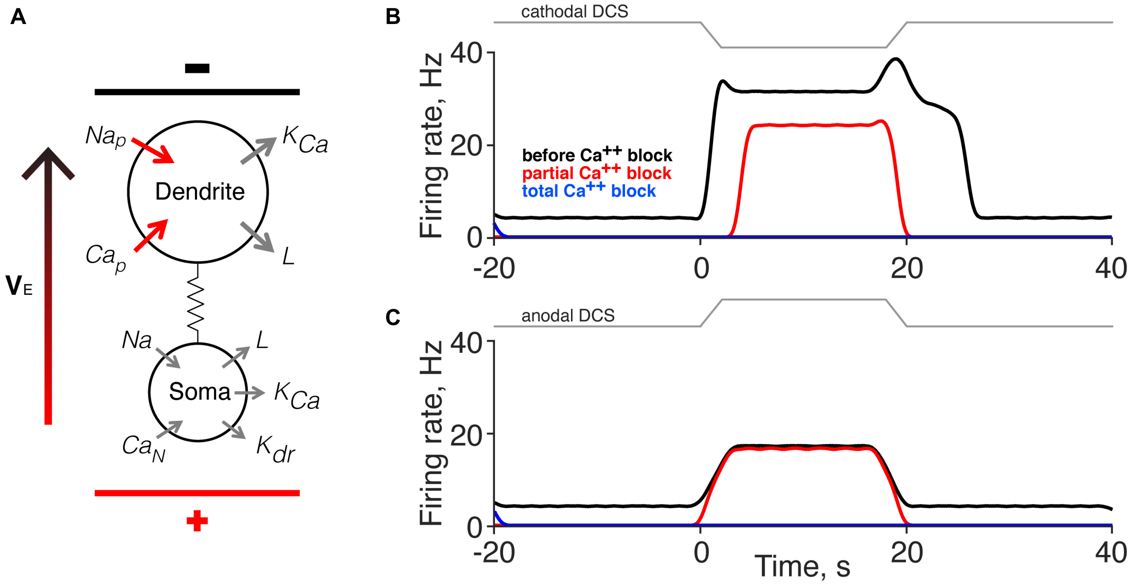

FIGURE 6 | Computer simulation of the effects of direct current stimulation (DCS) on the direct and persistent responses. **(A)** Schematic of the motoneuron model (Booth et al., 1997). Applied DCS was modeled as an external electrical field (V_E), which induces a current between soma and dendrite. The configuration in the model illustration corresponds to cathodal-tsDCS (c-tsDCS) in the experiment. Ca_p, Calcium, persistent; Ca_n, Calcium, N-like; K_{Ca}, Potassium, Ca^{2+} dependent; K_{dr}, Potassium, delayed rectified; L, maximal leakage conductance; Na, maximal Sodium conductance; Na_p, Sodium, persistent. **(B,C)** Computer simulation for response change produced by c-tsDCS **(B)** and anodal-tsDCS (a-tsDCS) **(C)**. The responses during c-tsDCS were stronger than that during a-tsDCS. Only c-tsDCS induced a persistent firing of motor units. The responses during c-tsDCS showed calcium channel-dependent; there was a reduction in the direct response and elimination of the persistent response. In contrast, the responses during a-tsDCS were not calcium channel dependent. Total calcium channel blockade eliminated all responses.

conductance reduction did not systematically and linearly reduce the direct response.

The model replicated the key features of the experimental findings. Parameters set for the model account for the presence of spontaneous activity (black line before and after DCS). Modeling cathodal DCS produced both direct and persistent responses (**Figure 6B**), similar to our experimental findings using c-tsDCS (**Figures 2D**, **4C**, pre-Nimodipine). Partial Ca^{2+} channel blockade reduced the direct response and eliminated the persistent response, which is similar to our experimental findings (**Figures 2D**, **4C**). By contrast, modeling anodal DCS produced only a direct response and this was unaffected by partial Ca^{2+} channel blockade (**Figure 6C**). Additionally, the direct response modeled by anodal DCS is smaller than during cathodal DCS. Results of our simulation suggest that both c-tsDCS and a-tsDCS activate motor units during tsDCS and this direct response is a balance between activation of the dendrites and the soma, whereas the persistent response is only present during c-tsDCS and is modulated by dendritic calcium channels.

DISCUSSION

Although the mechanisms of action of different neuromodulation strategies on spinal circuits are yielding to experimental and computational approaches, we are far from having a sufficient understanding to inform therapeutic decisions. We focused on tsDCS, a non-invasive neuromodulatory tool with the potential for improving motor function after neurological disease and injury (Rahman et al., 2013; Ahmed, 2014; Song et al., 2015, 2016; Mekhael et al., 2019; Abualait, 2020; Lamy et al., 2021). We show a novel action on motoneurons using single motor unit recordings; c-tsDCS produces a robust augmentation of spontaneous single motor unit firing that persists after stimulation stops. This response is blocked with Nimodipine, showing that L-type Ca^{2+} channels contribute to this neuromodulatory action and that PICs in motoneurons participate in the persistent response. A two-compartment somato-dendritic neuron computer simulation supports these experimental results. Knowledge that the actions of c-tsDCS produces spinal PIC-like responses informs therapeutic strategies for using tsDCS to promote function after injury.

Are Spinal Cord Neurons a Target Engaged by Trans-Spinal Direct Current Stimulation to Induce Persistent Motor Unit Firing?

It is not understood if the excitatory actions of c-tsDCS reflect membrane depolarization of spinal cord neurons or if it indirectly affects spinal neurons by depolarizing the axons of peripheral somatic sensory afferents and other intraspinal axons and terminals (Bolzoni and Jankowska, 2015; Formento et al., 2018), or supraspinal processing through ascending synaptic effects (Ahmed, 2013b; Bocci et al., 2014, 2015). Some studies suggest that a-tsDCS may affect axonal conduction, while c-tsDCS modulates interneuronal spinal networks (Bocci et al., 2014). Locally-applied (intraspinal) DC fields, in the microampere range, can enhance the excitability of intraspinal afferent fiber terminals (Bolzoni and Jankowska, 2015) and epidural direct current stimulation produces similar effects (Jankowska et al., 2017). Whereas there are multiple targets that could contribute to persistent firing, the well-known role for motoneuronal PICs is likely to be a dominant factor. We found that both cathodal and anodal stimulation produced a direct facilitatory effect (albeit a weaker anodal than cathodal response), but only cathodal stimulation produced a persistent response. Perhaps the absence of a direct cathodal facilitation with intracellular motoneuron recordings (Baczyk et al., 2019, 2020a) reflects the deeply anesthetized preparation. It is known that pentobarbital anesthesia does not support PICs (Button et al., 2006); there may be other molecular targets of tsDCS that are affected by deep anesthesia. The discrepancy may also be due to misalignment of the polarization field and dendrite orientation or sampling the activity of large motoneurons (Ahmed, 2016). Note that the enhanced motor unit firing during a-tsDCS is not significantly reduced by nimodipine, suggesting a source for activation other than the L-type Ca^{2+} channel. It is likely that there are multiple neural targets, especially if one considers both the direct and persistent effects. Further experiments and more sophisticated modeling [i.e., multi-compartment (Elbasiouny and Mushahwar, 2007)]; are needed to dissect the specificity of tsDCS actions. However, based on pharmacological blockade we propose that the L-type Ca^{2+} is a key mediator of the PIC.

Molecular-Level Mechanism of Trans-Spinal Direct Current Stimulation on Motoneuron

The effects of tsDCS, in both human and animal models, has been studied predominantly at the level of changes in motor cortex-evoked motor output [e.g., MEPs; also spinal LFPs; Ahmed (2011); Knikou et al. (2015), Song et al. (2015), and Song and Martin (2017)]. Changes in motoneuron excitability may reflect membrane polarization in response to the external applied electrical field, but also can be modulated through different ion channels (Booth et al., 1997; Rahman et al., 2013). Thus, changes in spontaneous activity of single motor units can provide insight into the molecular mechanism of tsDCS on motoneurons.

Similar to the facilitatory effect on motor cortex MEPs (Song et al., 2015), we also find facilitation of the spontaneous single motor unit response during c-tsDCS. However, in contrast to prior findings that a-tsDCS reduced motor cortex-evoked MEPs, the direct response during a-tsDCS increased, albeit less than for cathodal stimulation. This suggests differential actions of a-tsDCS on synaptically-evoked MEPs (Bolzoni and Jankowska, 2015) and on spontaneous single motor unit activity during the direct response (Bolzoni and Jankowska, 2015). Here, we show that tsDCS modulation of spontaneous activity is driven by intrinsic excitability mechanisms; in particular, the L-type calcium channel.

Polarization of hippocampal neurons in brain slices affects both spontaneous firing rate and synaptic efficacy (Lafon et al., 2017). We also found that tsDCS could modulate motoneuron PIC gain, with the c-tsDCS effect being substantially greater than that of a-tsDCS. The two-compartment model showed that the PIC arises predominantly from dendritic Ca^{2+} influx (Kurian et al., 2011). Although c-tsDCS could hyperpolarize the somatic membrane potential (i.e., DC-induced neuronal polarization), the strong inward current from the dendrite would be expected to depolarize the soma, causing a plateau potential. Our findings point to the principal mechanism for this augmentation as activation of the voltage-dependent calcium channel within the dendritic compartment to produce a PIC-like motoneuronal response.

Limitations of the Two-Compartment Model

We hoped to model the question of whether tsDCS field polarization, through actions on dendritic Ca^{2+} channels and PICs, can lead to persistent motor unit firing. Whereas tsDCS could act on spinal neurons through synaptic and network actions, persistent firing and PICs are largely an intrinsic membrane property and the action of motoneurons. This suggests that a two-compartment motoneuron model would be sufficient. The model accounted for the smaller anodal direct effect and the larger cathodal direct and persistent effects we observed experimentally. Further, it also accounted for L-type Ca channel blockade and the loss of the persistent effect, but not the direct effect. The two-compartment model did not capture the very long duration persistent responses after c-tsDCS. Although we were able to model the reduction in the c-tsDCS direct response and elimination of the persistent response to both polarities with a 10% reduction in Ca^{2+} conductance, systematically smaller reductions did not yield progressive response reductions. These findings stress non-linear dynamics underlying tsDCS neuromodulation (Elbasiouny and Mushahwar, 2007). What might contribute to these differences between experimental and modeling effects? The orientation of motoneuron dendritic arbors is heterogeneous. During c-tsDCS, some motoneurons would be expected to experience full cathodal stimulation, whereas others would simultaneously experience anodal stimulation because of differences in their somato-dendritic axes. The particular activity change of each motor unit during tsDCS could be the effect of a combination of c-tsDCS or a-tsDCS depending on its soma-dendritic orientation and susceptibility to polarization by the applied tsDCS. Although most dendrites of motoneurons are located dorsal to the soma (Balaskas et al., 2019), with a net orientation parallel to the applied tsDCS field, the soma-dendritic orientation relative to the external field varies (see **Figure 6**). A multicompartment motoneuron model showed that the non-linear properties of the voltage-gated Ca^{2+} channel could lead to suppression of PICs in both depolarized or hyperpolarized dendritic regions (Elbasiouny and Mushahwar, 2007). However, motoneuron dendrites were modeled with a radially symmetrical morphology around the soma, which may have led to different predictions and did not accord with our experimental results. Considering the single dendritic compartment in the model we developed, it suggests that two dominant factors leading to persistent firing after c-tsDCS are polarization of the dorsally- (or dorsomedially-) directed dendritic arbor and dendritic localization of the Ca channels.

Clinical Significance of Trans-Spinal Direct Current Stimulation for Rehabilitation After Injury

Phasic activation of spinal motor circuits holds much promise to improve motor function in humans after spinal cord injury (SCI) (Angeli et al., 2014, 2018; Pena Pino et al., 2020), and the effects of a similar phasic stimulation showed a frequency and segmental-level dependence (Vogelstein et al., 2006). Phasic spinal stimulation is thought to activate CPGs, possibly through activation of large-diameter proprioceptive inputs (Formento et al., 2018). Moreover, non-invasive phasic stimulation methods are being developed to target the human spinal cord after injury (Inanici et al., 2021). The noninvasive application of tsDCS using surface electrodes is appropriate for behaving animals and humans. By developing an understanding of the molecular mechanisms of tsDCS, we can better inform therapeutic strategies of this method for promoting function after spinal injury. The specific effect of augmenting PIC-like responses with c-tsDCS is a novel molecular target. It must be stressed that PIC-like responses are produced during naturally-occurring motor actions in rats and humans (Kiehn and Eken, 1989; Gorassini et al., 2002a,b). PICs are regarded to be an important component of normal motor control and, together with a wide-range of channel types in motoneurons, offer extraordinary flexibility for muscle force control (Heckmann et al., 2005). Enhancing the PIC-like response of motor units induced by c-tsDCS would be well-suited to potentiate motor strength after SCI.

After complete sacral transection, the 5-HT2_C receptor caudal to injury can become constitutively active, resulting in unregulated PICs that contribute to hyperreflexia and spasms (Murray et al., 2010). This is thought to reflect the loss of descending monoaminergic regulation of motoneuronal excitability. Since hyperreflexia and spasticity are considered to reflect enhances spinal excitability, would c-tsDCS exacerbate these conditions in the injured spinal cord? Or through its targeted use to counter the loss of descending excitatory control signals, might it interrupt the circle of loss of excitability leading to maladaptive hyperreflexia that occurs after SCI, and especially after perinatal corticospinal system injury (Cavarsan et al., 2019; Steele et al., 2020)? The mechanism for PIC-like motor unit firing induced by c-tsDCS, L-type Ca^{2+} channel activation, has recently been targeted pharmacologically with Nimodipine to ameliorate spasticity in mice after complete sacral SCI (Marcantoni et al., 2020). This adds to the well-known amelioration of spasticity after rehabilitation (Cote et al., 2014; Beverungen et al., 2020). C-tsDCS neuromodulation enhances PICs, and presumably force capacity, which is necessary to improve motor capacity post-injury. By contrast, Nimodipine reduces PICs and presumably force capacity, thereby exacerbating weakness but ameliorating hyperreflexia. Intriguingly, these two interventions might be recruited in different combinations and different times after motor system injury—as spinal excitability changes evolve and hyperreflexia and spasms develop—to modify PIC production bidirectionally for different rehabilitation goals.

DATA AVAILABILITY STATEMENT

The original contributions presented in the study are included in the article/supplementary material, further inquiries can be directed to the corresponding author/s.

ETHICS STATEMENT

The animal study was reviewed and approved by City University of New York Advanced Science Research Center IACUC.

AUTHOR CONTRIBUTIONS

WS performed the research and analyzed the data. JM supervised all aspects of work. Both authors designed the research, wrote the manuscript, and approved the submitted version.

FUNDING

This work was supported by the NIH (JM: 2R01NS064004) and New York State Spinal Cord Injury Board (JM: DOH01-C30606GG).

REFERENCES

Abualait, T. S. (2020). Effects of transcranial direct current stimulation of primary motor cortex on cortical sensory deficits and hand dexterity in a patient with stroke: a case study. *J. Int. Med. Res.* 48:300060519894137. doi: 10.1177/0300060519894137

Aguilar, J., Pulecchi, F., Dilena, R., Oliviero, A., Priori, A., and Foffani, G. (2011). Spinal direct current stimulation modulates the activity of gracile nucleus and primary somatosensory cortex in anaesthetized rats. *J. Physiol.* 589, 4981–4996. doi: 10.1113/jphysiol.2011.214189

Ahmed, Z. (2011). Trans-spinal direct current stimulation modulates motor cortex-induced muscle contraction in mice. *J. Appl. Physiol.* 110, 1414–1424. doi: 10.1152/japplphysiol.01390.2010

Ahmed, Z. (2013a). Effects of cathodal trans-spinal direct current stimulation on mouse spinal network and complex multijoint movements. *J. Neurosci.* 33, 14949–14957. doi: 10.1523/JNEUROSCI.2793-13.2013

Ahmed, Z. (2013b). Electrophysiological characterization of spino-sciatic and cortico-sciatic associative plasticity: modulation by trans-spinal direct current and effects on recovery after spinal cord injury in mice. *J. Neurosci.* 33, 4935–4946. doi: 10.1523/JNEUROSCI.4930-12.2013

Ahmed, Z. (2014). Trans-spinal direct current stimulation alters muscle tone in mice with and without spinal cord injury with spasticity. *J. Neurosci.* 34, 1701–1709. doi: 10.1523/JNEUROSCI.4445-13.2014

Ahmed, Z. (2016). Modulation of gamma and alpha spinal motor neurons activity by trans-spinal direct current stimulation: effects on reflexive actions and locomotor activity. *Physiol. Rep.* 4:e12696. doi: 10.14814/phy2.12696

Angeli, C. A., Boakye, M., Morton, R. A., Vogt, J., Benton, K., Chen, Y., et al. (2018). Recovery of over-ground walking after chronic motor complete spinal cord injury. *N. Engl. J. Med.* 379, 1244–1250. doi: 10.1056/NEJMoa1803588

Angeli, C. A., Edgerton, V. R., Gerasimenko, Y. P., and Harkema, S. J. (2014). Altering spinal cord excitability enables voluntary movements after chronic complete paralysis in humans. *Brain* 137, 1394–1409. doi: 10.1093/brain/awu038

Baczyk, M., Drzymala-Celichowska, H., Mrowczynski, W., and Krutki, P. (2019). Motoneuron firing properties are modified by trans-spinal direct current stimulation in rats. *J. Appl. Physiol. (1985)* 126, 1232–1241. doi: 10.1152/japplphysiol.00803.2018

Baczyk, M., Drzymala-Celichowska, H., Mrowczynski, W., and Krutki, P. (2020b). Polarity-dependent adaptations of motoneuron electrophysiological properties after 5-wk transcutaneous spinal direct current stimulation in rats. *J. Appl. Physiol. (1985)* 129, 646–655. doi: 10.1152/japplphysiol.00301.2020

Baczyk, M., Drzymala-Celichowska, H., Mrowczynski, W., and Krutki, P. (2020a). Long-lasting modifications of motoneuron firing properties by trans-spinal direct current stimulation in rats. *Eur. J. Neurosci.* 51, 1743–1755. doi: 10.1111/ejn.14612

Baczyk, M., Pettersson, L. G., and Jankowska, E. (2014). Facilitation of ipsilateral actions of corticospinal tract neurons on feline motoneurons by transcranial direct current stimulation. *Eur. J. Neurosci.* 40, 2628–2640. doi: 10.1111/ejn.12623

Balaskas, N., Abbott, L. F., Jessell, T. M., and Ng, D. (2019). Positional strategies for connection specificity and synaptic organization in spinal sensory-motor circuits. *Neuron* 102, 1143–1156 e1144. doi: 10.1016/j.neuron.2019.04.008

Beverungen, H., Klaszky, S. C., Klaszky, M., and Cote, M. P. (2020). Rehabilitation decreases spasticity by restoring chloride homeostasis through the brain-derived neurotrophic factor-KCC2 pathway after spinal cord injury. *J. Neurotrauma* 37, 846–859. doi: 10.1089/neu.2019.6526

Bikson, M., Inoue, M., Akiyama, H., Deans, J. K., Fox, J. E., Miyakawa, H., et al. (2004). Effects of uniform extracellular DC electric fields on excitability in rat hippocampal slices in vitro. *J. Physiol.* 557, 175–190. doi: 10.1113/jphysiol.2003.055772

Bocci, T., Marceglia, S., Vergari, M., Cognetto, V., Cogiamanian, F., Sartucci, F., et al. (2015). Transcutaneous spinal direct current stimulation modulates human corticospinal system excitability. *J. Neurophysiol.* 114, 440–446. doi: 10.1152/jn.00490.2014

Bocci, T., Vannini, B., Torzini, A., Mazzatenta, A., Vergari, M., Cogiamanian, F., et al. (2014). Cathodal transcutaneous spinal direct current stimulation (tsDCS) improves motor unit recruitment in healthy subjects. *Neurosci. Lett* .578, 75–79. doi: 10.1016/j.neulet.2014.06.037

Bolzoni, F., and Jankowska, E. (2015). Presynaptic and postsynaptic effects of local cathodal DC polarization within the spinal cord in anaesthetized animal preparations. *J. Physiol.* 593, 947–966. doi: 10.1113/jphysiol.2014.285940

Bolzoni, F., Baczyk, M., and Jankowska, E. (2013). Subcortical effects of transcranial direct current stimulation in the rat. *J. Physiol.* 591, 4027–4042. doi: 10.1113/jphysiol.2013.257063

Booth, V., Rinzel, J., and Kiehn, O. (1997). Compartmental model of vertebrate motoneurons for Ca2+-dependent spiking and plateau potentials under pharmacological treatment. *J. Neurophysiol.* 78, 3371–3385. doi: 10.1152/jn.1997.78.6.3371

Button, D. C., Gardiner, K., Marqueste, T., and Gardiner, P. F. (2006). Frequency-current relationships of rat hindlimb alpha-motoneurones. *J. Physiol.* 573, 663–677. doi: 10.1113/jphysiol.2006.107292

Carlson, A. P., Hanggi, D., Macdonald, R. L., and Shuttleworth, C. W. (2020). Nimodipine reappraised: an old drug with a future. *Curr. Neuropharmacol.* 18, 65–82. doi: 10.2174/1570159X17666190927113021

Cavarsan, C. F., Gorassini, M. A., and Quinlan, K. A. (2019). Animal models of developmental motor disorders: parallels to human motor dysfunction in cerebral palsy. *J. Neurophysiol.* 122, 1238–1253. doi: 10.1152/jn.00233.2019

Cote, M. P., Gandhi, S., Zambrotta, M., and Houle, J. D. (2014). Exercise modulates chloride homeostasis after spinal cord injury. *J. Neurosci.* 34, 8976–8987. doi: 10.1523/JNEUROSCI.0678-14.2014

Elbasiouny, S. M., and Mushahwar, V. K. (2007). Suppressing the excitability of spinal motoneurons by extracellularly applied electrical fields: insights from computer simulations. *J. Appl. Physiol. (1985)* 103, 1824–1836. doi: 10.1152/japplphysiol.00362.2007

Formento, E., Minassian, K., Wagner, F., Mignardot, J. B., Le Goff-Mignardot, C. G., Rowald, A., et al. (2018). Electrical spinal cord stimulation must preserve proprioception to enable locomotion in humans with spinal cord injury. *Nat. Neurosci.* 21, 1728–1741. doi: 10.1038/s41593-018-0262-6

Fritsch, B., Reis, J., Martinowich, K., Schambra, H. M., Ji, Y., Cohen, L. G., et al. (2010). Direct current stimulation promotes BDNF-dependent synaptic plasticity: potential implications for motor learning. *Neuron* 66, 198–204. doi: 10.1016/j.neuron.2010.03.035

Gorassini, M., Bennett, D. J., Kiehn, O., Eken, T., and Hultborn, H. (1999). Activation patterns of hindlimb motor units in the awake rat and their relation to motoneuron intrinsic properties. *J. Neurophysiol.* 82, 709–717. doi: 10.1152/jn.1999.82.2.709

Gorassini, M., Yang, J. F., Siu, M., and Bennett, D. J. (2002a). Intrinsic activation of human motoneurons: possible contribution to motor unit excitation. *J. Neurophysiol.* 87, 1850–1858. doi: 10.1152/jn.00024.2001

Gorassini, M., Yang, J. F., Siu, M., and Bennett, D. J. (2002b). Intrinsic activation of human motoneurons: reduction of motor unit recruitment thresholds by repeated contractions. *J. Neurophysiol.* 87, 1859–1866. doi: 10.1152/jn.00025.2001

Guidetti, M., Ferrucci, R., Vergari, M., Aglieco, G., Naci, A., Versace, S., et al. (2021). Effects of transcutaneous spinal direct current stimulation (tsDCS) in patients with chronic pain: a clinical and neurophysiological study. *Front. Neurol.* 12:695910. doi: 10.3389/fneur.2021.695910

Heckman, C. J., Lee, R. H., and Brownstone, R. M. (2003). Hyperexcitable dendrites in motoneurons and their neuromodulatory control during motor behavior. *Trends Neurosci.* 26, 688–695. doi: 10.1016/j.tins.2003.10.002

Heckmann, C. J., Gorassini, M. A., and Bennett, D. J. (2005). Persistent inward currents in motoneuron dendrites: implications for motor output. *Muscle Nerve* 31, 135–156. doi: 10.1002/mus.20261

Hernandez-Labrado, G. R., Polo, J. L., Lopez-Dolado, E., and Collazos-Castro, J. E. (2011). Spinal cord direct current stimulation: finite element analysis of the electric field and current density. *Med. Biol. Eng. Comput.* 49, 417–429. doi: 10.1007/s11517-011-0756-9

Hultborn, H. (2002). Plateau potentials and their role in regulating motoneuronal firing. *Adv. Exp. Med. Biol.* 508, 213–218. doi: 10.1007/978-1-4615-0713-0_26

Ievins, A., and Moritz, C. T. (2017). Therapeutic stimulation for restoration of function after spinal cord injury. *Physiology (Bethesda)* 32, 391–398. doi: 10.1152/physiol.00010.2017

Inanici, F., Brighton, L. N., Samejima, S., Hofstetter, C. P., and Moritz, C. T. (2021). Transcutaneous spinal cord stimulation restores hand and arm function after spinal cord injury. *IEEE Trans. Neural Syst. Rehabil. Eng.* 29, 310–319. doi: 10.1109/TNSRE.2021.3049133

Jack, A. S., Hurd, C., Martin, J., and Fouad, K. (2020). Electrical stimulation as a tool to promote plasticity of the injured spinal cord. *J. Neurotrauma* 37, 1933–1953. doi: 10.1089/neu.2020.7033

Jankowska, E. (2017). Spinal control of motor outputs by intrinsic and externally induced electric field potentials. *J. Neurophysiol* 118, 1221–1234. doi: 10.1152/jn.00169.2017

Jankowska, E., Kaczmarek, D., Bolzoni, F., and Hammar, I. (2017). Long-lasting increase in axonal excitability after epidurally applied DC. *J. Neurophysiol.* 118, 1210–1220. doi: 10.1152/jn.00148.2017

Kiehn, O., and Eken, T. (1989). Bistable firing properties of soleus motor units in unrestrained rats. *Acta Physiol. Scand.* 136, 383–394. doi: 10.1111/j.1748-1716.1989.tb08679.x

Kim, H. (2017). Impact of the localization of dendritic calcium persistent inward current on the input-output properties of spinal motoneuron pool: a computational study. *J. Appl. Physiol. (1985)* 123, 1166–1187. doi: 10.1152/japplphysiol.00034.2017

Knikou, M., Dixon, L., Santora, D., and Ibrahim, M. M. (2015). Transspinal constant-current long-lasting stimulation: a new method to induce cortical and corticospinal plasticity. *J. Neurophysiol.* 114, 1486–1499. doi: 10.1152/jn.00449.2015

Kurian, M., Crook, S. M., and Jung, R. (2011). Motoneuron model of self-sustained firing after spinal cord injury. *J. Comput. Neurosci.* 31, 625–645. doi: 10.1007/s10827-011-0324-1

Lafon, B., Rahman, A., Bikson, M., and Parra, L. C. (2017). Direct current stimulation alters neuronal input/output function. *Brain Stimul.* 10, 36–45. doi: 10.1016/j.brs.2016.08.014

Lamy, J. C., Varriale, P., Apartis, E., Mehdi, S., Blancher-Meinadier, A., Kosutzka, Z., et al. (2021). Trans-spinal direct current stimulation for managing primary orthostatic tremor. *Mov. Disord.* 36, 1835–1842. doi: 10.1002/mds.28581

Lefaucheur, J. P., Antal, A., Ayache, S. S., Benninger, D. H., Brunelin, J., Cogiamanian, F., et al. (2017). Evidence-based guidelines on the therapeutic use of transcranial direct current stimulation (tDCS). *Clin. Neurophysiol.* 128, 56–92. doi: 10.1016/j.clinph.2016.10.087

Li, Y., and Bennett, D. J. (2003). Persistent sodium and calcium currents cause plateau potentials in motoneurons of chronic spinal rats. *J. Neurophysiol.* 90, 857–869. doi: 10.1152/jn.00236.2003

Liebetanz, D., Koch, R., Mayenfels, S., Konig, F., Paulus, W., and Nitsche, M. A. (2009). Safety limits of cathodal transcranial direct current stimulation in rats. *Clin. Neurophysiol.* 120, 1161–1167. doi: 10.1016/j.clinph.2009.01.022

Marcantoni, M., Fuchs, A., Low, P., Bartsch, D., Kiehn, O., and Bellardita, C. (2020). Early delivery and prolonged treatment with nimodipine prevents the development of spasticity after spinal cord injury in mice. *Sci. Transl. Med.* 12:eaay0167. doi: 10.1126/scitranslmed.aay0167

McCreery, D. B., Agnew, W. F., Yuen, T. G., and Bullara, L. (1990). Charge density and charge per phase as cofactors in neural injury induced by electrical stimulation. *IEEE Trans. Biomed. Eng.* 37, 996–1001. doi: 10.1109/10.102812

Mekhael, W., Begum, S., Samaddar, S., Hassan, M., Toruno, P., Ahmed, M., et al. (2019). Repeated anodal trans-spinal direct current stimulation results in long-term reduction of spasticity in mice with spinal cord injury. *J. Physiol.* 597, 2201–2223. doi: 10.1113/JP276952

Monte-Silva, K., Kuo, M. F., Hessenthaler, S., Fresnoza, S., Liebetanz, D., Paulus, W., et al. (2013). Induction of late LTP-like plasticity in the human motor cortex by repeated non-invasive brain stimulation. *Brain Stimul.* 6, 424–432. doi: 10.1016/j.brs.2012.04.011

Murray, K. C., Nakae, A., Stephens, M. J., Rank, M., D'amico, J., Harvey, P. J., et al. (2010). Recovery of motoneuron and locomotor function after spinal cord injury depends on constitutive activity in 5-HT2C receptors. *Nat. Med.* 16, 694–700. doi: 10.1038/nm.2160

Pena Pino, I., Hoover, C., Venkatesh, S., Ahmadi, A., Sturtevant, D., Patrick, N., et al. (2020). Long-term spinal cord stimulation after chronic complete spinal cord injury enables volitional movement in the absence of stimulation. *Front. Syst. Neurosci.* 14:35. doi: 10.3389/fnsys.2020.00035

Picelli, A., Chemello, E., Castellazzi, P., Roncari, L., Waldner, A., Saltuari, L., et al. (2015). Combined effects of transcranial direct current stimulation (tDCS) and transcutaneous spinal direct current stimulation (tsDCS) on robot-assisted gait training in patients with chronic stroke: a pilot, double blind, randomized controlled trial. *Restor. Neurol. Neurosci.* 33, 357–368.

Rahman, A., Reato, D., Arlotti, M., Gasca, F., Datta, A., Parra, L. C., et al. (2013). Cellular effects of acute direct current stimulation: somatic and synaptic terminal effects. *J. Physiol.* 591, 2563–2578. doi: 10.1113/jphysiol.2012.247171

Song, W., Amer, A., Ryan, D., and Martin, J. H. (2016). Combined motor cortex and spinal cord neuromodulation promotes corticospinal system functional and structural plasticity and motor function after injury. *Exp. Neurol.* 277, 46–57. doi: 10.1016/j.expneurol.2015.12.008

Song, W., and Martin, J. H. (2017). Spinal cord direct current stimulation differentially modulates neuronal activity in the dorsal and ventral spinal cord. *J. Neurophysiol.* 117, 1143–1155. doi: 10.1152/jn.00584.2016

Song, W., Truong, D. Q., Bikson, M., and Martin, J. H. (2015). Transspinal direct current stimulation immediately modifies motor cortex sensorimotor maps. *J. Neurophysiol.* 113, 2801–2811. doi: 10.1152/jn.00784.2014

Steele, P. R., Cavarsan, C. F., Dowaliby, L., Westefeld, M., Katenka, N., Drobyshevsky, A., et al. (2020). Altered motoneuron properties contribute to motor deficits in a rabbit hypoxia-ischemia model of cerebral palsy. *Front. Cell Neurosci.* 14:69. doi: 10.3389/fncel.2020.00069

Stifani, N. (2014). Motor neurons and the generation of spinal motor neuron diversity. *Front. Cell Neurosci.* 8:293. doi: 10.3389/fncel.2014.00293

Vogelstein, R. J., Etienne-Cummings, R., Thakor, N. V., and Cohen, A. H. (2006). Phase-dependent effects of spinal cord stimulation on locomotor activity. *IEEE Trans. Neural Syst. Rehabil. Eng.* 14, 257–265. doi: 10.1109/TNSRE.2006.881586

Winkler, T., Hering, P., and Straube, A. (2010). Spinal DC stimulation in humans modulates post-activation depression of the H-reflex depending on current polarity. *Clin. Neurophysiol.* 121, 957–961. doi: 10.1016/j.clinph.2010.01.014

Yuen, T. G., Agnew, W. F., Bullara, L. A., Jacques, S., and Mccreery, D. B. (1981). Histological evaluation of neural damage from electrical stimulation: considerations for the selection of parameters for clinical application. *Neurosurgery* 9, 292–299. doi: 10.1227/00006123-198109000-00013

Conflict of Interest: The authors declare that the research was conducted in the absence of any commercial or financial relationships that could be construed as a potential conflict of interest.

frontiers | Frontiers in Neuroscience

ORIGINAL RESEARCH
published: 13 June 2022
doi: 10.3389/fnins.2022.908858

The Long-Term Stability of Intracortical Microstimulation and the Foreign Body Response Are Layer Dependent

Morgan E. Urdaneta[1]*, Nicolas G. Kunigk[2], Seth Currlin[1], Francisco Delgado[2], Shelley I. Fried[3,4] and Kevin J. Otto[1,2,5,6,7]*

[1] Department of Neuroscience, University of Florida, Gainesville, FL, United States, [2] J. Crayton Pruitt Family Department of Biomedical Engineering, University of Florida, Gainesville, FL, United States, [3] Department of Neurosurgery, Massachusetts General Hospital, Harvard Medical School, Boston, MA, United States, [4] Boston Veterans Affairs Healthcare System, Boston, MA, United States, [5] Department of Materials Science and Engineering, University of Florida, Gainesville, FL, United States, [6] Department of Neurology, University of Florida, Gainesville, FL, United States, [7] Department of Electrical and Computer Engineering, University of Florida, Gainesville, FL, United States

Intracortical microstimulation (ICMS) of the somatosensory cortex (S1) can restore sensory function in patients with paralysis. Studies assessing the stability of ICMS have reported heterogeneous responses across electrodes and over time, potentially hindering the implementation and translatability of these technologies. The foreign body response (FBR) and the encapsulating glial scar have been associated with a decay in chronic performance of implanted electrodes. Moreover, the morphology, intrinsic properties, and function of cells vary across cortical layers, each potentially affecting the sensitivity to ICMS as well as the degree of the FBR across cortical depth. However, layer-by-layer comparisons of the long-term stability of ICMS as well as the extent of the astrocytic glial scar change across cortical layers have not been well explored. Here, we implanted silicon microelectrodes with electrode sites spanning all the layers of S1 in rats. Using a behavioral paradigm, we obtained ICMS detection thresholds from all cortical layers for up to 40 weeks. Our results showed that the sensitivity and long-term performance of ICMS is indeed layer dependent. Overall, detection thresholds decreased during the first 7 weeks post-implantation (WPI). This was followed by a period in which thresholds remained stable or increased depending on the interfacing layer: thresholds in L1 and L6 exhibited the most consistent increases over time, while those in L4 and L5 remained the most stable. Furthermore, histological investigation of the tissue surrounding the electrode showed a biological response of microglia and macrophages which peaked at L1, while the area of the astrocytic glial scar peaked at L2/3. Interestingly, the biological response of these FBR markers is less exacerbated at L4 and L5, suggesting a potential link between the FBR and the long-term stability of ICMS. These findings suggest that interfacing depth can play an important role in the design of chronically stable implantable microelectrodes.

Keywords: neuroprostheses, cortex, brain computer interface, foreign body response (FBR), microelectrode array, glial scar, microglia

Edited by:
Luming Li,
Tsinghua University, China

Reviewed by:
Yao Chen,
Shanghai Jiao Tong University, China
Yiliang Lu,
Center for Excellence in Brain Science and Intelligence Technology, Institute of Neuroscience (CAS), China

****Correspondence:***
Morgan E. Urdaneta
morganu7@gmail.com
Kevin J. Otto
Kevin.Otto@bme.ufl.edu

Specialty section:
This article was submitted to Neural Technology, a section of the journal Frontiers in Neuroscience

Received: *31 March 2022*
Accepted: *16 May 2022*
Published: *13 June 2022*

Citation:
Urdaneta ME, Kunigk NG, Currlin S, Delgado F, Fried SI and Otto KJ (2022) The Long-Term Stability of Intracortical Microstimulation and the Foreign Body Response Are Layer Dependent. Front. Neurosci. 16:908858. doi: 10.3389/fnins.2022.908858

INTRODUCTION

The performance of brain-machine interface (BMI) technologies can be improved by receiving sensory feedback through intracortical microstimulation (ICMS) (Romo et al., 1998; Flesher et al., 2016; Salas et al., 2018). Clinical work has shown that ICMS of somatosensory cortex (S1) can elicit touch percepts in patients with paralysis (Flesher et al., 2016). The use of implantable microelectrodes allows for the spatial selectivity (Urdaneta et al., 2017) necessary to elicit naturalistic touch percepts in specific areas of the arm (Salas et al., 2018) or individual fingers (Flesher et al., 2016). While this is encouraging, the widespread implementation of ICMS technologies for chronic use requires further understanding of the challenges inherently associated with implantable microelectrodes, such as the foreign body response (FBR) (Biran et al., 2005) and the long-term stability of ICMS.

Studies assessing the stability of ICMS have found heterogeneous responses over time (Rousche and Normann, 1999; Bartlett et al., 2005; Koivuniemi et al., 2011; Davis et al., 2012; Callier et al., 2015; Hughes et al., 2021). Some reports find an immediate rise in microstimulation detection thresholds (Davis et al., 2012); in contrast, others report an initial decrease in thresholds followed by a period of either stable (Callier et al., 2015; Hughes et al., 2021) or increasing thresholds (Rousche and Normann, 1999; Koivuniemi et al., 2011).

One potential contributing factor to these heterogeneous responses is the FBR (Biran et al., 2005; Salatino et al., 2017), which has been associated with a decay in chronic performance of implanted microelectrodes (Prasad and Sanchez, 2012; Barrese et al., 2013). The disruption of the blood-brain barrier and the continuous presence of the device (Kozai et al., 2012) leads to infiltration of bloodborne macrophages (Woolley et al., 2013) and activation of microglia (Eles et al., 2017). These cells release proinflammatory cytokines (Giulian et al., 1994) that lead to the activation of astrocytes and the formation of an encapsulating glial scar around the electrode (Salatino et al., 2017; Campbell and Wu, 2018) that can act as a barrier limiting the delivery of charge to nearby neurons (Mercanzini et al., 2009).

Another potential factor leading to diverse ICMS stability responses is the cortical depth of the electrode interface. Indeed, studies have shown that both the intensity of the FBR (McConnell et al., 2009; Woolley et al., 2013; Kozai et al., 2014; Nolta et al., 2015) as well as the sensitivity of neurons to ICMS is non-uniform across cortical depth (DeYoe et al., 2005; Tehovnik and Slocum, 2009; Urdaneta et al., 2021). Given that the cellular morphology (Gouwens et al., 2019) and cortical dynamics (Harris and Shepherd, 2015) of the cortex are layer specific, the interfacing layer of the electrode can play an important role in the degree of the FBR and the long-term stability of the ICMS. However, to our knowledge, these questions remained unexplored.

Here, we compare the response to ICMS over time as a function of cortical depth and show an association between FBR and ICMS sensitivity at different cortical layers. For this, we implanted a silicon microelectrode device with electrode sites spanning all layers of the S1 cortex in rat. We measured ICMS detection thresholds at each site (i.e., across cortical depth) up to 40 weeks post-implantation (WPI). Post-mortem we histologically examined the area of the astrocytic glial scar and the microglial response across cortical depth. Our results show that the stability of ICMS changes over time in a layer-specific manner. Moreover, the extent of the astrocytic glial scar and microglia was dependent on cortical depth. These findings provide insights into the role of cortical depth in the FBR and the long-term stability of ICMS delivered *via* intracortical microelectrodes.

RESULTS

Rats were chronically implanted with a silicon multielectrode shank in the forepaw region of S1. The device had 16 evenly spaced microelectrodes that spanned all cortical layers (**Figure 1A**).

A stimulus response analysis (**Figures 1B,C**) and a post-mortem electrolytic lesion (Chen et al., 2009; **Figures 1C,D**) were used to confirm the implantation site and depth, respectively (see section "Materials and Methods").

Initial Sensitivity to Microstimulation

One key goal of the study was to assess how the sensitivity of S1 to ICMS changed across cortical depth and over time. To measure the ability of animals to detect ICMS we used a conditioned avoidance behavioral paradigm (Heffner and Heffner, 1995; Urdaneta et al., 2019, 2021; Saldanha et al., 2021). In this task, water-deprived rats were trained to stop licking from a spout upon presentation of an ICMS stimulus (**Figure 2A**, referred to as a "hit"). If the animal failed to stop drinking, the trial was considered a miss (**Figure 2A**, miss) and the animal received a mild electrocutaneous shock. Safe trials were used as a control to determine the animal's licking behavior in the absence of an ICMS stimulus (**Figure 2A**, bottom). Stimulation parameters were held constant throughout the duration of the study except for amplitude (**Figure 2B**), which was modulated based on the animal's response to determine ICMS detection thresholds (**Figure 2C**).

Experimental sessions started after 5 days of post-surgical recovery and consisted of obtaining detection thresholds from randomly selected channels until the animal was satiated. To determine the initial sensitivity of S1 to ICMS, we collected detection thresholds across all channels for 5 experimental sessions during the first 2 WPI. **Figure 2D** shows how the charge (amplitude × phase duration) necessary to evoke a response in S1 varies with cortical depth, with the most sensitive channels around 1 mm from the cortical surface ($R^2 = 0.63$, $p = 0.006$, Cubic fit). Laminar quantification showed that detection thresholds change significantly across layers (**Figure 2E**). The mean charge necessary to elicit a threshold in L5 (6.37 ± 3.93 nC·Phase^{-1}) and L4 (6.49 ± 3.47 nC·Phase^{-1}) was roughly half that in L1 (12.91 ± 6.09 nC·Phase^{-1}) and L6 (10.68 ± 6.66 nC·Phase^{-1}) (**Figure 2E**). These depth-dependent microstimulation thresholds served as a foundation to investigate how the long-term stability of ICMS in S1 changes across cortical layers.

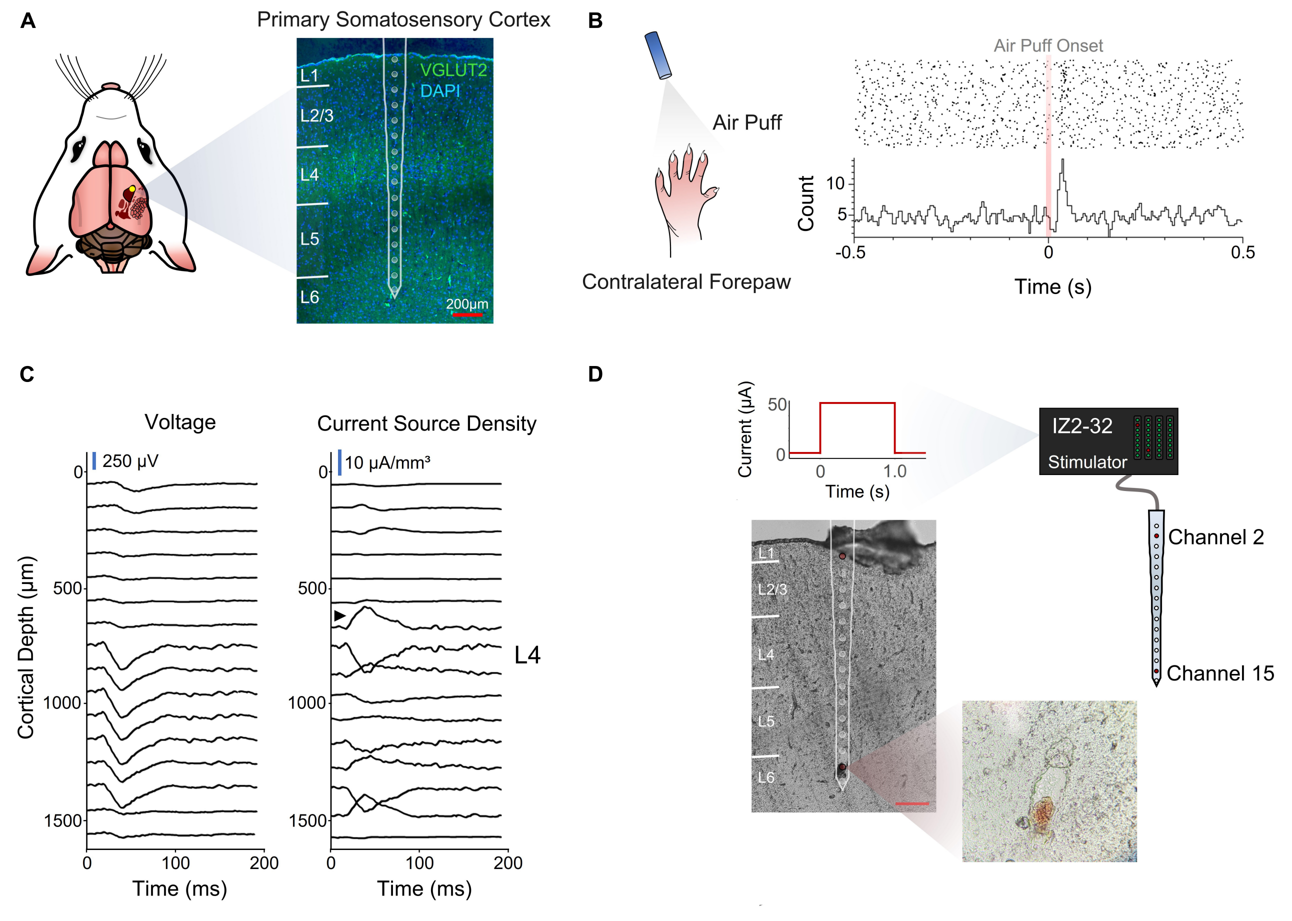

FIGURE 1 | Electrode implantation and cortical depth assessment. **(A)** Coronal section of the implantation site stained for VGLUT2 and DAPI for cortical layer identification. **(B)** Perievent stimulus time histogram of an air puff onset to the contralateral forepaw. **(C)** Voltage traces and inverse current source density. Black arrow designates sink characteristic of thalamic input into layer 4. **(D)** Post-mortem depth assessment *via* electrolytic lesion of the tissue.

Depth Dependent Longitudinal Microstimulation Performance

We measured detection thresholds across all channels up to 40 WPI by determining thresholds at least twice a week during the first 16 WPI, and at least twice a month afterward. If an electrode-site was able to elicit behavior at charges below 30 nC·Phase^{-1}, it was deemed active (see section "Materials and Methods"). The fraction of active channels (FAC) was computed by dividing the number of times an electrode was active over the number of experimental sessions for each subject. **Figure 3A** shows the average FAC across subjects ($N = 6$) over time. The FAC across all electrode-sites peaked in the second month post-implantation (0.90 ± 0.08) with roughly twice the number of active channels compared to 8 months post-implantation (0.54 ± 0.3). This result suggests that the number of electrodes able to evoke thresholds changes over time. In addition, the average FAC across the duration of the study was at least 18.9% higher for L5 (0.87 ± 0.19) than for any other layer. To expand on these layer-dependent changes in chronic stability, we analyzed how the charge necessary to evoke a response changed over time across cortical layers. **Figure 3B** shows an initial decrease in detection thresholds across all layers until reaching a minimum around the 7th week post-implantation. This is followed by a steep increase in mean thresholds of 134 and 96% until the week 40 for L1 and L6, respectively. In contrast, L5 remained more stable with an increase in thresholds of only 42% (**Figure 3B**). The initial decrease in thresholds (**Figure 3C**, blue shade) has been reported in the literature as subjects improve on the behavioral task, regardless of the time post-implantation (Callier et al., 2015). Hence, we denominated this period the learning phase. Given the layer-specific differences at chronic timespoints following the learning phase, the period following the minimum threshold was designated the chronic phase (**Figure 3C**, orange shade). To further understand how thresholds change across subjects and across layers during these time periods, we examined the learning and chronic phases in the following sections.

Learning Phase

The learning phase consisted of the period of initial decrease in detection thresholds observed on the first week of thresholds and up to the week in which thresholds reach a minimum (**Figure 4A**). Our first goal was to determine when the

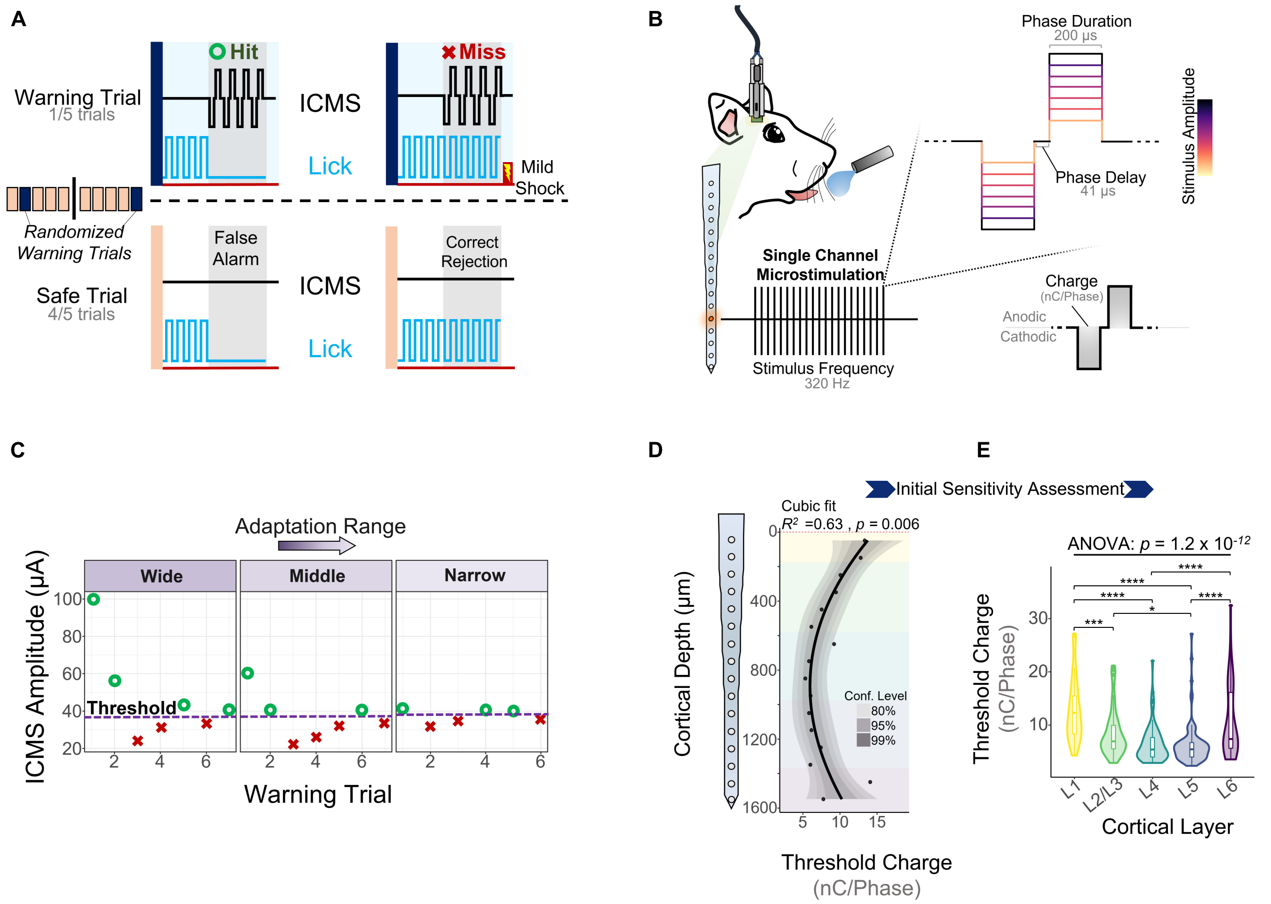

FIGURE 2 | Behavioral paradigm and microstimulation sensitivity over depth. **(A)** A conditioned avoidance behavioral paradigm was used to assess the ability of the animals to detect microstimulation. **(B)** Stimulation frequency, phase duration, and phase delay were kept constant throughout the experiment. Stimulus amplitude was modulated based on the animal's behavior using an adaptation protocol. **(C)** Adaptation protocol used to measure detection thresholds. Similar detection thresholds can be obtained regardless of the initial stimulation amplitudes. **(D)** Sensitivity of S1 to microstimulation as a function of cortical depth during the first five experimental sessions ($N = 6$). **(E)** Quantification of these thresholds across cortical layers (ANOVA with Tukey's *post-hoc* test) ($N = 6$). *$p \leq 0.05$, ***$p \leq 0.001$, ****$p \leq 0.0001$.

minimum threshold was reached for each subject. **Figure 4B** shows that on average, subjects reach the minimum threshold at different timespoints, ranging from 3.85 ± 0.72 weeks (subject 12) up to 7.25 ± 0.25 weeks (subject 1) post-implantation. We ran an analysis of variance to determine if the week of minimum threshold changed across layers for each animal, finding no statistical significance for any animals (**Figure 4B**: $p > 0.05$, One-way ANOVA). These observations suggest that animals reach the minimum threshold at different weeks, but this point is reached at roughly the same time across layers in each subject. Next, we plotted detection thresholds of the first 7 WPI across layers (**Figure 4C**). On average, detection thresholds decreased 44.1% from week 1 to week 7 at a rate of -1.93 nC·Phase^{-1}/month (**Figure 4C**). The inclusion of time as a covariate revealed no statistically significant differences in thresholds across layers during the first 7 WPI (**Figure 4C**). We used the slope of thresholds between the first session and the week of minimum threshold for each animal across layers as a performance metric for ICMS stability. **Figure 4D** shows that the mean slope of thresholds during this time period changes significantly across layers (**Figure 4D**). On average, L4 (-0.97 ± 0.95 nC·Phase^{-1}/month) had the shallowest slope, while L6 (-4.99 ± 1.47 nC·Phase^{-1}/month) had the steepest slope (**Figure 4D**). These results suggest layer-specific differences in learning tactile behavior in S1, consistent with previous reports (Diamond et al., 1994). To assess if the overall depth-dependent sensitivity to ICMS shifted during the learning phase, we quantified cumulative thresholds during the first 7 WPI across cortical depth (**Figures 4E,F**). Comparable to the initial sensitivity assessment of the first five experimental sessions (**Figures 2A,B**), the overall ICMS sensitivity during the learning phase is non-uniform across depth ($R^2 = 0.65$, $p = 0.005$, Cubic fit). L4 and L5 also persisted as the most sensitive layers (**Figures 4E,F**). Altogether, these observations indicate that the rate of threshold improvement as well as the overall sensitivity to ICMS during the learning phase change in a layer dependent manner.

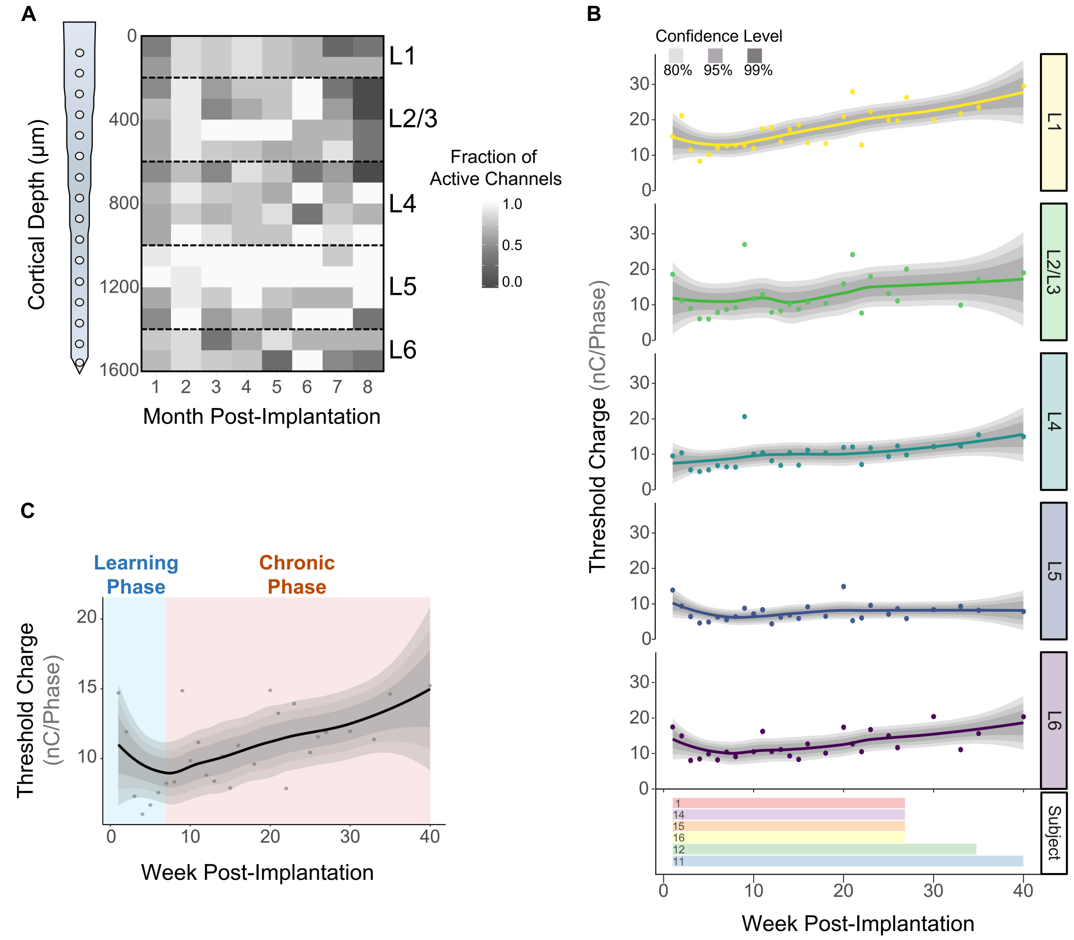

FIGURE 3 | Long term stability of ICMS across cortical layers. The fraction of active channels was computed by assessing the number of times an electrode-site was able to elicit thresholds at safe ICMS charges. **(A)** Average fraction of active channels over time across subjects (*N* = 6). **(B)** Longitudinal detection thresholds across cortical layers (top) and the amount of time post-implantation in which detection thresholds were obtained from each subject (bottom). **(C)** Average detection thresholds of all cortical layers showing an initial decrease in thresholds (learning phase), followed by a period of increased thresholds (chronic phase) (*N* = 6). For **(B,C)**: lines represent a locally fitted polynomial regression of the means and shaded areas represent confidence intervals.

Chronic Phase

The chronic phase started immediately after the learning phase and lasted the remaining duration of the study (**Figure 5A**). This period of time is characterized by an overall increase in detection thresholds across all layers (**Figure 5B**: 0.79 nC·Phase^{-1}/month, linear regression slope). We ran an ANCOVA to evaluate threshold differences across layers while controlling for the effects of time post-implantation. Our results showed significant differences in thresholds across cortical layers throughout the chronic phase (**Figure 5B**). To further elucidate the long-term stability of ICMS and account for different animal end points, the average slope per layer was calculated for each subject during the chronic phase. The heatmap in **Figure 5C** shows that the mean slope changes significantly across cortical layers. The cortical layer that showed the least steep slope over time was L5, increasing at an average rate of 0.65 ± 0.49 nC·Phase^{-1}/month, indicating that L5 has the most stable thresholds over time. In contrast, L1 displays the sharpest increase in thresholds (3.25 ± 0.51 nC·Phase^{-1}/month). For some subjects, channels in L1 and L6 were unresponsive to stimulation charges below 30 nC·Phase^{-1} by the endpoint (25 WPI) (**Figure 5C**, unresponsive channels). This result is consistent with our previous observation that the FAC across the duration of the study varied in a layer-dependent manner (**Figure 2A**). Lastly, to assess how ICMS sensitivity patterns change at chronic timespoints, we analyzed cumulative detection thresholds over depth at two different time periods in the chronic phase: from 8 to 20 WPI and >20 WPI. For both of these time points the ICMS sensitivity maintained a non-uniform trend across cortical depth (**Figures 5D,E**). Further laminar quantification revealed that sensitivity differences across cortical layers become more pronounced at chronic timespoints (**Figures 5F,G**). In particular, the percent increase in threshold amplitudes between L1 and L5 increased from 66.6% during 8–20 WPI to 91.0% on >20 WPI. These observations indicate that although the overall sensitivity

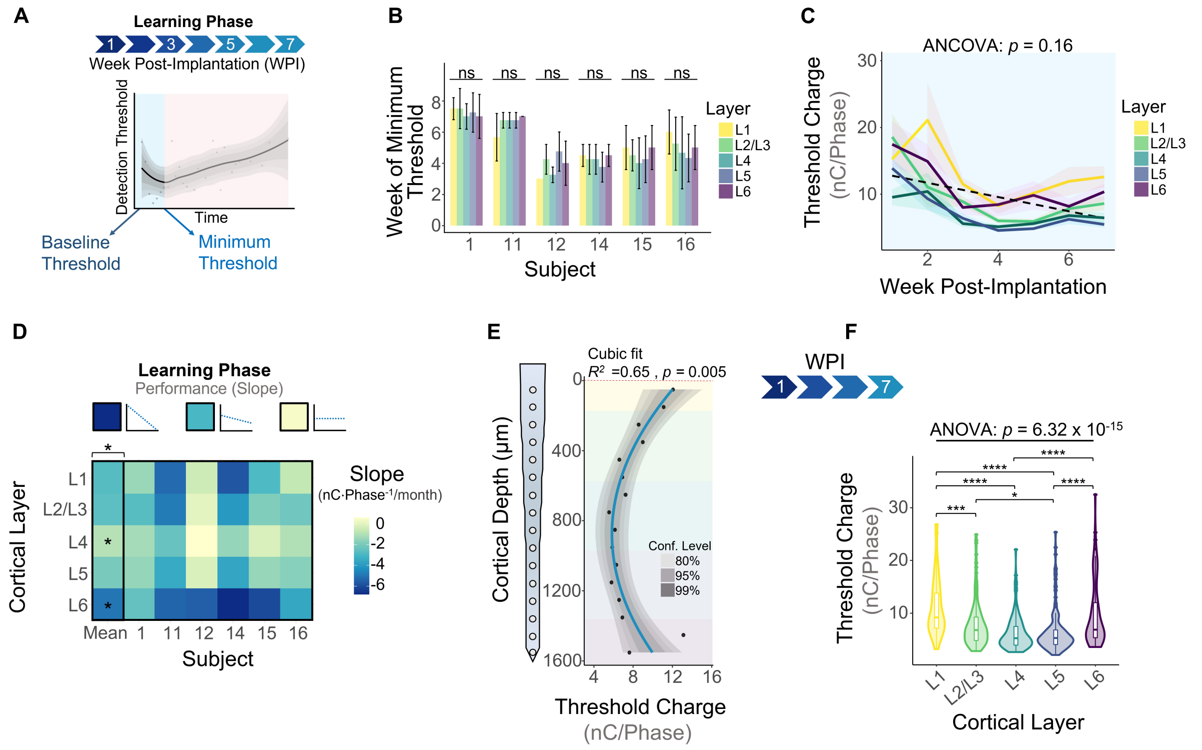

FIGURE 4 | Microstimulation detection thresholds during the learning phase. **(A)** Graphical representation of the period of initial decrease in thresholds (learning phase) in the context of longitudinal thresholds. **(B)** Bar plot graph showing the week in which subjects reached minimum thresholds across cortical layers. **(C)** Average detection thresholds during the learning phase. Dashed line represents a linear regression of the mean. **(D)** Heatmap of the slope of thresholds between the baseline and week of minimum threshold across subjects. **(E)** Sensitivity of thresholds during the learning phase and **(F)** laminar quantification. Analysis of variance and pairwise comparisons between layers were performed with a one-way ANOVA with Tukey's *post-hoc* test. Error bars in **(B)** and shaded areas in **(C)** indicate mean ± SEM. $^*p \leq 0.05$, $^{***}p \leq 0.001$, $^{****}p \leq 0.0001$.

pattern across cortical depth remains constant over time, threshold differences across layers become exacerbated in chronic time points. Altogether, these results reveal that the long-term stability of ICMS in S1 is dependent on the interfacing depth, raising the question of how biotic factors such as the FBR could be contributing to this depth-specific performance.

The Extent of the Astrocytic Glial Scar Over Depth

A decay in chronic performance of implantable microelectrodes has been associated with the FBR, specifically the astrocytic glial scar engulfing the electrode (Prasad and Sanchez, 2012; Prasad et al., 2014; Esquibel et al., 2020). The fluorescent intensity of glial fibrillary acidic protein (GFAP), a marker for astrocytes and indicative of the glial scar, has been reported to be higher near the cortical surface (McConnell et al., 2009). However, how the area of the astrocytic glial sheath varies across layers remains unexplored. To assess this question, we used DeepHisto (citation in review), a technique to evaluate the FBR across cortical depth. Following perfusion, systematic sectioning, and staining with GFAP (**Figures 6A–C**), the areas of the glial sheath and the explanted device hole (EDH) were measured using an automatic tracing tool (see section "Materials and Methods"). **Figure 6D** shows representative histological sections in which the areas of the EDH (blue outline) and the glial sheath (yellow outline) are non-uniform across cortical depth. **Figure 6E** shows how the average area of the EDH is up to 69.37% larger than the area of the device near the cortical surface. As we go down in cortical depth the area difference between the EDH and the device decreases, becoming almost negligible below 500 μm from the cortical surface. Given that both L1 and L6 had similar sensitivities to ICMS (**Figure 2D**), it is unlikely that this phenomenon was caused by higher microstimulation charges. Hence, it is more likely that this difference was caused by the device explantation or by micromotion.

Next, we quantified the area of the glial sheath engulfing the electrode. **Figure 6F** shows that the extent of the glial sheath is non-uniform across cortical depth ($R^2 = 0.85$, $p = 6.1 \times 10^{-5}$), peaking at 300 μm (69954 ± 41861 μm^2) from the cortical surface. Laminar quantification revealed that the area of the glial sheath is larger in L2/3 (**Figure 6F**) and changes significantly across cortical layers (**Figure 6G**). These observations reveal that the extent of astrocytic glial scar of chronically implanted electrodes can vary depending on the interfacing depth.

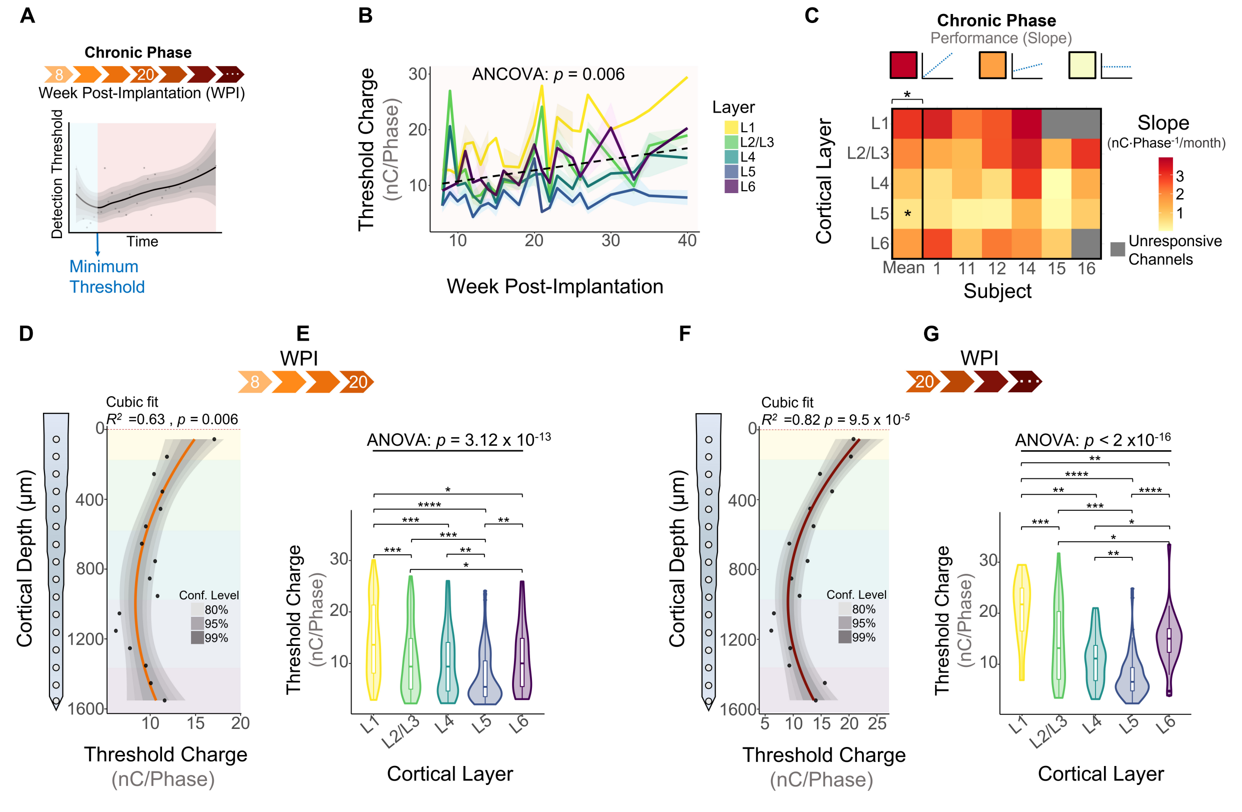

FIGURE 5 | Microstimulation detection thresholds during the chronic phase. **(A)** Graphical representation of longitudinal threshold showing the beginning of the chronic phase (orange shade) after the week of minimum thresholds. **(B)** Average detection thresholds during the chronic phase. Dashed line represents a linear regression of the mean. **(C)** Heatmap of the slope of thresholds between the week of minimum threshold and the last week of threshold across subjects. ICMS Sensitivity across cortical depth and laminar quantification during **(D,E)** 8–20 weeks-post-implantation and **(F,G)** >20 WPI. Analysis of variance and pairwise comparisons between layers were performed with a one-way ANOVA with Tukey's *post-hoc* test. Shaded areas in **(B)** indicate mean ± SEM. *$p \leq 0.05$, **$p \leq 0.01$, ***$p \leq 0.001$, ****$p \leq 0.0001$.

The Microglial Response Over Depth

DeepHisto sections were stained with Iba1, a marker specific for microglia/macrophages (Sasaki et al., 2001). **Figure 7A** shows that the fluorescent intensity of Iba1 is non-uniform across cortical depth, consistent with previous observations (Woolley et al., 2013). To quantify this pattern, we drew concentric rings diverging from the EDH (**Figure 7B**) and calculated the mean fluorescent intensity of each ring (**Figure 7C**). Similar to previous work (Biran et al., 2005; Gaire et al., 2018), our results show that fluorescent intensity of iba-1 consistently increased with proximity to the electrode (**Figure 7D**). Moreover, this change in fluorescent intensity became more pronounced in superficial layers (**Figure 7E**). Notably, the overall fluorescence intensity of microglia/macrophages for chronically implanted electrodes is higher near the cortical surface ($N = 5$). Laminar quantification showed a highly significant difference in Iba1 intensity across cortical layers [$F_{(4,531)} = 90.19, p < 2 \times 10^{-16}$; one-way ANOVA] with the highest intensity in L1 (**Figure 7E**; L1 vs. L2/3, L4, L5, L6 : $p <$ 0.00001, Tukey's *post-hoc* test). These findings indicate that the microglia/macrophage response to chronically implanted electrodes changes as a function of proximity to the electrode and as a function of cortical depth.

DISCUSSION

Our finding that longitudinal microstimulation had an initial decrease in thresholds followed by a period of irregular long-term stability complements previous ICMS work (Rousche and Normann, 1998; Bartlett et al., 2005; Koivuniemi et al., 2011; Callier et al., 2015; Hughes et al., 2021) while revealing layer-specific responses (Urdaneta et al., 2021). Consistent with our findings, several studies have reported an initial decrease in thresholds followed by a period of increased (Rousche and Normann, 1998; Koivuniemi et al., 2011) or stable thresholds (Bartlett et al., 2005; Callier et al., 2015; Hughes et al., 2021). However, the duration of the initial decrease in thresholds (learning phase) varies across the literature. Studies have reported a decrease in thresholds that reaches a minimum after days (Rousche and Normann, 1998; Bartlett et al., 2005; Koivuniemi et al., 2011), weeks (Rousche and Normann, 1998), and months after implantation (Callier et al., 2015; Hughes et al., 2021). Interestingly, this period of ICMS threshold improvement is even present in animals for which the ICMS regime started years after implantation (Callier et al., 2015). This suggests that the decrease in ICMS thresholds is not necessarily related to

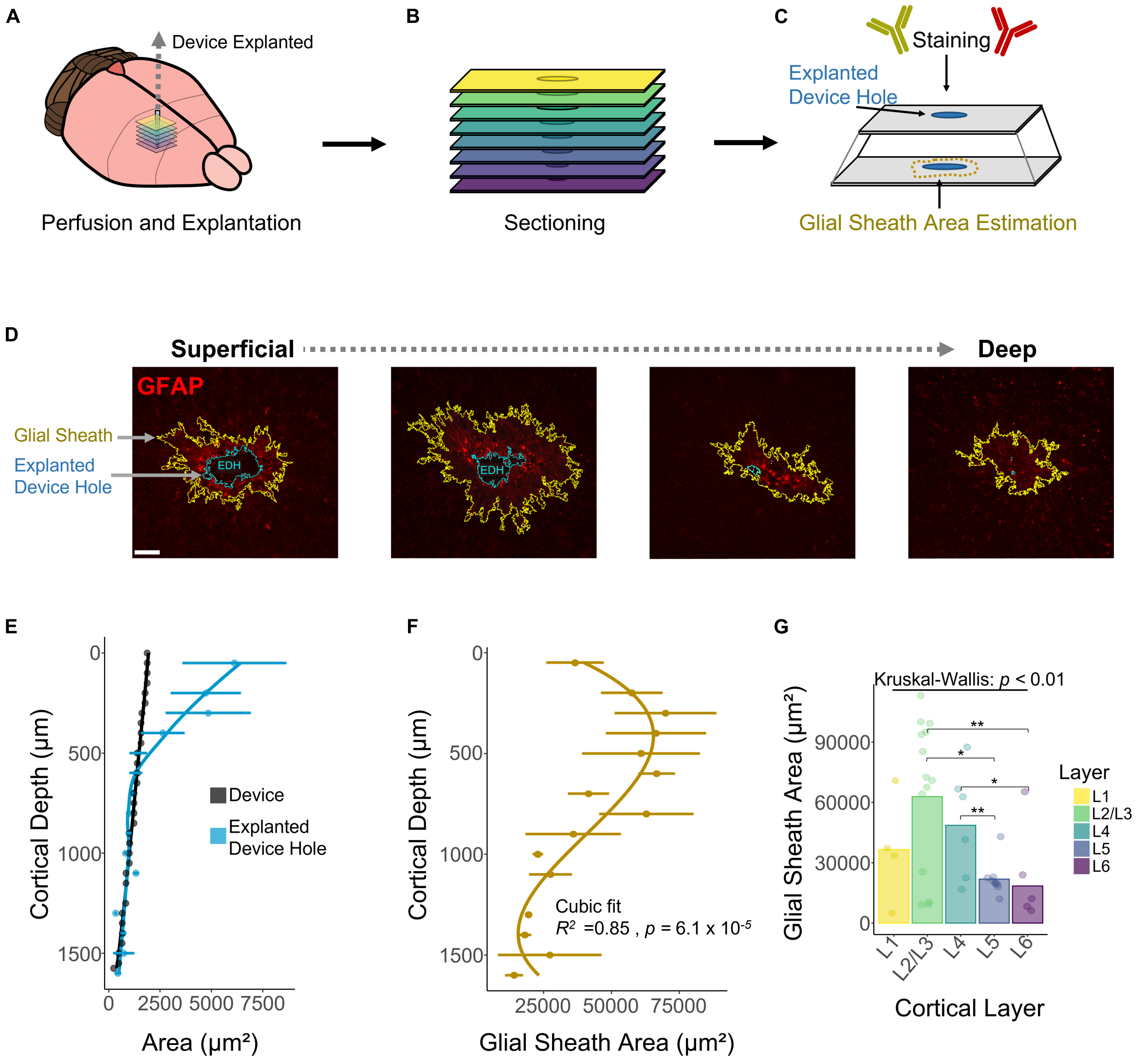

FIGURE 6 | Histological assessment and quantification of the astrocytic glial scar across cortical depth. Histological analysis across cortical depth was performed using DeepHisto. **(A)** After perfusion, the device was carefully extracted. **(B)** Horizontal tissue slices surrounding the device were systematically sectioned to keep track of cortical depth. **(C)** Samples were stained with GFAP and the area of the glial scar was measured. **(D)** Representative histological sections across cortical depth for one subject. Yellow outlines represent the astrocytic glial scar surrounding the electrode and the blue outlines represent the explanted device hole. **(E)** Quantification of the area of the explanted device hole in comparison with the cross-sectional area of the device. Lines represent a locally fitted polynomial regression of the mean. **(F)** Area of the astrocytic glial scar as a function of cortical depth. Line represents a cubic fit. **(G)** Laminar quantification of the area of the astrocytic glial scar. Analysis of variance and pairwise comparisons between layers were performed with a Kruskal–Wallis test and a Wilcoxon rank-sum test with Holm adjustment, respectively. Error bars in **(E,F)** indicate mean ± SEM. $^*p \leq 0.05$, $^{**}p \leq 0.01$.

acute biological changes occurring after implantation (Biran et al., 2005; Kozai et al., 2012; Salatino et al., 2017). Instead, this decrease could be related to the subject's ability to detect and interpret ICMS in the context of the behavioral task. In addition, our observation that the rate of change of threshold amplitudes varied significantly across layers could be related to layer-specific differences in cortical adaptation. Notably, L4 had the shallowest decrease in thresholds during the learning phase, and neurons in this layer have been shown to have the lowest levels of plasticity in tactile learning in adult rats (Diamond et al., 1994).

Following the learning phase, our average ICMS threshold charge increased during the chronic phase in a layer-dependent manner. Previous studies have found different chronic stability responses to ICMS, with some reporting increases in thresholds (Bartlett et al., 2005; Koivuniemi et al., 2011; Davis et al., 2012) and others reporting stable thresholds (Callier et al., 2015; Hughes et al., 2021). We found that whether thresholds increased or remained stable was highly dependent on the cortical layer. This finding could provide insights into the interelectrode variability observed in previous studies (Rousche and Normann, 1998; Hughes et al., 2021). For instance, Hughes et al. (2021)

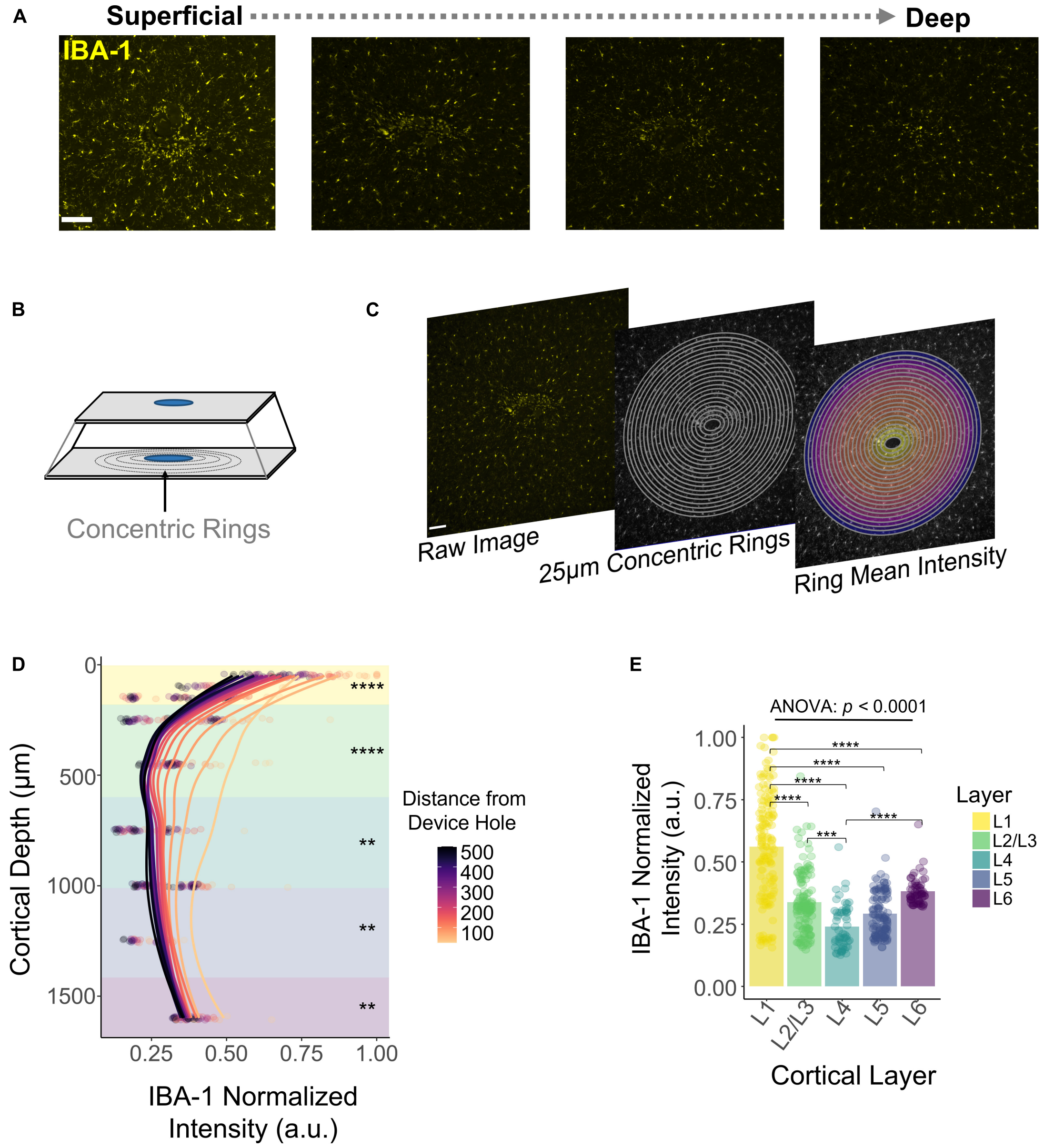

FIGURE 7 | Histological response of microglia and macrophages across cortical depth. **(A)** Representative histological sections stained with Iba1 for one subject showing a change in fluorescence intensity across cortical depth. **(B)** Graphical representation of concentric rings around the explanted device hole. **(C)** Concentric rings and mean intensity calculation from a representative tissue section. **(D)** Quantification of Iba1 fluorescence intensity with respect to the distance from the device hole across cortical depth. Lines represent a locally fitted polynomial regression of the mean of each concentric ring. **(E)** Quantification across layers of the Iba1 fluorescence intensity. Analysis of variance and pairwise comparisons between layers were performed with a one-way ANOVA with Tukey's *post-hoc* test. $^{**}p \leq 0.01$, $^{***}p \leq 0.001$, $^{****}p \leq 0.0001$.

reported that the long-term stability of ICMS in humans implanted with a Utah array in S1 varied across electrodes, and that electrodes with high thresholds were clustered together[13]. It is possible that, due to the non-planar geometry of the human cortex, some of the electrodes rested at a different cortical depth, leading to different ICMS stability responses over time. Based on our observation that the ICMS sensitivity of S1 changes across depth, it is possible that some of these electrodes were located at a different cortical depth, producing distinct long-term stability responses.

Our DeepHisto analysis showed that the overall fluorescent intensity of microglia/macrophages was higher in L1, consistent with previous observations. Different groups have reported that the extent of the microglial response is greater near the cortical surface at 4 WPI (Woolley et al., 2013) and up to 16 WPI (McConnell et al., 2009) for chronically implanted rats. Our findings expand on these studies by showing that this depth-dependent microglial trend persists up to 40 WPI. In the healthy brain, microglia play an important role in maintaining neuronal signaling and synapse regulation (Tremblay et al., 2011). However, microglia become activated after implantation, causing a change in morphology and the release of proinflammatory cytokines and reactive oxygen species (Polikov et al., 2005). Hence, long-term activation of microglia in a depth-dependent manner can have important implications for the health and function of cells in superficial cortical layers.

In addition, our assessment of the astrocytic glial scar engulfing the electrode revealed that its extent is also non-uniform across cortical depth, peaking around L2/3. Previous work has reported qualitative differences in FBR with increased responses near the cortical surface (Kozai et al., 2014; Nolta et al., 2015). McConnell et al. (2009) assessed the GFAP response of chronically implanted rats across four representative cortical depths (200, 600, 1000, and 1400 μm); these rats were implanted for different time periods ranging from 2 to 16 WPI (McConnell et al., 2009). The fluorescent intensity levels of GFAP decreased as a function of cortical depth after 8 WPI. These depth-dependent results were partially attributed to the thickness of the device, which tapers down as a function of cortical depth (McCreery et al., 1990). Our electrodes had a similar geometry; however, the increased spatial resolution of our assessment revealed that the extent of the glial scar is non-monotonic across depth. Specifically, we found that the area of the glial sheath did not peak at the depth of maximum thickness of the device (cortical surface and L1), instead reaching its maximum at 300 μm (L2/3). These layer-dependent changes in the glial scar could arise from morphological differences in astrocytes across cortical depth. Indeed, both the territorial volume of astrocytes as well as the orientation angle relative to the cortical surface peak at L2/3 (Lanjakornsiripan et al., 2018). Furthermore, the molecular profile of astrocytes also varies across layers (Bayraktar et al., 2020). For instance, the expression of *Chrdl1* in astrocytes peaks in L2/3 for both mice and humans (Bayraktar et al., 2020). *Chrdl1* is a bone morphogenetic protein (BMP) inhibitor (Cyr-Depauw et al., 2016), a key molecule in the regulation of the glial scar (Zhong and Zou, 2014). Further research is necessary to investigate the relationship between electrode size/geometry and the extent of the glial sheath across cortical depth. In addition, understanding the complexity of the glial scar across cortical depth can better inform groups developing therapeutics such as drug-delivery and coatings (Sommakia et al., 2014) for the mitigation of the FBR.

Changes in neuronal morphology and the FBR might lead to differences in ICMS threshold stability. Consistent with previous reports (Koivuniemi et al., 2011), our results showed that microstimulation electrodes near the cortical surface had lower long-term stability. The fact that the glial scar and microglia/macrophage densities are exacerbated in superficial layers could lead to the presumption that the FBR is directly responsible for the decay in ICMS chronic performance. However, this degradation process is more complex. The fluorescent intensity of microglia/macrophages was lower at deeper layers and the area of the glial sheath was the lowest in L6. Concurrently, this layer had one of the poorest ICMS longitudinal performances. Hence, the layer specific decay in longitudinal stability of ICMS could not be solely attributed to depth-specific changes in the FBR. The chronic stability of implantable microelectrodes is a multivariate process constituted by abiotic and biotic factors. For instance, abiotic factors such as the structural integrity of the device, composition of the electrode material (Prasad et al., 2014) (i.e., flexibility) and its dimensions represent abiotic factors that might affect the long-term stability of ICMS. Analogously, biotic factors such as the health and function of neurons surrounding the electrode (Biran et al., 2005; Salatino et al., 2017) can also affect the behavioral response to ICMS. Indeed, layer-specific changes in neuronal morphology and function (Lanjakornsiripan et al., 2018; Gouwens et al., 2019) could lead to different sensitivities to ICMS (Aberra et al., 2018; see: Urdaneta et al., 2021) for an extended discussion). We found that channels with high initial thresholds tended to have fewer active channels over time with higher detection thresholds over time. Future research is necessary to assess the impact of chronic microstimulation charges in the health and function of neuronal populations across cortical layers.

In conclusion, we found that the long-term sensitivity to ICMS and the number of active sites over time is layer dependent. Similarly, a post-mortem analysis showed that the astrocytic glial scar and microglia response are non-uniform across cortical depth. This approach to evaluating the long-term ICMS performance in S1 and the FBR across cortical depth have important implications in the design of neuroprosthetic devices and future ICMS studies.

MATERIALS AND METHODS

Device Implantation

All animal experiments and surgeries were performed under the approval and guidance of the University of Florida's Institutional Animal Care and Use Committee. The specific details of the surgical implantation have been described elsewhere. Briefly, six male Sprague-Dawley rats (450–650 g, Charles River, Chicago, IL, United States) were initially induced with 5% isoflurane (Zoetis, Parsippany, NJ, United States) in oxygen at 1.5–2 L/min. The isoflurane was reduced after 5 min and sustained at 1.5–3% throughout the surgical procedure. Meloxicam (1–2 mg/kg, SQ, Loxicom, Norbrook Laboratories, Newry, Northern Ireland) was administered subcutaneously. A 1 mm^2 cranial window was performed over the forepaw region of the primary somatosensory cortex [0.5 mm, 3.5 mm (Paxinos and Watson, 2006)]. Burr holes were drilled to secure four titanium bone screws (United Titanium, OH, United States). After a durotomy, a micro-insertion system (PiLine M663, Physik Instrumente, Karlsruhe, Germany) was used to implant a silicon microelectrode device (A1 × 16–3 mm-100-703-HZ16, NeuroNexus, Ann Arbor, MI, United States). The device (previously sterilized with ethylene oxide) was rinsed with sterile saline and inserted 1.6 mm from the cortical surface at 100 mm/s. This device had 16 iridium oxide electrode-sites with a surface area of 703 μm^2 with a pitch of 100 μm (**Figure 1A**). The site of the craniotomy was filled with a silicone elastomer (Kwik-Sil, WPI, Sarasota, FL, United States). Once the elastomer thickened, UV-cured dental composite (DentalSource, CA, United States) was used to secure the connectors in place. After surgical recovery, the animal was placed in a Faraday cage and an air puff stimulus was directed to the contralateral forepaw while neural recordings were obtained using a PZ5 Neuro digitizer amplifier (Tucker Davis Technologies, Alachua, FL, United States). The custom-made air puff system was controlled by an RZ5D Bioamp processor (Tucker Davis Technologies, Alachua, FL, United States). Epochs from the air puff were used to calculate an inverse current source density (iCSD) (Pettersen et al., 2006) using MATLAB (2019b, Mathworks, MA, United States). Moreover, coronal sections stained for Anti-VGluT2 Antibody (1:500–AB2241, Sigma-Aldrich) were used to corroborate the length of cortical layers in S1 (Meyer et al., 2013).

Behavioral Paradigm

A conditioned avoidance behavioral paradigm was used to assess the ability of rats to detect ICMS. Specific details have been described elsewhere (Koivuniemi et al., 2011). The animal's behavior was monitored through a custom-made RPvds code and a RZ5D Bioamp processor (Tucker Davis Technologies, Alachua, FL, United States). Briefly, rats were trained to stop licking behavior upon presentation of an ICMS stimulus (**Figure 2A**). If the animal failed to stop drinking, a percutaneous shock was delivered through the spout. Trials were organized into blocks consisting of one warning trial and four safe trials. The ICMS stimulus was only present in warning trials and the order of the warning trial within a block was pseudo-randomly chosen. Safe trials contained no stimulus and were used to keep track of the licking behavior and ignore trials in which the animal stopped drinking in the absence of stimulus. Specifically, a false alarm was counted if the animal stopped drinking for more than 20% out of the 650 ms decision window. If a block of five trials contained more than two false alarms, the entire block was invalidated and repeated. Analogously, if during a warning trial the animal successfully avoided licking for more than 20% of the ICMS stimulus presentation phase (650 ms), the trial was considered a hit; otherwise, it was considered a miss (**Figure 2A**). If an animal successfully avoided to lick (hit), the stimulus amplitude of the next warning trial was reduced. Conversely, if the animal failed the trial, the stimulus amplitude was increased. A shift from hit to miss and vice versa was denominated a reversal. After three reversals, the average of amplitude of the last five trials was calculated and determined as the detection threshold.

Longitudinal Microstimulation Experiments

Microstimulation was delivered to a single electrode-site on the implanted device *via* an IZ-32 stimulator with an LZ48-200 battery (Tucker-Davis Technologies, Alachua, FL, United States). Microstimulation consisted of 0.2 ms phase duration cathode-leading symmetric waveforms with a phase delay of 0.04 ms and a frequency of 320 Hz. Detection thresholds were reported in charge per phase (nC) by multiplying the stimulus amplitude (μA) by the phase duration (ms). Experimental sessions started after 5 days of post-surgical recovery. Each session consisted of obtaining detection thresholds from randomly selected channels (typically 8 to 16 channels) until the animal was satiated. A custom-made metallic protective cap was placed on the headstage after each session to avoid damage to the connectors. Thresholds were measured at least twice a week during the first 16 WPI, and at least twice a month afterward. To avoid tissue damage due to high microstimulation charges (Cogan et al., 2016), the total charge delivered was limited to a maximum of 30 nC·Phase^{-1} (Urdaneta et al., 2021).

Tissue Processing and Cryosectioning

After conclusion of the ICMS experiments, subjects were anesthetized with 5% isoflurane in 2 L/min oxygen. A transcardial perfusion was carried out using phosphate buffered saline (PBS) followed by 4% paraformaldehyde (PFA) solution. Next, the skulls were incubated in 4% PFA at 4°C for 3 days. After several washes in PBS, the skulls were surgically resected, and the microelectrode was meticulously pulled out of the cortex (**Figure 6A**). The brains were then incubated in a 30% sucrose solution at 4°C for cryoprotection. Once the samples sank into the bottom of the vial (typically after 72 h), these were flash frozen in 2-methylbutane (Sigma Aldrich, St. Louis, MO, United States) at −40°C. Next, tissue within a 5 mm radius from the EDH was resected and mounted on a cryosection chuck with Tissue-Plus O.C.T. Compound (23-730-571, Fisher). The samples were then serially sectioned to track cortical depth. In brief, 20 μm tissue sections tangential to the explanted device were sliced using a cryostat (CM 1520, Leica) at −20°C. The first tissue slice on slide 1 represents a cortical depth of 0 to 20 μm, the first slice on slide 2 corresponds to cortical depth 20 to 40 μm, and so on (**Figure 6B**).

Immunohistochemistry and Imaging

After leaving the slides at room temperature for 1 h, they were washed with PBS in three 5 min cycles. Next, the slides were incubated in Animal-free R.T.U. Blocker (SP-5035, Vector Laboratories Inc.) overnight at 4°C. To identify astrocytes and microglia/macrophages, immunohistochemistry was performed using the primary antibodies Anti-GFAP (CPCA-GFAP, EnCor Biotech.) and Anti-Iba-1 (019-19741, Wako Chem.), respectively. Primary antibodies were diluted to 1:500 in Animal-free Blocker, R.T.U (SP-5035, Vector Laboratories Inc). The primary antibodies were then distributed across the slides and incubated at 4°C for 36 h (**Figure 6C**). Following three 10 min PBS wash cycles, slides were stained with secondary antibodies (Cy3 anti-rabbit, 711-165-152, Jackson Immuno.) (Cy5 anti-chicken, 703-175-155, Jackson Immuno.) diluted 1:500 in animal-free blocker and incubated at 4°C for 24 h. After three 10 min PBS washes the excess liquid was aspirated, and glass coverslips were mounted using Vector Shield medium with DAPI (H-1200, Vector Labs). Slides were kept in the dark at RT for 24 h before imaging. Image acquisition was performed on a Leica DMi8 microscope running LAS X Premium software. Peripheral components include a DFC9000 GT camera, EL-6000 light source (30 ms), HC PL APO 10x/0.45 objective, and Leica Y3 and Y5 filter cubes. Acquisitions were centered over the EDH (**Figure 6C**).

Foreign Body Response Quantification

After manual selection of the area of the EDH, the mean gray value intensity of 25 μm concentric rings around the device was measured. This process was repeated across cortical depth. The fluorescence intensity values were then normalized using min-max normalization and plotted across cortical depth. Quantification of the glial scar area was traced with an automatic tracing tool in which the tolerance value was manually adjusted by blind evaluators. All slide quantification analyses were performed with a custom-made script in Fiji (Schindelin et al., 2012).

Statistics

Parametric comparisons were assessed *via* one-way ANOVA followed by a Tukey's *post-hoc* test. Layer-specific differences in thresholds with time as a covariate were assessed using an ANCOVA. For datasets with non-normal distribution (Shapiro Wilks test) or with less than 20 samples per group (**Figure 7**), analysis of variance and pairwise comparison were performed *via* a Kruskal–Wallis test and a Wilcoxon rank-sum test with Holm adjustment, respectively. $^{*}p \leq 0.05$, $^{**}p \leq 0.01$, $^{***}p \leq 0.001$, $^{****}p \leq 0.0001$. All statistical analyses were performed in R Statistical Software Version 4.0.0 (Vienna, Austria).

DATA AVAILABILITY STATEMENT

The raw data supporting the conclusions of this article will be made available by the authors, upon reasonable request.

ETHICS STATEMENT

The animal study was reviewed and approved by the University of Florida Institutional Animal Care and Use Committee (IACUC).

AUTHOR CONTRIBUTIONS

MU, NK, SC, FD, SF, and KO conceived and designed the study and reviewed and edited the manuscript. MU, NK, and FD set up the behavioral rig. MU performed the surgical implantations and wrote the manuscript. MU and NK collected threshold data and analyzed the microstimulation and histological data. SC performed histology and imaging. All authors contributed to the article and approved the submitted version.

FUNDING

This work was funded by the NIH (NIH-U01NS099700) and by the DoD/CDMRP (VR170089).

ACKNOWLEDGMENTS

We thank the University of Florida's NeuroProstheses Research Lab and Janak Gaire for their support and assistance.

REFERENCES

Aberra, A. S., Peterchev, A. V., and Grill, W. M. (2018). Biophysically realistic neuron models for simulation of cortical stimulation. *J. Neural Eng.* 15:066023. doi: 10.1088/1741-2552/aadbb1

Barrese, J. C., Rao, N., Paroo, K., Triebwasser, C., Vargas-Irwin, C., Franquemont, L., et al. (2013). Failure mode analysis of silicon-based intracortical microelectrode arrays in non-human primates. *J. Neural Eng.* 10:066014. doi: 10.1088/1741-2560/10/6/066014

Bartlett, J. R., DeYoe, E. A., Doty, R. W., Lee, B. B., Lewine, J. D., Negrão, N., et al. (2005). Psychophysics of electrical stimulation of striate cortex in macaques. *J. Neurophysiol.* 94, 3430–3442. doi: 10.1152/jn.00406.2005

Bayraktar, O. A., Bartels, T., Holmqvist, S., Kleshchevnikov, V., Martirosyan, A., Polioudakis, D., et al. (2020). Astrocyte layers in the mammalian cerebral cortex revealed by a single-cell in situ transcriptomic map. *Nat. Neurosci.* 23, 500–509. doi: 10.1038/s41593-020-0602-1

Biran, R., Martin, D. C., and Tresco, P. A. (2005). Neuronal cell loss accompanies the brain tissue response to chronically implanted silicon microelectrode arrays. *Exp. Neurol.* 195, 115–126. doi: 10.1016/j.expneurol.2005.04.020

Callier, T., Schluter, E. W., Tabot, G. A., Miller, L. E., Tenore, F. V., and Bensmaia, S. J. (2015). Long-term stability of sensitivity to intracortical microstimulation of somatosensory cortex. *J. Neural Eng.* 12:056010. doi: 10.1088/1741-2560/12/5/056010

Campbell, A., and Wu, C. (2018). Chronically implanted intracranial electrodes: tissue reaction and electrical changes. *Micromachines* 9:430. doi: 10.3390/mi9090430

Chen, Y. Y., Lai, H. Y., Lin, S. H., Cho, C. W., Chao, W. H., Liao, C. H., et al. (2009). Design and fabrication of a polyimide-based microelectrode array: application in neural recording and repeatable electrolytic lesion in rat brain. *J. Neurosci. Methods* 182, 6–16. doi: 10.1016/j.jneumeth.2009.05.010

Cogan, S. F., Ludwig, K. A., Welle, C. G., and Takmakov, P. (2016). Tissue damage thresholds during therapeutic electrical stimulation. *J. Neural Eng.* 13:021001. doi: 10.1088/1741-2560/13/2/021001

Cyr-Depauw, C., Northey, J. J., Tabariès, S., Annis, M. G., Dong, Z., Cory, S., et al. (2016). Chordin-like 1 suppresses bone morphogenetic protein 4-induced breast cancer cell migration and invasion. *Mol. Cell Biol.* 36, 1509–1525. doi: 10.1128/MCB.00600-15

Davis, T. S., Parker, R. A., House, P. A., Bagley, E., Wendelken, S., Normann, R. A., et al. (2012). Spatial and temporal characteristics of V1 microstimulation during chronic implantation of a microelectrode array in a behaving macaque. *J. Neural Eng.* 9:065003. doi: 10.1088/1741-2560/9/6/065003

DeYoe, E. A., Lewine, J. D., and Doty, R. W. (2005). Laminar variation in threshold for detection of electrical excitation of striate cortex by macaques. *J. Neurophysiol.* 94, 3443–3450. doi: 10.1152/jn.00407.2005

Diamond, M. E., Huang, W., and Ebner, F. F. (1994). Laminar comparison of somatosensory cortical plasticity. *Science* 265, 1885–1888.

Eles, J. R., Vazquez, A. L., Snyder, N. R., Lagenaur, C., Murphy, M. C., Kozai, T. D., et al. (2017). Neuroadhesive L1 coating attenuates acute microglial attachment to neural electrodes as revealed by live two-photon microscopy. *Biomaterials* 113, 279–292. doi: 10.1016/j.biomaterials.2016.10.054

Esquibel, C. R., Wendt, K. D., Lee, H. C., Gaire, J., Shoffstall, A., Urdaneta, M. E., et al. (2020). Second harmonic generation imaging of collagen in chronically implantable electrodes in brain tissue. *Front. Neurosci.* 14:95. doi: 10.3389/fnins.2020.00095

Flesher, S. N., Collinger, J. L., Foldes, S. T., Weiss, J. M., Downey, J. E., Tyler-Kabara, E. C., et al. (2016). Intracortical microstimulation of human somatosensory cortex. *Sci. Transl. Med.* 8, 1–11.

Gaire, J., Lee, H. C., Hilborn, N., Ward, R., Regan, M., and Otto, K. J. (2018). The role of inflammation on the functionality of intracortical microelectrodes. *J. Neural Eng.* 15:066027. doi: 10.1088/1741-2552/aae4b6

Giulian, D., Li, J., Li, X., George, J., and Rutecki, P. A. (1994). The impact of microglia-derived cytokines upon gliosis in the CNS. *Dev. Neurosci.* 16, 128–136. doi: 10.1159/000112099

Gouwens, N. W., Sorensen, S. A., Berg, J., Lee, C., Jarsky, T., Ting, J., et al. (2019). Classification of electrophysiological and morphological neuron types in the mouse visual cortex. *Nat. Neurosci.* 22, 1182–1195. doi: 10.1038/s41593-019-0417-0

Harris, K. D., and Shepherd, G. M. G. (2015). The neocortical circuit: themes and variations. *Nat. Neurosci.* 18, 170–181. doi: 10.1038/nn.3917

Heffner, H. E., and Heffner, R. S. (1995). "Conditioned avoidance," in *Methods In Comparative Psychoacoustics*, eds G. M. Klump, R. J. Dooling, R. R. Fay and W. C. Stebbins (Cham: Springer), 79–93.

Hughes, C. L., Flesher, S. N., Weiss, J. M., Downey, J. E., Boninger, M., Collinger, J. L., et al. (2021). Neural stimulation and recording performance in human sensorimotor cortex over 1500 days. *J. Neural Eng.* 18:045012. doi: 10.1088/1741-2552/ac18ad

Koivuniemi, A., Wilks, S. J., Woolley, A. J., and Otto, K. J. (2011). Multimodal, longitudinal assessment of intracortical microstimulation. *Prog. Brain Res.* 194, 131–144. doi: 10.1016/B978-0-444-53815-4.00011-X

Kozai, T. D. Y., Li, X., Bodily, L. M., Caparosa, E. M., Zenonos, G. A., Carlisle, D. L., et al. (2014). Effects of caspase-1 knockout on chronic neural recording quality and longevity: insight into cellular and molecular mechanisms of the reactive tissue response. *Biomaterials* 35, 9620–9634. doi: 10.1016/j.biomaterials.2014.08.006

Kozai, T. D. Y., Vazquez, A. L., Weaver, C. L., Kim, S. G., and Cui, X. T. (2012). In vivo two-photon microscopy reveals immediate microglial reaction to implantation of microelectrode through extension of processes. *J. Neural Eng.* 9:66001. doi: 10.1088/1741-2560/9/6/066001

Lanjakornsiripan, D., Pior, B. J., Kawaguchi, D., Furutachi, S., Tahara, T., Katsuyama, Y., et al. (2018). Layer-specific morphological and molecular differences in neocortical astrocytes and their dependence on neuronal layers. *Nat. Commun.* 9:1623. doi: 10.1038/s41467-018-03940-3

McConnell, G. C., Rees, H. D., Levey, A. I., Gutekunst, C. A., Gross, R. E., and Bellamkonda, R. V. (2009). Implanted neural electrodes cause chronic, local inflammation that is correlated with local neurodegeneration. *J. Neural Eng.* 6:056003. doi: 10.1088/1741-2560/6/5/056003

McCreery, D. B., Agnew, W. F., Yuen, T. G. H., and Bullara, L. (1990). Charge density and charge per phase as cofactors in neural injury induced by electrical stimulation. *IEEE Trans. Biomed. Eng.* 37, 996–1001. doi: 10.1109/10.102812

Mercanzini, A., Colin, P., Bensadoun, J. C., Bertsch, A., and Renaud, P. (2009). In vivo electrical impedance spectroscopy of tissue reaction to microelectrode arrays. *IEEE Trans. Biomed. Eng.* 56, 1909–1918. doi: 10.1109/TBME.2009.2018457

Meyer, H. S., Egger, R., Guest, J. M., Foerster, R., Reissl, S., and Oberlaender, M. (2013). Cellular organization of cortical barrel columns is whisker-specific. *Proc. Natl. Acad. Sci. U.S.A.* 110, 19113–19118. doi: 10.1073/pnas.1312691110

Nolta, N. F., Christensen, M. B., Crane, P. D., Skousen, J. L., and Tresco, P. A. (2015). BBB leakage, astrogliosis, and tissue loss correlate with silicon microelectrode. *Biomaterials* 53, 753–762. doi: 10.1016/j.biomaterials.2015.02.081

Paxinos, G., and Watson, C. (2006). *The rat Brain in Stereotaxic Coordinates: Hard Cover Edition*. Amsterdam: Elsevier.

Pettersen, K. H., Devor, A., Ulbert, I., Dale, A. M., and Einevoll, G. T. (2006). Current-source density estimation based on inversion of electrostatic forward solution: effects of finite extent of neuronal activity and conductivity discontinuities. *J. Neurosci. Methods* 154, 116–133. doi: 10.1016/j.jneumeth.2005.12.005

Polikov, V. S., Tresco, P. A., and Reichert, W. M. (2005). Response of brain tissue to chronically implanted neural electrodes. *J. Neurosci. Methods* 148, 1–18. doi: 10.1016/j.jneumeth.2005.08.015

Prasad, A., and Sanchez, J. C. (2012). Quantifying long-term microelectrode array functionality using chronic in vivo impedance testing. *J. Neural Eng.* 9:026028. doi: 10.1088/1741-2560/9/2/026028

Prasad, A., Xue, Q. S., Dieme, R., Sankar, V., Mayrand, R. C., Nishida, T., et al. (2014). Abiotic-biotic characterization of Pt/Ir microelectrode arrays in chronic implants. *Front. Neuroengineering.* 7:2. doi: 10.3389/fneng.2014.00002

Romo, R., Hernández, A., Zainos, A., and Salinas, E. (1998). Somatosensory discrimination based on cortical microstimulation. *Nature* 392, 387–390. doi: 10.1038/32891

Rousche, P. J., and Normann, R. A. (1998). Chronic recording capability of the utah intracortical electrode array in cat sensory cortex. *J. Neurosci. Methods* 82, 1–15. doi: 10.1016/s0165-0270(98)00031-4

Rousche, P. J., and Normann, R. A. (1999). Chronic intracortical microstimulation (ICMS) of cat sensory cortex using the Utah Intracortical Electrode Array. *IEEE Trans. Rehabil. Eng.* 7, 56–68. doi: 10.1109/86.750552

Salas, M. A., Bashford, L., Kellis, S., Jafari, M., Jo, H., Kramer, D., et al. (2018). Proprioceptive and cutaneous sensations in humans elicited by intracortical microstimulation. *eLife* 7:e32904. doi: 10.7554/eLife.32904

Salatino, J. W., Ludwig, K. A., Kozai, T. D. Y., and Purcell, E. K. (2017). Glial responses to implanted electrodes in the brain. *Nat. Biomed. Eng.* 1, 862–877.

Saldanha, R. L., Urdaneta, M. E., and Otto, K. J. (2021). The role of electrode-site placement in the long-term stability of intracortical microstimulation. *Front. Neurosci.* 15:712578. doi: 10.3389/fnins.2021.712578

Sasaki, Y., Ohsawa, K., Kanazawa, H., Kohsaka, S., and Imai, Y. (2001). Iba1 is an actin-cross-linking protein in macrophages/microglia. *Biochem. Biophys. Res. Commun.* 286, 292–297. doi: 10.1006/bbrc.2001.5388

Schindelin, J., Arganda-Carreras, I., Frise, E., Kaynig, V., Longair, M., Pietzsch, T., et al. (2012). Fiji: an open-source platform for biological-image analysis. *Nat. Methods* 9, 676–682. doi: 10.1038/nmeth.2019

Sommakia, S., Lee, H. C., Gaire, J., and Otto, K. J. (2014). Materials approaches for modulating neural tissue responses to implanted microelectrodes through mechanical and biochemical means. *Curr. Opin. Solid State Mater. Sci.* 18, 319–328. doi: 10.1016/j.cossms.2014.07.005

Tehovnik, E. J., and Slocum, W. M. (2009). Depth-dependent detection of microampere currents delivered to monkey V1. *Eur. J. Neurosci.* 29, 1477–1489. doi: 10.1111/j.1460-9568.2009.06695.x

Tremblay, M. È, Stevens, B., Sierra, A., Wake, H., Bessis, A., and Nimmerjahn, A. (2011). The role of microglia in the healthy brain. *J. Neurosci.* 31, 16064–16069.

Urdaneta, M. E., Koivuniemi, A. S., and Otto, K. J. (2017). Central nervous system microstimulation: towards selective micro-neuromodulation. *Curr. Opin. Biomed. Eng.* 4, 65–77.

Urdaneta, M. E., Kunigk, N. G., Delgado, F., Fried, S. I., and Otto, K. J. (2021). Layer-specific parameters of intracortical microstimulation of the somatosensory cortex. *J. Neural Eng.* 18:055007. doi: 10.1088/1741-2552/abedde

Urdaneta, M. E., Kunigk, N., Delgado, F., Otto, K. J., and Member, S. (2019). "Somatosensory cortex microstimulation: behavioral effects of phase duration and asymmetric waveforms," in *Proceedings of the 41st Annual International Engineering Medicine Biology Society*, (Berlin). doi: 10.1109/EMBC.2019.8856579

Woolley, A. J., Desai, H. A., and Otto, K. J. (2013). Chronic intracortical microelectrode arrays induce non-uniform, depth-related tissue responses Related content. *J. Neural Eng.* 10:026007. doi: 10.1088/1741-2560/10/2/026007

Zhong, J., and Zou, H. (2014). BMP signaling in axon regeneration. *Curr. Opin. Neurobiol.* 27, 127–134. doi: 10.1016/j.conb.2014.03.009

Conflict of Interest: The authors declare that the research was conducted in the absence of any commercial or financial relationships that could be construed as a potential conflict of interest.

frontiers | Frontiers in Neuroscience

ORIGINAL RESEARCH
published: 17 June 2022
doi: 10.3389/fnins.2022.909434

The Effects of Sensory Threshold Somatosensory Electrical Stimulation on Users With Different MI-BCI Performance

Long Chen[1†], *Lei Zhang*[1†], *Zhongpeng Wang*[2], *Bin Gu*[2], *Xin Zhang*[2] *and Dong Ming*[1,2*]

[1] *Department of Biomedical Engineering, Academy of Medical Engineering and Translational Medicine, Tianjin University, Tianjin, China,* [2] *Department of Biomedical Engineering, College of Precision Instruments & Optoelectronics Engineering, Tianjin University, Tianjin, China*

Motor imagery-based brain-computer interface (MI-BCI) has been largely studied to improve motor learning and promote motor recovery. However, the difficulty in performing MI limits the widespread application of MI-BCI. It has been suggested that the usage of sensory threshold somatosensory electrical stimulation (st-SES) is a promising way to guide participants on MI tasks, but it is still unclear whether st-SES is effective for all users. In the present study, we aimed to examine the effects of st-SES on the MI-BCI performance in two BCI groups (High Performers and Low Performers). Twenty healthy participants were recruited to perform MI and resting tasks with EEG recordings. These tasks were modulated with or without st-SES. We demonstrated that st-SES improved the performance of MI-BCI in the Low Performers, but led to a decrease in the accuracy of MI-BCI in the High Performers. Furthermore, for the Low Performers, the combination of st-SES and MI resulted in significantly greater event-related desynchronization (ERD) and sample entropy of sensorimotor rhythm than MI alone. However, the ERD and sample entropy values of MI did not change significantly during the st-SES intervention in the High Performers. Moreover, we found that st-SES had an effect on the functional connectivity of the fronto-parietal network in the alpha band of Low Performers and the beta band of High Performers, respectively. Our results demonstrated that somatosensory input based on st-SES was only beneficial for sensorimotor cortical activation and MI-BCI performance in the Low Performers, but not in the High Performers. These findings help to optimize guidance strategies to adapt to different categories of users in the practical application of MI-BCI.

Keywords: motor imagery, brain-computer interface, sensory threshold somatosensory electrical stimulation, functional connectivity, EEG

Edited by:
Liming Li,
Shanghai Jiao Tong University, China

Reviewed by:
Yoshikatsu Hayashi,
University of Reading, United Kingdom
Jing Jin,
East China University of Science and Technology, China

***Correspondence:**
Dong Ming
richardming@tju.edu.cn

[†] *These authors have contributed equally to this work and share first authorship*

Specialty section:
This article was submitted to Neural Technology, a section of the journal Frontiers in Neuroscience

Received: *31 March 2022*
Accepted: *23 May 2022*
Published: *17 June 2022*

Citation:
Chen L, Zhang L, Wang Z, Gu B, Zhang X and Ming D (2022) The Effects of Sensory Threshold Somatosensory Electrical Stimulation on Users With Different MI-BCI Performance. Front. Neurosci. 16:909434. doi: 10.3389/fnins.2022.909434

INTRODUCTION

Brain-computer interface (BCI) constructs a communication pathway and control channel between brain activity and various devices, which enables users to interact with the external environment without relying on the muscle tissues (Wolpaw et al., 2002; Wang et al., 2019). In particular, BCIs based on electroencephalography (EEG) signals have been developed for different tasks and applications. The popular EEG-based BCI paradigms include steady state visual evoked potential (SSVEP), P300 event-related potential (ERP), motor imagery (MI), etc (Wang et al., 2019). As a mental rehearsal of limb movement, MI can induce neural activations over sensorimotor regions. The cortical activities generated by MI are usually observed as event-related desynchronization (ERD) or synchronization (ERS) in alpha and beta rhythms that can be detected and used for BCI control (Pfurtscheller and Neuper, 2001; Jeon et al., 2011). The BCIs based on MI (MI-BCIs) promote motor-related cortical plasticity and have been widely used in the field of motor rehabilitation and motor learning. Several studies have shown that MI-BCIs are effective in functional improvements of limb and drive significant recovery in stroke patients (Mrachacz-Kersting et al., 2016; Biasiucci et al., 2018).

Although MI-BCIs have a promising prospect in stroke rehabilitation, many users seem unable to produce ideal brain activity for the BCI control. There is about 15–30 percent of subjects are incapable of controlling a BCI at all, this lack of control is termed as "BCI illiteracy" or "BCI inefficiency" phenomenon (Allison and Neuper, 2010). Meanwhile, the MI-BCI performance of the most of remaining BCI literate participants was also mediocre (Jeunet et al., 2014). Therefore, various strategies need to be developed to improve MI-BCI performance and facilitate the practical applications of MI-BCI. In recent years, many researchers have devoted themselves to developing advanced machine learning algorithms to increase the decoding accuracy of brain signals. As invented for binary classification problems, Support Vector Machine (SVM) is capable of separating EEG signals between two classes by building a hyperplane with the largest margin (Bhuvaneswari and Kumar, 2013). In addition to traditional algorithms, deep learning methods are also introduced in MI-BCI to increase the classification accuracy (Zhao et al., 2019). Although, these advanced algorithms have achieved a slew of promising results in MI patterns recognition applications, the achievement of higher decoding accuracy is still limited by the inability of some subjects to produce reliable EEG responses (Ren et al., 2020; Li et al., 2021). This may be due to the subjects' inability to perform MI tasks properly. Therefore, several research works focused on developing appropriate MI guidance strategies to assist subjects to perform MI efficiently and accurately. Choi et al. found that providing a virtual reality (VR) as guidance induces neural patterns with greater discriminability (Choi et al., 2020). Similar results were also reported by Škola et al. where VR-based visual guidance succeeded in the improvement of the MI-BCI performance (Škola et al., 2019). In addition, somatosensory afference, which is essential for building internal body representation in MI tasks, has also attracted much attention recently. Compared with visual guidance, somatosensory afference is a more natural guidance strategy for subjects (Cincotti et al., 2007). Yao et al. demonstrated that enhancement of MI-BCI performance can be achieved by using tactile stimulation to optimize guidance strategy (Yao et al., 2013). Shu et al. showed in stroke patients that the application of tactile stimulation to the ipsilateral wrist achieved stronger motor-related cortical activation (Shu et al., 2018a). As a promising tool for motor rehabilitation, neuromuscular electrical stimulation (NMES) can induce muscular contraction and convey somatosensory afference. Yi et al. demonstrated that electrical stimulation combined with MI can increase the decoding accuracy of neural patterns (Yi et al., 2017). Reynolds et al. showed that the combination of MI and NMES induces a stronger sensorimotor rhythms ERD than MI alone (Reynolds et al., 2015). Although somatosensory stimulation is appropriate to improve motor imagery patterns, stimulation with excessive intensity may interfere with MI patterns and makes users unable to concentrate on imagining movement (Corbet et al., 2018). Recently, Tu-Chan et al. showed that sensory threshold somatosensory electrical stimulation (st-SES) can modulate activity in the sensorimotor cortices, and thus promote the recovery of hand motor function (Tu-Chan et al., 2017). NMES involves the application of repetitive transcutaneous electrical stimulation to superficial skeletal muscles, with the main objective to generate visible muscle contractions by depolarizing motor axons. In the same way that motor axons are recruited by NMES, sensory axons are also depolarized (Bergquist et al., 2011). However, devices such as NMES units can also deliver sensory threshold stimulation. Compared with conventional NEMS, st-SES can convey proprioceptive signals primarily by activating sensory axons without triggering large muscular contraction. Veldman et al. observed that a larger activation of sensorimotor regions and cortical connectivity was associated to somatosensory inputs in the form of st-SES (Veldman et al., 2018). Corbet et al. showed that st-SES during MI increased connectivity between the frontal-parietal network and significantly improved the accuracy of classifier for discriminating MI from resting state (Corbet et al., 2018). These studies demonstrated that st-SES is an effective way to modulate the brain patterns of somatosensory cortices and promote BCI performance.

Although past studies have shown that the guidance based on somatosensory afference contributes to the improvement of BCI performance, somatosensory afference guidance does not appear to be effective for all subjects. Park et al. reported that BCI illiterate subjects achieve significantly higher MI-BCI classification accuracy when subjects are asked to perform the somatosensory-motor imagery, but BCI literate subjects experience a slight decrease in classification performance (Park et al., 2021). In addition, Kaiser et al. showed that cortical effects of BCI training are only found in BCI illiterate subjects but not in BCI literate subjects (Kaiser et al., 2011). This means that some guidance strategies may not be suitable for all users. However, most of the previous studies have not explored the impact of somatosensory afference guidance on different categories of subjects. To our knowledge, no study has reported the different effects of somatosensory stimulation on MI performance in high and low BCI performers, which is not conducive to adapt the guidance strategy to each user. Therefore, although st-SES has shown great potential in fostering BCI performance, it is worth exploring whether st-SES is appropriate to assist subjects with different BCI performance.

In this study, we aim to investigate the effect of combining MI and st-SES on cortical activation and MI-BCI classification performances in high and low BCI performers. Considering the physical and psychological differences between high and low BCI performers (Shu et al., 2018b), we presume that st-SES have different effects on the two categories of subjects. In addition, Corbet et al. demonstrated the st-SES is feasible in improving the accuracy of discriminating MI combined with st-SES and resting state (Corbet et al., 2018). However, the stimulation effect of st-SES on a brain-switch BCI used to distinguish between task state and resting state is still unclear. Thus, the current study focused on evaluating brain-switch BCI performance when st-SES was constantly applied during both MI task and resting state. Offline BCI performances were evaluated with or without st-SES modulation. Further, to investigate the effect of st-SES on cortical activation, we compared the activation intensity of the sensorimotor cortex between MI combined with st-SES and MI alone.

MATERIALS AND METHODS

Participants

Twenty able-bodied subjects (11 males, mean age 23.4 ± 0.6, right-handed) participated in this study. All participants have no history of neurological or psychiatric disorders. The experimental procedure described in this study was approved by the ethical committee of Tianjin University. The detailed process of the experiment was clearly explained to each participant before experimental data were recorded. All participants signed an informed consent form.

EEG Recording and St-SES Intervention

During the whole experiment, subjects were instructed to sit in a relaxed position about 1.5 m in front of the screen with palms facing up. EEG signals were recorded using the SynAmps2 system (Neuroscan, Victoria, Australia) with 60 standard Ag/AgCl electrodes, which were placed on the scalp according to the international 10–20 system. A ground electrode was placed on the forehead and a reference electrode was placed on the nose. EEG signals were recorded at a sampling rate of 1,000 Hz and a notch filter with 50 Hz was used in the acquisition process. The impedances were kept under 10 kΩ during the data acquisition.

St-SES was generated using VitalStim Therapy (Chattanooga Group, TN, USA). Two electrodes were placed on the participants' flexor digitorum superficialis at the anterior face of the right forearm. The frequency of stimulation was set to 30 Hz for all participants. The stimulation amplitude of st-SES was individually evaluated for each participant before EEG recordings. The amplitude was gradually increased from 0 mA until the participants reported a closure sensation of the affected hand, while the amplitude was adjusted to avoid eliciting any visible movement. The stimulation intensity varied between 4 and 6 mA according to the subject-dependent sensory threshold.

Design of the Experimental Paradigm

This study contained four different experiment conditions (MI, SES, MI-SES, and Rest). Before the experiment began, participants performed gripping movements to familiarize themselves with the imaginary proprioceptive sensations. For MI and MI-SES conditions, the instructions given to the participants were the following: "You have to perform kinesthetic imagery of right-hand grasp movement (RH-MI) while seeing the visual guidance on the screen. During the task period, you should imagine the proprioceptive sensation of the hand closing without eliciting any muscular contraction. You should perform continuous MI instead of repetitive MI and keep a consistent MI strategy across trials." For SES and Rest conditions, the instructions were the following: "You should keep fully relaxed and avoid any movement of limbs. You have to avoid paying attention to your hands and should not think about your hands." In SES condition, the participants received st-SES and were instructed to remain at rest. In the MI-SES condition, the participants were instructed to perform RH-MI and st-SES was applied on the participants' forearms during MI. In MI and Rest conditions, even if the st-SES was not applied, the electrodes were anyway placed on the skin to ensure consistent tactile stimulation.

The experiment included four runs. Each run consisted of four conditions (10 trials per condition) and trials were performed in random order, with 40 trials per condition at the end of the experiment. The number of trials for each condition was consistent with Corbet et al.'s study to eliminate discrepancies in results that might be caused by trial size (Corbet et al., 2018). The experimental paradigm of each trial is represented in **Figure 1**. The trial began with a green cross which appeared on the center of the screen as a preparation cue for the task and lasted for 1 s. Then, an initiation cue in the form of a green cross with or without a red arrow is presented in the middle of the screen for 4 s, indicating the onset of the task period. During this period, participants should perform RH-MI (red arrow on the green cross) or stay at rest (green cross alone) until the cue disappeared. In order to prevent the attention on MI from being disturbed by st-SES in MI-SES condition, st-SES was not activated until 2 s after the task period onset. Similarly, in the SES condition, st-SES was activated 2 s after the task began. When the initiation cue disappeared, the screen turned black. The time interval between trials varied randomly between 3 and 5 s to prevent adaptation. The participants were advised to restrict movements such as blinking or swallowing during the task period which may produce artifacts.

Pre-Processing

For decoding analysis, EEG signals were only filtered into 8–28 Hz and down sampled to 250 Hz. For the rest of the analysis, raw EEG data were firstly band-pass filtered in the frequency band between 0.5 and 100 Hz to remove high-frequency noise and baseline drift. The signals were then down sampled to 250 Hz. Independent component analysis (ICA)

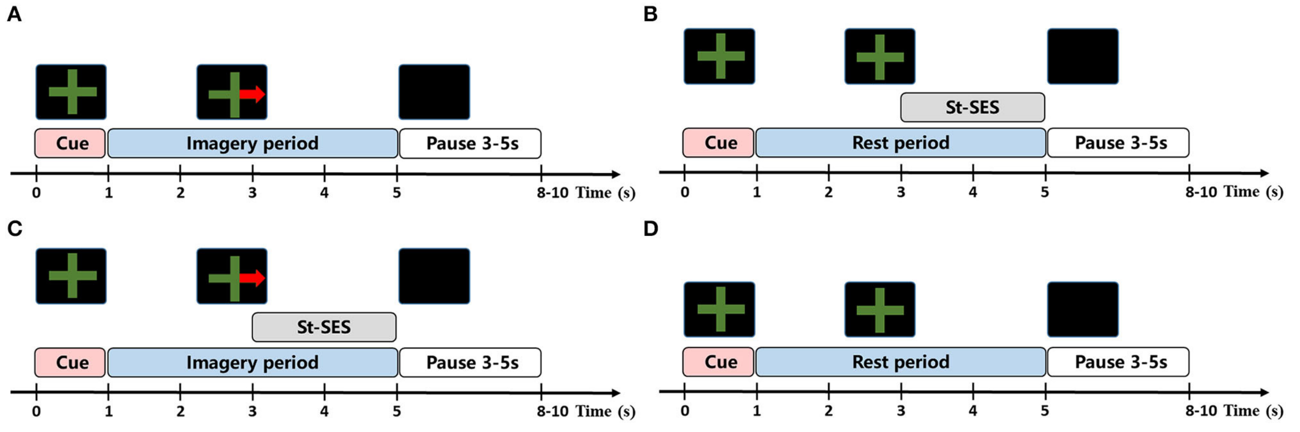

FIGURE 1 | The task procedure of experimental condition. **(A)** MI condition. In each trial of MI condition, the subjects were required to perform MI task according to the cue. **(B)** SES condition. In each trial of SES condition, the subjects were asked to remain at rest and received st-SES intervention. **(C)** MI-SES condition. In each trial of MI-SES condition, the subjects were instructed to perform MI task according to the cue and st-SES was applied to subjects during MI. **(D)** Rest condition. In each trial of Rest condition, the subjects were asked to remain relax.

was applied to filter out the components related to ocular and electromyographic artifacts. The rank-deficiency problem was accounted for by reducing the number of ICs. We then performed the surface Laplacian transform to eliminate the low-frequency coupling among electrodes. After that, the noisy trials, which were detected post-experiment by visual inspection, were discarded in the analysis.

Classification Analysis

EEG features of each condition were extracted by the common spatial pattern (CSP) algorithm. The CSP algorithm is commonly used to extract discriminative spatial features from EEG by maximizing the variance difference between two classes. The data of the period from 1 to 5 s after the preparation cue appeared were utilized for decoding analysis. The features were extracted from the frequency band between 8 and 28 Hz which was associated with sensorimotor rhythm. The log-variance of the first and last four components generated by CSP filters were selected to construct feature vectors. After that, a SVM classifier with a linear kernel was used to classify the users' neural patterns, with the regularization parameter C of the classifier set to the default value of 1. One classifier was trained to discriminate MI-SES condition from SES condition, and another classifier was used to discriminate MI condition from Rest condition. In addition, we also investigated the accuracy of each of the two class classifiers that discriminates MI-SES or SES conditions from the Rest condition. All classifiers were evaluated through the leave-one-out cross-validation method. The 80 trials of two class were randomly divided into forty sets. Each set included one sample of each class. In each fold, one set was selected as the testing set and the remaining samples as the training set. The final classification accuracy was the average of all fold classifications.

The participants were assigned to Low and High performers based on their classification accuracy in discriminating MI condition from Rest condition described in the previous paragraph. In this study, High performers were defined as those with a classification accuracy of more than 80%. According to the decoding accuracy, 10 participants were assigned to High performers group, and the other 10 participants were assigned to the Low performers group. Previous studies typically set the inefficiency threshold for two-class MI-based BCI (distinguishing two brain states) at 70% accuracy (Brunner et al., 2010; Shu et al., 2018b). However, Allison and Neuper showed that the inefficiency threshold should be determined based on the type of BCI (Allison and Neuper, 2010). Compared with two-class BCI, brain-switch BCI is designed to detect only one brain state (Pfurtscheller et al., 2010). In addition, some studies suggested that a threshold of at least 80% should be used to determine BCI literate subjects (Kaplan et al., 2016; Horowitz et al., 2021). Thus, we used a threshold of 80% in the brain-switch BCI.

Time–Frequency Analysis

In order to evaluate the effect of somatosensory input on cerebral cortex activity, we computed event-related spectral perturbation (ERSP) for three conditions (MI, SES, and MI-SES). ERSP describes the power changes of EEG signals in the time-frequency domain (Makeig et al., 2004). The increase or decrease of power relative to baseline in a specific frequency band can be represented in the form of ERS or ERD. Some studies have demonstrated that somatosensory input has a significant effect on cortical activation of MI. In this study, we mainly compared the differences in ERSP values between MI and MI-SES conditions for each group. The calculation formula of ERSP for n trials was defined as follow:

$$ERSP\left(f,t\right) = \frac{1}{n}\sum_{k=1}^{n} F_k(f,t)^2 \quad (1)$$

where $F_k(f,t)$ represents the spectral estimation of kth trial at frequency f and time t. The short-time Fourier transform (STFT) with a Hanning-tapered window from EEGlab was applied to compute the ERSP (dB) (Delorme and Makeig, 2004). Window width was set as 256 sampling points (Yi et al., 2017). The ERSP values were normalized by subtracting the mean power changes during a baseline period of [−1 −0.2] s. The average ERSP values across all subjects at key channel C3 were mainly analyzed. For quantifying the cortex activation in each condition, ERSP values at channel C3 were averaged over task time (3–5 s) and within alpha (8–13 Hz) and beta (14–28 Hz) rhythm bands. A paired *t*-test be used to compare the averaged ERSP values between MI-SES and MI conditions in each rhythm band for each group only if the normality test (Shapiro–Wilk test) was satisfied. If the normality was not satisfied, the Wilcoxon signed-rank test was used.

Further, the coefficient of determination r^2 was calculated to assess the differences in signal spectra between MI and resting state with or without st-SES modulation. The r^2 value is between 0 and 1, where r^2 value close to 1 indicates that two states are well discriminative, and r^2 value close to 0 indicates that two states can be difficult to distinguish (Meng et al., 2018). For each subject, r^2 value of each channel was averaged over the frequency band of [8 28] Hz and time interval of [3 5] s, and then averaged across all subjects.

Signal Complexity Analysis

The brain is a complex non-linear system, and neural activity measured by EEG signals exhibits non-linear dynamic properties. To estimate the complexity of the EEG signal, the sample entropy of EEG data for MI-SES and MI conditions was calculated. Sample entropy (SampEn) is the negative natural logarithm of the conditional probability that two data sequences are similar for length *m* remain similar for length $m + 1$, where a larger value corresponds to the greater probability of generating new patterns in time series and the higher complexity in sequences (Richman and Moorman, 2000). Therefore, SampEn can be used to assess the complexity of EEG during motor imagery. The SampEn was computed as follow:

For a time series X with N data points, m consecutive X data points were extracted from that to form a sequence $X_m(i)$.

$$X_m(i) = \{x_i, \ldots, x_{i+m-1}\},\ 1 \le i \le N - m \tag{2}$$

where m is the embedding dimension, i represents starting at the ith point. The distance between two sequence $X_m(i)$ and $X_m(j)$ is denoted as $d[X_m(i), X_m(j)]$ which is defined to be the maximum absolute difference between their corresponding scalar components. The number of all sequence pairs with the $d[X_m(i), X_m(j)] \le r$ is counted and represented as $B_i^m(r)$. The r denotes the tolerance and is defined as $r = g \times SD$, where SD is the standard deviation of the time series X. Then, a parameter $B_m(r)$ can be defined as:

$$B_m(r) = \frac{1}{N-m}\sum_{i=1}^{N-m}\frac{B_i^m(r)}{N-m-1} \tag{3}$$

After the embedding dimension is set to $m + 1$, the above process is repeated to obtain $B_{m+1}(r)$. Finally, the SampEn of time series is defined as:

$$SampEn(x, m, r) = -\ln\frac{B_{m+1}(r)}{B_m(r)} \tag{4}$$

Here, the embedding dimension was set as $m = 2$ and the tolerance was set as $r = 0.1 \times SD$. The baseline SampEn of each trial was computed using EEG data in [−1, −0.2] s. To obtain the relative SampEn, SampEn values within task period [3 5] s were normalized by subtracting the baseline SampEn value and divided by this same baseline SampEn value. Then the relative SampEn values of the trials in each condition were averaged. The relative SampEn values at channel C3 and within [8 28] Hz were calculated for further analysis. Then, a statistical analysis was performed to compare relative SampEn values between MI-SES and MI conditions in each group.

Functional Connectivity Analysis

In order to inspect differences in brain area interactions between High performers and Low performers, the weighted phase lag index (wPLI) was used for functional connectivity analysis. The wPLI is a method to estimate the asymmetry in the distribution of instantaneous phase differences between two time series (Vinck et al., 2011). The larger the wPLI value, the greater the phase consistency between brain regions. The wPLI has been shown to be insensitive to zero-lag phase relations typically caused by contaminations from volume conduction. The wPLI is defined as:

$$wPLI_{xyt} = \frac{n^{-1}\sum_{t=1}^{n}\left|imag\left(s_{xyt}\right)\right| sign(imag(s_{xyt}))}{n^{-1}\sum_{t=1}^{n}\left|imag\left(s_{xyt}\right)\right|} \tag{5}$$

whereby $imag(s_{xyt})$ indicates the imaginary component of the cross-spectrum between time series x and y at time point t, and *sign* denotes the sign function ($-1, +1$ or 0).

In this case, the EEG of 30 channels overlying the frontal, sensorimotor, and parietal areas was selected to construct a connectivity network. These channels include F line channels (F1–F6), FC line channels (FC1–FC6), C line channels (C1–C6), CP line channels (CP1–CP6) and P line channels (P1–P6). Here, wPLI values were calculated from EEG data within time period of [3 5] s and frequency range of alpha (8–13 Hz) and beta (14–28 Hz) by function ft_connectivity_wpli.m implemented in the Fieldtrip toolbox (Oostenveld et al., 2011). After that, the wPLI values in each pair of channels were normalized by subtracting the mean wPLI value of baseline period [−1, −0.2] s and divided by the standard deviation of wPLI value during the baseline period. Then, the statistical significance of non-zero wPLI values was assessed by a permutation test based on the t-statistic. The significant functional connectivity between channels was defined as the *p*-value below the critical threshold of 0.005 according to previous studies (Jin et al., 2017; Li et al., 2020).

RESULTS

Classification Performance

The offline accuracies of brain-switch BCI in High Performers group and Low Performers group are presented in **Figure 2**. The classification accuracies for both High and Low Performers groups were normally distributed, as assessed by the Shapiro–Wilk test ($p > 0.05$). We compared the performance of the MI-SES vs. SES classifier and MI vs. Rest classifier. For High Performers group, a paired t-test revealed a significant decrement in classification accuracy for MI-SES vs. SES classifier compared with MI vs. Rest classifier (0.83±0.07 vs. 0.89±0.03, $p < 0.01$). More specifically, nine out of 10 participants had lower classification accuracy with the st-SES intervention. However, the accuracy of MI-SES vs. SES classifier was significantly higher than that of MI vs. Rest classifier in Low Performers group (0.74 ± 0.09 vs. 0.68 ± 0.07, $p = 0.047$). Most of the Low Performers achieved better classification accuracy with the st-SES intervention, but still, three out of 10 participants showed a slight reduction in accuracy of MI-SES vs. SES classifier compared with MI vs. Rest classifier.

Furthermore, we investigated whether somatosensory input could make the neural pattern in the MI task more distinguishable from that in the resting state. We compared the classification accuracies of classifiers that distinguish three conditions (MI-SES, MI, SES) from the Rest condition in each group (**Figure 3**). Through one-way repeated measures ANOVA, we found that there was a significant difference in accuracy among the three classifiers in both High Performers ($F(2, 18) = 80.3$, $p < 0.01$) and Low Performers ($F(1.3, 11.67) = 24.78$, $p < 0.01$). In the High Performers group, the Bonferroni *post-hoc* analysis indicated that the accuracy of both MI-SES vs. Rest and MI vs. Rest classifiers was significantly higher than that of the SES vs. Rest classifier (0.61 ± 0.06, $p < 0.01$ both comparisons). However, there was no significant difference between MI-SES vs. Rest classifier and MI vs. Rest classifier (0.87 ± 0.07 vs. 0.89±0.03). Specifically, only five out of 10 participants achieved higher accuracy in MI-SES vs. Rest classifier as compared with the performance in MI vs. Rest classifier. For the Low Performers group, the Bonferroni *post-hoc* analysis demonstrated that MI-SES vs. Rest classifier achieved significantly higher accuracy than MI vs. Rest classifier (0.77 ± 0.06 vs. 0.68 ± 0.07, $p < 0.01$). All participants in Low Performers group achieved better classification performance in MI-SES vs. Rest classifier than in MI vs. Rest classifier. In addition, the classification performance of both MI-SES vs. Rest and MI vs. Rest classifiers was greater than that of the SES vs. Rest classifier (0.56 ± 0.11, $p < 0.01$ and $p = 0.025$, respectively). From the results of these analyses, the st-SES only improved the classification performance of the Low Performers group, but not the classification accuracy of the High Performers group.

Time-Frequency Results

In order to better understand the effect of somatosensory stimulation on neural response during MI, we analyzed the band power changes of EEG in the sensorimotor cortex under three conditions (MI-SES, MI, SES). The average time-frequency maps of ERSP values at channel C3 (in the contralateral hemisphere) in each group are presented in **Figure 4**. The ERSP within alpha and beta rhythms can be used as a measure of cortical activation. As shown in **Figure 4**, ERD could be observed in alpha and beta frequency bands for all conditions in both groups, indicating that the sensorimotor cortex was activated in all three conditions. However, more visible ERD was found in MI-SES condition after st-SES was activated compared with MI and SES conditions. This result is consistent with previous studies showing that the motor cortex excitability can be improved by the combination of MI and somatosensory stimulation (Corbet et al., 2018; Vidaurre et al., 2019). In addition, the ERD patterns during MI tasks indicated that motor cortex activation in the High Performers group was stronger than that in the Low Performers group. Moreover, compared with High Performers group, the Low Performers group had difficulty maintaining a consistent ERD pattern during the task period under MI conditions.

Additionally, in order to quantitatively analyze the effectiveness of st-SES on sensorimotor cortical activation, we compared averaged ERSP values between MI-SES and MI conditions in different EEG frequency bands, including the alpha (8–13 Hz) and beta (14–28 Hz) (**Figure 5**). The Shapiro–Wilk test indicated that the averaged ERSP values in the alpha band for both High and Low Performers group were normally distributed ($p > 0.05$). In the beta band, the averaged ERSP values in the MI condition of High Performers group ($p = 0.034$) and the MI-SES condition of Low Performers group ($p < 0.01$) were not normally distributed, as assessed by Shapiro–Wilk test. For High Performers group, the averaged ERSP values of both alpha and beta bands were lower in MI-SES condition compared with the MI condition, yet these differences were not significant (alpha: paired t-test, $p = 0.065$; beta: Wilcoxon signed-rank test, $p = 0.139$). In contrast, for the Low Performers group, the averaged ERSP values of both alpha and beta bands in MI-SES condition were significantly smaller than those under MI condition (alpha: paired t-test, $p = 0.018$; beta: Wilcoxon signed-rank test, $p < 0.01$). The unpaired t-test confirmed that there was no significant difference in average ERSP values in the SES condition between the High Performers group and Low Performers group (alpha: $p = 0.379$; beta: $p = 0.11$). These results suggested that somatosensory stimulation combined with motor imagery could significantly promote lateralized sensorimotor cortex activities in Low Performers.

The spatial distributions of r^2 values for the High Performers and Low Performers groups are presented in **Figure 6**. The topographies of the r^2 values revealed that the discriminative information was mostly focused on the left somatosensory cortex. For High Performers group, the r^2 values for comparison between MI-SES and SES conditions were lower than those for comparison between MI and Rest conditions, implying that st-SES modulation reduced the separability of neural patterns between MI and resting state. On the contrary, for the Low Performers group, st-SES modulation elicited an enhancement in r^2 values for comparison between MI and resting state.

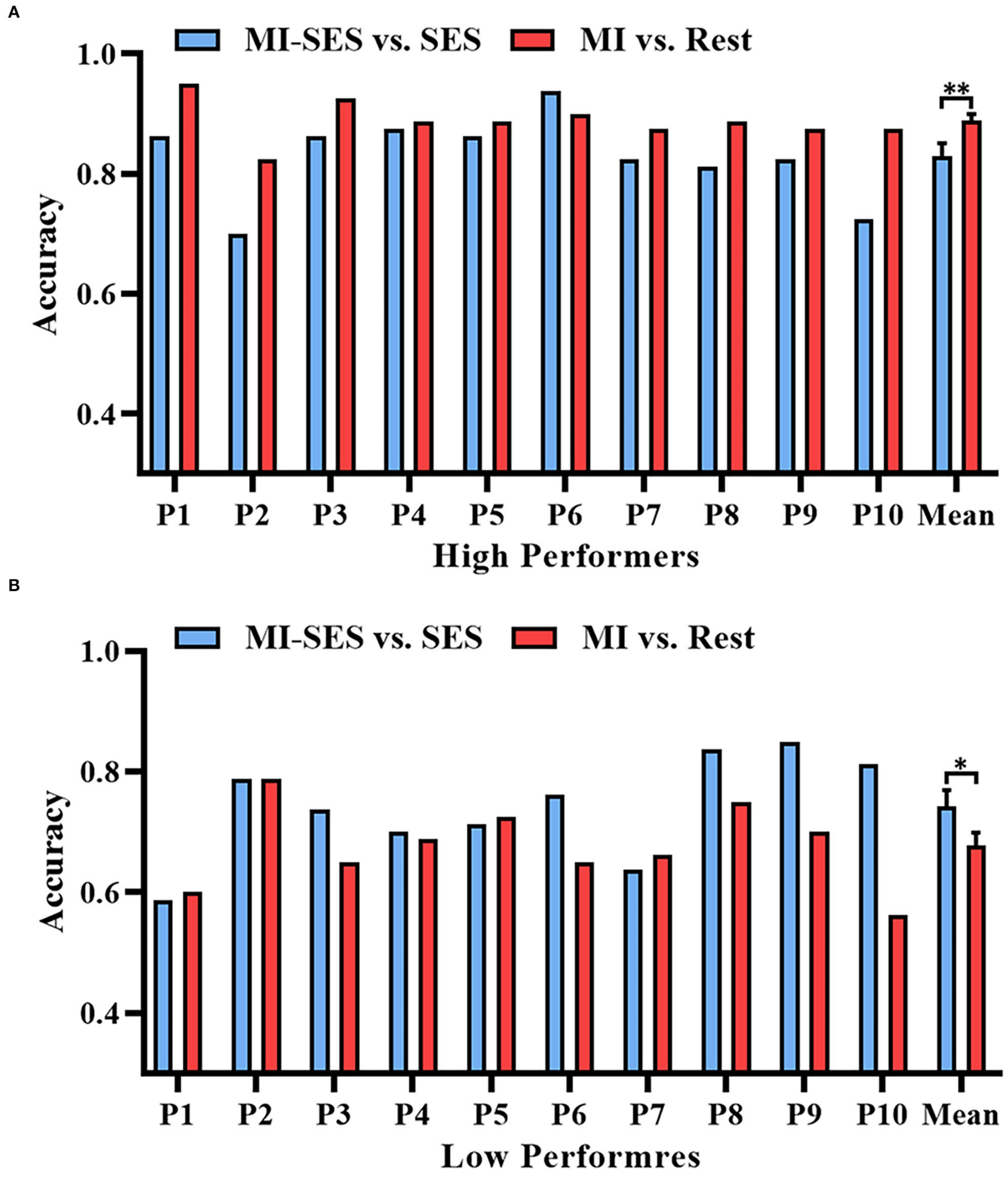

FIGURE 2 | Offline accuracies of brain-switch BCI with or without st-SES modulated. **(A)** Classification accuracy results in High Performers group. **(B)** Classification accuracy results in Low Performers group. Error bars represent standard error of mean. "*" indicates $p < 0.05$, "**" indicates $p < 0.01$.

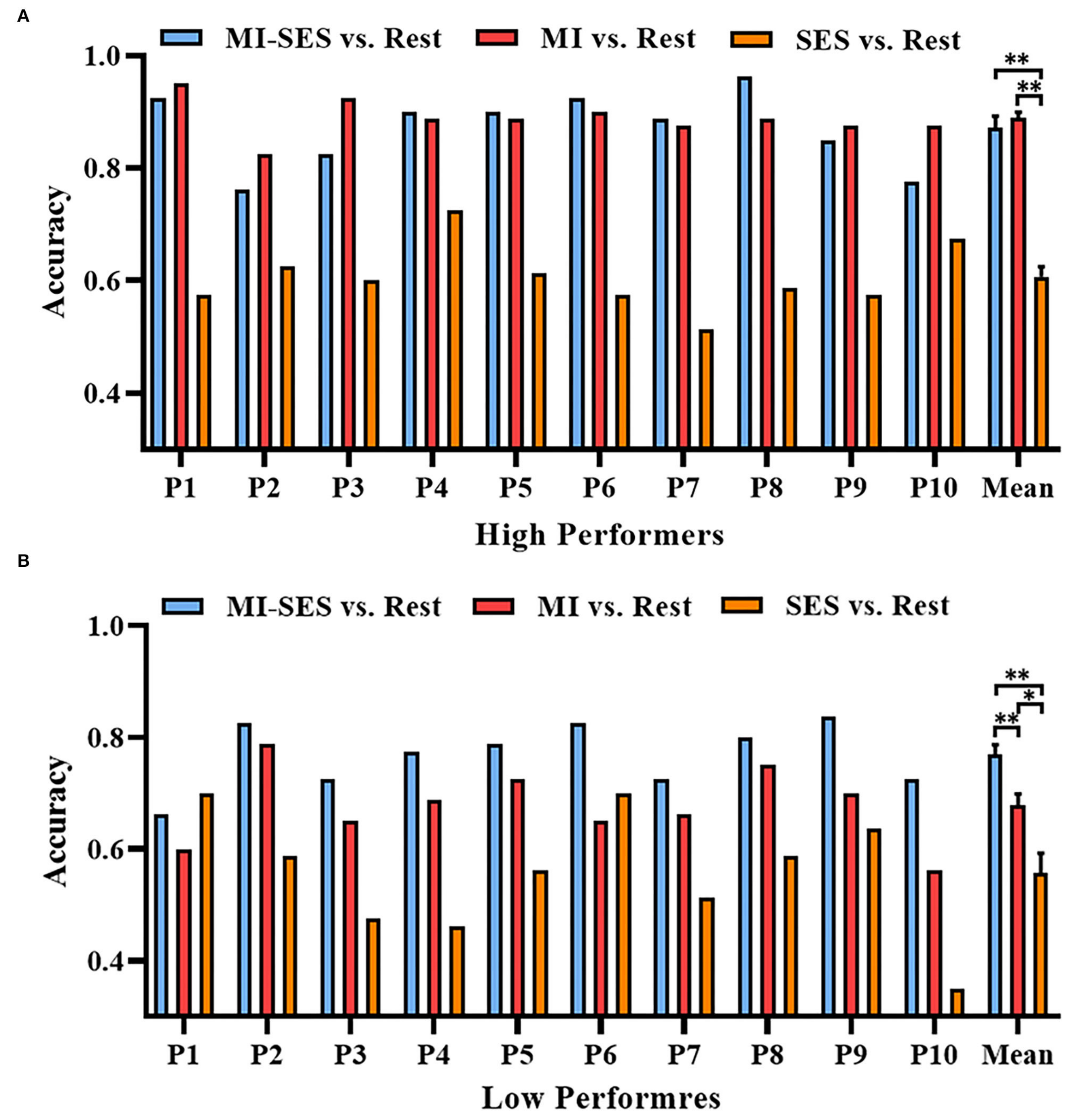

FIGURE 3 | Offline accuracies of distinguishing three conditions (MI-SES, MI, SES) from Rest condition. **(A)** Classification accuracy results in High Performers group. **(B)** Classification accuracy results in Low Performers group. Error bars represent standard error of mean. “*” indicates $p < 0.05$, “**” indicates $p < 0.01$.

Sample Entropy Results

The SampEn values provided further insight into the effects of somatosensory stimulation on EEG complexity. The relative SampEn values of channel C3 in MI-SES and MI conditions for both High Performers and Low Performers are presented in **Figure 7**. Both MI-SES and MI conditions showed higher relative SampEn values in High Performers group compared with Low Performers group. The relative SampEn values in MI-SES condition for High Performers were not normally distributed, as assessed by Shapiro–Wilk test ($p = 0.032$). In the High Performers group, although the relative SampEn values under MI-SES conditions were greater than those in the MI condition, there was no significant difference in the relative SampEn values of the two conditions (Wilcoxon signed-rank test, $p = 0.169$).

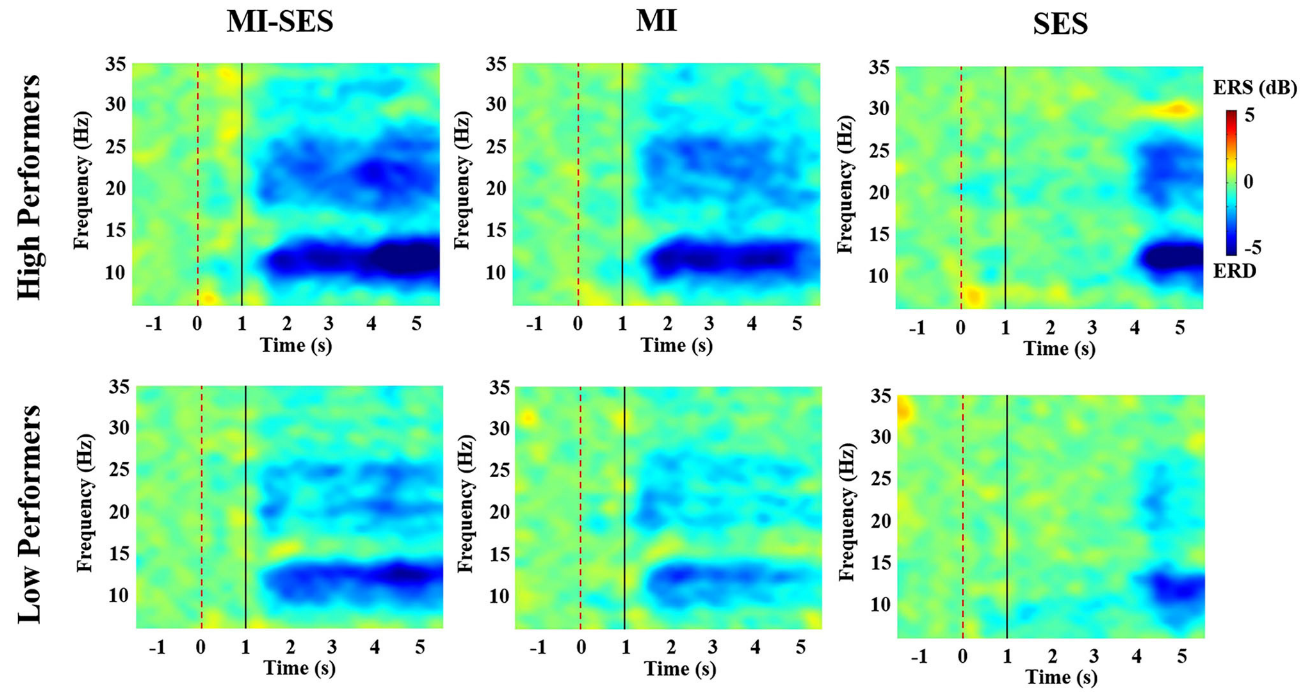

FIGURE 4 | The average time-frequency maps over C3 channel for all High Performers and all Low Performers. The period [1 5] s indicated the MI or rest task. The period [3 5] s corresponds to st-SES in MI-SES and SES conditions.

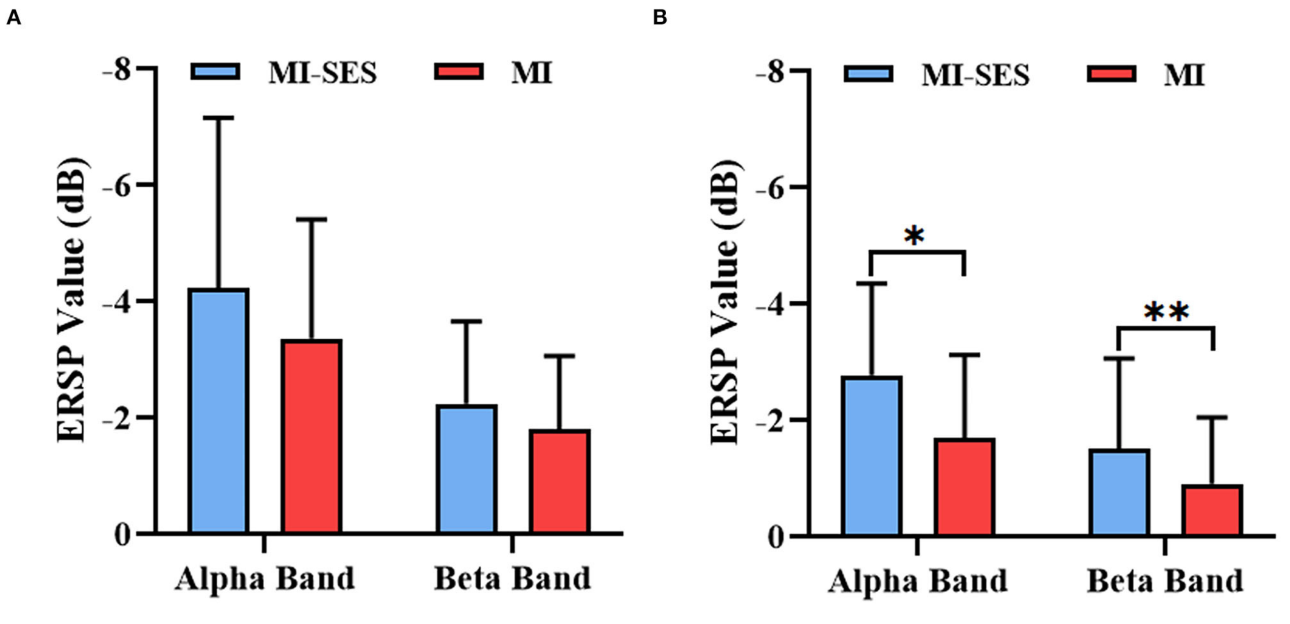

FIGURE 5 | Averaged ERSP values of alpha (8–13 Hz) and beta (14–28 Hz) rhythms during period [3 5] s for MI-SES and MI conditions. **(A)** High Performers group. **(B)** Low Performers group. Error bars represent the standard deviation. "*" indicates $p < 0.05$, "**" indicates $p < 0.01$.

For the Low Performers group, however, we found that the relative SampEn values were significantly higher in the MI-SES condition compared with the MI condition (paired t-test, $p < 0.01$).

Functional Connectivity Results

Figure 8 shows the functional connectivity alterations between MI task and resting state in each group. These alterations in functional connectivity involved both intra-hemispheric

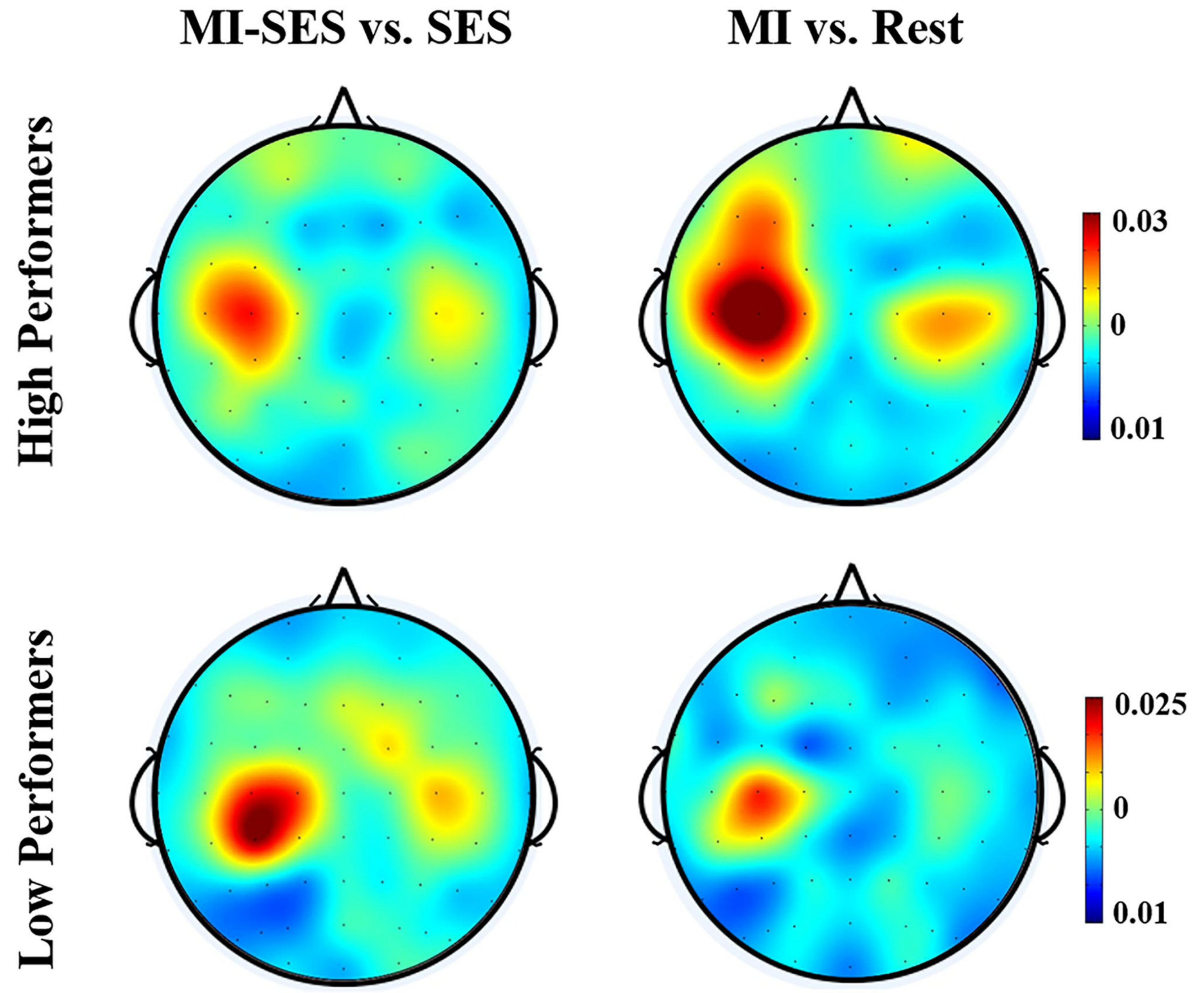

FIGURE 6 | Averaged topographical distributions of r^2 during period [3 5] s for all High Performers and all Low Performers.

and inter-hemispheric interactions. Notably, we detected phase consistency of the contralateral sensorimotor network decreased significantly in the MI task compared with the resting state. In the High Performers group, a lateralized network at the alpha band could be clearly observed in the contralateral hemisphere during MI-SES and MI conditions. However, no obvious differences in the frontoparietal network were found between the MI-SES condition and MI condition in the alpha band. In contrast, for the beta band, the number of functional connectivity in the left fronto-parietal network was higher in the MI condition compared with the MI-SES condition. For the Low Performers group, a lateralized network at the alpha band was only found in the MI-SES condition, but not in the MI condition. In the beta band, there were no obvious differences in the contralateral fronto-parietal network between the MI-SES condition and the MI condition.

DISCUSSION

In the present study, we investigated the effect of the combination of st-SES and MI on subjects with different BCI performances. The results demonstrated that st-SES combined with MI fostered the decoding accuracy of brain-switch BCI in Low Performers group, but resulted in a decrease in the brain-switch BCI accuracy in High Performers group. In addition, we found that st-SES only improved the neural response patterns during MI in Low Performers group, but not in High Performers group.

Differences in Classification Performance

MI-BCI is an effective tool to promote recovery in stroke patients. However, most users are unable to generate reliable neural response patterns to control MI-BCI effectively. This limits the application of MI-BCI in clinical practice. Over the past few

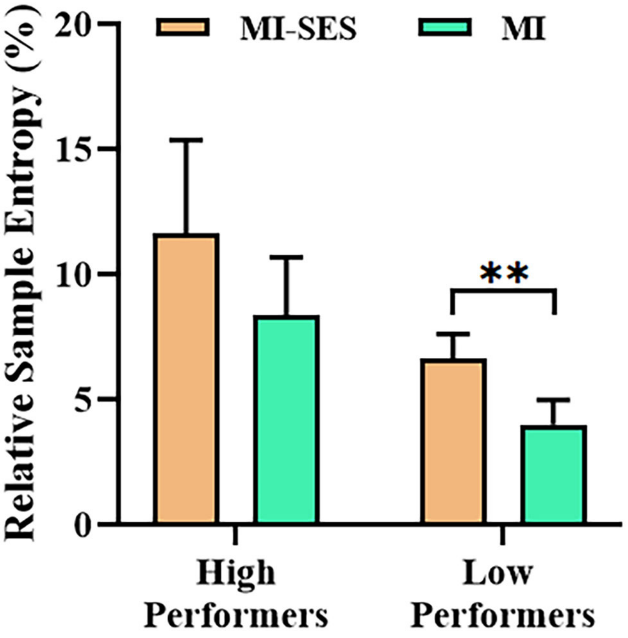

FIGURE 7 | Averaged relative sample entropy values of C3 channel in MI-SES and MI conditions. Error bars represent standard error of mean. "**" indicates $p < 0.01$.

decades, intensive research have been conducted to improve the performance of MI-BCI. Some researchers are devoted to increasing MI-BCI accuracy by developing feature extraction and classification algorithms (Chen et al., 2020; Hang et al., 2020). Although these techniques have achieved some success, further improvements in BCI performance are still impeded by the inconsistent MI patterns produced by subjects unfamiliar with MI (Vidaurre et al., 2019; Ren et al., 2020). Thus, it is necessary to develop suitable MI guidance strategies to help subjects understand how to perform MI properly.

Visual and somatosensory stimulation are two commonly used guidance strategies (Ren et al., 2020). Compared with visual stimulation, somatosensory stimulation has the advantage of not occupying the vision and providing more natural guidance for MI tasks (Zhang et al., 2021). St-SES, which can provide somatosensory afference to the targeted limb, has been demonstrated to enhance the activation of the sensorimotor cortex during MI tasks and the performance of MI-BCI (Corbet et al., 2018). However, the results in this study show that the guidance strategy based on st-SES does not seem to be effective in improving the MI-BCI accuracy for all subjects. With the integration of st-SES, the classification accuracy of distinguishing MI task from resting state was significantly improved in the Low Performers group. In contrast, we found that the performance of brain-switch BCI was significantly reduced when st-SES was applied in the High Performance group. Therefore, st-SES may have different effects on neural response patterns in High and Low Performers groups. This interpretation is consistent with the results showing that the r^2 values between MI and resting state were greater during the st-SES intervention in the Low Performers group, where st-SES caused a decrease in the r^2 values for the High Performers group. This indicated that the st-SES intervention made the brain patterns between MI and resting state more separable in the Low Performers group while reducing the distinguishability of neural patterns between MI and resting state in the High Performers group.

In addition, we also observed that the decoding accuracy of the MI-SES vs. Rest classifier was significantly higher than that of the MI vs. Rest classifier only in the Low Performers group, but not in High Performers group. This may be due to the lack of significant difference in sensorimotor cortical activation between MI-SES condition and MI condition in the High Performers group, whereas st-SES induced greater cortical activation during MI in the Low Performers group. This interpretation is consistent with the results showing that the significant differences in ERSP values between MI-SES and MI conditions were found only in the Low Performers group, but not in the High Performers group. However, these findings are inconsistent with a previous study in which the classification accuracy was significantly greater with MI-SES condition compared with MI condition. In fact, Corbet et al. found that st-SES modulation contributed to the improvement of the MI-BCI performance when the data of the first day was used as the training set and the data of the second day was used as the test set (Corbet et al., 2018). When the same day data was divided into training and test sets, there was no significant difference in classification performance between the MI-SES condition and the MI condition. Vidaurre et al. showed that whereas decoding neural patterns from MI conditions using a classifier trained on data from MI-SES conditions results in better classification accuracy, st-SES had no significant effect on the accuracy of identifying MI tasks in MI-SES conditions (Vidaurre et al., 2019). In addition, previous studies have not compared the differences in MI-BCI performance between the High and Low Performers groups during the st-SES intervention (Corbet et al., 2018; Vidaurre et al., 2019). This may obscure the reality that st-SES has different effects on different categories of subjects.

Dissimilarity in Neural Response Patterns

It has been previously demonstrated that somatosensory stimulation combined with MI can increase sensorimotor cortical activation intensity. The results of this study further indicated that st-SES had different effects on neural patterns of MI in high and low BCI performers. As demonstrated in time-frequency analysis, the sensorimotor cortex activation in Low Performers group, evaluated with averaged ERSP values, was significantly higher during the MI-SES condition than the MI condition. In the High Performers group, however, no significant difference in averaged ERSP values was found between the MI-SES and MI conditions, neither in the alpha or beta bands. One possible interpretation for these results is that differences in motor memory of a given movement resulted in varying feelings of st-SES intervention between the High Performers and the Low Performers. MI has been defined as a mental event in which motor memory of a prior movement is retrieved from the brain, resulting in the experience of

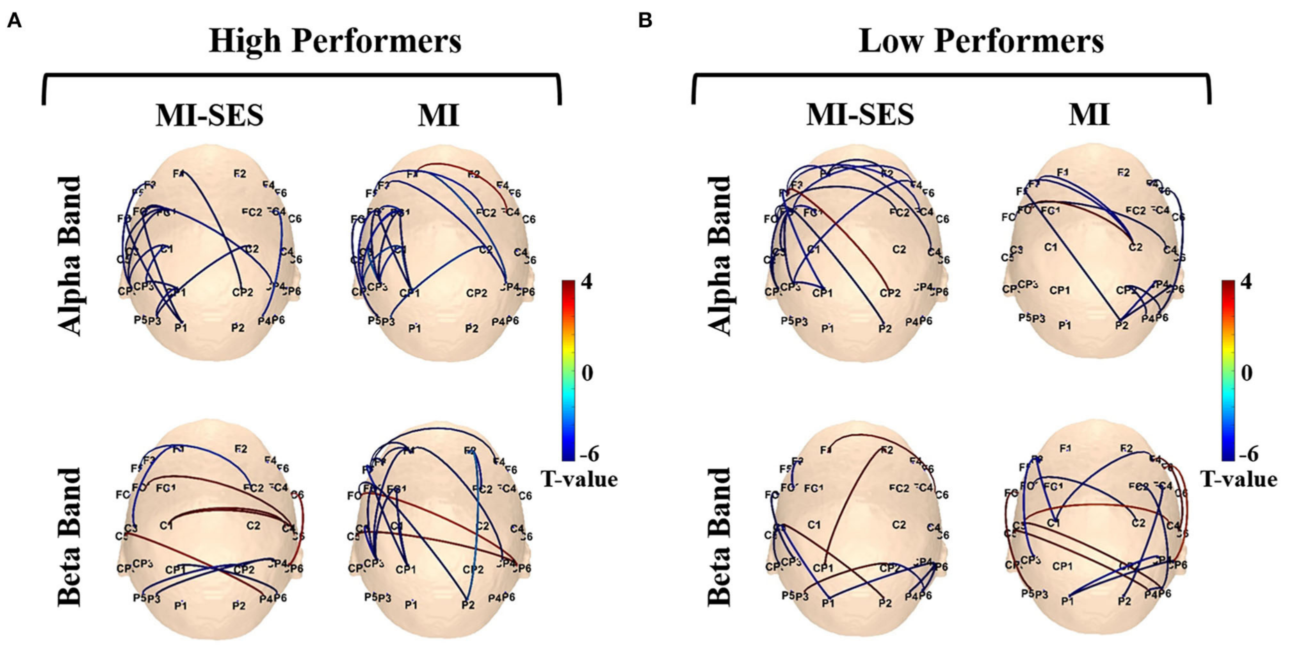

FIGURE 8 | The connectivity networks of alpha and beta rhythms for MI-SES and MI conditions. **(A)** High Performers group. **(B)** Low Performers group. The line between channels represents functional connectivity with significantly different wPLI values between MI and resting states.

re-performing the movement (Lacourse et al., 2005). Indeed, experts with better motor memory performance produce more effective motor imagery for specific movements than novices (Fourkas et al., 2008; Wei and Luo, 2010). This is consistent with our finding that the amplitude of ERD patterns of MI task was higher in the High Performers group compared with the Low Performers group. However, MI involves not only the mental simulation of a movement but also the anticipation of sensory consequences of imagined movements (Kilteni et al., 2018; Vidaurre et al., 2020). Recent evidence has shown that after the motor command is sent, motor imagery, similar to motor execution, predicts both the body state following the upcoming movement and the likely sensory consequences produced by the movement (Kilteni et al., 2018). During motor execution, these predictions are combined with the actual sensory feedback of movement to generate an accurate estimate of the body state. For motor imagery, the representation of our body state can be built up by somatosensory afferents from external devices (Corbet et al., 2018). Moreover, the artificial somatosensory afference, which is more consistent with sensory feedback generated by actual action, is more beneficial for properly representing the body state (Tajadura-Jiménez et al., 2017). Appropriate body representation is critical for MI performance (Ehrsson et al., 2003). Although the st-SES intervention could provide proprioceptive information, there was still a gap between this information and the sensory feedback elicited by the actual movement. High Performers with more efficient motor memory may produce more accurate sensory predictions for a given imagined movement. As demonstrated by Mihara et al., sensory feedback inconsistent with the neural responses failed to induce enhancement in cortical activation (Mihara et al., 2012). The High Performers may be more likely to perceive mismatches between the somatosensory afferents elicited by st-SES and sensory predictions. This may be detrimental to the formation of better body representations through st-SES in the High Performers, which resulted in the sensorimotor cortical activation under MI-SES condition was not significantly different from that in the MI condition. In contrast, Low Performers may be unable to produce accurate sensory predictions according to motor memory during MI. The previous study has shown that new memories associated with external interventions are created when existing memories cannot predict sensory consequences accurately and precisely (Oh and Schweighofer, 2019). Thus, st-SES intervention may help the Low Performers to develop motor memory strategies related to artificial somatosensory afference during MI. This interpretations is consistent with the results showing that the ERSP values of MI-SES condition were significantly smaller than those of MI condition in the Low Performers group.

Additionally, the results of the analysis in the time-frequency domain showed that there was a clear ERD pattern appeared in the contralateral sensorimotor cortex during the SES condition. This may be the main reason for the poor separability of the signal spectrum between MI-SES condition and SES condition in the High Performers group. The ERD pattern in the SES condition may be due to the somatosensory stimulation elicited by st-SES that focused the subjects' attention on the limb sensation. Indeed, Yao et al. showed that the somatosensory cortex was activated when subjects shifted their somatosensory attention to a body part (Yao et al., 2016).

The activity of brain rhythms can also be quantitively analyzed by signal complexity. The previous study has demonstrated that entropy-based methods can be used to quantify the complex dynamics of brain activity (Song et al., 2012). Sun et al. have shown that the activation of the motor cortex can be represented by the entropy-based estimate (Sun et al., 2017). Also, Hanslmayr et al. demonstrated that the desynchronization of sensorimotor rhythm is positively related to the complexity of information processed in the brain (Hanslmayr et al., 2012). In this study, the relative sample entropy of the MI-SES condition was significantly higher than that of the MI condition in the Low Performers group. In the High Performers group, there was no significant difference in relative sample entropy between the MI-SES condition and the MI condition. This could be attributed to the fact that st-SES intervention promoted the activation of the sensorimotor cortex during MI in the Low Performers group, but had no significant effect on the cortical activation in the High Performers group.

Variation in Functional Connectivity

Functional connectivity quantifies the information exchange across electrodes, allowing us to inspect the communication between brain regions during the MI task. Previous study demonstrated that connections between motor areas increased during MI, while information exchange was suppressed in the resting state (Li et al., 2019). Therefore, we expected that there was a significant increase in frontal-parietal connectivity during the MI task compared with the resting state. However, the results of wPLI showed that in the contralateral sensorimotor network, the functional connectivity during the MI task was lower than that during the resting state. One possible reason for these results is that the decrease in functional connectivity may be related to the cognitive load required for MI. Indeed, Leeuwis et al. found that functional connectivity during the resting state was greater than that during MI in both BCI illiterate and BCI literate subjects (Leeuwis et al., 2021). Mylonas et al. have shown that the decrements of phase synchronization at the alpha and beta bands are associated with the sensorimotor integration that contributes to motor performance (Mylonas et al., 2016). Also, Tzvi et al. reported that the decrease of alpha phase coupling in frontal-parietal network may reflect the allocation of cognitive resources to promote memory encoding (Tzvi et al., 2018). Therefore, our findings suggest that the decrements in phase synchronization of the sensorimotor network are critical for performing MI tasks. In the Low Performers group, the number of functional connectivity representing alpha phase desynchronization was obviously increased in the MI-SES condition relative to the MI condition and focused on the contralateral sensorimotor cortex. These alterations in functional connectivity may imply that Low Performers performed better MI and had greater sensorimotor cortex activation in the MI-SES condition than in the MI condition. In the High Performers group, there was no discernible difference in the functional connectivity between the MI-SES condition and MI condition in the alpha band. In addition, the number of functional connectivity representing beta phase desynchronization was higher in the MI condition compared with the MI-SES condition. This may imply that the st-SES intervention was not beneficial for the High Performers to perform the MI task. In addition, for the High Performers group, we found that the differences in functional connectivity alterations between the MI-SES condition and the MI condition were mainly observed in the beta band. On the other hand, for the Low Performers group, the differences between the MI-SES and MI conditions focused on the alpha band. This may be due to the distinct roles of the alpha and beta bands during MI. Previous studies demonstrated that alpha rhythm is associated with memory retrieval, whereas beta rhythm is involved in motor planning and motor preparation (Tzagarakis et al., 2010; Meirovitch et al., 2015). As mentioned above, st-SES intervention may have a positive effect on motor memory in the Low Performers group, but interfere with the process involving sensory prediction in the High Performers group.

Limitations of Current Study

Some limitations of the current study need to be mentioned. First, although the different effects of the st-SES intervention on high and low BCI performers have been validated in this study, more subjects should be recruited to draw a generalized conclusion. In particular, we found that some subjects in Low Performers group did not achieve better brain-switch BCI classification performance with st-SES intervention. Although this study has underlined the fact that st-SES may be promising to improve neural responses and MI-BCI performance in the low BCI performers, further studies on greater sample size are needed to clarify the effect of the st-SES intervention. Second, the sensations induced by st-SES may vary depending on the frequency and intensity of the stimulation. Thus, further studies need to be carried out to clarify the effect of different stimulation parameters on the subjects. Third, the effects of somatosensory afference investigated in this study were specific to st-SES. The influence of guidance based on other types of somatosensory afference, such as vibrotactile stimulation, needs to be investigated in the future.

In addition, for the majority of subjects in the Low Performers group, the MI-SES vs. SES classifier achieved better classification performance than MI vs. Rest classifier even in the presence of ERD pattern induced by st-SES intervention in the SES condition. Therefore, the somatosensory input based on st-SES may contribute to the BCI system to better distinguish subjects' neural states between active control and attentive idleness. This is beneficial for low BCI performers to achieve asynchronous control of the BCI system. Further studies involving the application of st-SES intervention in the online BCI system will be needed to understand the advantages and limitations of the st-SES intervention in asynchronous control.

CONCLUSIONS

The main purpose of our work consists in exploring the effect of st-SES on motor imagery tasks in high and low BCI performers. Our findings showed that st-SES intervention improved brain-switch BCI performance in the Low Performers group, but led to a decrease in BCI performance for the High Performers group. Moreover, in the Low Performers group, the electrophysiological analysis demonstrated that st-SES combined with MI achieved significantly higher sensorimotor cortical activation than MI alone. For the High Performers group, st-SES had no significant effect on neural responses during MI. We also found significantly decreased functional connectivity in the frontal-parietal network during the MI task compared with the resting state, and this decrease in functional connectivity may contribute to the execution of the MI task. Notably, st-SES affected the functional connectivity alterations at the beta band in the High Performers group and the alpha band in the Low Performers group, respectively. These results altogether indicated that st-SES intervention may be promising to improve the MI-BCI performance and sensorimotor cortical activation during MI in the Low Performers group but not in the High Performers group.

DATA AVAILABILITY STATEMENT

The original contributions presented in the study are included in the article/supplementary files, further inquiries can be directed to the corresponding author/s.

ETHICS STATEMENT

This study was reviewed and approved by the Ethics Committee of Tianjin University. The patients/participants provided their written informed consent to participate in this study.

AUTHOR CONTRIBUTIONS

LC, LZ, and DM designed the research. LZ conducted the experiment and wrote the original draft. LZ and ZW analyzed the data. BG visualized the results. LC and XZ reviewed and edited the manuscript. All authors contributed to the article and approved the submitted version.

FUNDING

This work was supported by the National Natural Science Foundation of China (Nos. 81925020, 82001939, 62006171, and 82102174) and the Tianjin Key Technology R&D Program (No. 20JCYBJC00930).

ACKNOWLEDGMENTS

The authors sincerely thank all participants for their voluntary participation.

REFERENCES

Allison, B. Z., and Neuper, C. (2010). "Could anyone use a BCI?," in *Brain-computer Interfaces* (London: Springer), 35–54. doi: 10.1007/978-1-84996-272-8_3

Bergquist, A. J., Clair, J. M., Lagerquist, O., Mang, C. S., Okuma, Y., and Collins, D. F. (2011). Neuromuscular electrical stimulation: implications of the electrically evoked sensory volley. *Eur. J. Appl. Physiol.* 111, 2409–2426. doi: 10.1007/s00421-011-2087-9

Bhuvaneswari, P., and Kumar, J. S. (2013). Support vector machine technique for EEG signals. *Int. J. Comput. Appl.* 63. doi: 10.5120/10523-5503

Biasiucci, A., Leeb, R., Iturrate, I., Perdikis, S., Al-Khodairy, A., Corbet, T., et al. (2018). Brain-actuated functional electrical stimulation elicits lasting arm motor recovery after stroke. *Nat. Commun.* 9, 1–13. doi: 10.1038/s41467-018-04673-z

Brunner, C., Allison, B. Z., Krusienski, D. J., Kaiser, V., Müller-Putz, G. R., Pfurtscheller, G., et al. (2010). Improved signal processing approaches in an offline simulation of a hybrid brain–computer interface. *J. Neurosci. Methods* 188, 165–173. doi: 10.1016/j.jneumeth.2010.02.002

Chen, Y., Hang, W., Liang, S., Liu, X., Li, G., Wang, Q., et al. (2020). A novel transfer support matrix machine for motor imagery-based brain computer interface. *Front. Neurosci.* 14:606949. doi: 10.3389/fnins.2020.606949

Choi, J. W., Huh, S., and Jo, S. (2020). Improving performance in motor imagery BCI-based control applications via virtually embodied feedback. *Comput. Biol. Med.* 127, 104079. doi: 10.1016/j.compbiomed.2020.104079

Cincotti, F., Kauhanen, L., Aloise, F., Palomäki, T., Caporusso, N., Jylänki, P., et al. (2007). Vibrotactile feedback for brain-computer interface operation. *Comput. Intell. Neurosci.* 2007, 48937. doi: 10.1155/2007/48937

Corbet, T., Iturrate, I., Pereira, M., Perdikis, S., and del R. Millán, J. (2018). Sensory threshold neuromuscular electrical stimulation fosters motor imagery performance. *Neuroimage* 176, 268–276. doi: 10.1016/j.neuroimage.2018.04.005

Delorme, A., and Makeig, S. (2004). EEGLAB: an open source toolbox for analysis of single-trial EEG dynamics including independent component analysis. *J. Neurosci. Methods* 134, 9–21. doi: 10.1016/j.jneumeth.2003.10.009

Ehrsson, H. H., Geyer, S., and Naito, E. (2003). Imagery of voluntary movement of fingers, toes, and tongue activates corresponding body-part-specific motor representations. *J. Neurophysiol.* 90, 3304–3316. doi: 10.1152/jn.01113.2002

Fourkas, A. D., Bonavolont,à, V., Avenanti, A., and Aglioti, S. M. (2008). Kinesthetic imagery and tool-specific modulation of corticospinal representations in expert tennis players. *Cereb. Cortex* 18, 2382–2390. doi: 10.1093/cercor/bhn005

Hang, W., Feng, W., Liang, S., Wang, Q., Liu, X., and Choi, K.-S. (2020). Deep stacked support matrix machine based representation learning for motor imagery EEG classification. *Comput. Methods Programs Biomed.* 193, 105466. doi: 10.1016/j.cmpb.2020.105466

Hanslmayr, S., Staudigl, T., and Fellner, M.-C. (2012). Oscillatory power decreases and long-term memory: the information via desynchronization hypothesis. *Front. Hum. Neurosci.* 6:74. doi: 10.3389/fnhum.2012.00074

Horowitz, A. J., Guger, C., and Korostenskaja, M. (2021). What external variables affect sensorimotor rhythm brain-computer interface (SMR-BCI) performance? *HCA Healthc. J. Med.* 2, 2. doi: 10.36518/2689-0216.1188

Jeon, Y., Nam, C. S., Kim, Y.-J., and Whang, M. C. (2011). Event-related (De) synchronization (ERD/ERS) during motor imagery tasks: implications for brain–computer interfaces. *Int. J. Ind. Ergon.* 41, 428–436. doi: 10.1016/j.ergon.2011.03.005

Jeunet, C., Cellard, A., Subramanian, S., Hachet, M., N'Kaoua, B., and Lotte, F. (2014). "How well can we learn with standard BCI training approaches? A pilot study," in *6th International Brain-Computer Interface Conference*. doi: 10.3217/978-3-85125-378-8-83

Jin, J.-N., Wang, X., Li, Y., Jin, F., Liu, Z.-P., and Yin, T. (2017). The effects of rTMS combined with motor training on functional connectivity in alpha frequency band. *Front. Behav. Neurosci.* 11:234. doi: 10.3389/fnbeh.2017.00234

Kaiser, V., Bauernfeind, G., Kaufmann, T., Kreilinger, A., Kübler, A., and Neuper, C. (2011). Cortical effects of user learning in a motor-imagery BCI training. *Int. J. Bioelectromagn.* 13, 60–61. doi: 10.3389/fpsyg.2018.01976

Kaplan, A., Vasilyev, A., Liburkina, S., and Yakovlev, L. (2016). "Poor BCI performers still could benefit from motor imagery training," in *International Conference on Augmented Cognition* (Springer), 46–56. doi: 10.1007/978-3-319-39955-3_5

Kilteni, K., Andersson, B. J., Houborg, C., and Ehrsson, H. H. (2018). Motor imagery involves predicting the sensory consequences of the imagined movement. *Nat. Commun.* 9, 1–9. doi: 10.1038/s41467-018-03989-0

Lacourse, M. G., Orr, E. L. R., Cramer, S. C., and Cohen, M. J. (2005). Brain activation during execution and motor imagery of novel and skilled sequential hand movements. *Neuroimage* 27, 505–519. doi: 10.1016/j.neuroimage.2005.04.025

Leeuwis, N., Yoon, S., and Alimardani, M. (2021). Functional connectivity analysis in motor imagery brain computer interfaces. *Front. Hum. Neurosci.* 15:732946. doi: 10.3389/fnhum.2021.732946

Li, F., Yi, C., Song, L., Jiang, Y., Peng, W., Si, Y., et al. (2019). Brain network reconfiguration during motor imagery revealed by a large-scale network analysis of scalp EEG. *Brain Topogr.* 32, 304–314. doi: 10.1007/s10548-018-0688-x

Li, X., La, R., Wang, Y., Hu, B., and Zhang, X. (2020). A deep learning approach for mild depression recognition based on functional connectivity using electroencephalography. *Front. Neurosci.* 14:192. doi: 10.3389/fnins.2020.00192

Li, Y., Guo, L., Liu, Y., Liu, J., and Meng, F. (2021). A temporal-spectral-based squeeze-and-excitation feature fusion network for motor imagery EEG decoding. *IEEE Trans. Neural Syst. Rehabil. Eng.* 29, 1534–1545. doi: 10.1109/TNSRE.2021.3099908

Makeig, S., Debener, S., Onton, J., and Delorme, A. (2004). Mining event-related brain dynamics. *Trends Cogn. Sci.* 8, 204–210. doi: 10.1016/j.tics.2004.03.008

Meirovitch, Y., Harris, H., Dayan, E., Arieli, A., and Flash, T. (2015). Alpha and beta band event-related desynchronization reflects kinematic regularities. *J. Neurosci.* 35, 1627–1637. doi: 10.1523/JNEUROSCI.5371-13.2015

Meng, J., Edelman, B. J., Olsoe, J., Jacobs, G., Zhang, S., Beyko, A., et al. (2018). A study of the effects of electrode number and decoding algorithm on online EEG-based BCI behavioral performance. *Front. Neurosci.* 12:227. doi: 10.3389/fnins.2018.00227

Mihara, M., Miyai, I., Hattori, N., Hatakenaka, M., Yagura, H., Kawano, T., et al. (2012). Neurofeedback using real-time near-infrared spectroscopy enhances motor imagery related cortical activation. *PLoS ONE* 7:e32234. doi: 10.1371/journal.pone.0032234

Mrachacz-Kersting, N., Jiang, N., Thomas Stevenson, A. J., Niazi, I. K., Kostic, V., Pavlovic, A., et al. (2016). Efficient neuroplasticity induction in chronic stroke patients by an associative brain-computer interface. *J. Neurophysiol.* 115, 1410–1421. doi: 10.1152/jn.00918.2015

Mylonas, D. S., Siettos, C. I., Evdokimidis, I., Papanicolaou, A. C., and Smyrnis, N. (2016). Modular patterns of phase desynchronization networks during a simple visuomotor task. *Brain Topogr.* 29, 118–129.

Oh, Y., and Schweighofer, N. (2019). Minimizing precision-weighted sensory prediction errors via memory formation and switching in motor adaptation. *J. Neurosci.* 39, 9237–9250. doi: 10.1523/JNEUROSCI.3250-18.2019

Oostenveld, R., Fries, P., Maris, E., and Schoffelen, J.-M. (2011). FieldTrip: open source software for advanced analysis of MEG, EEG, and invasive electrophysiological data. *Comput. Intell. Neurosci.* 2011, 156869. doi: 10.1155/2011/156869

Park, S., Ha, J., Kim, D.-H., and Kim, L. (2021). Improving motor imagery-based brain-computer interface performance based on sensory stimulation training: An approach focused on poorly performing users. *Front. Neurosci.* 15:732545. doi: 10.3389/fnins.2021.732545.eCollection 2021

Pfurtscheller, G., and Neuper, C. (2001). Motor imagery and direct brain-computer communication. *Proc. IEEE* 89, 1123–1134. doi: 10.1109/5.939829

Pfurtscheller, G., Solis-Escalante, T., Ortner, R., Linortner, P., and Muller-Putz, G. R. (2010). Self-paced operation of an SSVEP-Based orthosis with and without an imagery-based "brain switch:" a feasibility study towards a hybrid BCI. *IEEE Trans. neural Syst. Rehabil. Eng.* 18, 409–414. doi: 10.1109/TNSRE.2010.2040837

Ren, S., Wang, W., Hou, Z.-G., Liang, X., Wang, J., and Shi, W. (2020). Enhanced motor imagery based brain-computer interface via FES and VR for lower limbs. *IEEE Trans. Neural Syst. Rehabil. Eng.* 28, 1846–1855. doi: 10.1109/TNSRE.2020.3001990

Reynolds, C., Osuagwu, B. A., and Vuckovic, A. (2015). Influence of motor imagination on cortical activation during functional electrical stimulation. *Clin. Neurophysiol.* 126, 1360–1369. doi: 10.1016/j.clinph.2014.10.007

Richman, J. S., and Moorman, J. R. (2000). Physiological time-series analysis using approximate entropy and sample entropy. *Am. J. Physiol. Circ. Physiol.* 278, H2039–H2049 . doi: 10.1152/ajpheart.2000.278.6.H2039

Shu, X., Chen, S., Meng, J., Yao, L., Sheng, X., Jia, J., et al. (2018a). Tactile stimulation improves sensorimotor rhythm-based bci performance in stroke patients. *IEEE Trans. Biomed. Eng.* 66, 1987–1995. doi: 10.1109/TBME.2018.2882075

Shu, X., Chen, S., Yao, L., Sheng, X., Zhang, D., Jiang, N., et al. (2018b). Fast recognition of BCI-inefficient users using physiological features from EEG signals: a screening study of stroke patients. *Front. Neurosci.* 12:93. doi: 10.3389/fnins.2018.00093

Škola, F., Tinková, S., and Liarokapis, F. (2019). Progressive training for motor imagery brain-computer interfaces using gamification and virtual reality embodiment. *Front. Hum. Neurosci.* 13:329. doi: 10.3389/fnhum.2019.00329

Song, Y., Crowcroft, J., and Zhang, J. (2012). Automatic epileptic seizure detection in EEGs based on optimized sample entropy and extreme learning machine. *J. Neurosci. Methods* 210, 132–146. doi: 10.1016/j.jneumeth.2012.07.003

Sun, R., Wong, W., Wang, J., and Tong, R. K. (2017). Changes in electroencephalography complexity using a brain computer interface-motor observation training in chronic stroke patients: a fuzzy approximate entropy analysis. *Front. Hum. Neurosci.* 11:444. doi: 10.3389/fnhum.2017.00444

Tajadura-Jiménez, A., Cohen, H., and Bianchi-Berthouze, N. (2017). Bodily sensory inputs and anomalous bodily experiences in complex regional pain syndrome: evaluation of the potential effects of sound feedback. *Front. Hum. Neurosci.* 11:379. doi: 10.3389/fnhum.2017.00379

Tu-Chan, A. P., Natraj, N., Godlove, J., Abrams, G., and Ganguly, K. (2017). Effects of somatosensory electrical stimulation on motor function and cortical oscillations. *J. Neuroeng. Rehabil.* 14, 1–9. doi: 10.1186/s12984-017-0323-1

Tzagarakis, C., Ince, N. F., Leuthold, A. C., and Pellizzer, G. (2010). Beta-band activity during motor planning reflects response uncertainty. *J. Neurosci.* 30, 11270–11277. doi: 10.1523/JNEUROSCI.6026-09.2010

Tzvi, E., Bauhaus, L. J., Kessler, T. U., Liebrand, M., Wöstmann, M., and Krämer, U. M. (2018). Alpha-gamma phase amplitude coupling subserves information transfer during perceptual sequence learning. *Neurobiol. Learn. Mem.* 149, 107–117. doi: 10.1016/j.nlm.2018.02.019.Epub2018Feb21

Veldman, M. P., Maurits, N. M., Zijdewind, I., Maffiuletti, N. A., van Middelkoop, S., Mizelle, J. C., et al. (2018). Somatosensory electrical stimulation improves skill acquisition, consolidation, and transfer by increasing sensorimotor activity and connectivity. *J. Neurophysiol.* 120, 281–290. doi: 10.1152/jn.00860.2017

Vidaurre, C., Haufe, S., Jorajuría, T., Müller, K.-R., and Nikulin, V. V. (2020). Sensorimotor functional connectivity: a neurophysiological factor related to BCI performance. *Front. Neurosci.* 14:575081. doi: 10.3389/fnins.2020.575081

Vidaurre, C., Ramos Murguialday, A., Haufe, S., Gómez, M., Müller, K. R., and Nikulin, V. V. (2019). Enhancing sensorimotor BCI performance with assistive afferent activity: an online evaluation. *Neuroimage* 199, 375–386. doi: 10.1016/j.neuroimage.2019.05.074

Vinck, M., Oostenveld, R., Van Wingerden, M., Battaglia, F., and Pennartz, C. M. A. (2011). An improved index of phase-synchronization for electrophysiological data in the presence of volume-conduction, noise and sample-size bias. *Neuroimage* 55, 1548–1565. doi: 10.1016/j.neuroimage.2011.01.055

Wang, Z., Zhou, Y., Chen, L., Gu, B., Yi, W., Liu, S., et al. (2019). BCI monitor enhances electroencephalographic and cerebral hemodynamic activations during motor training. *IEEE Trans. Neural Syst. Rehabil. Eng.* 27, 780–787. doi: 10.1088/1741-2552/ab377d

Wei, G., and Luo, J. (2010). Sport expert's motor imagery: Functional imaging of professional motor skills and simple motor skills. *Brain Res.* 1341, 52–62. doi: 10.1016/j.brainres.2009.08.014

Wolpaw, J. R., Niels, B., McFarland, D. J., Pfurtscheller, G., and Vaughan, T. M. (2002). Brain-computer interfaces for communication and control. *Clin. Neurophysiol.* 113, 767–791. doi: 10.1145/1941487.1941506

Yao, L., Meng, J., Zhang, D., Sheng, X., and Zhu, X. (2013). Combining motor imagery with selective sensation toward a hybrid-modality BCI. *IEEE Trans. Biomed. Eng.* 61, 2304–2312. doi: 10.1109/TBME.2013.2287245

Yao, L., Sheng, X., Zhang, D., Jiang, N., Farina, D., and Zhu, X. (2016). A BCI system based on somatosensory attentional orientation. *IEEE Trans. Neural Syst. Rehabil. Eng.* 25, 81–90. doi: 10.1109/TNSRE.2016.2572226

Yi, W., Qiu, S., Wang, K., Qi, H., Zhao, X., He, F., et al. (2017). Enhancing performance of a motor imagery based brain–computer interface by incorporating electrical stimulation-induced SSSEP. *J. Neural Eng.* 14, 26002. doi: 10.1088/1741-2552/aa5559

Zhang, W., Song, A., Zeng, H., Xu, B., and Miao, M. (2021). Closed-loop phase-dependent vibration stimulation improves motor imagery-based brain-computer interface performance. *Front. Neurosci.* 15:638638. doi: 10.3389/fnins.2021.638638

Zhao, X., Zhang, H., Zhu, G., You, F., Kuang, S., and Sun, L. (2019). A multi-branch 3D convolutional neural network for EEG-based motor imagery classification. *IEEE Trans. Neural Syst. Rehabil. Eng.* 27, 2164–2177. doi: 10.1109/TNSRE.2019.2938295

Conflict of Interest: The authors declare that the research was conducted in the absence of any commercial or financial relationships that could be construed as a potential conflict of interest.

frontiers | Frontiers in Neuroscience

ORIGINAL RESEARCH
published: 20 June 2022
doi: 10.3389/fnins.2022.894798

Transcranial Direct Current Stimulation Over the Left Dorsolateral Prefrontal Cortex Reduced Attention Bias Toward Negative Facial Expression: A Pilot Study in Healthy Subjects

Shuang Liu*[1]*, Siyu Zhai*[1]*, Dongyue Guo*[1]*, Sitong Chen*[2]*, Yuchen He*[1]*, Yufeng Ke*[1] *and Dong Ming*[1,2]

[1] Academy of Medical Engineering and Translational Medicine, Tianjin University, Tianjin, China, *[2] School of Precision Instruments and Optoelectronics Engineering, Tianjin University, Tianjin, China*

Edited by:
Tianruo Guo,
University of New South Wales,
Australia

Reviewed by:
Siwei Bai,
Technical University of Munich,
Germany
Zhipeng Liu,
Chinese Academy of Medical
Sciences and Peking Union Medical
College, China
Shuang Qiu,
Institute of Automation (CAS), China

***Correspondence:**
Dong Ming
richardming@tju.edu.cn

Specialty section:
This article was submitted to
Neural Technology,
a section of the journal
Frontiers in Neuroscience

Received: 12 March 2022
Accepted: 09 May 2022
Published: 20 June 2022

Citation:
Liu S, Zhai S, Guo D, Chen S,
He Y, Ke Y and Ming D (2022)
Transcranial Direct Current Stimulation
Over the Left Dorsolateral Prefrontal
Cortex Reduced Attention Bias
Toward Negative Facial Expression:
A Pilot Study in Healthy Subjects.
Front. Neurosci. 16:894798.
doi: 10.3389/fnins.2022.894798

Research in the cognitive neuroscience field has shown that individuals with a stronger attention bias for negative information had higher depression risk, which may be the underlying pathogenesis of depression. This dysfunction of affect-biased attention also represents a decline in emotion regulation ability. Clinical studies have suggested that transcranial direct current stimulation (tDCS) treatment can improve the symptoms of depression, yet the neural mechanism behind this improvement is still veiled. This study aims to investigate the effects of tDCS on affect-biased attention. A sample of healthy participants received 20 min active ($n = 22$) or sham tDCS ($n = 19$) over the left dorsolateral prefrontal cortex (DLPFC) for 7 consecutive days. Electroencephalographic (EEG) signals were recorded while performing the rest task and emotional oddball task. The oddball task required response to pictures of the target (positive or negative) emotional facial stimuli and neglecting distracter (negative or positive) or standard (neutral) stimuli. Welch power spectrum estimation algorithm was applied to calculate frontal alpha asymmetry (FAA) in the rest task, and the overlapping averaging method was used to extract event-related potentials (ERP) components in the oddball task. Compared to sham tDCS, active tDCS caused an obvious increment in FAA in connection with emotion regulation ($p < 0.05$). Also, participants in the active tDCS group show greater P3 amplitudes following positive targets ($p < 0.05$) and greater N2 amplitudes following negative distracters ($p < 0.05$), reflecting emotion-related attention biases. These results offer valuable insights into the relationship between affect-biased attention and the effects of tDCS, which may be of assistance in exploring the neuropathological mechanism of depression and anxiety and new treatment strategies for tDCS.

Keywords: tDCS, DLPFC, attention bias, ERP, emotion regulation

INTRODUCTION

Initiated in automatic or controlled ways, selective attention refers to the cognitive processes that serve to filter relevant external and internal information for further processing (Stevens and Bavelier, 2012). In the context of emotional processing, selective attention is a crucial mechanism that influences our emotional experience and functioning by determining how the organism perceives and interprets emotional information in the environment (Gross et al., 2011; Sanchez et al., 2015). Attention bias is a sort of selective attention that occurs when individuals have high sensitivity to certain specific information (Bar-Haim et al., 2007). Studies have suggested that individual differences in attention bias underlie difficulties in emotion regulation processes, especially for depressed people (Joormann and D'Avanzato, 2010). Healthy individuals under negative emotion states transfer their attention more frequently to positive stimuli (Sanchez et al., 2014) and take attention away more rapidly from negative stimuli (Ellenbogen et al., 2002). However, individuals suffering from anxiety and depression show negative biases in selective attention (Armstrong and Olatunji, 2012). For instance, signal detection studies (Wiens et al., 2008) have found that individuals with anxiety disorders have lower detection thresholds for threatening stimuli, and research on spatial attention suggests that these decreased thresholds lead to increased orienting toward threats Mogg et al., 2002), which indicates that patients with anxiety disorders show attentional bias toward threats. This negative bias may increase state anxiety by causing increased awareness of threats (Armstrong and Olatunji, 2012). Besides, a small number of studies have observed reduced attention toward positive stimuli in depressed individuals relative to controls (Peckham et al., 2013). More seriously, people susceptible to depression have been characterized as attending to and remembering negative information (Siegle et al., 2002). This attentional style could lead to distorted beliefs and assumptions about the world (Armstrong and Olatunji, 2012).

The negative bias could be seen as reduced responsiveness or drive to engage with positive stimuli from surroundings, namely a positive attenuation effect. Alternatively, negative bias has been interpretable in terms of overwhelming attention to negative information, which can be thought of as a negative potentiation effect (Rottenberg et al., 2005). The attention bias toward negative stimuli would be related to a lack of inhibition of negative material, resulting from faulty inhibitory processes of interference control (Waters et al., 2006). Attentional bias mechanisms may be particularly active and impactful when processing socioemotional information, such as others' emotional facial expressions (Gotlib et al., 2004a). Facial expressions are among the most commonly perceived visual stimuli and transmit and evoke emotion simultaneously. For instance, an attention bias toward sad or threatening faces more or less increases one's negative emotions and leads to terrible representations in social communication (Frewen and Dozois, 2005). One of the hallmarks of depression is impaired social function, and previous research has documented that this manifestation stems from different attentional biases toward different facial expressions (Persad and Polivy, 1993).

Many behavioral studies have shown that there are some differences in the attention to different emotional faces between depressed and healthy groups. These findings can correspond to and verify the above hypotheses. Depressed groups gazed and engaged attention into negative faces for a longer time (Fritzsche et al., 2010), and were more likely to attend to negative facial expressions in a series of facial stimuli with different valence (Karparova et al., 2010). Even more, healthy subjects were more inclined to pay attention to negative faces after negative emotions' induction (Kujawa et al., 2011). Some articles also reported that depressed groups attended to positive information insufficiently, manifesting that they pay less attention to happy faces than sad faces in the same conditions (Suslow et al., 2004). In general, depressed groups showed abnormally larger attention bias toward negative facial expressions compared with healthy controls.

Cognitive neuroscience has provided a new perspective on revealing brain mechanisms behind psychological phenomena theoretically and technically. There is an increase in the research on underlying neural correlates of attention biases toward facial expressions *via* neuroscience methods such as the event-related potentials (ERP) technique, which can uniquely complement traditional behavioral measures. Emotional facial expressions can evoke different ERP components well, some of that are related to attention processing (Schindler and Bublatzky, 2020). The P1, N1, and P2 belong to exogenous ERP components, which are easily affected by stimulus characteristics due to the early automatic attention mechanism, reflecting the bottom-up processing of attention. N2 and P3 are endogenous ERP components, occurring in later stages of processing and are closely related to cognition, reflecting the top-down processing of attention (Hopfinger and West, 2006; Brosch et al., 2011). Previous studies have reported that the abnormality of attention may be caused by the inefficient engagement of top-down control (Friedman-Hill et al., 2010; Delchau et al., 2019). Therefore, examining P3 and N2 could help discover the underlying neural processes behind attention biases to understand attention and inhibition behaviors better.

A new viewpoint noted that affect-biased attention is considered to be a form of emotion regulation (Bram et al., 2018). Growing evidence indicates that depression is always accompanied by dysregulation of emotion (Berking et al., 2014; Vanderlind et al., 2020). With the development of measuring methods in brain activities, frontal alpha asymmetry (FAA) has been increasingly seen as a reliable index of the capability of emotion regulation. FAA examines the activity of the left and right frontal alpha waves (typically at F3 and F4 electrodes). The intensity of alpha wave activity is inversely proportional to the intensity of activity in the corresponding cortical region. A strong alpha wave represents a weak activity in the brain and vice versa (Kline et al., 2007; Zhong et al., 2011). The left and right prefrontal cortex hemispheres show different attention biases to different emotional stimuli. The left frontal cortical activity is associated with positive effects, while the right frontal area might be susceptible to negative emotions (Davidson, 1998; Harmon-Jones et al., 2010). It is believed that individuals with high emotional regulation ability generally have greater left frontal activity (Dagmar Kr et al., 2010). The increase in left frontal activity tends to enhance the positive emotional experience (Tomarken et al., 1992). Anxiety and depressive symptoms caused by mood regulation disorders are associated with decreased left frontal lobe activity (Smit et al., 2007).

Neuroimaging studies demonstrate an interactive network of corticolimbic pathways playing a central role in the top-down regulation of emotions (Johnstone et al., 2007; Wager et al., 2008). Specifically, a functional balance between ventral [ventral anterior cingulate cortex (ACC), limbic structures] with dorsal compartments in the brain [dorsal ACC, dorsolateral prefrontal cortex (DLPFC)] is necessary for maintaining homeostatic emotional control (Ochsner and Gross, 2005). These brain structures are also involved in the attentional processing of emotional information (Fragopanagos et al., 2005), with the DLPFC as an important region for the implementation of top-down attentional control (MacDonald Angus et al., 2000). Therefore, emotional attentional biases associated with the dysregulation of emotional states can be understood as the result of failures in top-down attentional control implemented by the DLPFC (De Raedt et al., 2015). Therefore, the variation of activities in DLPFC might be associated with the formation of depression. Clinical studies have suggested that lesions of the left DLPFC are often associated with depression, while damages in the right DLPFC lead to elevated mood (Schmitz et al., 2006). Hypoactivity of the left DLPFC is thought to play a key role in the pathophysiology of depression, sometimes accompanied by increased right DLPFC functioning (Schutter and Honk, 2005; Hecht, 2010).

In recent years, transcranial direct current stimulation (tDCS) has shown promise as a neuromodulatory tool to study neuropsychological functioning (Shin et al., 2015). Constant low-intensity direct current (typically 0.5–2 mA) is applied to modulate spontaneous cortical activity. The application of current produces polarity-specific subthreshold changes in the excitability of underlying targeted cortical areas. Research has demonstrated that anodal stimulation increases cortical excitability, whereas cathodal stimulation decreases cortical activity (Nitsche and Paulus, 2001; Nitsche et al., 2003). To date, tDCS has been reported to significantly modulate a range of cognitive and affective abilities in healthy participants and patients with depression (Boggio et al., 2009; Wolkenstein and Plewnia, 2013; Salehinejad et al., 2016; Yadollahpour et al., 2017). However, few results have yielded the mechanism of tDCS. Combined with the importance of emotional attentional bias on patients, we hypothesized that tDCS could modulate the affective abilities of subjects by improving the negative cognitive bias.

In this study, we aimed to disentangle the effect of prefrontal tDCS on attention bias toward emotional information and emotion regulation abilities in healthy subjects. Considering the advantages of high temporal resolution and low cost, we used EEG to record the changes of cortical activity after tDCS to explore the neural correlation of attention towards emotional information. This study contained a rest task and a modified emotional oddball task consisting of six blocks, which could response attention bias. EEGs were recorded during rest and oddball task phases, respectively. Hereby, we selected healthy subjects rather than depressed patients to exclude the influence of clinical treatments such as antidepressant medications. Therefore, this study could be regarded as a preliminary attempt to investigate how appropriate tDCS protocol works in the treatment of depression. Since the main purpose is to explore the effects of tDCS in the treatment of depression, given the above-mentioned importance of the left DLPFC in depression, we performed only left DLPFC anodal stimulation in this study.

MATERIALS AND METHODS

Participants

A total of forty-one healthy participants (25 females; mean age = 23.41) were included in this study. The healthy participants were college students or graduate students of Tianjin University, meeting the following criteria: (1) right-handed; (2) aged 18–25; (3) Chinese native; (4) no history of neurological disorders or brain injuries; and (5) no metal object and implantable devices in brain. The healthy participants were randomly assigned into two groups: 22 in the active tDCS group and 19 in the sham tDCS group.

The study protocol was approved by the Tianjin University, and all investigative procedures were conducted according to the principles expressed in the Declaration of Helsinki. Written informed consent was obtained after the nature of the procedures was explained and before any study procedures.

The healthy participants need to complete the questionnaires to measure the anxiety level and emotion regulation ability twice before and after tDCS. The anxiety level was assessed with the State-Trait Anxiety Inventory (STAI) (Spielberger, 1970) and emotion regulation ability was assessed with the Difficulties in Emotion Regulation Scale (DERS) (Gratz and Roemer, 2008).

Procedures

The study was conducted on 7 consecutive days and involved three stages: pre-treatment test, stimulation, and post-treatment test. Day 1 started with the pre-treatment test phase consisting of rest and oddball tasks. Then all participants underwent 20 min active or sham tDCS over the left DLPFC for 7 consecutive days. On day 7, after the last time of stimulation, the participants completed the post-treatment test phase with the same contents as the pre-treatment. **Figure 1** shows the overall flow of the experiment. EEG data were acquired in both pre- and post-treatment test phases. In addition, participants filled out the STAI and DERS questionnaires before EEG recording. The whole experiment was executed using Matlab 2013b with Psychtoolbox 3.0.11 (Brainard, 1997).

Rest Task

The participants were seated in front of a computer monitor and instructed to be relaxed in a sound-attenuated laboratory. The recorded voice prompts guided subjects to open (O) and close (C) their eyes during the 8-min rest task. A red circle appeared in the center of the screen as a visual reference point when the rest task started. In the meantime, their EEG signals were collected.

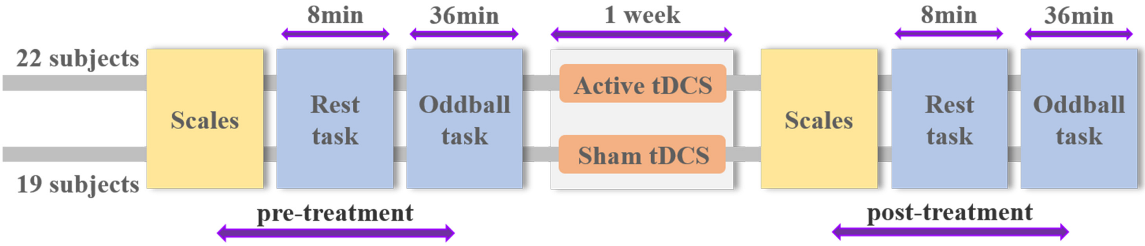

FIGURE 1 | Schematic overview of experimental design and procedure.

The rest task contained eight 1-min intervals in the order of "OCCOCOOC" (see **Figure 2**). We averaged across eyes open and eyes closed conditions because both were highly correlated ($r = 0.83$, $p < 0.001$). Spearman–Brown corrected reliability was 0.91 for the eyes open and eyes closed conditions and the average of the two conditions could produce a more reliable estimate of frontal asymmetry than either single condition (Hagemann, 2004; Tomarken et al., 2010). Split half reliability between the first and second 4 min of data assessment of 0.98 indicates excellent reliability and suggests stability of measurement at least for our 8 min of data recording.

Experimental Stimuli

Human faces with different emotions were planned to use as stimulus materials. But research has shown that there is a racial bias in human face recognition, i.e., people can better recognize the facial expressions of their countries of ethnic groups (McAndrew, 1986). To avoid the interference of stimulus materials, emotional faces were selected from the Chinese Facial Affective Picture System (CFAPS) (Bai et al., 2005), including 162 positive faces, 162 negative faces, and 126 neutral faces. Male and female faces have an equal number in the chosen pictures.

Oddball Task

Participants were seated in front of the monitor, and all relevant instructions were shown on the computer screen initially. The three-stimulus visual oddball paradigm was applied in the session. The session comprised six blocks, and each oddball task block had 180 trials. Each trial began with a fixed white cross appearing in the center of the screen for 250 ms, and then a facial stimulus was presented for 750 ms with the interstimulus interval of 1,000 ms. In each block, the order of the 180 trial presentations was pseudo-random with overall proportions of 70% frequent standards, 15% rare targets, and 15% rare distracters. The targets were separated by at least one non-target stimuli.

Before the experiment began, the participants were allowed to be familiar with a short practice block. For the formal experiment, they were required to focus on the middle of the screen and respond by hitting the space bar on the keyboard as quickly as possible to present target stimuli during oddball tasks.

In the session, each participant completed three blocks in which positive faces were targets and three blocks in which negative faces were targets. The opposite emotional valence served as distracters (e.g., negative distracters in the block with positive targets), while neutral faces were the frequently presented standard stimuli. Each block had 27 positive, 27 negative, and 126 neutral facial expression stimuli. Each target and distracter stimulus was presented only once during the whole oddball task. Within each task block, the gender of faces was balanced. Each task block lasted 6 min, and participants were given short breaks between blocks. The block order was counterbalanced across subjects. The schematic experimental procedure of the oddball paradigm is illustrated in **Figure 3**.

Transcranial Direct Current Stimulation

Transcranial direct current stimulation was delivered by a battery-driven constant current stimulator (DC-Stimulator PLUS, NeuroConn GmbH, Ilmenau, Germany) using a pair of rubber electrodes in a 5 × 5 cm saline-soaked synthetic sponge. The anode was placed over the left DLPFC (electrode position F3) and the cathode was placed over the right DLPFC (electrode position F4) according to the international 10–20 EEG system. According to healthy subjects, for active tDCS, a constant current of 1.5 mA for 20 min was applied with a gradual ramp up/down of the current over the first and last 30 s, respectively. For sham stimulation, the current ramped up to 1.5 mA within 15s at the beginning of the stimulation and then ramped down within 15s later. The protocols that applied from 1 to 2 mA of current (current density: 0.28–0.57 A/cm^2) for 20 min between 5 and 15 sessions have been demonstrated to be safe (Jasper et al., 1958; Loo et al., 2009, 2012; Palm et al., 2012).

Electrophysiological Data Recording and Preprocessing

During the experiment, 64 channels EEG signals were recorded continuously using a Neuroscan 4.5 amplifier system. The electrodes were placed on the scalp according to the extension of the international 10–20 electrode positioning system. The electrode impedances were kept below 5 KΩ. All signals were amplified with a 0.05–100 Hz band-pass and sampled at the rate of 1,000 Hz, using a right mastoid reference electrode.

Offline analysis was performed using EEGLAB Toolbox (Delorme and Makeig, 2004), which are open-source Matlab packages for EEG analysis. The EEG signals were re-referenced to the average of the bilateral mastoid electrodes. The signals were resampled to 200 Hz and low-pass filtered with 45 Hz.

Eye blinks and movement artifacts were eliminated with independent components analysis (ICA). EEG waveforms were time-locked to each stimulus onset and were segmented from

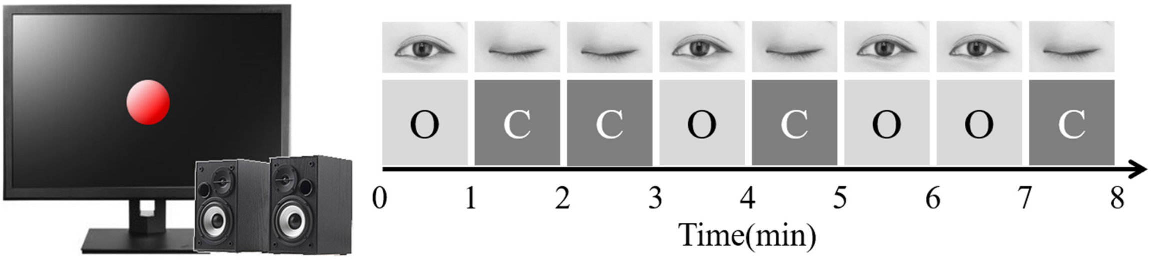

FIGURE 2 | Rest task procedure. "O" means "open," "C" means "closed."

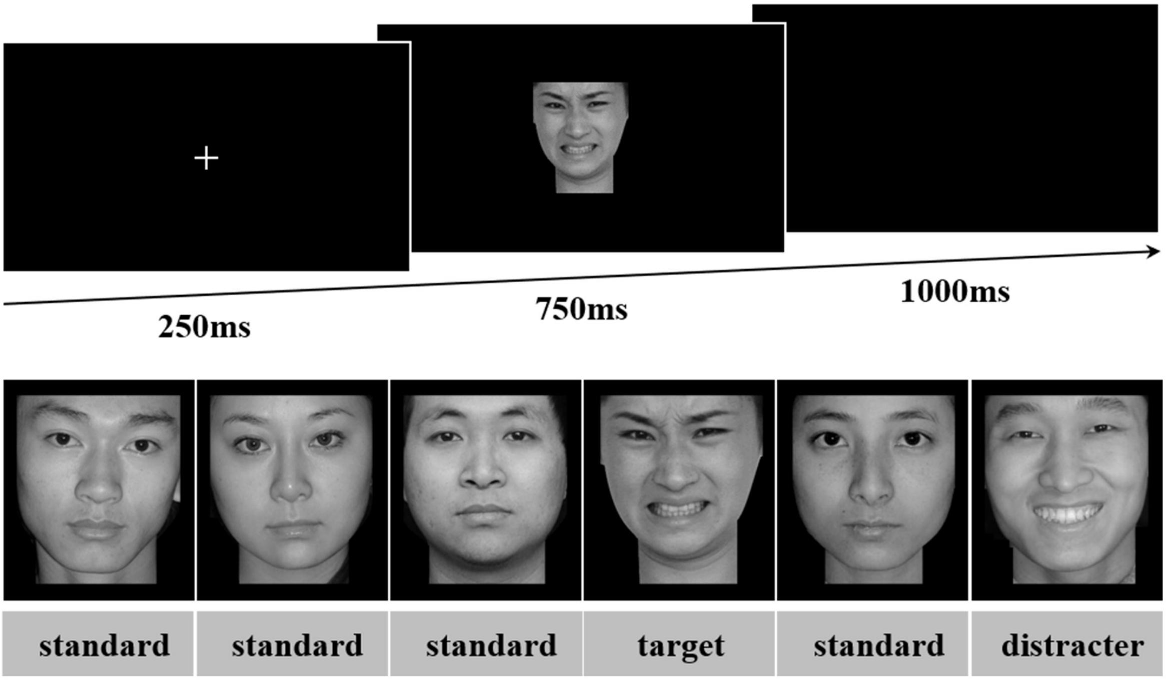

FIGURE 3 | Oddball task. A single trial of the oddball task is shown, with the fixation, stimulus, and blank screen sequence depicted. A sequence of stimuli that could be presented is shown with trial-type labels added in the figure for easier identification. This sequence would be within a block in which negative faces served as targets. Source for the photos: the Chinese Face Affective Picture System.

200 ms before the stimulus onset to 1,000 ms after stimulus onset. All epochs were baseline-corrected with respect to the mean voltage over the 200 ms preceding the stimulus onset. Trials containing activity exceeding ±80 μV at any site were excluded from averaging.

Data Analysis

In the study, we calculate the FAA values based on EEG signals of the rest task. The ERP waveforms were acquired when the stimuli appeared, and collected behavioral data were performed for statistical analysis in the oddball task.

Frontal Alpha Asymmetry

Welch spectrum energy spectrum estimation of alpha was applied to calculate the value of FAA. This study used the pwelch function in Matlab to realize the power spectrum estimation of the resting EEG data. The 1–45 Hz frequency band of each lead of the 60-lead EEG data is divided into five frequency bands for power spectral density estimation. The definitions of the bands are as follows: delta (1–4 Hz), theta (4–8 Hz), alpha (8–12 Hz), beta (12–30 Hz), and gamma (30–45 Hz). In this experiment, the EEG data were segmented every 5 s as a sample and the power spectrum of each band sample of each lead was calculated. The power value of the power spectrum of each lead in a specific frequency band was the sum of each frequency point in the band. The method to calculate the FAA value is to record the alpha wave intensity of the left frontal lobe and the right frontal lobe EEG at rest, and then calculate the natural logarithm of the alpha wave intensity of the right frontal lobe electrode point and the left frontal lobe. The FAA indexes were obtained by subtracting the two natural logarithms (right minus left): ln (R) – ln (L).

Behavioral Data

For behavioral data, trials were excluded if the reaction time was shorter than 200 ms or longer than 1,500 ms. The data whose average value was greater than or less than the average of all participants in each group plus/minus three times the variance would not be adopted during statistics. The paired-sample *t*-test was used to analyze the behavioral data of each group before and after treatment, and the independent-sample *t*-test was used to perform the statistical analysis between the two groups.

The changes in the reaction time, accuracy, and errors of the commission have naturally become the focus of behavioral results. The reaction time was calculated by correct trials of the oddball task, representing the speed of attentional processing under targeted emotional stimuli. The accuracy shows whether the subject responded correctly to targets, indicating the accurate identification of targeted emotional stimuli. These two types of behavioral data reflect the attentional bias to different emotional stimuli, which indicate faster attention occupancy and more accurate attention recognition (Most et al., 2005). Errors of commission are referred to the proportion of incorrect button responses to task-irrelevant stimuli including distracters and neutral standards. The commission errors of distracters include two types: taking negative as positive when targets are defined positive, and taking positive as negative when targets are defined negative. The commission errors of neutral standards include taking neutral as positive and neutral as negative.

Event-Related Potentials

For ERP data, the average amplitudes were overlaid for correct trials in the three positive blocks and negative blocks. This study focused on the P3 and N2 components elicited by positive, negative, and neutral facial stimuli in two groups. For each participant, the target P3 value consisted of the mean amplitude from standard trials subtracted from the mean amplitude of target trials. The distracter N2 value was derived by subtracting standard trials from distracter trials. To isolate the primary ERP components associated with attention to emotional facial expressions, a traditional windowed analysis was conducted on individual average files. The P3 amplitude was calculated at the Pz electrode site between 400 and 600 ms. To examine the N2 component, the 250–450 ms temporal window and FCz location were selected.

RESULTS

Questionnaire Data

Validity test was conducted on the collected questionnaires and invalid questionnaires were eliminated. Since incomplete filling questionnaires, 20 were effectively received in the active tDCS group and 15 in the sham tDCS group. The STAI could calculate the state anxiety and trait anxiety scores, while the DERS showed the emotion regulation score. The STAI analysis proved that all subjects' state and trait anxiety before and after the experiment belonged to the normal range. The DERS analysis found no significant difference in the emotion regulation ability of the subjects before and after the experiment in both the groups ($p > 0.05$). The state anxiety and trait scores and emotion regulation ability scale scores are shown in **Table 1**.

TABLE 1 | Mean score of two groups by STAI and DERS.

Group	Testing time	State anxiety (M ± SD)	Trait anxiety (M ± SD)	Emotion regulation (M ± SD)
Active group				
	Pre-treatment	31.35 ± 7.99	38.50 ± 8.03	75.50 ± 14.25
	Post-treatment	35.10 ± 8.48	37.30 ± 7.98	72.83 ± 16.04
Sham group				
	Pre-treatment	34.00 ± 6.51	41.60 ± 9.47	75.36 ± 18.84
	Post-treatment	31.40 ± 6.70	37.20 ± 7.51	75.21 ± 20.48

Behavioral Data

Reaction Time

For the active group, the average reaction time of the positive targets in the pre- and post-treatment tests was 601 ± 44 and 607 ± 57 ms, while the reaction time of the negative targets was 604 ± 43 and 611 ± 45 ms. For the sham group, the average reaction time of positive targets in the pre- and post-treatment tests was 618 ± 76 and 618 ± 54 ms, while the reaction time of negative targets was 631 ± 78 and 619 ± 54 ms. But there were no significant differences between the pre- and post-treatment tests in both the active and sham groups ($p > 0.05$).

Accuracy

For the active group, the accuracy of positive targets in the pre- and post-treatment tests was 84.8 ± 11.8% and 86.6 ± 9.9%, while the accuracy of negative targets was 89.3 ± 9.4% and 87.8 ± 11.4%. For the sham group, the accuracy of positive targets in the pre- and post-treatment tests was 85.5 ± 7.8% and 88.6 ± 7.4%, while the accuracy of negative targets was 89.2 ± 7.9% and 90.7 ± 5.8%. But there were no significant differences between the pre- and post-treatment tests in both the active and sham groups ($p > 0.05$).

Commission Error

The commission errors of distracters between the pre- and post-treatment tests in the active and sham groups had no significant differences ($p > 0.05$). For the commission errors of neutral standards, significant differences were found between the two phases test and two groups (see **Tables 2**, **3**).

Frontal Alpha Asymmetry Data

In the previous studies, FAA mostly applied the scores of the dorsal position such as F4-F3, F6-F5 as the main indicator, and some studies also used the FP2-FP1 score of the frontal position as the asymmetry index. Here, we calculated asymmetry coefficients at the four paired-electrodes of F4-F3, F6-F5, F8-F7, and FP2-FP1.

Table 4 shows the asymmetry coefficients of the pre- and post-treatment tests at the four paired electrodes in the active/sham groups. Paired *t*-test was used to examine the differences in FAA between the pre- and post-treatment in the active/sham

TABLE 2 | The commission errors rates of neutral standards between pre- and post-treatment test in two groups.

Group	Type	Pre-treatment (M ± SD)	Post-treatment (M ± SD)	*P*-value
Active group				
	Neu as Pos	0.212 ± 0.359	0.178 ± 0.329	0.329
	Neu as Neg	0.256 ± 0.377	0.156 ± 0.276	0.011*
Sham group				
	Neu as Pos	0.106 ± 0.314	0.042 ± 0.037	0.385
	Neu as Neg	0.053 ± 0.079	0.047 ± 0.079	0.599

"Neu" means "Neutral," "Pos" means "Positive," "Neg" means "Negative."
$^{*}P < 0.05$.

TABLE 3 | The commission errors rates of neutral standards differences before and after treatment between two groups.

Type	Active group (M ± SD)	Sham group (M ± SD)	*P*-value
Neu as Pos	–0.035 ± 0.159	0.008 ± 0.032	0.248
Neu as Neg	–0.101 ± 0.161	–0.006 ± 0.048	0.020*

"Neu" means "Neutral," "Pos" means "Positive," "Neg" means "Negative."
$^{*}P < 0.05$.

TABLE 4 | The asymmetry coefficients in different paired-electrodes before and after treatment in two groups.

Group	Paired-electrodes	Pre-treatment value (M ± SD)	Post-treatment value (M ± SD)	*P*-value
Active group				
	F4-F3	–0.290 ± 0.650	0.164 ± 0.402	0.025*
	F6-F5	–0.304 ± 0.712	0.199 ± 0.473	0.041*
	F8-7	0.081 ± 0.745	0.342 ± 0.556	0.189
	FP2-P1	–0.107 ± 0.862	0.064 ± 0.620	0.462
Sham group				
	F4-3	–0.063 ± 0.453	–0.164 ± 0.620	0.497
	F6-5	0.041 ± 0.626	–0.028 ± 0.589	0.949
	F8-7	–0.221 ± 0.958	–0.390 ± 0.915	0.576
	FP2-P1	–0.067 ± 0.786	–0.112 ± 0.585	0.809

$^{*}P < 0.05$.

group. The asymmetry coefficients of F4-F3 and F6-F5 positions increased significantly after tDCS in the active group ($p = 0.025$, $p = 0.041$) and no significant differences were found at the F8-F7 and FP2-FP1 positions ($p > 0.05$). There were no significant differences in the asymmetry coefficients at the four paired electrodes in the sham group.

To further verify the differences between the two groups, an independent t-test was performed to analyze the values in the pre-treatment test and difference values (post-treatment value minus pre-treatment value) of the active and sham groups. For asymmetry coefficients in the pre-treatment test, no significant difference was found in the four paired electrodes between the two groups ($p > 0.05$). It indicated that subjects in different groups had no baseline difference, thus the changes between the two groups after treatment were comparable. The asymmetry coefficient difference of the active group was greater than that of the sham group at the F4-F3 and F6-F5 positions, but significance was found only in the F4-F3 position (see **Table 5**).

Event-Related Potentials Data

The difference in the ERP amplitude in the oddball paradigm reflects the different attention levels to standard and deviant stimulus. As this experiment included three types of stimulus (targets, distracters, and standards), the ERP waveforms of different stimulus types were examined at first. Referring to other studies using the oddball paradigm, the waveform changes at the midline leads are mainly preferred. Pz was selected here to draw the ERP waveforms when the positive and negative emotional faces are targets, and they were shown in **Figure 4**, respectively. For ERP components, this article focused on the changes in the P3 and N2 components before and after tDCS. The original ERP waveform after tDCS in the active group was taken as an example here. It can be seen from **Figure 4** that the amplitudes of P3 and N2 were subject to targets > distracters > standards, which conformed to the waveform distribution of the three-stimulus type oddball paradigm.

To study the effect of tDCS on attention biases for different emotional faces, the ERP amplitude changes of positive and negative targets (or distracters) before and after tDCS in the active/sham tDCS group were compared, respectively. To avoid the impact of other properties on the ERP of targets (or distracters), the ERP difference wave that was equal to the targets (or distracters) minus the standard reported value was used to present the results, for the same rules might exist in some ERP components between targets (or distracters) and standards.

P3 Event-Related Potentials Data

A statistical analysis of ERP difference wave amplitudes was performed using a paired t-test, and the results are shown in **Figure 5**. The post-treatment test showed greater amplitude in the P3 window than the pre-treatment test inactive group following positive targets ($t = –2.294$, $p = 0.032$) but not negative targets ($t = –1.107$, $p = 0.281$). A significant decrease in positive targets was observed in the P3 time window in the post-treatment test compared with the pre-treatment test in the sham group ($t = 2.184$, $p = 0.042$); while there were no significant changes in the P3 amplitudes of negative targets in the sham group ($t = –0.771$, $p = 0.451$).

N2 Event-Related Potentials Data

N2 difference waveform shifts of two groups are shown in **Figure 6**. Subjects in the active group had significantly increased amplitudes of negative distracters on the condition of positive targets after treatment ($t = 2.508$, $p = 0.020$), while there was

TABLE 5 | The asymmetry coefficients differences before and after treatment between two groups.

Paired-electrodes	Active group (M ± SD)	Sham group (M ± SD)	*P*-value
F4-F3	0.454 ± 0.810	–0.101 ± 0.600	0.026*
F6-F5	0.504 ± 1.004	0.013 ± 0.826	0.120

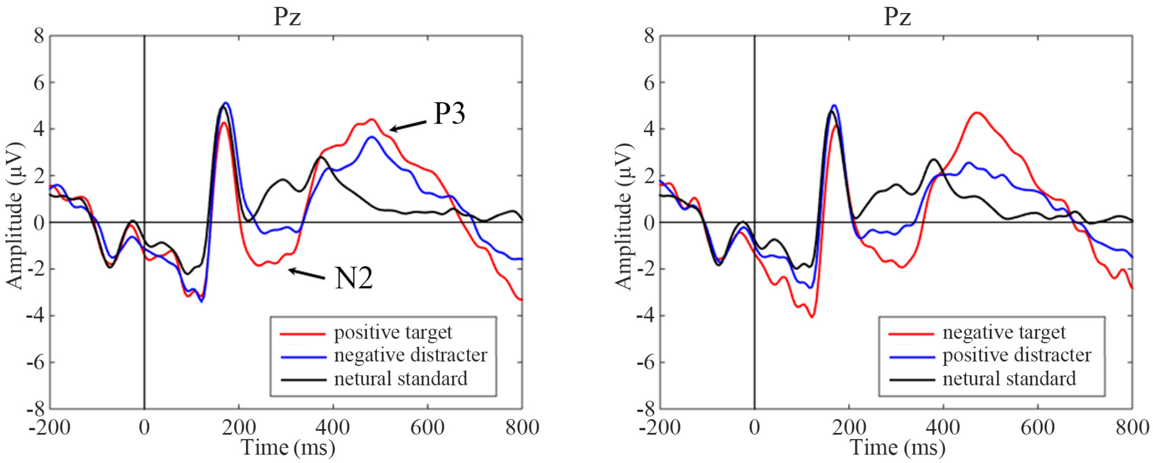

FIGURE 4 | Event-related potentials (ERP) waves on different task conditions at pre-treatment test in the sham group as an illustration. Black vertical lines indicate the initial time, and P3 and N2 components are marked with arrows. Positive target task shows on the left and negative target task on the right. For ERP plots, the *y*-axis displays amplitude (μV) and the x-axis displays time (ms).

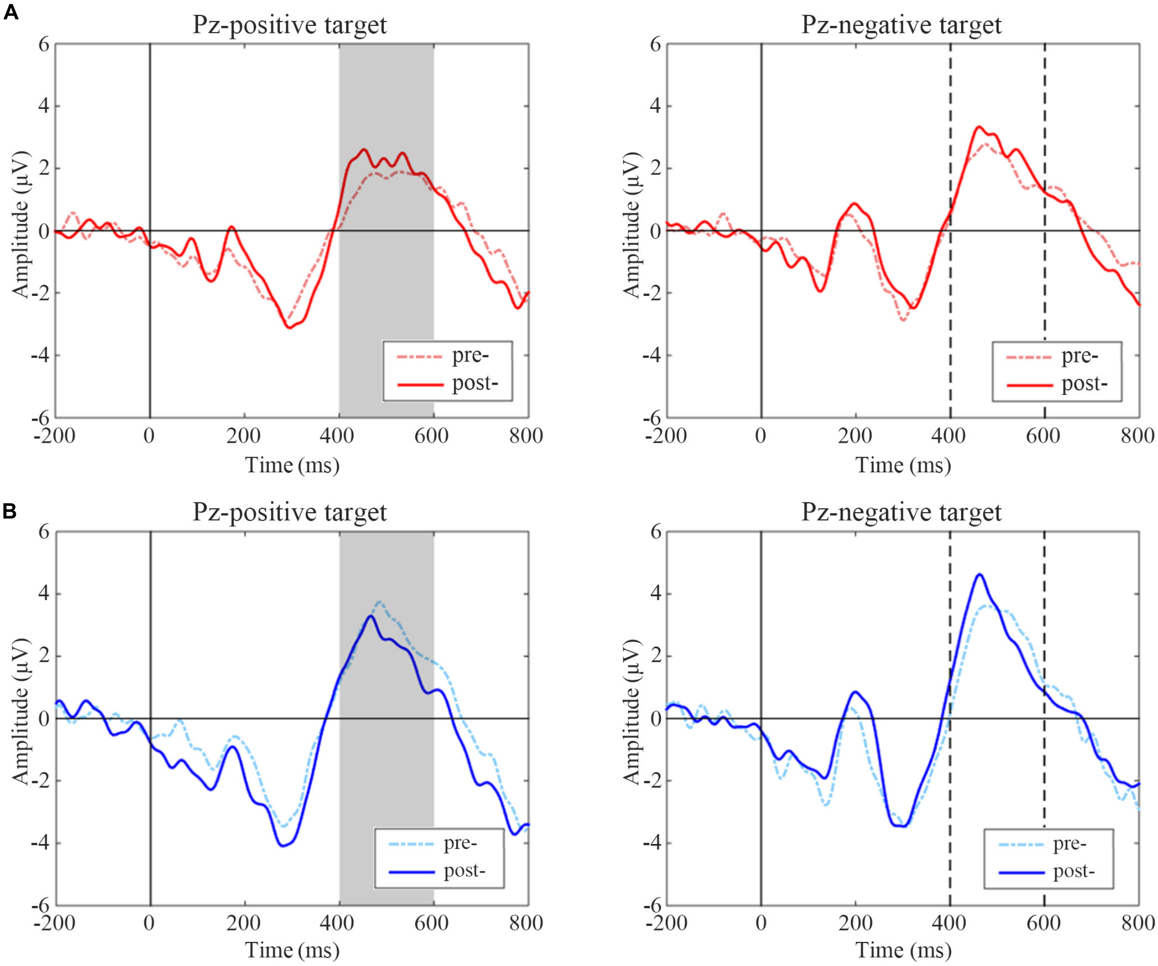

FIGURE 5 | Event-related potentials (ERP) difference waves of pre- and post-treatment tests for positive and negative targets in two groups. **(A)** Active group, **(B)** Sham group. The gray-filled area indicates the period with a significant difference. The gray dotted lines indicate the time points at 400 and 600 ms.

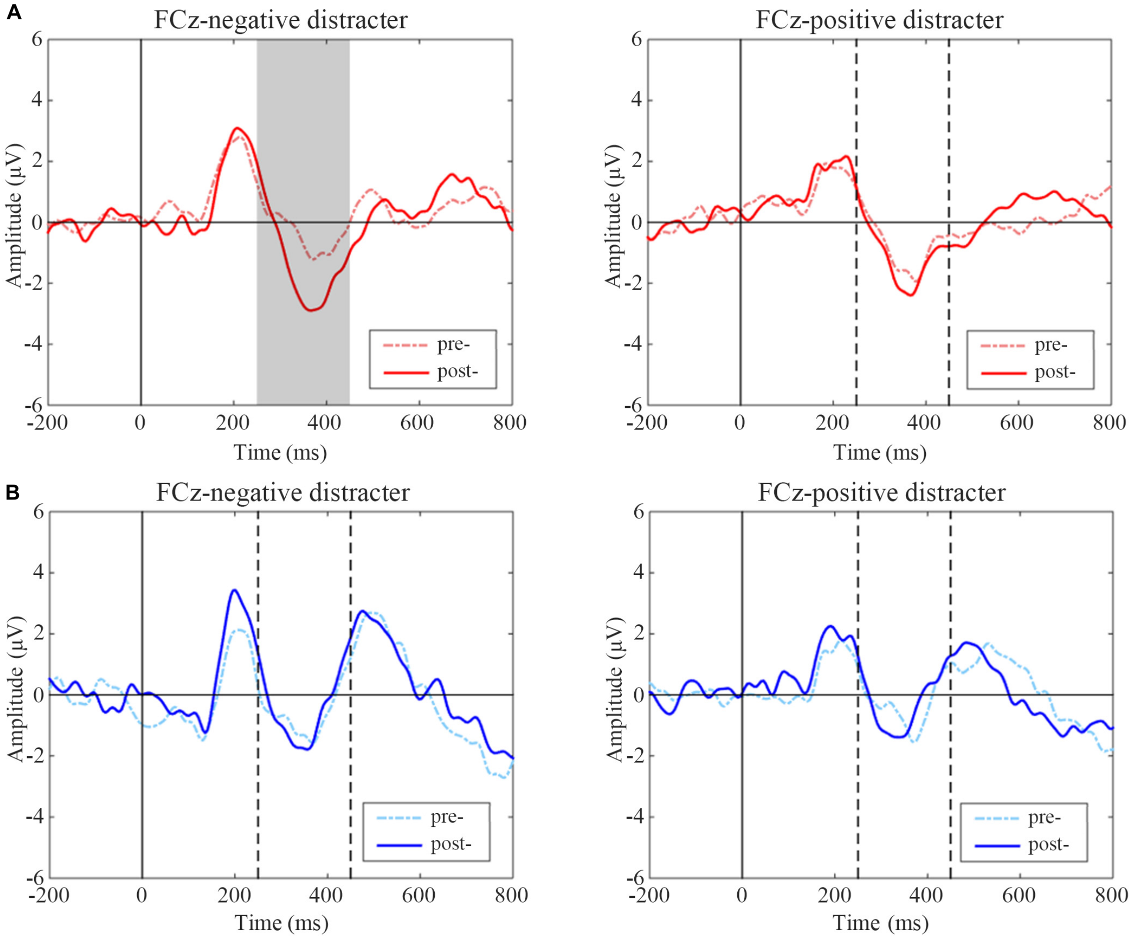

FIGURE 6 | Event-related potentials (ERP) difference waves of pre- and post-treatment tests for negative and positive distracters in two groups. **(A)** Active group, **(B)** Sham group. The gray-filled area indicates the period with a significant difference and the gray dotted lines indicate the time points at 250 and 450 ms.

no significant change of positive distracters on the condition of negative targets ($t = -0.578$, $p = 0.570$). In sham group, there was no significant difference between pre- and post-treatment on two conditions ($t = -0.381$, $p = 0.707$; $t = 0.518$, $p = 0.610$).

DISCUSSION

Recently, many researchers generally agreed that affect-biased attention is a form of emotion regulation. Also, affect-biased attention is tuned through experience over development (Todd et al., 2012), and individuals with different personality traits tend to show different attention biases (Paelecke et al., 2012). Several studies have suggested that depressive patients show a stronger attention bias for negative information, which may be related to the severity of depressive symptoms (Gotlib et al., 2004b; Sanchez et al., 2013). TDCS could improve depression and anxiety behaviors shown in clinical studies using enhancing cognitive control (Regni et al., 2010; Peña-Gómez et al., 2011). Few studies have explored the influence of tDCS on attentional bias. Thus, this study investigated attentional processing before and after tDCS within a healthy sample. TDCS reduced the commission error of taking neutral as negative, but there were no significant differences in the reaction time and accuracy. We found enhanced frontal alpha asymmetry coefficients after active tDCS treatment. The ERP results showed greater P3 amplitudes following positive targets and greater N2 amplitudes following negative distracters in the active tDCS group.

For behavioral data, only commission error of taking neutral as negative was significantly decreased after tDCS treatment and results including reaction time as well as accuracy showed no significant differences. It must be mentioned that all of the participants were healthy college students. It was not difficult for them to complete the simple oddball task. Therefore, we speculated there might exist the ceiling effect, resulting in the barely noticeable difference before and after tDCS treatment. And that is why we designed this study and analyzed the electrophysiological signals of the subjects. With high-time resolution, ERP could react to the real variations of subjects during the oddball task.

The P3 is thought to indicate processes involved in salient stimulus and is known to be modulated by attention (Becker and Shapiro, 1980; Heinze et al., 1990). The P3 amplitude has further been used to measure attentional allocation of cognitive processing resources in multiple tasks (Polich and Kok, 1995; Sawaki and Katayama, 2008). Affective stimuli can induce P3 signals well, and negative stimuli evokes greater P3 amplitudes than positive stimuli in healthy subjects (Morita et al., 2001). Compared to healthy groups, depressed individuals showed an enhanced P3 response to negative stimuli and a smaller P3 for positive stimuli (Ilardi et al., 2007). This can be seen as increased attention to the negative and a failure to attend sufficiently to the positive. However, many behavioral and psychophysiological findings showed that attention deficiency is widespread in anxiety, depression, and even attention deficit hyperactivity disorder (ADHD). Reduced P3 amplitude for task-relevant stimuli were observed in depressed groups as compared to the controls (Singh et al., 2000). In this study, we found increased P3 amplitudes following positive targets in the active group after receiving tDCS. This result suggests that tDCS may improve the allocation of attention to task-relevant positive stimuli in a healthy sample. P3 signals evoked by positive targets decreased significantly in the sham group. It is probably because the subjects' attention to positive stimuli declined after being familiar with the paradigm.

Our results also provide somewhat evidence to suggest that tDCS may affect response inhibition to negative emotional stimuli in a healthy sample. In previous electrophysiological studies, the fronto-central N2 component has traditionally been interpreted as an index of response inhibition (Falkenstein et al., 1999; Falkenstein, 2006). Response inhibition research commonly applied Go/Nogo paradigms, which require the execution of a motor response on a Go stimulus and its inhibition on a Nogo stimulus (Kaiser et al., 2006). Decreased N2 amplitude has been implicated in a failure of inhibiting or task-irrelevant disinhibition. Accumulating evidence demonstrated that depression is associated with difficulty in inhibiting negative information. Some studies found abnormally decreased N2 amplitude following task-irrelevant or distracting negative affective pictures or facial stimuli in the depressed group (Joormann and Gotlib, 2008; Krompinger and Simons, 2009). From a general cognitive functioning perspective, this might be negative bias in attentional processing resulting in inhibitory deficits in the depressed group (Botvinick et al., 2001). We observed increased N2 following negative distracters significantly in the active group after treatment. Nevertheless, no significant amplitude changes were observed following positive distracters as well as in the sham group. Such difference before and after treatment could be explained in that tDCS may improve response inhibition to negative information in healthy subjects.

Besides, previous research on frontal lobe EEG lateralization found that frontal lobe EEG lateralization is associated with depression, anxiety, schizophrenia, aggressiveness, and other emotional and behavioral disorders (Aftanas and Pavlov, 2005; Mathersul et al., 2008; Reznik and Allen, 2017). A recent research's result showed that frontal EEG lateralization can be used as a neurological indicator of depression (Gollan et al., 2014). Individuals with anxiety and depression have weakened left frontal lobe activity, while individuals with high emotional regulation ability have stronger left frontal lobe activity (Goodman et al., 2013). Thus, the implementation of emotional regulation and the use of emotional regulation strategies have enhanced left frontal lobe activity (Choi et al., 2016). In this study, we found that the FAA values of F4-F3 and F6-F5 positions increased significantly after tDCS in the active group, indicating the elevated emotion regulation ability.

Additionally, the DLPFC is of great importance in the top-down regulation of affective processing and highly correlated to emotion regulation (Baeken et al., 2010). Some studies have shown that tDCS has regulatory effects on DLPFC activity (Boggio et al., 2009) maybe by mediating cerebral blood flow and metabolism (Shiozawa et al., 2015). Anodal tDCS targeting the left DLPFC has reported significant antidepressant effects and improvement in emotional cognitive control, while tDCS over the right DLPFC leads to the generation of attentional impairments (Sanchez et al., 2016, 2018). A recent tDCS study showed a lateralized role of left and right DLPFC activity in enhancing/worsening the top-down regulation of emotional attention processing (Allaert et al., 2019). Our findings from two tasks were consistent with the above conclusions, illustrating the probable link between affect-bias attention and emotion regulation. But through Pearson correlation analysis and the mediating effect analysis, we did not find out the explicit link between ERP waveforms and FAA values statistically.

Some limitations should be considered in this study. First, our results could only reflect the effects of tDCS on electrophysiological data, while the results of behavioral data could not support the electrophysiological results. That means that the conclusions of this study are still inconclusive. TDCS could affect the subjects' ERP and FAA, but the relationship between these results and emotional attention bias is still uncertain. In the above discussion, we only provide a possible explanation direction that these electrophysiological results may reflect attentional bias. Second, this study employed three types of emotional facial stimuli, i.e., positive, negative, and neutral, to analyze the affect-biased attention in emotional processing. However, we have made a basic classification of emotional stimuli only in terms of valence roughly. The effect of tDCS is unknown when the emotional stimulus is classified as multiple categories and dimensions in more fine-grained details. Third, our results should be considered in the light of our sample. We recruited a restricted sample from a young college student population with an education level above average. Thus, it remains to be elucidated whether results from this study generalize to other groups. Additionally, the results of the correlation analysis between FAA and ERP did not show the exact link between emotional processing and the functional connection of the prefrontal areas. Nonetheless, considering the underlying mechanism, future studies should think about how to explain the regulation of emotional attention by the prefrontal cortex better physiologically.

In sum, our findings offered some electrophysiological insight into how tDCS works in the treatment of depression. TDCS treatment may raise the level of attention allocation to the positive target stimulus, reduce the negative cognitive bias, and enhance emotion regulation ability. To some extent, results of

ERP in oddball task and FAA in rest task may reflect the improvement of affect-bias attention and emotional regulation ability after tDCS. The above conclusions were only evidenced by physiological data significantly, excluding the inaccuracy and deception of self-assessment. Despite the limitations, this study adds to our understanding of changes that occurred in the brain region and may support the rationale for new therapies based on neuromodulation techniques. Future research is needed to replicate, extend, and refine these findings in depressed or dysphoric individuals to explore the feasibility of tDCS application toward emotional disorders.

DATA AVAILABILITY STATEMENT

The raw data supporting the conclusions of this article will be made available by the authors, without undue reservation.

ETHICS STATEMENT

The studies involving human participants were reviewed and approved by the Ethics Committee of Tianjin Hospital, Tianjin University. The patients/participants provided their written informed consent to participate in this study. Written informed consent was obtained from the individual(s) for the publication of any potentially identifiable images or data included in this article.

AUTHOR CONTRIBUTIONS

SL and DM conceived of the presented idea. SL designed the experiment. SZ performed the experiments. YH performed the computations. DG and SC verified the analytical methods. YK and DM helped supervise the project. All authors discussed the results and contributed to the final manuscript.

FUNDING

This work was supported in part by the National Key Research and Development Program of China under grant 2017YFB1002504, and in part by the National Natural Science Foundation of China (Nos. 81925020 and 81630051).

ACKNOWLEDGMENTS

We thank all the participants in this study.

REFERENCES

Aftanas, L. I., and Pavlov, S. V. (2005). Trait anxiety impact on posterior activation asymmetries at rest and during evoked negative emotions: EEG investigation. *Int. J. Psychophysiol.* 55, 85–94. doi: 10.1016/j.ijpsycho.2004.06.004

Allaert, J., Sanchez-Lopez, A., Raedt, R. D., Baeken, C., and Vanderhasselt, M. A. (2019). Inverse effects of tDCS over the left versus right DLPC on emotional processing: a pupillometry study. *PLoS One* 45:S67. doi: 10.1016/j.encep.2019.04.011

Armstrong, T., and Olatunji, B. O. (2012). Eye tracking of attention in the affective disorders: a meta-analytic review and synthesis. *Clin. Psychol. Rev.* 32, 704–723. doi: 10.1016/j.cpr.2012.09.004

Baeken, C., Raedt, R. D., Schuerbeek, P. V., Vanderhasselt, M. A., Mey, J. D., Bossuyt, A., et al. (2010). Right prefrontal HF-rTMS attenuates right amygdala processing of negatively valenced emotional stimuli in healthy females. *Behav. Brain Res.* 214, 450–455. doi: 10.1016/j.bbr.2010.06.029

Bai, L., Ma, H., Huang, Y. X., and Luo, Y. J. (2005). The development of native chinese affective picture system-a pretest in 46 college students. *Chin. Mental Health J.* 19, 719–722. doi: 10.1016/j.molcatb.2005.02.001

Bar-Haim, Y., Lamy, D., Pergamin, L., Bakermans-Kranenburg, M. J., and van Ijzendoorn, M. H. (2007). Threat-related attentional bias in anxious and nonanxious individuals: a meta-analytic study. *Psychol. Bull.* 133, 1–24. doi: 10.1037/0033-2909.133.1.1

Becker, D. E., and Shapiro, D. (1980). Directing attention toward stimuli affects the P300 but not the orienting response. *Psychophysiology* 17, 385–389. doi: 10.1111/j.1469-8986.1980.tb00168.x

Berking, M., Wirtz, C. M., Svaldi, J., and Hofmann, S. G. (2014). Emotion regulation predicts symptoms of depression over five years. *Behav. Res. Therapy* 57, 13–20. doi: 10.1016/j.brat.2014.03.003

Boggio, P. S., Zaghi, S., and Fregni, F. (2009). Modulation of emotions associated with images of human pain using anodal transcranial direct current stimulation (tDCS). *Neuropsychologia* 47, 212–217. doi: 10.1016/j.neuropsychologia.2008.07.022

Botvinick, M. M., Braver, T. S., Barch, D. M., Carter, C. S., and Cohen, J. D. C. (2001). Conflict monitoring and cognitive control. *Psychol. Rev.* 108, 624–652. doi: 10.1037/0033-295x.108.3.624

Brainard, D. H. (1997). The psychophysics toolbox. *Spat Vis.* 10, 433–436.

Bram, V. B., Notebaert, L., and Colin, M. (2018). The effects of attentional bias modification on emotion regulation. *J. Behav. Therapy Exp. Psychiatry* 38, 225–236. doi: 10.1016/j.jbtep.2018.08.010

Brosch, T., Pourtois, G., Sander, D., and Vuilleumier, P. (2011). Additive effects of emotional, endogenous, and exogenous attention: behavioral and electrophysiological evidence. *Neuropsychologia* 49, 1779–1787. doi: 10.1016/j.neuropsychologia.2011.02.056

Choi, D., Sekiya, T., Minote, N., and Watanuki, S. (2016). Relative left frontal activity in reappraisal and suppression of negative emotion: evidence from frontal alpha asymmetry (FAA). *Int. J. Psychophysiol.* 109, 37–44. doi: 10.1016/j.ijpsycho.2016.09.018

Dagmar Kr, H., Doxie, J., Bell, M. A., Ollendick, T. H., and Wolfe, C. D. (2010). A longitudinal study of emotion regulation and anxiety in middle childhood: associations with frontal EEG asymmetry in early childhood. *Dev. Psychobiol.* 52, 197–204. doi: 10.1002/dev.20425

Davidson, R. J. (1998). Affective style and affective disorders: perspectives from affective neuroscience. *Cogn. Emot.* 12, 307–330. doi: 10.1080/026999398379628

De Raedt, R., Vanderhasselt, M.-A., and Baeken, C. (2015). Neurostimulation as an intervention for treatment resistant depression: from research on mechanisms towards targeted neurocognitive strategies. *Clin. Psychol. Rev.* 41, 61–69. doi: 10.1016/j.cpr.2014.10.006

Delchau, H. L., Christensen, B. K., O'Kearney, R., and Goodhew, S. C. (2019). What is top-down about seeing enemies? Social anxiety and attention to threat. *Attention Perception & Psychophysics* 82, 1779–1792. doi: 10.3758/s13414-019-01920-3

Delorme, A., and Makeig, S. (2004). EEGLAB: an open source toolbox for analysis of single-trial EEG dynamics including independent component analysis. *J. Neurosci. Methods* 134, 9–21. doi: 10.1016/j.jneumeth.2003.10.009

Ellenbogen, M. A., Schwartzman, A. E., Stewart, J., and Walker, C.-D. (2002). Stress and selective attention: the interplay of mood, cortisol levels, and emotional information processing. *Psychophysiology* 39, 723–732. doi: 10.1111/1469-8986.3960723

Falkenstein, M. (2006). Inhibition, conflict and the Nogo-N2. *Clin. Neurophysiol.* 117, 1638–1640. doi: 10.1016/j.clinph.2006.05.002

Falkenstein, M., Hoormann, J., and Hohnsbein, J. (1999). ERP components in Go/Nogo tasks and their relation to inhibition. *Acta Psychol.* 101, 267–291. doi: 10.1016/S0001-6918(99)00008-6

Fragopanagos, N., Kockelkoren, S., and Taylor, J. G. (2005). A neurodynamic model of the attentional blink. *Cogn. Brain Res.* 24, 568–586. doi: 10.1016/j.cogbrainres.2005.03.010

Frewen, P. A., and Dozois, D. (2005). Recognition and interpretation of facial expressions in dysphoric women. *J. Psychopathol. Behav. Assess.* 27, 305–315. doi: 10.1007/s10862-005-2410-z

Friedman-Hill, S. R., Wagman, M. R., Gex, S. E., Pine, D. S., Leibenluft, E., and Ungerleider, L. G. (2010). What does distractibility in ADHD reveal about mechanisms for top-down attentional control? *Cognition* 115, 93–103. doi: 10.1016/j.cognition.2009.11.013

Fritzsche, A., Dahme, B., Gotlib, I. H., Joormann, J., and Leupoldt, A. V. (2010). Specificity of cognitive biases in patients with current depression and remitted depression and in patients with asthma. *Psychol. Med.* 40, 815–826. doi: 10.1017/S0033291709990948

Gollan, J. K., Hoxha, D., Chihade, D., Pflieger, M. E., Rosebrock, L., and Cacioppo, J. (2014). Frontal alpha EEG asymmetry before and after behavioral activation treatment for depression. *Biol. Psychol.* 99, 198–208. doi: 10.1016/j.biopsycho.2014.03.003

Goodman, R. N., Rietschel, J. C., Lo, L. C., Costanzo, M. E., and Hatfield, B. D. (2013). Stress, emotion regulation and cognitive performance: the predictive contributions of trait and state relative frontal EEG alpha asymmetry. *Int. J. Psychophysiol.* 87, 115–123. doi: 10.1016/j.ijpsycho.2012.09.008

Gotlib, I. H., Kasch, K. L., Traill, S., Joormann, J., Arnow, B. A., and Johnson, S. L. (2004a). Coherence and specificity of information-processing biases in depression and social phobia. *J. Abnorm. Psychol.* 113:386. doi: 10.1037/0021-843X.113.3.386

Gotlib, I. H., Krasnoperova, E., Yue, D. N., and Joormann, J. (2004b). Attentional biases for negative interpersonal stimuli in clinical depression. *J. Abnorm. Psychol.* 113, 121–135. doi: 10.1037/0021-843X.113.1.121

Gratz, K. L., and Roemer, L. (2008). Multidimensional assessment of emotion regulation and dysregulation: development. Factor structure, and initial validation of the difficulties in emotion regulation scale. *J. Psychopathol. Behav. Assess.* 30:315. doi: 10.1023/B:JOBA.0000007455.08539.94

Gross, J. J., Sheppes, G., and Urry, H. L. (2011). Cognition and emotion lecture at the 2010 SPSP emotion preconference. *Cogn. Emot.* 25, 765–781. doi: 10.1080/02699931.2011.555753

Hagemann, D. (2004). Individual differences in anterior EEG asymmetry: methodological problems and solutions. *Biol. Psychol.* 67, 157–182. doi: 10.1016/j.biopsycho.2004.03.006

Harmon-Jones, E., Gable, P. A., and Peterson, C. K. (2010). The role of asymmetric frontal cortical activity in emotion-related phenomena: a review and update. *Biol. Psychol.* 84, 451–462. doi: 10.1016/j.biopsycho.2009.08.010

Hecht, D. J. N. R. (2010). Depression and the hyperactive right-hemisphere. *Neurosci. Res.* 68, 77–87. doi: 10.1016/j.neures.2010.06.013

Heinze, H. J., Luck, S. J., Mangun, G. R., and Hillyard, S. A. (1990). Visual event-related potentials index focused attention within bilateral stimulus arrays. I. Evidence for early selection. *Electroencephalogr. Clin. Neurophysiol.* 75, 511–527. doi: 10.1016/0013-4694(90)90139-B

Hopfinger, J. B., and West, V. M. (2006). Interactions between endogenous and exogenous attention on cortical visual processing. *Neuroimage* 31, 774–789.

Ilardi, S. S., Atchley, R. A., Enloe, A., Kwasny, K., and Garratt, G. (2007). Disentangling attentional biases and attentional deficits in depression: an event-related potential P300 analysis. *Cogn. Ther. Res.* 31, 175–187. doi: 10.1007/s10608-006-9113-y

Jasper, H. H., Jasper, H. H., Jasper, H. H., and Jasper, H. H. (1958). Report of the committee on methods of clinical examination in electroencephalography. *Electroencephalogr. Clin. Neurophysiol.* 10, 370–375. doi: 10.1016/0013-4694(58)90053-1

Johnstone, T., Reekum, C. V., Urry, H. L., Kalin, N. H., and Davidson, R. J. (2007). Failure to regulate: counterproductive recruitment of top-down prefrontal-subcortical circuitry in major depression. *J. Neurosci.* 27, 8877–8884. doi: 10.1523/JNEUROSCI.2063-07.2007

Joormann, J., and D'Avanzato, C. (2010). Emotion regulation in depression: examining the role of cognitive processes. *Cogn. Emot.* 24, 913–939. doi: 10.1080/02699931003784939

Joormann, J., and Gotlib, I. H. (2008). Updating the contents of working memory in depression: interference from irrelevant negative material. *J. Abnorm. Psychol.* 117, 182–192. doi: 10.1037/0021-843X.117.1.182

Kaiser, S., Weiss, O., Hill, H., Markela-Lerenc, J., Kiefer, M., and Weisbrod, M. (2006). N2 event-related potential correlates of response inhibition in an auditory Go/Nogo task. *Int. J. Psychophysiol.* 61, 279–282. doi: 10.1016/j.ijpsycho.2005.09.006

Karparova, S. P., Kersting, A., and Suslow, T. (2010). Disengagement of attention from facial emotion in unipolar depression. *Psychiatry Clin. Neurosci.* 59, 723–729. doi: 10.1111/j.1440-1819.2005.01443.x

Kline, J. P., Blackhart, G. C., and Williams, W. C. (2007). Anterior EEG asymmetries and opponent process theory. *Int. J. Psychophysiol.* 63, 302–307. doi: 10.1016/j.ijpsycho.2006.12.003

Krompinger, J. W., and Simons, R. F. (2009). Electrophysiological indicators of emotion processing biases in depressed undergraduates. *Biol. Psychol.* 81, 153–163. doi: 10.1016/j.biopsycho.2009.03.007

Kujawa, A. J., Torpey, D., Kim, J., Hajcak, G., Rose, S., Gotlib, I. H., et al. (2011). Attentional biases for emotional faces in young children of mothers with chronic or recurrent depression. *J. Abnorm. Child Psychol.* 39, 125–135. doi: 10.1007/s10802-010-9438-6

Loo, C. K., Alonzo, A., Martin, D., Mitchell, P. B., and Sachdev, P. (2012). Transcranial direct current stimulation for depression: 3-week, randomised, sham-controlled trial. *Br. J. Psychiatry J. Ment. Sci.* 200:52. doi: 10.1192/bjp.bp.111.097634

Loo, C. K., Sachdev, P., Martin, D., Pigot, M., and Mitchell, P. (2009). A double-blind, sham-controlled trial of transcranial direct current stimulation for the treatment of depression. *Int. J. Neuropsychopharmacol.* 13, 61–69. doi: 10.1017/S1461145709990411

MacDonald Angus, W., Cohen Jonathan, D., Stenger, V. A., and Carter Cameron, S. (2000). Dissociating the role of the dorsolateral prefrontal and anterior cingulate cortex in cognitive control. *Science* 288, 1835–1838. doi: 10.1126/science.288.5472.1835

Mathersul, D., Williams, L. M., Hopkinson, P. J., and Kemp, A. H. (2008). Investigating models of affect: relationships among eeg alpha asymmetry. *Depress. Anxiety. Emot.* 8, 560–572. doi: 10.1037/a0012811

McAndrew, F. (1986). A cross-cultural study of recognition thresholds for facial expressions of emotion. *J. Cross Cult. Psychol.* 17, 211–224. doi: 10.1177/0022002186017002005

Mogg, K., Bradley, B. P. J. B. R., and Therapy. (2002). Selective orienting of attention to masked threat faces in social anxiety. *Behav. Res. Ther.* 40, 1403–1414. doi: 10.1016/S0005-7967(02)00017-7

Morita, Y., Morita, K., Yamamoto, M., Waseda, Y., and Maeda, H. (2001). Effects of facial affect recognition on the auditory P300 in healthy subjects. *Neurosci. Res.* 41, 89–95. doi: 10.1016/S0168-0102(01)00248-6

Most, S. B., Chun, M. M., Widders, D. M., and Zald, D. H. (2005). Attentional rubbernecking: cognitive control and personality in emotion-induced blindness. *Psychon. Bull. Rev.* 12, 654–661. doi: 10.3758/BF03196754

Nitsche, M. A., and Paulus, W. (2001). Sustained excitability elevations induced by transcranial DC motor cortex stimulation in humans. *Neurology* 57, 1899–1901. doi: 10.1212/wnl.57.10.1899

Nitsche, M. A., Fricke, K., Henschke, U., Schlitterlau, A., Liebetanz, D., Lang, N., et al. (2003). Pharmacological modulation of cortical excitability shifts induced by transcranial direct current stimulation in humans. *J. Physiol.* 553(Pt 1), 293–301. doi: 10.1113/jphysiol.2003.049916

Ochsner, K. N., and Gross, J. J. (2005). The cognitive control of emotion. *Trends Cogn. Sci.* 9, 242–249. doi: 10.1016/j.tics.2005.03.010

Paelecke, M., Paelecke-Habermann, Y., and Borkenau, P. (2012). Temperament and attentional bias in vocal emotional stroop tasks. *Eur. J. Pers.* 26, 111–122. doi: 10.1002/per.1848

Palm, U., Schiller, C., Fintescu, Z., Obermeier, M., Keeser, D., Reisinger, E., et al. (2012). Transcranial direct current stimulation in treatment resistant depression: a randomized double-blind, placebo-controlled study. *Brain Stimul.* 5, 242–251. doi: 10.1016/j.brs.2011.08.005

Peckham, A. D., McHugh, R. K., and Otto, M. W. (2013). A meta-analysis of the magnitude of biased attention in depression. *Depress. Anxiety* 30:407. doi: 10.1002/da.22092

Peña-Gómez, C., Vidal-Piñeiro, D., Clemente, I. C., Pascual-Leone, A., and Bartrés-Faz, D. (2011). Down-regulation of negative emotional processing by transcranial direct current stimulation: effects of personality characteristics. *PLoS One* 6:e22812. doi: 10.1371/journal.pone.0022812

Persad, S. M., and Polivy, J. (1993). Differences between depressed and nondepressed individuals in the recognition of and response to facial emotional cues. *J. Abnorm. Psychol.* 102, 358–368. doi: 10.1037//0021-843x.102.3.358

Polich, J., and Kok, A. (1995). Cognitive and biological determinants of P300: an integrative review. *Biol. Psychol.* 41, 103–146. doi: 10.1016/0301-0511(95)05130-9

Regni, F. F., Boggio, P. S., Nitsche, M. A., Marcolin, M. A., Rigonatti, S. P., and Pascual-Leone, A. (2010). Treatment of major depression with transcranial direct current stimulation. *Bipolar Disord.* 8:203. doi: 10.1111/j.1399-5618.2006.00291.x

Reznik, S. J., and Allen, J. J. B. (2017). Frontal asymmetry as a mediator and moderator of emotion: an updated review. *Psychophysiology* 55:12965. doi: 10.1111/psyp.12965

Rottenberg, J., Gross, J. J., and Gotlib, I. H. (2005). Emotion context insensitivity in major depressive disorder. *J. Abnorm. Psychol.* 114, 627–639. doi: 10.1037/0021-843x.114.4.627

Salehinejad, M. A., Ghanavai, E., Rostami, R., and Nejati, V. (2016). Cognitive control dysfunction in emotion dysregulation and psychopathology of major depression (MD): evidence from transcranial brain stimulation of the dorsolateral prefrontal cortex (DLPFC). *J. Affect. Disord.* 210:241. doi: 10.1016/j.jad.2016.12.036

Sanchez, A., Everaert, J., De Putter, L. M. S., Mueller, S. C., and Koster, E. H. W. (2015). Life is . . . great! Emotional attention during instructed and uninstructed ambiguity resolution in relation to depressive symptoms. *Biol. Psychol.* 109, 67–72. doi: 10.1016/j.biopsycho.2015.04.007

Sanchez, A., Vanderhasselt, M. A., Baeken, C., and De Raedt, R. (2016). Effects of tDCS over the right DLPFC on attentional disengagement from positive and negative faces: an eye-tracking study. *Cogn. Affect. Behav. Neurosci.* 16, 1–12. doi: 10.3758/s13415-016-0450-3

Sanchez, A., Vazquez, C., Gomez, D., and Joormann, J. (2014). Gaze-fixation to happy faces predicts mood repair after a negative mood induction. *Emotion* 14, 85–94. doi: 10.1037/a0034500

Sanchez, A., Vazquez, C., Marker, C., Lemoult, J., and Joormann, J. (2013). Attentional disengagement predicts stress recovery in depression: an eye-tracking study. *J. Abnorm. Psychol.* 122, 303–313. doi: 10.1037/a0031529

Sanchez, L., Vanderhasselt, A., Marie, A., Jens, A., et al. (2018). Neurocognitive mechanisms behind emotional attention: inverse effects of anodal tDCS over the left and right DLPFC on gaze disengagement from emotional faces. *Cogn. Affect. Behav. Neurosci.* 18, 485–494. doi: 10.3758/s13415-018-0582-8

Sawaki, R., and Katayama, J. I (2008). Top-down directed attention to stimulus features and attentional allocation to bottom-up de*via*tions. *J. Vis.* 8, 4–8.

Schindler, S., and Bublatzky, F. (2020). Attention and emotion: an integrative review of emotional face processing as a function of attention. *Cortex* 130, 362–386. doi: 10.1016/j.cortex.2020.06.010

Schmitz, T. W., Rowley, H. A., Kawahara, T. N., and Johnson, S. C. (2006). Neural correlates of self-evaluative accuracy after traumatic brain injury. *Neuropsychologia* 44, 762–773. doi: 10.1016/j.neuropsychologia.2005.07.012

Schutter, D. J. L. G., and Honk, J. V. (2005). A framework for targeting alternative brain regions with repetitive transcranial magnetic stimulation in the treatment of depression. *J. Psychiatry Neurosci.* 30, 91–97.

Shin, Y.-I., Foerster, Á, and Nitsche, M. A. (2015). Transcranial direct current stimulation (tDCS) - application in neuropsychology. *Neuropsychologia* 69, 154–175. doi: 10.1016/j.neuropsychologia.2015.02.002

Shiozawa, P., Silva, M., and Cordeiro, Q. (2015). Transcranial direct current stimulation for treating depression in a patient with right hemispheric dominance: a case study. *J. Ect* 31, 201–202. doi: 10.1097/yct.0000000000000180

Siegle, G. J., Ingram, R. E., and Matt, G. E. (2002). Affective interference: an explanation for negative attention biases in dysphoria? *Cogn. Therapy Res.* 26, 73–87. doi: 10.1023/A:1013893705009

Singh, R., Shukla, R., Dalal, P. K., Sinha, P. K., and Trivedi, J. K. (2000). P 300 event related potential in depression. *Indian J. Psychiatry* 42:402.

Smit, D., Posthuma, D., Boomsma, D. I., and Geus, E. (2007). The relation between frontal EEG asymmetry and the risk for anxiety and depression. *Biol. Psychol.* 74, 26–33. doi: 10.1016/j.biopsycho.2006.06.002

Spielberger, C. D. (1970). *Manual For The State-Trait Anxietry, Inventory*. Palo Alto, CA: Consulting Psychologist.

Stevens, C., and Bavelier, D. (2012). The role of selective attention on academic foundations: a cognitive neuroscience perspective. *Dev. Cogn. Neurosci.* 2, S30–S48. doi: 10.1016/j.dcn.2011.11.001

Suslow, T., Dannlowski, U., Lalee-Mentzel, J., Donges, U. S., Arolt, V., and Kersting, A. (2004). Spatial processing of facial emotion in patients with unipolar depression: a longitudinal study. *J. Affect. Disord.* 83, 59–63. doi: 10.1016/j.jad.2004.03.003

Todd, R. M., Cunningham, W. A., Anderson, A. K., and Thompson, E. (2012). Affect-biased attention as emotion regulation. *Trends Cogn. Sci.* 16, 365–372. doi: 10.1016/j.tics.2012.06.003

Tomarken, A. J., Davidson, R. J., Wheeler, R. E., and Doss, R. C. (1992). Individual differences in anterior brain asymmetry and fundamental dimensions of emotion. *J. Pers. Soc. Psychol.* 62, 676–687. doi: 10.1037//0022-3514.62.4.676

Tomarken, A. J., Davidson, R. J., Wheeler, R. E., and Kinney, L. (2010). Psychometric properties of resting anterior EEG asymmetry: temporal stability and internal consistency. *Psychophysiology* 29:576. doi: 10.1111/j.1469-8986.1992.tb02034.x

Vanderlind, W. M., Millgram, Y., Baskin-Sommers, A. R., Clark, M. S., and Joormann, J. (2020). Understanding positive emotion deficits in depression: from emotion preferences to emotion regulation. *Clin. Psychol. Rev.* 76:101826. doi: 10.1016/j.cpr.2020.101826

Wager, T. D., Davidson, M. L., Hughes, B. L., Lindquist, M. A., and Ochsner, K. N. (2008). Prefrontal-Subcortical pathways mediating successful emotion regulation. *Neuron* 59, 1037–1050. doi: 10.1016/j.neuron.2008.09.006

Waters, F., Badcock, J. C., and Maybery, M. T. (2006). Selective attention for negative information and depression in schizophrenia. *Psychol. Med.* 36, 455–464. doi: 10.1017/S0033291705007026

Wiens, S., Peira, N., Golkar, A., and Öhman, A. (2008). Recognizing masked threat : fear betrays, but disgust you can trust. *Emotion* 8, 810–819. doi: 10.1037/a0013731

Wolkenstein, L., and Plewnia, C. (2013). Amelioration of cognitive control in depression by transcranial direct current stimulation. *Biol. Psychiatry* 73, 646–651. doi: 10.1016/j.biopsych.2012.10.010

Yadollahpour, A., Jalilifar, M., and Rashidi, S. (2017). Transcranial direct current stimulation for the treatment of depression: a comprehensive review of the recent advances. *Int. J. Ment. Health Addict.* 15, 434–443. doi: 10.1007/s11469-017-9741-3

Zhong, M., Wang, X., Xiao, J., Yi, J., Zhu, X., Liao, J., et al. (2011). Amygdala hyperactivation and prefrontal hypoactivation in subjects with cognitive vulnerability to depression. *Biol. Psychol.* 88, 233–242. doi: 10.1016/j.biopsycho.2011.08.007

Conflict of Interest: The authors declare that the research was conducted in the absence of any commercial or financial relationships that could be construed as a potential conflict of interest.

frontiers | Frontiers in Neuroscience

ORIGINAL RESEARCH
published: 06 July 2022
doi: 10.3389/fnins.2022.914876

Effects of Degrees of Degeneration on the Electrical Excitation of Human Spiral Ganglion Neurons Based on a High-Resolution Computer Model

Albert M. Croner[1,2]*, *Amirreza Heshmat*[3], *Anneliese Schrott-Fischer*[3], *Rudolf Glueckert*[3], *Werner Hemmert*[1,2] *and Siwei Bai*[1,2]

[1] *Department of Electrical and Computer Engineering, Technical University of Munich, Munich, Germany,* [2] *Munich Institute of Biomedical Engineering, Technical University of Munich, Garching, Germany,* [3] *Laboratory for Inner Ear Biology, Medical University of Innsbruck, Innsbruck, Austria*

After hearing loss retrograde degeneration of spiral ganglion neurons (SGNs) has been described. Studies modeling the effects of degeneration mostly omitted peripheral processes (dendrites). Recent experimental observations indicated that degenerating SGNs manifested also a reduced diameter of their dendrites. We simulated populations of 400 SGNs inside a high resolution cochlear model with a cochlear implant, based on µCT scans of a human temporal bone. Cochlear implant stimuli were delivered as biphasic pulses in a monopolar configuration. Three SGN situations were simulated, based on our previous measurements of human SGN dendrites: (A) SGNs with intact dendrites (before degeneration), (B) degenerating SGNs, dendrites with a smaller diameter but original length, (C) degenerating SGNs, dendrites omitted. SGN fibers were mapped to characteristic frequency, and place pitch was estimated from excitation profiles. Results from degenerating SGNs (B, C) were similar. Most action potentials were initiated in the somatic area for all cases (A, B, C), except for areas near stimulating electrodes in the apex with intact SGNs (A), where action potentials were initiated in the distal dendrite. In most cases, degenerating SGNs had lower thresholds than intact SGNs (A) (down to –2 dB). Excitation profiles showed increased ectopic activation, i.e., activation of unintended neuronal regions, as well as similar neuronal regions excited by different apical electrodes, for degenerating SGNs (B, C). The estimated pitch showed cases of pitch reversals in apical electrodes for intact SGNs (A), as well as mostly identical pitches evoked by the four most apical electrodes for degenerating SGNs (B, C). In conclusion, neuronal excitation profiles to electrical stimulation exhibited similar traits in both ways of modeling SGN degeneration. Models showed degeneration of dendrites caused increased ectopic activation, as well as similar excitation profiles and pitch evoked by different apical electrodes. Therefore, insertion of electrodes beyond approximately 450° may not provide any benefit if SGN dendrites are degenerated.

Keywords: cochlear implant, computational model, human, spiral ganglion neurons, neural degeneration, ectopic activation, personalized model, deep insertion

Edited by:
Liming Li,
Shanghai Jiao Tong University, China

Reviewed by:
Xiaohong Sui,
Shanghai Jiao Tong University, China
Paul Avan,
Institut de l'Audition, Institut Pasteur, France

***Correspondence:**
Albert M. Croner
albert.croner@tum.de

Specialty section:
This article was submitted to Neural Technology, a section of the journal Frontiers in Neuroscience

Received: *07 April 2022*
Accepted: *13 June 2022*
Published: *06 July 2022*

Citation:
Croner AM, Heshmat A, Schrott-Fischer A, Glueckert R, Hemmert W and Bai S (2022) Effects of Degrees of Degeneration on the Electrical Excitation of Human Spiral Ganglion Neurons Based on a High-Resolution Computer Model. Front. Neurosci. 16:914876. doi: 10.3389/fnins.2022.914876

1. INTRODUCTION

In normal hearing humans, a sound consisting of a single frequency will excite neurons in a limited and specific area within the cochlea, with high frequencies exciting neurons more in the base, and low frequencies exciting neurons more in the apex (von Békésy, 1960). This tonotopic arrangement of the cochlea is also exploited for cochlear implants (CIs), where multiple electrodes are placed in the cochlea at different positions. The coding strategy of the CI converts sound which is recorded by a microphone behind the ear into stimulation currents delivered to individual electrodes, which in turn stimulate distinct neuron populations (Loizou, 1999; Wilson, 2008). Overall, CIs are able to restore speech understanding in otherwise profoundly hearing impaired patients to a surprisingly high degree, which makes them the most successful neuroimplants today. However, the extent to which hearing fidelity is restored in CI patients still differs, with hearing performance varying strongly between individual subjects (Blamey et al., 1996; Holden et al., 2013). There are multiple possible reasons contributing to this variance in performance. One such reason may be that every human has an individual cochlea, i.e., when two inner ears are implanted with the same CI, differing cochlear geometries may lead to differences in electric current flow. This is especially relevant as electric stimulation impedes the precision of neural excitation compared to acoustic, i.e., with electric stimulation it is not possible to perfectly exploit the tonotopic arrangement of the cochlea. Imperfect exploitation of the tonotopic map manifests as e.g., a low number of independent frequency channels in CI stimulation (Croghan et al., 2017), or stimulation of unintended neuronal regions (e.g., "cross-turn" stimulation, Kalkman et al., 2014; "tip-shifts," Nelson et al., 2008). Another reason may lie within the spiral ganglion neurons (SGNs) responsible for the transmission of sound information, which may degenerate or die (Glueckert et al., 2005) and thereby affect the auditory information transmitted to the brain.

In order to estimate how cochlear geometry and state of SGNs, i.e., their morphology, influence the performance of CI subjects in experiments, it would be necessary to measure both cochlear geometry and SGN morphology. The former can be measured to a limited degree in living patients, e.g., using CT (Nogueira et al., 2016). However, measurements in living patients, especially of implanted cochleae, will only yield rough measures such as the height and diameter of the cochlea. Higher resolution can only be measured post-mortem, e.g., using slice preparations or μCT scans. Therefore, as cochlear measurements in living patients are severely limited, several volume conduction models of human cochleae were developed over the years. Cochlea models employed to simulate CI stimulation started out as manually created geometries, e.g., a model of an unrolled tube (Finley et al., 1990), or of a coiled, tapering tube (Frijns et al., 2001; Hanekom, 2001), including basic structures such as cochlear scalae. Those manually created geometries were later employed to generate "personalized" models, i.e., by fitting the model geometries to measurements of actual human cochleae, such as height, diameter, or post-mortem mid-modiolar cross-sections (Kalkman et al., 2014; Malherbe et al., 2016; Nogueira et al., 2016). Those models, while including some degree of personalization, were still based on simple geometries. A more recent development is the creation of models based on high-definition μCT scans of post-mortem human cochleae, including segmentation of individual structures. As creating such detailed models is especially labor intensive, there exist only a small number of those to date. Nevertheless, they offer the advantage of including fine details of structures present in physical cochleae, which influence the current spread in the cochlea under CI stimulation (Bai et al., 2019; Potrusil et al., 2020).

Cochlear volume conduction models allow for examination of current spread within the cochlea, but do not give information about whether the actual neurons in the auditory nerve are excited. Therefore, they are generally combined with multi-compartment neuron models, representing type I SGNs. However, SGNs may manifest different morphologies which need to be taken into account, especially in profoundly hearing impaired subjects who are candidates for a CI implantation. One hearing-loss-induced change in SGN morphology is the retrograde degeneration of peripheral neuronal processes, caused by deafferentiation to inner hair cells. Such neural degeneration has been observed in both animals (Bichler et al., 1983; Spoendlin, 1984; Wise et al., 2017) and humans (Nadol, 1990; Glueckert et al., 2005; Linthicum and Fayad, 2009; Rask-Andersen et al., 2010). Neural degeneration has, therefore, been incorporated in several models, in most cases by modeling neuron populations with both an intact peripheral process and a completely missing peripheral process (Rattay et al., 2001, 2013; Briaire and Frijns, 2006; Smit et al., 2008, 2010; Snel-Bongers et al., 2013; Kalkman et al., 2014; Malherbe et al., 2015; Potrusil et al., 2020). Intact and missing peripheral processes are the extremes of neural degeneration of the auditory nerve, excluding the actual death of SGNs. It is, however, not clear how the degenerative process proceeds in between those two extremes, especially for humans. A possible intermediate degenerative state is the shrinking of peripheral processes' diameter, as described by Heshmat et al. (2020).

In this study, we present a detailed model of the human inner ear, consisting of a high resolution finite element (FE) volume conduction model of a human cochlea and a population of modeled type I SGNs. The FE cochlea model was based on μCT scans of an implanted human cochlea and included reconstructed nerve fiber paths (Bai et al., 2019). Neuron populations were based on the multi-compartment model from Rattay et al. (2013) and modeled 400 auditory nerve fibers (ANFs) spread out along the tonotopic axis. With the modeled neuron population, differences in excitation behavior based on different degenerative stages were investigated, including an intermediate stage with thin peripheral processes. In this study, the peripheral process of a modeled ANF is denoted as "dendrite" and the central process as "axon."

2. METHODS

2.1. Reconstruction of the Cochlea Model

The FE cochlea model with an implanted electrode array was reconstructed from a set of μCT scans of a human cadaveric temporal bone. The implanted cochlea model was

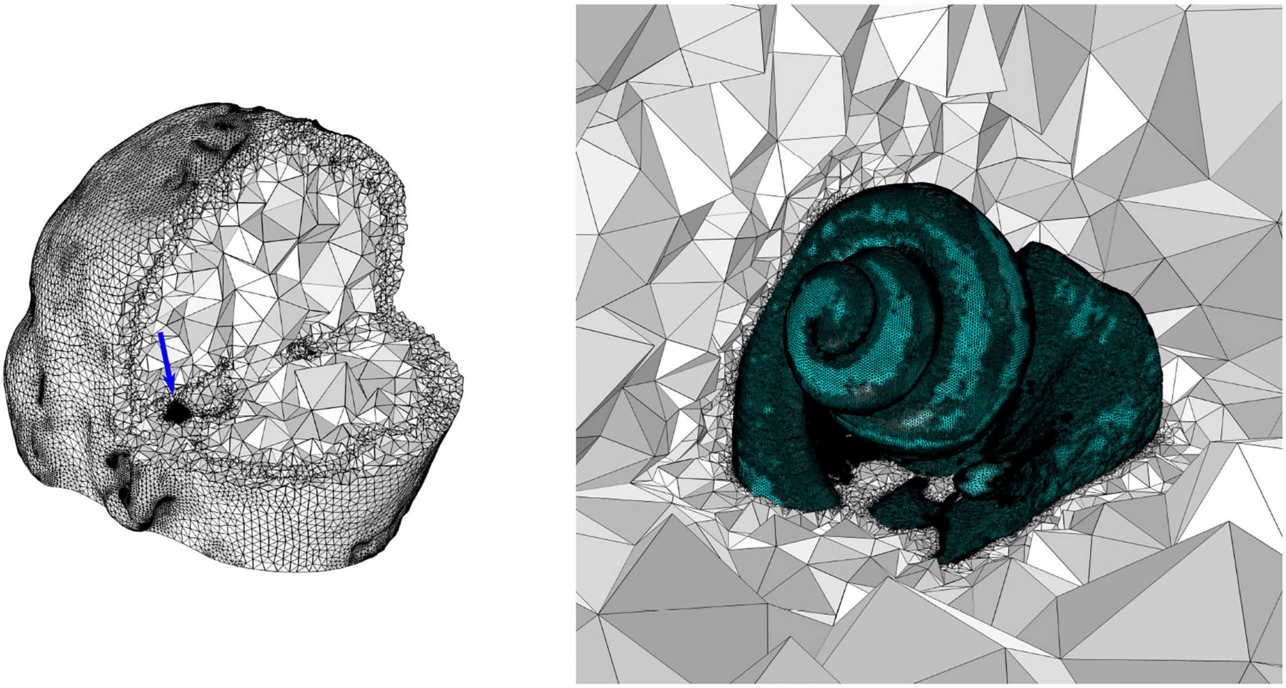

FIGURE 1 | Left: A dissected view of the FE mesh of the whole head model. The blue arrow indicates the location of the cochlea. Right: A zoomed-in view of the cochlea (and the nerve), indicated by the blue arrow in the left image.

then placed in a human head model at the petrous part of the left temporal bone, which was necessary to correctly place the CI ground electrode. This resulted in a FE model with 21,937,778 volumetric mesh elements, shown in **Figure 1**. The trajectories of 400 ANFs spanning from the base to the apex of the cochlea were reconstructed based on the FE mesh of the auditory nerve. The lengths of the reconstructed neuron paths ranged from 5.5 to 8.2 mm. Neuron paths are illustrated in **Figure 2**. The complete FE model was subsequently imported into COMSOL Multiphysics (COMSOL AB, Sweden) for calculating the electric potential V in a volume conduction model. The CI electrode array was modeled representing a MED-EL (Innsbruck, Austria) Standard electrode, which comprises 12 pairs of electrode contacts ($\equiv$ 12 electrodes), and was based on the geometry of a dummy electrode array physically inserted into the temporal bone sample. The MED-EL Standard electrode is considered a lateral wall electrode array. Note that the electrode array inserted into our preserved cadaveric temporal bone punctured the basilar membrane at approximately 270° into the cochlea, thereby traversing from the scala tympani into the scala vestibuli. As consequence, the modeled electrode array was situated in the scala vestibuli from electrode 6 upwards. Traversal of electrode arrays into the scala vestibuli is regularly observed in implanted cochleae, with arrays either partially or entirely located in scala vestibuli (e.g., approximately 25% of cochleae, Wardrop et al., 2005; approximately 5% of cochleae, O'Connell et al., 2016; Risi, 2018). The presence of scala traversal may, however, be a limitation of the model. It is yet to be studied whether the traversal would influence modeling outcomes.

Electrode contact pairs were numbered with the most basal electrode pair as "electrode 1," and the most apical electrode pair as "electrode 12." The CI stimulation scheme in this study was monopolar: the current-controlled stimulus was delivered from a single electrode, with the ground electrode placed extracochlearly on the left temporal bone of the skull. Electrode-neuron distance, i.e., the shortest distance from an electrode to either the beginning of a neuron path or to the nearest point along a neuron path, ranged from approximately 0.5 mm to 1 mm, as depicted in **Figure 3**. For the purpose of calculating electrode-neuron distance, the coordinate of an electrode was determined as the center point between the two electrode contacts of a pair. Finally, the electric potentials on all points along the ANF paths were extracted from the FE simulation.

A detailed description of the reconstruction and electrical properties of the FE model, as well as the reconstruction of neuron trajectories, can be found in Bai et al. (2019). Electrode dimensions and the conductivity values of the FE model can also be found in **Supplementary Table S1**, available in the online version of this article.

2.2. Multi-Compartment Neuron Model

A multi-compartment model adapted from Rattay et al. (2013, 2001) was implemented. Our ANF model followed the description in the original publication except for the morphology of dendrites and axons. Simulations were run with a population of 400 ANFs. Population simulation was done by simulating

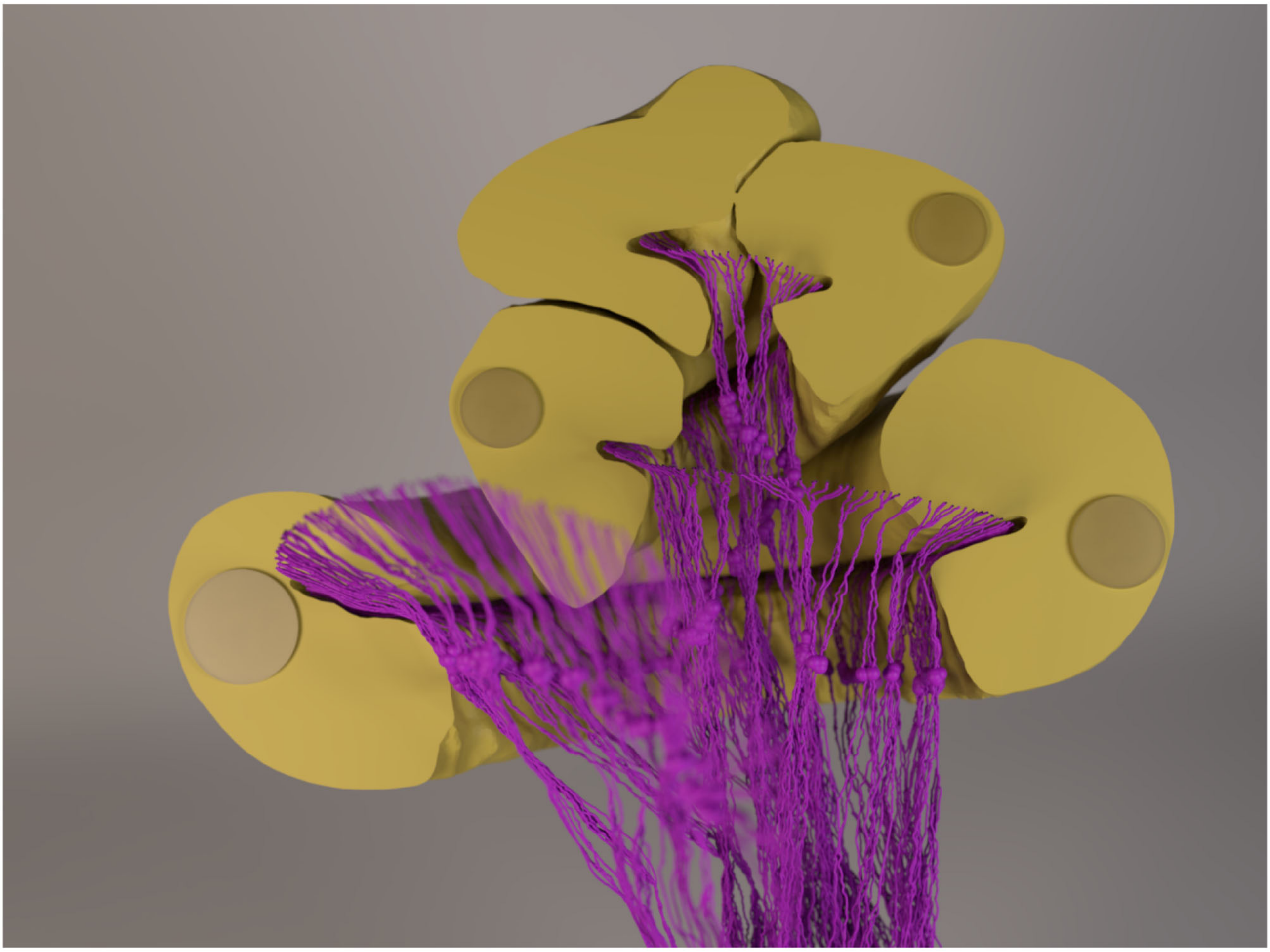

FIGURE 2 | A rendered image of the 3D cochlea model and the neurons with 1.5-mm-long dendrites. The cochlear canal, as well as the implanted electrode, was cut to provide a better view of the neurons. The "out-of-focus" neurons in the image sit in front of the cut-plane. Note that the diameter of the fibers (and the somata) is amplified for visualization purposes, i.e., they are not to scale.

the multi-compartment neuron model with extracellular electric potential values obtained from the FE model at the 400 previously reconstructed neuronal paths.

The model from Rattay et al. (2013) was originally designed with a 1 μm dendrite diameter and a 2 μm axon diameter. However, histograms from our recent measurements on dendrite diameter exhibited a unimodal distribution for normal hearing cases with a maximum at 2 μm diameter, and a bimodal distribution for patients with hearing loss, peaking at 0.5 and 2 μm diameters (Heshmat et al., 2020). Therefore, we used a dendrite diameter of 2 μm in our model to represent "intact" dendrites. Based on the ratio of $\frac{diameter_{axon}}{diameter_{dendrite}} = 2$ in Rattay et al. (2013), the axon in our model was, thus, implemented with a diameter of 4 μm; this also lies around the upper limit of type I SGN axon diameters observed (Arnesen and Osen, 1978; Nadol, 1990; Nadol et al., 1990). In addition to "intact," non-degenerated dendrites, we also modeled two further degenerative states. Based on the measurements with hearing-loss cases, a "partially degenerated" dendrite was modeled with a diameter of 0.5 μm, and a "completely degenerated" dendrite was modeled by omitting the entire dendrite, modeling the neurons with only soma and axon. In both degenerated cases, the axon diameter was kept identical to the "intact" case, with a diameter of 4 μm. Heshmat et al. (2020) also included measurements on myelin thickness in dendrites (peaking at 0.6 μm for normal hearing, and at 0.6 μm and 0.15 μm for hearing loss), which were implemented in our model as well, with "intact" dendrites having a myelin thickness of 0.6 μm, and "partially degenerated" dendrites a myelin thickness of 0.15 μm.

Regarding dendrite length, we implemented two versions, as in Rattay et al. (2001): one with a dendrite length of 2.3 mm, and the other with a dendrite length of 1.5 mm, to account for shorter dendrites in the middle turn of the cochlea and longer dendrites in the base and apex (Potrusil et al., 2020). In a single simulation run, dendrite lengths were kept uniform for all 400 neurons, whereas the axon lengths were adapted

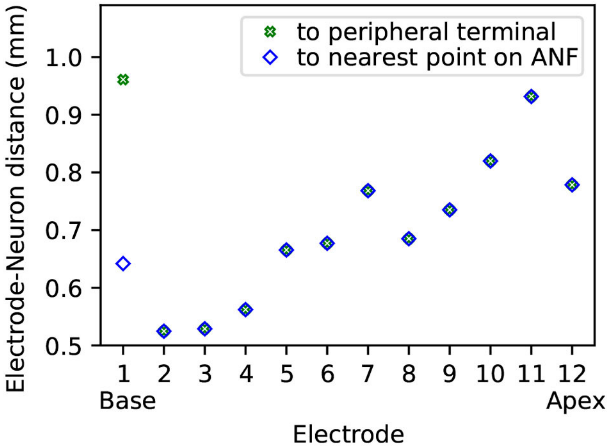

FIGURE 3 | Electrode-neuron distance for each of the twelve electrodes in the model. The distance is displayed both as distance to the closest point along the beginning of the reconstructed neuron paths (≡ modeled peripheral terminals), and as distance to the closest point along the entire length of all reconstructed neuron paths (≡ modeled ANFs).

by adding or removing node-internode pairs so that all fibers ended with an internode at the end of their reconstructed paths. Intact ANFs started with their peripheral terminal (first dendritic compartment) at the beginning of the reconstructed paths, i.e., in the spiral lamina attached at the level of inner hair cells. As described above, three degenerative states were implemented for the neuron population: "intact" dendrites, "partially degenerated" dendrites with narrower diameter, and "completely degenerated" dendrites with the entire dendrite removed. Hence, we have the following six combinations, also illustrated in **Figure 4**:

- $FD_{2.3}$: **Full** (intact) **D**endrite. 2.3 mm dendrite length and 2 µm dendrite diameter.
- $TD_{2.3}$: **T**hin **D**endrite. 2.3 mm dendrite length and 0.5 µm dendrite diameter.
- $ND_{2.3}$: **N**o **D**endrite. Soma, as well as the axon, positioned at the same location as $FD_{2.3}$ and $TD_{2.3}$, therefore, the first neuronal compartment (soma) offset by 2.3 mm from the beginning of the path.
- $FD_{1.5}$: **F**ull (intact) **D**endrite. 1.5 mm dendrite length and 2 µm dendrite diameter.
- $TD_{1.5}$: **T**hin **D**endrite. 1.5 mm dendrite length and 0.5 µm dendrite diameter.
- $ND_{1.5}$: **N**o **D**endrite. Soma, as well as the axon, positioned at the same location as $FD_{1.5}$ and $TD_{1.5}$, therefore, the first neuronal compartment (soma) offset by 1.5 mm from the beginning of the path.

Parameters of the multi-compartment neuron model can be found in **Supplementary Table S1**, available in the online version of this article.

2.3. Processing

Neuron models were implemented in Python 3.5, using the Brian2 package (Goodman and Brette, 2009), and simulations were conducted on a computing cluster in parallel using the Thorns package (Rudnicki, 2022). Differential equations were solved using an exponential Euler method with a 1 µs timestep. The current stimulus used for neuronal stimulation was a single biphasic (cathodic-first) pulse with 40 µs/phase. For each of the six simulated degenerative states and 12 stimulation electrodes, the minimum current necessary to elicit an action potential (AP) in at least a single fiber, i.e., threshold, and all 400 fibers was determined. The range spanned between those two current values would then define the electric dynamic range (EDR). Afterward, each degenerative state and stimulation electrode was simulated with 80 current stimuli linearly spaced along within the EDR. For all simulations, voltage traces were saved and subsequently evaluated to determine the AP initiation site for all amplitudes.

Initial results were the "excitation profiles," which show when ANFs were excited, i.e., generated an AP, for a neuron population within its entire EDR. To compare excitation profile shapes of different degenerative states, the difference of individual fiber thresholds in dB was computed, using Equation 1,

$$20 \cdot log_{10}\left(\frac{thr_{a,i}}{thr_{b,i}}\right) \tag{1}$$

where thr is the threshold of an individual fiber, a and b denote the degenerative state, i.e., FD or TD for a, and ND for b, and i denotes the individual fiber, numbered from 1 to 400.

To represent characteristic frequencies (CF) of individual fibers, ANFs were mapped to frequencies using the Greenwood frequency map (Greenwood, 1990). For mapping purposes, relevant fiber coordinates were the positions of peripheral tips of the fibers, i.e., the starting point of the peripheral terminals. Fiber tip coordinates were transformed into 1-dimensional coordinates, i.e., describing only the distance along the fiber tip trajectory, with the most basal fiber (fiber 1) denoting the starting point. 1-dimensional fiber coordinates were then divided by total cochlear length (i.e., distance from the most basal to the most apical fiber along the fiber tip trajectory) and used as x for the Greenwood equation (Equation 2). Note that in the original equation Greenwood defined x as the fraction of cochlear length with $x = 1$ at the basal end. As this is inverted to our definition, it was necessary to replace x in the original equation with $(1 - x)$, resulting in Equation 2.

$$CF = 165.4\,\text{Hz} \cdot (10^{2.1\cdot(1-x)} - 0.88) \tag{2}$$

In addition, Laneau et al. (2004) observed that a model predicting place pitch based on the centroid of the excited cochlear area fits well with the results from their pitch ranking experiments on CI subjects. Therefore, we employed excitation profiles to reconstruct an approximation of "perceived" place pitch, based on the centroid of excited fibers and the Greenwood frequency map. The centroids were computed as the mean of 1-dimensional fiber tip coordinates of only the excited fibers, for any individual stimulation current. An illustration describing centroid reconstruction and corresponding pitch is displayed in **Figure 5**. Note that it was not distinguished whether there was a gap in excited fibers (i.e., due to ectopic activation, e.g., **Figure 5**,

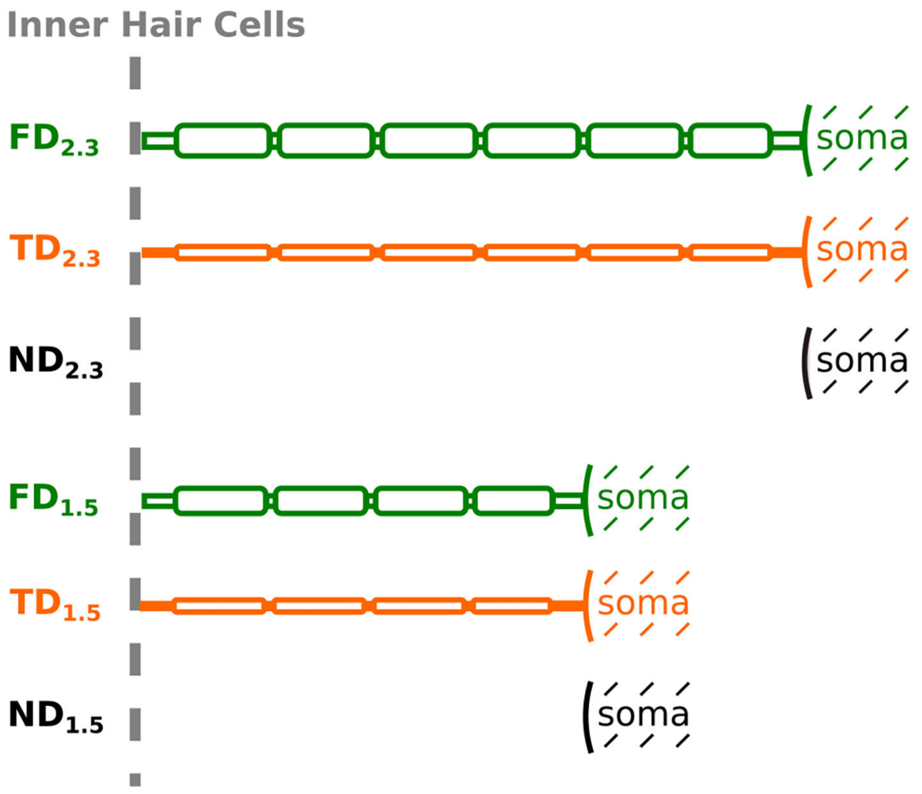

FIGURE 4 | Schematic representation of an ANF for different degenerative states and dendrite lengths, depicted up to soma (not to scale). Degenerative state is indicated by name [FD, Full (intact) Dendrite; TD, Thin Dendrite; ND, No Dendrite] and dendrite length is indicated by the subscript.

electrode 5), which could potentially lead to a perception of two separate pitches instead of one. The reconstructed pitch was then further evaluated by computing the difference in pitch between adjacent electrodes, for four selected percentages (5%, 10%, 15%, and 20%) of EDR. Pitch difference was calculated in octaves, i.e., $log_2\left(\frac{F_a}{F_b}\right)$, with F_a being the pitch of the more apical electrode, and F_b being the pitch of the more basal electrode.

3. RESULTS

3.1. Neural Excitation

3.1.1. Absolute Threshold

Absolute threshold refers to the lower limit of the EDR, i.e., the minimum current necessary to elicit an AP in at least one ANF in a simulated population. In **Supplementary Figure S1**, the voltage traces of selected ANFs at and just below the absolute threshold have been included. Absolute thresholds, as shown in **Figure 6**, ranged from approximately −12 dB re 1 mA (= 0.25 mA) to approximately −4 dB re 1 mA (= 0.63 mA). In general, dendritic degeneration lead to a slight reduction in the absolute threshold, which was unexpected. Compared to FD, absolute thresholds for TD and ND were reduced in base and apex for 2.3 mm dendrites, and over most of the cochlear length for 1.5 mm dendrites. Within individual stimulation electrodes, absolute thresholds of TD and ND were within approximately 2 dB difference compared to their FD counterpart, and within 1 dB difference when compared with each other. TD absolute thresholds were slightly below ND absolute thresholds in most cases.

3.1.2. Excitation Profile

Excitation profiles depict the stimulation amplitude at which each fiber was activated and include the location of initial "effective" excitation within each fiber. Hereby, the "effective" excitation refers to the excitation that produces an afferent AP. For example, if a neuron is first excited in its dendrite, but before the AP propagates to the axon, it is excited independently in the axon as well, then the initial "effective" excitation is determined to originate from the axon. Excitation profiles for 2.3 mm dendrites are shown in **Figure 7**, and for 1.5 mm dendrites in **Figure 8**. Ectopic activation was observed in the excitation profiles. Here, ectopic activation is defined as independent activation of regions distant to stimulating electrodes; for example in **Figure 7** $TD_{2.3}$ activation from electrode 7 at approximately 150 Hz and 2 kHz, as well as electrode 9 at approximately 30 Hz and 2 kHz.

For $FD_{2.3}$ (**Figure 7**), it could be observed that AP initiation sites were mostly proximal to the soma, except for regions close to the electrodes, where AP initiation happened in the distal region of the dendrite, especially for middle and apical stimulation electrodes, but less so for basal stimulation electrodes. This may indicate that stimulation of neurons in the basal turn might be affected less by degeneration, as APs initiated in the somatic

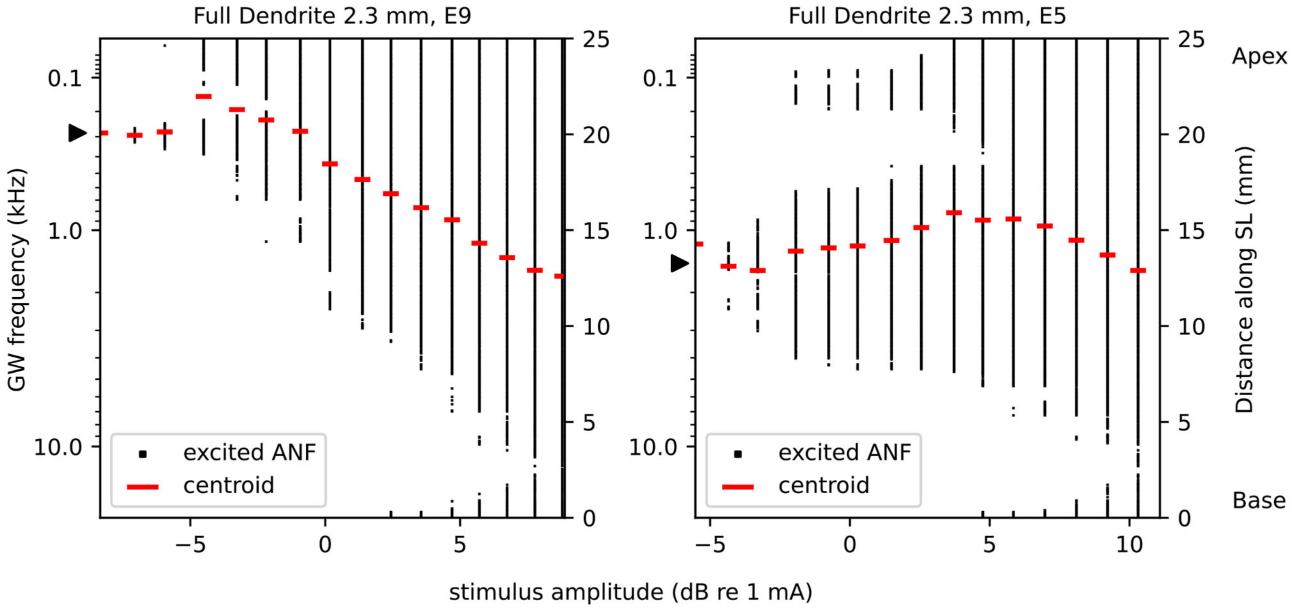

FIGURE 5 | Excited fibers and corresponding centroids, exemplary for $FD_{2.3}$ electrode 9 (left) and electrode 5 (right). Electrode 9 features a decrease and subsequent increase of pitch corresponding to the centroids with increasing stimulation amplitude. Electrode 5 features ectopic activation. For purpose of better visualization, we included here only a selective number of stimulation amplitudes. The electrode position is mapped to its nearest fiber, indicated by a black triangle. The left ordinate shows the frequency map, right ordinate the position of ANFs along the spiral lamina (SL).

area are less likely to be influenced by changes in dendrite morphology. Ectopic activation could be observed especially for stimulation in the middle of the cochlea. Regarding $TD_{2.3}$ and $ND_{2.3}$, visual inspection showed very similar stimulation patterns between each other. The activation initiated in the distal region of the dendrites in the case of $FD_{2.3}$ was largely missing in both degenerated cases, in spite of that dendrites were still present with $TD_{2.3}$. The most striking difference between the two degenerated cases is that for $TD_{2.3}$, most APs initiated just before the soma, while for $ND_{2.3}$, most APs initiated in the soma. Excitation profiles for individual apical electrodes (electrodes 9 and upward) showed very similar patterns among each other, both for $TD_{2.3}$ and $ND_{2.3}$. Ectopic activation was very prominent for both $TD_{2.3}$ and $ND_{2.3}$, especially in the middle and apex, where in most cases individual fiber thresholds were lower for ectopic activation than for fibers near the stimulation electrodes (e.g., electrode 7, activation at approximately 150 Hz). In summary, degeneration of 2.3 mm dendrites increased ectopic activation, caused less to no stimulation in the distal region of the dendrite, and reduced differences between apical stimulation electrodes.

In contrast to 2.3 mm dendrites, 1.5 mm dendrites (**Figure 8**) had the vast majority of APs initiated proximal to the soma, even for $FD_{1.5}$, and more APs initiated in the axon for stimuli at high amplitudes. $FD_{1.5}$ showed some initiations in the distal region of dendrites in the apex, but far less than $FD_{2.3}$. Overall, differences among $FD_{1.5}$, $TD_{1.5}$, and $ND_{1.5}$ were small, except for the few distal dendrite activations in $FD_{1.5}$. Ectopic activation was only prominent in the apex for all degenerative states (e.g., electrode 11, activation at approximately 1 kHz). Similar to $TD_{2.3}$ and $ND_{2.3}$, excitation profiles for $TD_{1.5}$ and $ND_{1.5}$ showed little difference between individual apical electrodes.

For ND, most APs were initiated in the soma. On closer inspection, the vast majority of APs initiated in the soma (approximately 93%) showed indistinguishable AP peak timings and highly similar potential values (average difference at approximately 0.01 mV) to corresponding postsomatic compartments, i.e., APs initiated simultaneously in both the soma and the postsomatic compartment (not shown). Simultaneous AP initiation in both the soma and postsomatic compartment may indicate an excitation that originated from the axon hillock or axon initial segment, the interfaces between soma and axon.

Considering results from short dendrites to be more accurate in the middle of the cochlea, and results from long dendrites to be more accurate in the base and apex, the largest impact of degeneration may be in the apex, causing prominent ectopic activation and a small difference in areas stimulated by different electrodes. Ectopic activation in the base and middle of the cochlea was mostly cross-turn activation, i.e., activation at ±360° to the electrode.

3.1.3. Individual Threshold Differences

Based on the excitation profiles, differences in individual fiber thresholds between degenerative states were computed, comparing how similar FD and TD were to ND. Differences (dB) are displayed in **Figure 9**. In all cases, ND was more similar to TD than to FD; the TD vs. ND difference median was on average at approximately –0.5 dB, with interquartile ranges of 1–2 dB. With 2.3 mm dendrites, electrodes in the middle showed

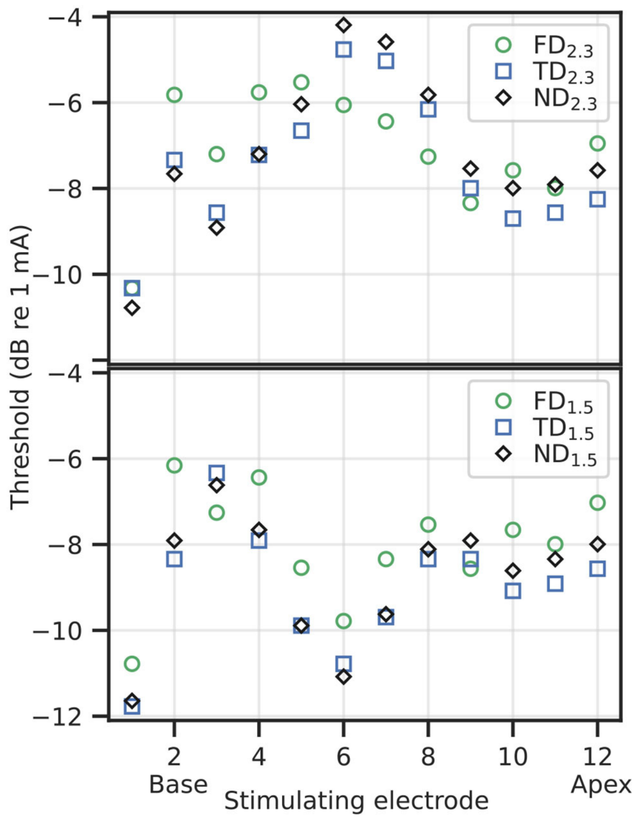

FIGURE 6 | Thresholds for individual stimulation electrodes and degenerative states, 2.3 mm dendrite on top, 1.5 mm dendrite on bottom.

outliers down to approximately −4 dB for $TD_{2.3}$ vs $ND_{2.3}$. $FD_{2.3}$ vs. $ND_{2.3}$ showed the largest differences, with difference medians from approximately -3 to 0 dB, and interquartile ranges of approximately 3 to 7 dB. $FD_{1.5}$ vs. $ND_{1.5}$ differences were larger than $TD_{1.5}$ vs. $ND_{1.5}$, but not as pronounced as for 2.3 mm dendrites. In general, differences between degenerative states of 1.5 mm dendrites were smaller than differences between degenerative states of 2.3 mm dendrites, and differences between TD and ND were much smaller than differences between FD and ND.

3.2. Pitch

Pitch was reconstructed based on the centroid of excited area and the Greenwood frequency map (see also **Figure 5**). Reconstructed pitch for all electrodes and degenerative states along each corresponding EDR is displayed in **Figure 10**. At larger stimulus amplitudes (greater than approximately 20% EDR), pitch of apical electrodes largely overlapped. This partly applied to middle electrodes as well, especially for long dendrites. Below approximately 20% EDR, however, pitch for different electrodes differed depending on degenerative state and dendrite length, as detailed below. Note that for higher percentages of EDR, reconstructed pitch would automatically converge to approximately 1,700 Hz, corresponding to the middle of the cochlea. For example, with 50% of ANFs excited, the average excited position would always result within the innermost 50% of fibers (i.e., ANF 101 to ANF 300, for 400 ANFs), therefore the centroid of the excitation would correspond to a CF between approximately 400 Hz and 6 kHz. Consequently, with 100% of ANFs excited, the average excited position would always be at the middle of the cochlear length, corresponding to approximately 1700 Hz.

For FD, the pitch at the absolute threshold was mostly well spaced for all electrodes, with pitch usually evoked close to stimulating electrodes. With increasing stimulus, at approximately 10% EDR for $FD_{2.3}$ and 5% for $FD_{1.5}$, the pitch of apical stimulation electrodes increasingly overlapped. In contrast, for both TD and ND there were overlapping pitches even at the absolute threshold. There, for $TD_{2.3}$ and $ND_{2.3}$, electrodes 9–12 evoked pitch at approximately 30–40 Hz, which increased to approximately 80 Hz at 5% EDR. Note that the Greenwood frequency map with parameters suggested for humans starts at approximately 20 Hz (Greenwood, 1990). Evoked pitches of middle electrodes (5–8) were not close to any of the middle electrodes but instead offset toward either the apex (electrodes 6–8) or the base (electrode 5). For $TD_{1.5}$ and $ND_{1.5}$, all electrodes 9–12 evoked pitch at approximately 190 Hz (between electrodes 9 and 10) at the absolute threshold. No pitch was evoked close to electrodes 4, 7, 8, 9, 11, and 12 at the absolute threshold, with no pitch evoked close to electrodes 11 and 12 even with increased stimulus. The pitch evoked by basal stimulating electrodes was similar to FD pitch for all TD and ND. Yet another interesting observation was a few cases of pitch reversals, i.e., an apical electrode generating a higher pitch than a more basal electrode. Pitch reversals were seen with some apical electrodes at specific ranges of EDR, e.g., electrode 12 generated higher pitches than electrodes 9–11 for $FD_{2.3}$ at approximately 10–25% of EDR.

With increased stimulation amplitude, abrupt changes in reconstructed pitch were often observed, especially for apical electrodes. This can generally be attributed to ectopic activation, where a new group of neurons is excited and thereby changes the overall pitch (e.g., $TD_{2.3}$ electrode 7). In real CIs, however, this might cause a second, parallel pitch perception instead of a shift in pitch. In addition, while we investigated stimulation by individual, independent electrodes, in implanted CIs sounds will likely activate more than a single electrode, therefore a perceived pitch would be the outcome of a combination of multiple activated electrodes.

In summary, FD showed mostly independent and tonotopic frequency channels for different electrodes, especially near the absolute threshold, but TD and ND both lead to the unification of several frequency channels, especially for apical electrodes. TD and ND showed similar pitch values compared to each other. In some cases, pitch reversals were observed.

3.2.1. Pitch Difference

Pitch difference, depicted in **Figure 11**, was mostly in the 0 to −1 octave range. All configurations showed almost no differences for apical electrodes when averaged over the four selected percentages. However, note that for FD this was the case because of pitch reversals occurring, and differences in individual EDR

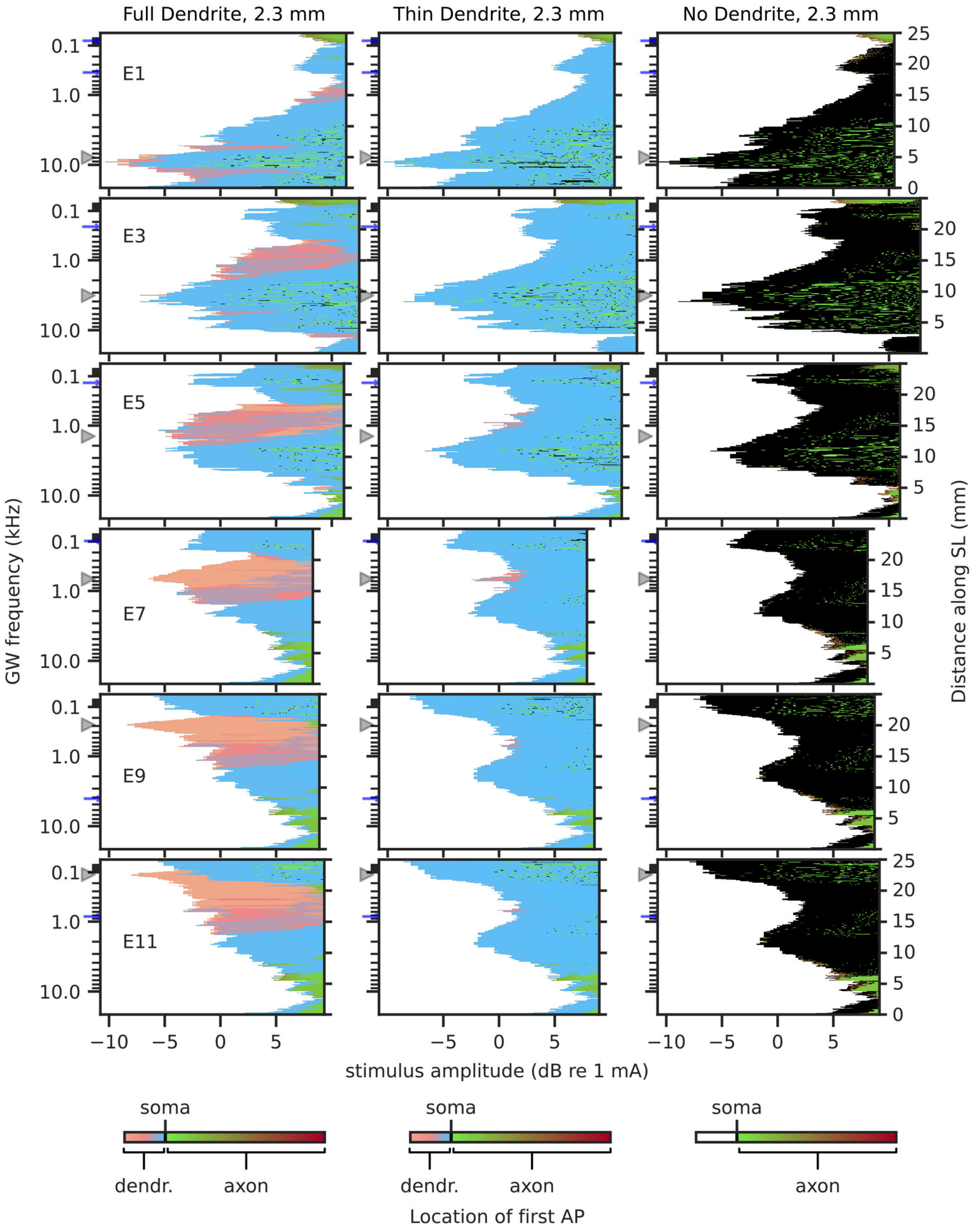

FIGURE 7 | Excitation profiles for 2.3 mm dendrites. Greenwood frequency mapping performed for all 400 fibers, marked on the left ordinate. Fiber position along spiral lamina marked on the right ordinate. AP initiation site is color-coded, soma marked with black color. Stimulation electrodes labeled on the left. Electrode position is mapped to its nearest fiber and indicated by gray triangles, blue arrows mark fibers at ±360° to the stimulation electrodes.

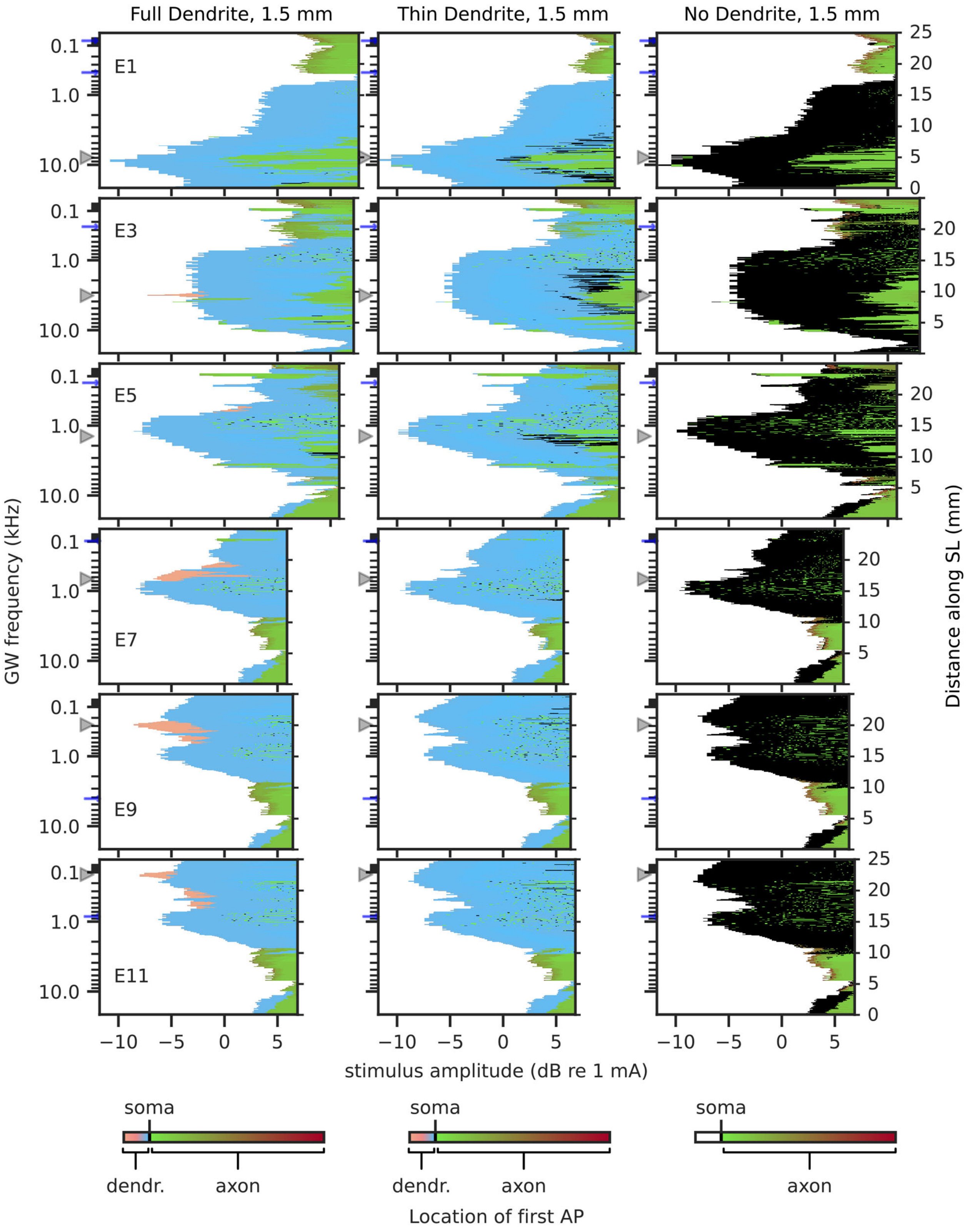

FIGURE 8 | Excitation profiles for 1.5 mm dendrites. Greenwood frequency mapping performed for all 400 fibers, marked on the left ordinate. Fiber position along spiral lamina marked on the right ordinate. AP initiation site is color-coded, soma marked with black color. Stimulation electrodes labeled on the right. Electrode position is mapped to its nearest fiber and indicated by gray triangles, blue arrows mark fibers at ±360° to the stimulation electrodes.

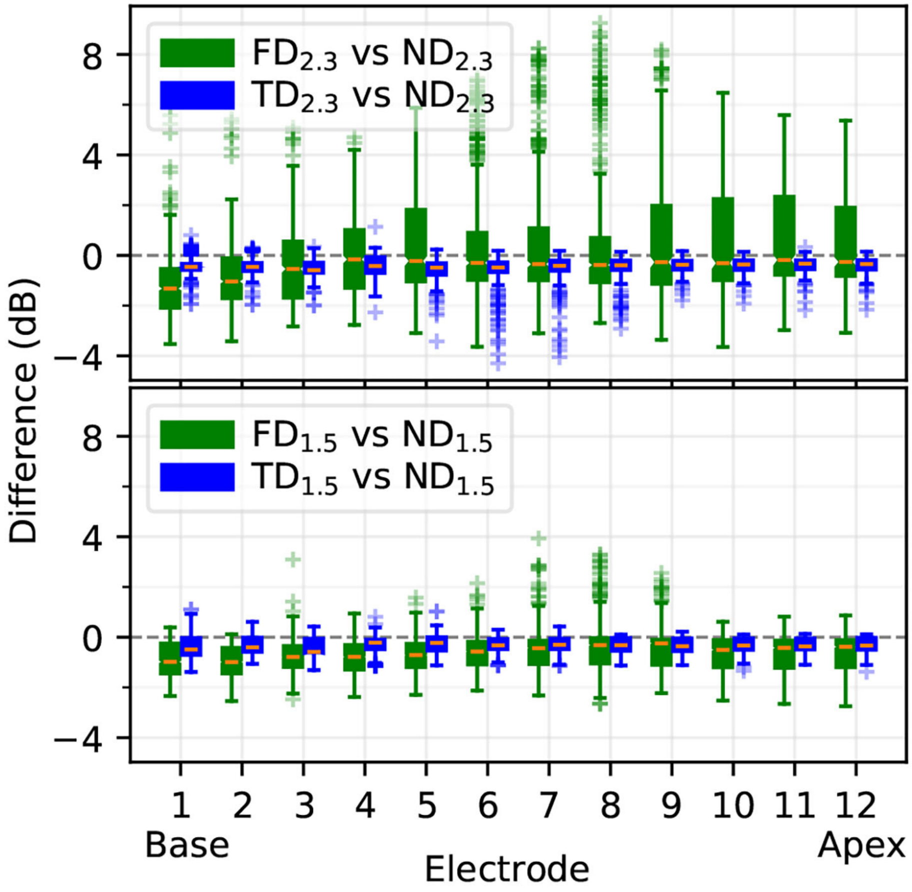

FIGURE 9 | Difference of individual ANF thresholds between ND and other degenerative states, computed as in Equation 1. Boxplots show medians, lower and upper quartiles, whiskers (encompassing values contained in quartiles ± 1.5 times the interquartile range), and outliers.

percentages were mostly non-zero. In contrast, TD and ND showed almost no differences in the apex not only for the averaged values but for most of the individual EDR percentages as well, indicating similar pitches evoked by different apical electrodes over an extended current range. This was especially prominent for $TD_{2.3}$ and $ND_{2.3}$, where differences were close to zero octaves for electrodes 8–12. $TD_{1.5}$ and $ND_{1.5}$ differences were close to zero octaves only for electrodes 10–12. Differences for $TD_{2.3}$ were similar to differences for $ND_{2.3}$, and differences for $TD_{1.5}$ were similar to differences for $ND_{1.5}$.

4. DISCUSSION

The present study investigated CI excitation of ANFs with different degrees of degeneration, based on morphological measurements on human SGN dendrites and a high resolution FE model of a human cochlea. Recent measurements indicated that intact human SGN dendrites possess a diameter of approximately 2.0 µm and that degeneration of SGNs may also manifest in a reduced diameter of approximately 0.5 µm (Heshmat et al., 2020). The cochlea FE model was based on µCT scans of a human cochlea and, therefore, generated a highly personalized model, including fine details of cochlear structures down to the porous structure of the modiolar bone (Bai et al., 2019). The cochlea model was implanted with a MED-EL Standard electrode array consisting of 12 electrode pairs and stimulated in a monopolar configuration with biphasic pulses. Potential distributions were obtained from the FE model and used as a stimulus for a large population of Hodgkin-Huxley-based biophysical multi-compartment neuron models adapted to represent human ANFs (Rattay et al., 2013), spread out along the entire cochlea. Primary simulation results consisted of detailed excitation profiles covering both cochlear length and electric dynamic range for all 12 electrodes of the implant.

Studies modeling retrograde degeneration of ANFs commonly modeled degeneration by removing either the entire dendrite or peripheral parts of it (Rattay et al., 2001, 2013; Briaire and Frijns, 2006; Smit et al., 2008, 2010; Snel-Bongers et al., 2013; Kalkman et al., 2014; Malherbe et al., 2015; Potrusil et al., 2020). This study included an "intermediate" degenerative state as well, a thin dendrite with only a 0.5 µm diameter, based on measurements from Heshmat et al. (2020). A shrinkage of dendrite diameter in the process of degeneration was also observed by Wise et al. (2017) in guinea pigs, though only manifesting in reduced diameter of the axoplasma, but not the surrounding myelin sheath. Differences between myelin

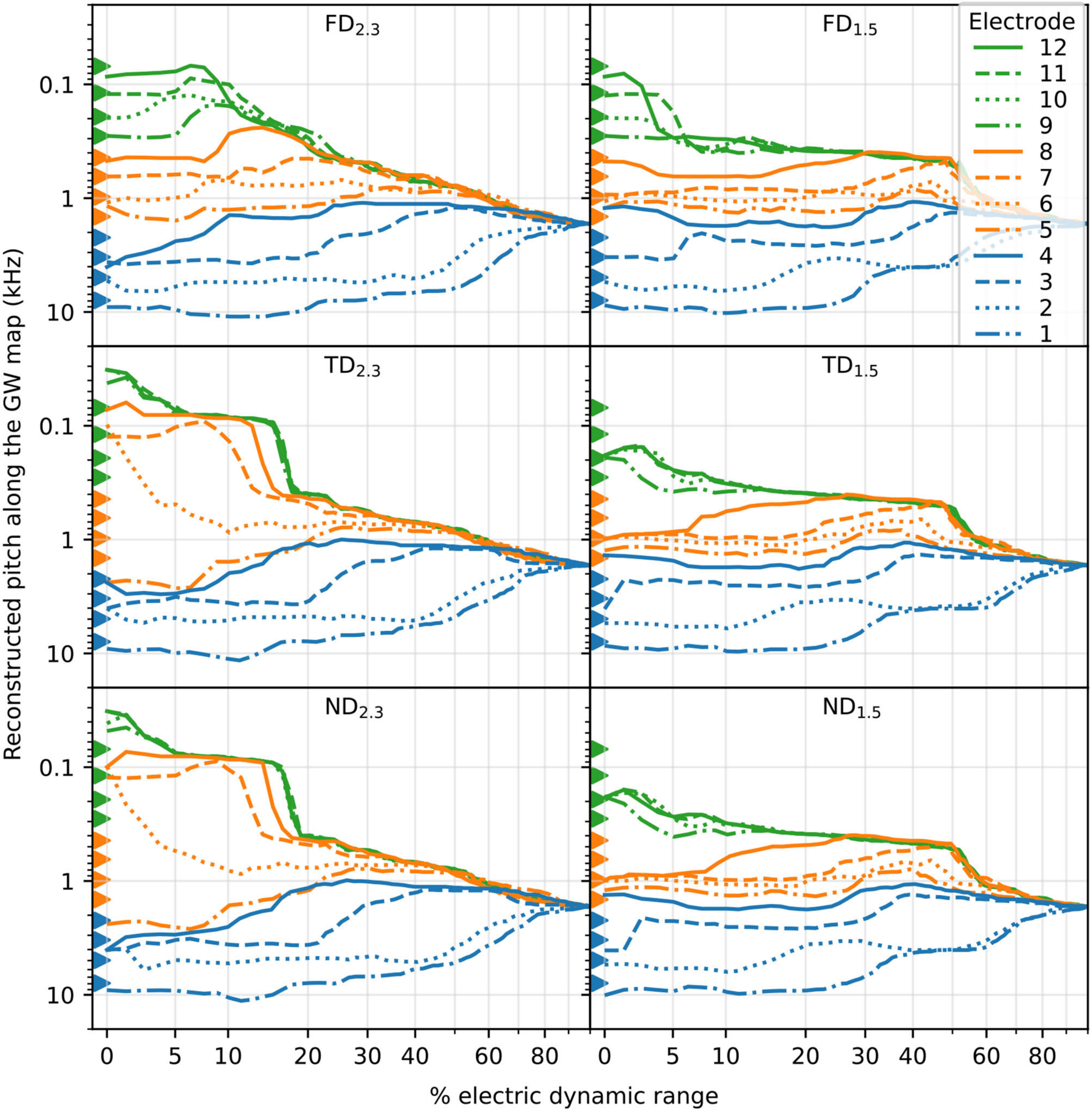

FIGURE 10 | The reconstructed pitch along % of EDR. Pitch reconstruction was based on the centroid of the excited area and the Greenwood map. Basal, middle, and apical electrode stimulations are marked by color, and individual electrodes are marked by line style. Electrode position, corresponding to the pitch of its nearest fiber, is marked with triangles.

sheath measurements may be due to examinations performed on different species, with Heshmat et al. measuring humans and Wise et al. measuring guinea pigs. Our study modeled axon and myelin sheath diameter according to Heshmat et al. (2020). In addition, we modeled homogeneous degeneration in the entire cochlea. This is likely not the case in real implanted cochleae, where there may be heterogeneous degeneration. For example, assuming that hearing loss correlates with degeneration of ANFs since age-related hearing loss generally is more pronounced in high frequencies (Brant and Fozard, 1990; Wiley et al., 2008), it could be concluded that basal ANFs are more likely to degenerate than apical ANFs, at least for most aged implanted subjects. Nevertheless, investigation of different degeneration patterns in the cochlea was beyond the scope of this study. Surprisingly,

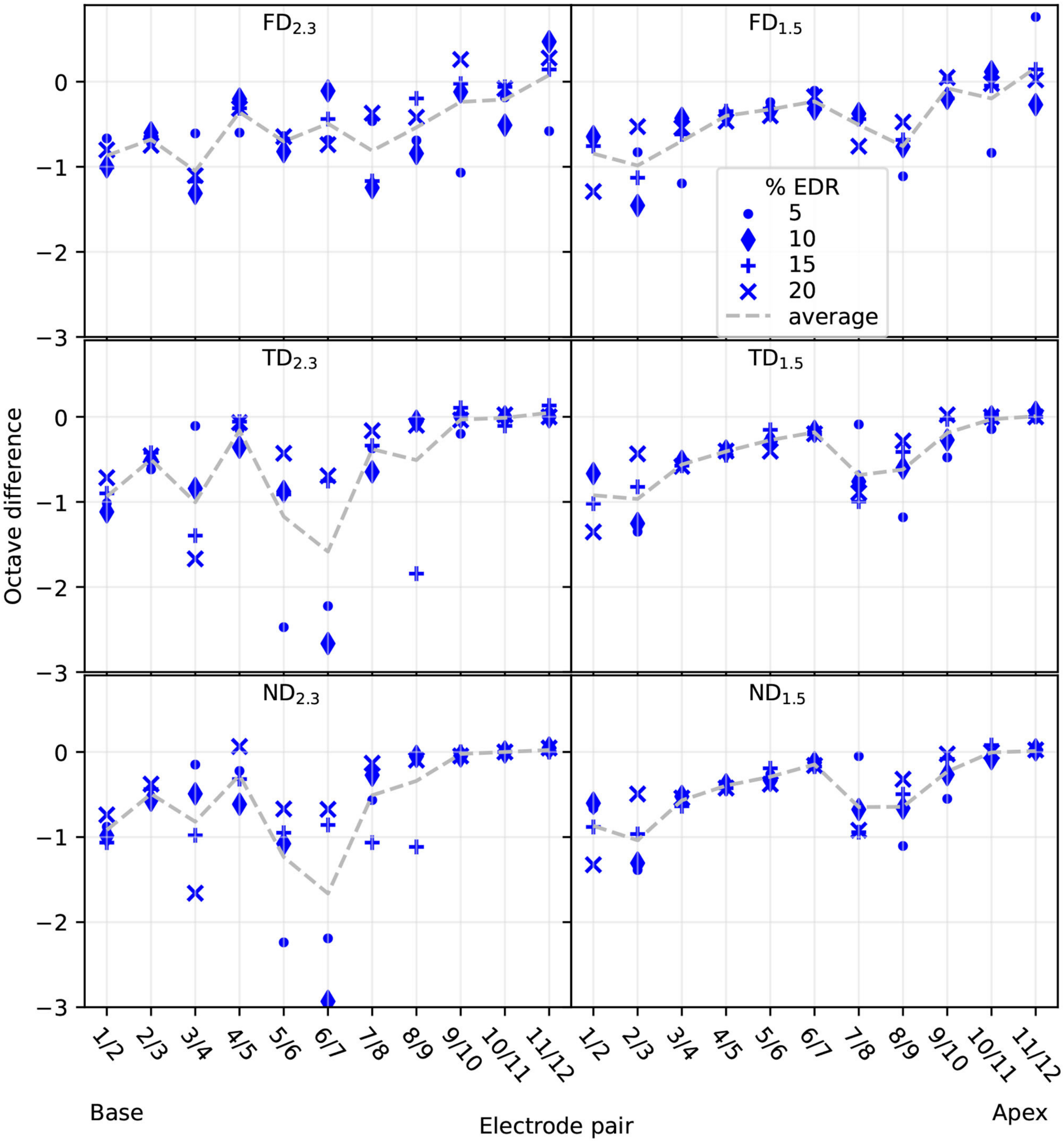

FIGURE 11 | Reconstructed pitch difference between neighboring electrodes. Differences displayed for 5, 10, 15, and 20% of EDR, as well as the average of the four differences. Electrode pair refers to which electrodes were used to compute the difference.

results were largely identical between thin dendrite and no dendrite states, especially in contrast to intact dendrite state, for all investigated parameters, including absolute and individual thresholds, excitation profiles, and reconstructed pitches. This may be attributed to the diameter of 0.5 μm being already very close to failing to be able to transmit APs through the soma when modeled as a deterministic model (<0.4 μm, Heshmat et al., 2020), leading to a largely "inactive" dendrite in terms of neuronal excitation. As the diameter of 0.5 μm was picked to represent one of two peaks in a quantity distribution, with the other peak being 2 μm, representing "intact" dendrites, simulating an additional diameter other than the two values would be arbitrary. Therefore, it may be concluded that simulation of ANF degeneration by only removal of dendrites is sufficiently accurate. An important constraint to this conclusion, however, is that other cochleae and stimulation configurations (i.e., monopolar vs. multipolar, alternate pulse shape) may show larger amounts of excitation in the distal part of the dendrite for TD than observed in our investigation, where we considered only monopolar biphasic stimulation. Therefore, multipolar stimulation might increase the difference between TD and ND, making the simulation of intermediate degenerative states necessary.

Absolute thresholds for individual electrodes were defined as the current necessary to excite at least a single ANF of a population. Intuitively, one would expect that with increasing degeneration absolute thresholds would increase as well, as the nearest part of an ANF to stimulating electrodes in lateral electrode arrays is generally the peripheral terminal (Stakhovskaya et al., 2007; Mistrík et al., 2017). Therefore, degeneration would increase the electrode-neuron distance, which is often attributed proportionality to the perceptual threshold (Pfingst and Xu, 2004; Goldwyn et al., 2010; Long et al., 2014; Bierer et al., 2015). In this study, however, not only an absolute threshold increase with degeneration was observed, but also an absolute threshold decrease. This appears counterintuitive only at first glance, however, when inspecting AP initiation sites, it could be observed that the absolute threshold was reduced with increased degeneration whenever fibers were initially excited proximal to the soma for FD. This could be explained using the intracellular resistance R_a of the dendrite: if the dendrite is reduced in diameter or removed, dendritic R_a is increased. More specifically, from FD to TD resistance would increase by a factor of 16 (approximately 1.6 MΩ for 10 μm length of dendrite with 2.0 μm diameter, and approximately 25.5 MΩ for 10 μm length of dendrite with 0.5 μm diameter), and for ND resistance would essentially increase to $\infty\,\Omega$ ($R_a = \frac{resisitivity \cdot length}{radius^2 \cdot \pi}$). Such an increase in dendritic intracellular resistance would lead to less or no outward current flow from the soma toward the dendrite, therefore facilitating the charging of cell membranes in the somatic area when compared to a neuron with a thicker dendrite. Therefore, whenever APs at the absolute threshold were initiated in or at the soma for FD, this effect would manifest in a reduction of the absolute threshold for TD and ND. Conversely, this did not apply in all cases, however. For absolute thresholds where APs originally initiated in the distal end of the dendrite, absolute thresholds tended to increase with degeneration. However, there were exceptions where thresholds would still decrease, e.g., electrode 11 as shown in **Figure 7**, where ectopic activation initiated at the soma for low currents already and compensated for threshold increase of ANFs near the electrode. Threshold differences between degenerated states TD and ND were small, with ND mostly displaying slightly higher absolute thresholds. This could be attributed to APs in ND being mostly initiated at the interface between soma and axon, which appears to be less "optimal" than AP initiation directly before the soma.

While excitation of ANFs in natural hearing originates from inner hair cells, and therefore, excites ANFs at their peripheral terminal, excitation of ANFs under CI stimulation has been shown to happen at several distinct sites along the fibers (Miller et al., 2003). Suggested initial excitation sites are peripheral terminal, dendrite, and axon in general (Rattay et al., 2001; Briaire and Frijns, 2006; Kalkman et al., 2014; Potrusil et al., 2020), as well as areas proximal to somata (Cartee, 2006; Cartee et al., 2006). In general, APs in our model were initiated at one of three "preferred" sites: the distal end of the dendrite, compartments directly peripheral to the soma, or the interface between soma and axon. Only for very large stimuli (>10 dB re absolute threshold) extended initiation in midst of the axon was observed, where stimulation may very well be above maximum loudness levels acceptable for CI subjects (dynamic ranges of patients with CI are on average at approximately 10 dB for low pulse rates Kreft et al., 2004; Zhou et al., 2012).

Our results showed AP initiation in the distal end of the dendrite happened only in areas near stimulation electrodes, and for the most part only in the apex and when dendrites were intact (FD), given that short dendrites hardly had any AP initiation in the distal end of dendrites for electrodes in the middle of the cochlea. Overall, initiations in the distal part of the dendrite and the axon were the minority, especially for degenerated dendrites (TD and ND). Therefore, most APs initiated in the somatic area, either directly before the soma (TD) or at the interface between soma and axon (ND). In terms of excitation profile shape, differences were the smallest between TD and ND. Except when TD was initiated in the distal end of the dendrite, the same currents generally excited the same neurons for both TD and ND. Initial excitation in the distal end of the dendrite for TD happened only in a minuscule number of neurons in the middle of the cochlea and in no case at the absolute threshold.

Ectopic stimulation, including cross-turn stimulation, is both seen in modeling studies (Frijns et al., 2001; Hanekom, 2001; Briaire and Frijns, 2006; Kalkman et al., 2014) and discussed or suspected in patient studies (Frijns et al., 2002; Arnoldner et al., 2008; Finley et al., 2008). Our results showed prominent ectopic activation in the excitation profiles, especially for degenerated dendrites and apical regions. Most importantly, for apical stimulation electrodes and degenerated dendrites, the same neuronal regions were excited preferentially, essentially independent of the stimulation electrode and likely generating an identical pitch perception. Ectopic activation manifested as both cross-turn activation (e.g., **Figure 7** electrode 5), and non-cross-turn activation, i.e., neurons activated at an offset position to the stimulation electrode, but not at a distance of an entire turn (e.g., **Figure 7** electrode 9). The existence of ectopic activation of less than 360° to the electrode position is less intuitive than cross-turn activation but has been mentioned in literature before, e.g., being suspected as the underlying cause for "tip-shifts" in forward masking spatial tuning curves with CI patients by Nelson et al. (2008). In summary, ectopic activation especially occurred for degenerated ANFs, mainly impacting stimulation in the apex. Stimulation in the base and middle of the cochlea showed less ectopic activation for degenerated dendrites than in the apex, assuming longer (2.3 mm) dendrites in the base and apex and shorter (1.5 mm) dendrites in the middle of the cochlea. This was likely due to most APs initiating near the soma with FD in the basal and middle turns. In contrast, with FD most activation in the apex happened at the peripheral terminal for ANFs near the stimulation electrodes, which was absent with degenerated neurons.

Excitation profiles give a good overview of the way the ANF population is excited, but given that the purpose of a CI is to elicit sound perception, such profiles are still abstract. In order to approximate the perception of the simulated results, stimulated neurons were mapped to place pitch using the centroid of the excited area (Laneau et al., 2004) and Greenwood's frequency map (Greenwood, 1990). Frequency mapping was performed for the entire EDR. However, not the entire EDR is relevant, but only the interval between perceptual threshold and maximum comfortable loudness of CI patients. Maximum comfortable loudness was arbitrarily estimated to correspond to 4 mm of neurons excited along together with the organ of Corti by Briaire and Frijns (2006). With an average Organ of Corti length of approximately 33 mm (Stakhovskaya et al., 2007), this would correspond to approximately 10% of fibers excited. For this reason, the reconstructed pitch was only inspected in detail for low percentages of EDR, up to approximately 20% of EDR. Results showed that for FD, individual stimulation electrodes generated individual pitches for low percentages of EDR, albeit less so for apical electrodes. With degenerated dendrites, however, pitches obtained for apical stimulation electrodes (especially electrode 9 upwards) were very similar, which essentially meant that different electrodes evoked the same pitch perception. With electrode 9 positioned at 450° insertion into the cochlea, it indicates that insertion of cochlear electrode arrays deeper than approximately 450° may not provide any benefit when ANFs are degenerated. A similar observation was drawn from the model of Kalkman et al. (2014), where electrodes beyond approximately 540° insertion stimulated nearly identical regions in the cochlea when ANFs were degenerated. Increased pitch confusion in the apex, i.e., the inability to correctly rank electrodes according to their pitch, was also observed in patient studies with deeply inserted electrodes (Deman et al., 2004; Gani et al., 2007; Landsberger et al., 2014). For example, Deman et al. observed that for CIs with electrode insertion depth between 471 and 662° about half of their subjects had similar pitch percepts for apical stimulation electrodes in pitch ranking experiments. Consequently, based on our results that degenerated ANFs lead to highly similar pitches in the apex, increased pitch confusion for deeply inserted apical electrodes could be an indicator of the neural health of apical neurons. In addition to similar reconstructed pitches for apical electrodes, our results showed pitch reversals in some cases. Pitch reversals are defined as pitch elicited from a more apically located electrode being perceived as higher than pitch elicited from a more basally located electrode, despite more apical positions corresponding to lower frequencies on the tonotopic map of the cochlea. Pitch reversals have been occasionally observed in psychophysical experiments as well, e.g., Fielden et al. (2015).

In conclusion, "intermediate" degenerative states of ANF dendrites in our model generally showed very similar effects to completely degenerated ANF dendrites. The largest impact of degeneration is expected in the apex, where different electrodes stimulate the same neurons for degenerated ANFs. Therefore, a deep insertion of electrode arrays into the cochlea may not provide any benefits for patients with degenerated ANFs. However, the impact of degeneration for electrodes up to approximately 450° insertion angle may be small. Nevertheless, it is important to note that this observation is based on monopolar biphasic stimulation of a single human cochlea. Multipolar stimulation is expected to be more heavily impacted by neural degeneration (Goldwyn et al., 2010; Zhu et al., 2012; Long et al., 2014; George et al., 2015; Heshmat et al., 2021), and different pulse-shapes are believed to preferentially stimulate different parts of an ANF (Rattay et al., 2001), which may increase the impact of degeneration and induce more differences between TD and ND. In addition, given that performance of patients with CI often varies between individuals, we can not make any judgment on how well the subject on whose temporal bone our cochlea model was based would have performed with a CI. However, we are currently working on building an extended set of FE models based on additional high-definition scans of human temporal bones. Therefore, the current investigation into specific SGN morphologies presents a starting point for highly personalized models which take into consideration the influence of fine details of cochlear structures. This will be expanded in future studies building on the current work, including not only additional cochleae but also investigations into further stimulation configurations and SGN morphologies. Therefore, using a larger number of high resolution cochlea models, we will investigate possible diagnostic methods for neural health in CI subjects, and whether the impact of degeneration on CI stimulation can be estimated based on preoperative measurements (e.g., cochlea shape from CT scans), possibly aiding in the selection of CI electrode design and insertion depth.

DATA AVAILABILITY STATEMENT

The datasets presented in this study can be found in online repositories. The names of the repository/repositories and accession number(s) can be found below: https://gin.g-node.org/Croner/dendritic_sgn_degeneration.

AUTHOR CONTRIBUTIONS

AC conducted the simulations and contributed to study design, ANF cable model implementation, data analysis, visualization, and manuscript writing. AH contributed to study design, SGN morphology measurements, and manuscript revision. AS-F contributed to study design, SGN morphology measurements, funding acquisition, and supervision. RG contributed to SGN morphology measurements and manuscript revision. WH contributed to study design, data analysis, manuscript revision, funding acquisition, and supervision. SB contributed to study design, FE model reconstruction, ANF path reconstruction, manuscript revision, and supervision. All authors contributed to the article and approved the submitted version.

FUNDING

This project was funded by the Deutsche Forschungsgemeinschaft (DFG, German Research

Foundation)–Projektnummer 415658392, the Austrian Science Fund (FWF) Grant No. l4147-B, and within the project "Modeling the electrical stimulation of the human cochlear nerve based on segmented high-resolution micro-computer tomography scans" under the D-A-CH program.

ACKNOWLEDGMENTS

The authors would like to thank Dr. Frank Böhnke for providing the original μCT scans of the cadaveric temporal bone, Dr. Jörg Encke for his contribution to the ANF path reconstruction algorithms, and Carmen Castañeda Gonzales for her helpful comments on the manuscript.

SUPPLEMENTARY MATERIAL

The Supplementary Material for this article can be found online at: https://www.frontiersin.org/articles/10.3389/fnins.2022.914876/full#supplementary-material

REFERENCES

Arnesen, A. R., and Osen, K. K. (1978). The cochlear nerve in the cat: topography, cochleotopy, and fiber spectrum. *J. Compar. Neurol.* 178, 661–678. doi: 10.1002/cne.901780405

Arnoldner, C., Riss, D., Kaider, A., Mair, A., Wagenblast, J., Baumgartner, W.-D., et al. (2008). The intensity-pitch relation revisited: monopolar versus bipolar cochlear stimulation. *Laryngoscope* 118, 1630–1636. doi: 10.1097/MLG.0b013e3181799715

Bai, S., Encke, J., Obando-Leitón, M., Weiβ, R., Schäfer, F., Eberharter, J., et al. (2019). Electrical stimulation in the human cochlea: a computational study based on high-resolution micro-ct scans. *Front. Neurosci.* 13, 1312. doi: 10.3389/fnins.2019.01312

Bichler, E., Spoendlin, H., and Rauchegger, H. (1983). Degeneration of cochlear neurons after amikacin intoxication in the rat. *Arch. Otorhinolaryngol.* 237, 201–208. doi: 10.1007/BF00453725

Bierer, J. A., Deeks, J. M., Billig, A. J., and Carlyon, R. P. (2015). Comparison of signal and gap-detection thresholds for focused and broad cochlear implant electrode configurations. *J. Assoc. Res. Otolaryngol.* 16, 273–284. doi: 10.1007/s10162-015-0507-y

Blamey, P., Arndt, P., Bergeron, F., Bredberg, G., Brimacombe, J., Facer, G., et al. (1996). Factors affecting auditory performance of postlinguistically deaf adults using cochlear implants. *Audiol. Neurootol.* 1, 293–306. doi: 10.1159/000259212

Brant, L. J., and Fozard, J. L. (1990). Age changes in pure-tone hearing thresholds in a longitudinal study of normal human aging. *J. Acoust. Soc. Am.* 88, 813–820. doi: 10.1121/1.399731

Briaire, J., and Frijns, J. (2006). The consequences of neural degeneration regarding optimal cochlear implant position in scala tympani: a model approach. *Hear. Res.* 214, 17–27. doi: 10.1016/j.heares.2006.01.015

Cartee, L. A. (2006). Spiral ganglion cell site of excitation II: numerical model analysis. *Hear. Res.* 215, 22–30. doi: 10.1016/j.heares.2006.02.011

Cartee, L. A., Miller, C. A., and van den Honert, C. (2006). Spiral ganglion cell site of excitation I: comparison of scala tympani and intrameatal electrode responses. *Hear. Res.* 215, 10–21. doi: 10.1016/j.heares.2006.02.012

Croghan, N. B. H., Duran, S. I., and Smith, Z. M. (2017). Re-examining the relationship between number of cochlear implant channels and maximal speech intelligibility. *J. Acoust. Soc. of Am.* 142, EL537–EL543. doi: 10.1121/1.5016044

Deman, P. R., van Dijk, B., Offeciers, F.-E., and Govaerts, P. J. (2004). Pitch estimation of a deeply inserted cochlear implant electrode. *Int. J. Audiol.* 43, 363–368. doi: 10.1080/14992020400050046

Fielden, C. A., Kluk, K., Boyle, P. J., and McKay, C. M. (2015). The perception of complex pitch in cochlear implants: a comparison of monopolar and tripolar stimulation. *J. Acoust. Soc. Am.* 138, 2524–2536. doi: 10.1121/1.4931910

Finley, C., Wilson, B., and White, M. (1990). "Models of neural responsiveness to electrical stimulation," in *Cochlear Implants*, eds J. M. Miller and F. A. Spelman (New York, NY: Springer).

Finley, C. C., Holden, T. A., Holden, L. K., Whiting, B. R., Chole, R. A., Neely, G. J., et al. (2008). Role of electrode placement as a contributor to variability in cochlear implant outcomes. *Otol. Neurotol.* 29, 920–928. doi: 10.1097/MAO.0b013e318184f492

Frijns, J. H., Briaire, J. J., and Grote, J. J. (2001). The importance of human cochlear anatomy for the results of modiolus-hugging multichannel cochlear implants. *Otol. Neurotol.* 22, 340–349. doi: 10.1097/00129492-200105000-00012

Frijns, J. H. M., Briaire, J. J., de Laat, J. A. P. M., and Grote, J. J. (2002). Initial evaluation of the Clarion CII cochlear implant: speech perception and neural response imaging. *Ear. Hear.* 23, 184–197. doi: 10.1097/00003446-200206000-00003

Gani, M., Valentini, G., Sigrist, A., Kós, M.-I., and Boëx, C. (2007). Implications of deep electrode insertion on cochlear implant fitting. *J. Assoc. Res. Otolaryngol.* 8, 69–83. doi: 10.1007/s10162-006-0065-4

George, S. S., Wise, A. K., Fallon, J. B., and Shepherd, R. K. (2015). Evaluation of focused multipolar stimulation for cochlear implants in long-term deafened cats. *J. Neural Eng.* 12, 036003. doi: 10.1088/1741-2560/12/3/036003

Glueckert, R., Pfaller, K., Kinnefors, A., Rask-Andersen, H., and Schrott-Fischer, A. (2005). The human spiral ganglion: New insights into ultrastructure, survival rate and implications for cochlear implants. *Audiol. Neurotol.* 10, 258–273. doi: 10.1159/000086000

Goldwyn, J. H., Bierer, S. M., and Bierer, J. A. (2010). Modeling the electrode-neuron interface of cochlear implants: effects of neural survival, electrode placement, and the partial tripolar configuration. *Hear. Res.* 268, 93–104. doi: 10.1016/j.heares.2010.05.005

Goodman, D. F. M., and Brette, R. (2009). The brian simulator. *Front. Neurosci.* 3, 2009. doi: 10.3389/neuro.01.026.2009

Greenwood, D. D. (1990). A cochlear frequency–position function for several species—29 years later. *J. Acoust. Soc. Am.* 87, 2592–2605. doi: 10.1121/1.399052

Hanekom, T. (2001). Three-dimensional spiraling finite element model of the electrically stimulated cochlea. *Ear. Hear.* 22, 300–315. doi: 10.1097/00003446-200108000-00005

Heshmat, A., Sajedi, S., Johnson Chacko, L., Fischer, N., Schrott-Fischer, A., and Rattay, F. (2020). Dendritic degeneration of human auditory nerve fibers and its impact on the spiking pattern under regular conditions and during cochlear implant stimulation. *Front. Neurosci.* 14, 1182. doi: 10.3389/fnins.2020.599868

Heshmat, A., Sajedi, S., Schrott-Fischer, A., and Rattay, F. (2021). Polarity sensitivity of human auditory nerve fibers based on pulse shape, cochlear implant stimulation strategy and array. *Front. Neurosci.* 15, 751599. doi: 10.3389/fnins.2021.751599

Holden, L. K., Finley, C. C., Firszt, J. B., Holden, T. A., Brenner, C., Potts, L. G., et al. (2013). Factors affecting open-set word recognition in adults with cochlear implants. *Ear. Hear.* 34, 342–360. doi: 10.1097/AUD.0b013e3182741aa7

Kalkman, R. K., Briaire, J. J., Dekker, D. M. T., and Frijns, J. H. M. (2014). Place pitch versus electrode location in a realistic computational model of the implanted human cochlea. *Hear. Res.* 315, 10–24. doi: 10.1016/j.heares.2014.06.003

Kreft, H. A., Donaldson, G. S., and Nelson, D. A. (2004). Effects of pulse rate on threshold and dynamic range in Clarion cochlear-implant users (L). *J. Acoust. Soc. Am.* 115, 1885–1888. doi: 10.1121/1.1701895

Landsberger, D. M., Mertens, G., Punte, A. K., and Van De Heyning, P. (2014). Perceptual changes in place of stimulation with long cochlear implant electrode arrays. *J. Acoust. Soc. Am.* 135, EL75–EL81. doi: 10.1121/1.4862875

Laneau, J., Wouters, J., and Moonen, M. (2004). Relative contributions of temporal and place pitch cues to fundamental frequency discrimination in cochlear implantees. *J. Acoust. Soc. Am.* 116, 3606–3619. doi: 10.1121/1.1823311

Linthicum, F., and Fayad, J. (2009). Spiral ganglion cell loss is unrelated to segmental cochlear sensory system degeneration in humans. *Otol. Neurotol.* 30, 418–422. doi: 10.1097/MAO.0b013e31819a8827

Loizou, P. (1999). Introduction to cochlear implants. *IEEE Eng. Med. Biol. Mag*. 18, 32–42. doi: 10.1109/51.740962

Long, C. J., Holden, T. A., McClelland, G. H., Parkinson, W. S., Shelton, C., Kelsall, D. C., et al. (2014). Examining the electro-neural interface of cochlear implant users using psychophysics, CT scans, and speech understanding. *J. Assoc. Res. Otolaryngol*. 15, 293–304. doi: 10.1007/s10162-013-0437-5

Malherbe, T. K., Hanekom, T., and Hanekom, J. J. (2015). The effect of the resistive properties of bone on neural excitation and electric fields in cochlear implant models. *Hear. Res*. 327, 126–135. doi: 10.1016/j.heares.2015.06.003

Malherbe, T. K., Hanekom, T., and Hanekom, J. J. (2016). Constructing a three-dimensional electrical model of a living cochlear implant user's cochlea. *Int. J. Numer. Method Biomed. Eng*. 32, 2751. doi: 10.1002/cnm.2751

Miller, C. A., Abbas, P. J., Nourski, K. V., Hu, N., and Robinson, B. K. (2003). Electrode configuration influences action potential initiation site and ensemble stochastic response properties. *Hear. Res*. 175, 200–214. doi: 10.1016/S0378-5955(02)00739-6

Mistrík, P., Jolly, C., Sieber, D., and Hochmair, I. (2017). Challenging aspects of contemporary cochlear implant electrode array design. *World J. Otorhinolaryngol. Head Neck Surg*. 03, 192–199. doi: 10.1016/j.wjorl.2017.12.007

Nadol, J. B. (1990). Degeneration of cochlear neurons as seen in the spiral ganglion of man. *Hear. Res*. 49, 141–154. doi: 10.1016/0378-5955(90)90101-T

Nadol, J. B., Burgess, B. J., and Reisser, C. (1990). Morphometric analysis of normal human spiral ganglion cells. *Ann. Otol. Rhinol. Laryngol*. 99, 340–348. doi: 10.1177/000348949009900505

Nelson, D. A., Donaldson, G. S., and Kreft, H. (2008). Forward-masked spatial tuning curves in cochlear implant users. *J. Acoust. Soc. Am*. 123, 1522–1543. doi: 10.1121/1.2836786

Nogueira, W., Schurzig, D., Büchner, A., Penninger, R. T., and Würfel, W. (2016). Validation of a cochlear implant patient-specific model of the voltage distribution in a clinical setting. *Front. Bioeng. Biotechnol*. 4, 84. doi: 10.3389/fbioe.2016.00084

O'Connell, B. P., Cakir, A., Hunter, J. B., Francis, D. O., Noble, J. H., Labadie, R. F., et al. (2016). Electrode location and angular insertion depth are predictors of audiologic outcomes in cochlear implantation. *Otol. Neurotol*. 37, 1016–1023. doi: 10.1097/MAO.0000000000001125

Pfingst, B. E., and Xu, L. (2004). Across-site variation in detection thresholds and maximum comfortable loudness levels for cochlear implants. *J. Assoc. Res. Otolaryngol*. 5, 11–24. doi: 10.1007/s10162-003-3051-0

Potrusil, T., Heshmat, A., Sajedi, S., Wenger, C., Johnson Chacko, L., Glueckert, R., et al. (2020). Finite element analysis and three-dimensional reconstruction of tonotopically aligned human auditory fiber pathways: a computational environment for modeling electrical stimulation by a cochlear implant based on micro-ct. *Hear. Res*. 393, 108001. doi: 10.1016/j.heares.2020.108001

Rask-Andersen, H., Liu, W., and Linthicum, F. (2010). Ganglion cell and 'dendrite' populations in electric acoustic stimulation ears. *Adv. Otorhinolaryngol*. 67, 14–27. doi: 10.1159/000262593

Rattay, F., Lutter, P., and Felix, H. (2001). A model of the electrically excited human cochlear neuron i. contribution of neural substructures to the generation and propagation of spikes. *Hear. Res*. 153, 43–63. doi: 10.1016/S0378-5955(00)00256-2

Rattay, F., Potrusil, T., Wenger, C., Wise, A. K., Glueckert, R., and Schrott-Fischer, A. (2013). Impact of morphometry, myelinization and synaptic current strength on spike conduction in human and cat spiral ganglion neurons. *PLoS ONE* 8, e79256. doi: 10.1371/journal.pone.0079256

Risi, F. (2018). Considerations and rationale for cochlear implant electrode design - past, present and future. *J. Int. Adv. Otol*. 14, 382–391. doi: 10.5152/iao.2018.6372

Rudnicki, M. (2022). *Thorns*. Available online at: https://github.com/mrkrd/thorns (accessed March 25, 2022).

Smit, J. E., Hanekom, T., and Hanekom, J. J. (2008). Predicting action potential characteristics of human auditory nerve fibres through modification of the Hodgkin-Huxley equations : research article. *South Afr. J. Sci*. 104, 284–292. doi: 10.10520/EJC96819

Smit, J. E., Hanekom, T., van Wieringen, A., Wouters, J., and Hanekom, J. J. (2010). Threshold predictions of different pulse shapes using a human auditory nerve fibre model containing persistent sodium and slow potassium currents. *Hear. Res*. 269, 12–22. doi: 10.1016/j.heares.2010.08.004

Snel-Bongers, J., Briaire, J. J., van der Veen, E. H., Kalkman, R. K., and Frijns, J. H. M. (2013). Threshold levels of dual electrode stimulation in cochlear implants. *J. Assoc. Res. Otolaryngol*. 14, 781–790. doi: 10.1007/s10162-013-0395-y

Spoendlin, H. (1984). Factors inducing retrograde degeneration of the cochlear nerve. *Ann. Otol. Rhinol. Laryngol*. 93(4_suppl), 76–82. doi: 10.1177/00034894840930S415

Stakhovskaya, O., Sridhar, D., Bonham, B. H., and Leake, P. A. (2007). Frequency map for the human cochlear spiral ganglion: implications for cochlear implants. *J. Assoc. Res. Otolaryngol*. 8, 220–233. doi: 10.1007/s10162-007-0076-9

von Békésy, G. (1960). *Experiments in Hearing*. New York, NY: McGraw-Hill.

Wardrop, P., Whinney, D., Rebscher, S. J., Roland, J. T., Luxford, W., and Leake, P. A. (2005). A temporal bone study of insertion trauma and intracochlear position of cochlear implant electrodes. I: comparison of nucleus banded and nucleus contour$^{\mathrm{TM}}$electrodes. *Hear. Res*. 203, 54–67. doi: 10.1016/j.heares.2004.11.006

Wiley, T. L., Chappell, R., Carmichael, L., Nondahl, D. M., and Cruickshanks, K. J. (2008). Changes in hearing thresholds over 10 years in older adults. *J. Am. Acad. Audiol*. 19, 281–292; quiz 371. doi: 10.3766/jaaa.19.4.2

Wilson, B. S. (2008). Cochlear implants: current designs and future possibilities. *J. Rehabil. Res. Dev*. 45, 695–730. doi: 10.1682/JRRD.2007.10.0173

Wise, A. K., Pujol, R., Landry, T. G., Fallon, J. B., and Shepherd, R. K. (2017). Structural and ultrastructural changes to Type I spiral ganglion neurons and schwann cells in the deafened guinea pig cochlea. *J. Assoc. Res. Otolaryngol*. 18, 751–769. doi: 10.1007/s10162-017-0631-y

Zhou, N., Xu, L., and Pfingst, B. E. (2012). Characteristics of detection thresholds and maximum comfortable loudness levels as a function of pulse rate in human cochlear implant users. *Hear Res*. 284, 25–32. doi: 10.1016/j.heares.2011.12.008

Zhu, Z., Tang, Q., Zeng, F.-G., Guan, T., and Ye, D. (2012). Cochlear implant spatial selectivity with monopolar, bipolar and tripolar stimulation. *Hear. Res*. 283, 45–58. doi: 10.1016/j.heares.2011.11.005

Conflict of Interest: The authors declare that the research was conducted in the absence of any commercial or financial relationships that could be construed as a potential conflict of interest.

frontiers | Frontiers in Neuroscience

ORIGINAL RESEARCH
published: 08 July 2022
doi: 10.3389/fnins.2022.909602

A Co-driven Functional Electrical Stimulation Control Strategy by Dynamic Surface Electromyography and Joint Angle

Rui Xu[1,2], Xinyu Zhao[1], Ziyao Wang[1], Hengyu Zhang[1], Lin Meng[1]* and Dong Ming[1,2]*

[1] Laboratory of Motor Rehabilitation, Academy of Medical Engineering and Translational Medicine, Tianjin University, Tianjin, China, [2] College of Precision Instruments and Optoelectronics Engineering, Tianjin University, Tianjin, China

Edited by:
Liming Li,
Shanghai Jiao Tong University, China

Reviewed by:
Yanjuan Geng,
Shenzhen Institutes of Advanced Technology (CAS), China
Toshihiro Kawase,
Tokyo Denki University, Japan

***Correspondence:**
Lin Meng
linmeng@tju.edu.cn
Dong Ming
richardming@tju.edu.cn

Specialty section:
This article was submitted to
Neural Technology,
a section of the journal
Frontiers in Neuroscience

Received: 31 March 2022
Accepted: 13 June 2022
Published: 08 July 2022

Citation:
Xu R, Zhao X, Wang Z, Zhang H, Meng L and Ming D (2022) A Co-driven Functional Electrical Stimulation Control Strategy by Dynamic Surface Electromyography and Joint Angle. Front. Neurosci. 16:909602. doi: 10.3389/fnins.2022.909602

Functional electrical stimulation (FES) is widely used in neurorehabilitation to improve patients' motion ability. It has been verified to promote neural remodeling and relearning, during which FES has to produce an accurate movement to obtain a good efficacy. Therefore, many studies have focused on the relationship between FES parameters and the generated movements. However, most of the relationships have been established in static contractions, which leads to an unsatisfactory result when applied to dynamic conditions. Therefore, this study proposed a FES control strategy based on the surface electromyography (sEMG) and kinematic information during dynamic contractions. The pulse width (PW) of FES was determined by a direct transfer function (DTF) with sEMG features and joint angles as the input. The DTF was established by combing the polynomial transfer functions of sEMG and joint torque and the polynomial transfer functions of joint torque and FES. Moreover, the PW of two FES channels was set based on the muscle synergy ratio obtained through sEMG. A total of six healthy right-handed subjects were recruited in this experiment to verify the validity of the strategy. The PW of FES applied to the left arm was evaluated based on the sEMG of the right extensor carpi radialis (ECR) and the right wrist angle. The coefficient of determination (R^2) and the normalized root mean square error (NRMSE) of FES-included and voluntary wrist angles and torques were used to verify the performance of the strategy. The result showed that this study achieved a high accuracy ($R^2 = 0.965$ and NRMSE $= 0.047$) of joint angle and a good accuracy ($R^2 = 0.701$ and NRMSE $= 0.241$) of joint torque reproduction during dynamic movements. Moreover, the DTF in real-time FES system also had a nice performance of joint angle fitting ($R^2 = 0.940$ and NRMSE $= 0.071$) and joint torque fitting ($R^2 = 0.607$ and NRMSE $= 0.303$). It is concluded that the proposed strategy is able to generate proper FES parameters based on sEMG and kinematic information for dynamic movement reproduction and can be used in a real-time FES system combined with bilateral movements for better rehabilitation.

Keywords: surface electromyography, functional electrical stimulation, joint torque control, polynomial fitting, kinematics

INTRODUCTION

Functional electrical stimulation (FES) is widely used in neurorehabilitation such as the rehabilitation of spinal cord injury and stroke (Glanz et al., 1996). It applies an electric current to one or more muscles to stimulate its peripheral motor nerves, producing muscle contractions and prompting the limbs to complete corresponding functional motions (Lynch and Popovic, 2008). FES has been proven to be effective in improving upper extremity motor abilities in patients with stroke (Glanz et al., 1996; Chan et al., 2009; Knutson et al., 2016) and has been combined with rehabilitation robots and rehabilitation training games (Hodkin et al., 2018; Fu et al., 2020), as it promotes neural remodeling and relearning in the patients with nerve damage (Quandt and Hummel, 2014). At present, most practical applications of FES use preset parameters to stimulate muscles, i.e., a specific waveform, intensity, and frequency according to a predetermined procedure (Lynch and Popovic, 2008). Although the triggered FES can better promote nerve remodeling and improve the treatment effect due to the combination of the user's active intention (Kimberley et al., 2004; Barsi et al., 2008), more biomimetic FES strategies may better facilitate the relearning process.

Functional electrical stimulation combined with bilateral movement (FES-BM) is one of the FES training methods that allows patients to actively participate. It allows the patients with hemiplegia to use the healthy side to control FES of the paralyzed side, and it can control not only the triggering but also the intensity of FES (Knutson et al., 2007). It was reported that FES-BM can better restore the motor function of the patient's upper limbs than cyclic FES (Chan et al., 2009; Knutson et al., 2014, 2016) due to FES-BM combines FES and the bilateral symmetrical movement which has been proven to improve the patient's motor function better than unilateral exercise training (Summers et al., 2004). This may be due to upper limbs are centrally linked as a coordinative structure unit (Bernstein, 1966) and mirror-symmetrical movements are the classic coordination modes in the human repertoire (Kelso, 1995).

Building an accurate mapping relationship from voluntary movement intention to FES can make the stimulated movement of patient's affected limb more precise (Zhou et al., 2020) and improve the recovery (Schick et al., 2017). Kinematic information (Knutson et al., 2007; Ruiz-Olaya et al., 2019; Malesevic et al., 2021) has been used as the feedback for FES control in some studies. For example, Knutson et al. (2007) adjusted the amplitude of FES proportionally according to the bending angle of the finger. However, kinematic information cannot reflect the patient's movement intention well when there are external forces such as grasping objects with different strengths. Thus, the control based on muscle force is considered superior to the control based on kinematic information.

Therefore, many efforts have been made to establish the relationship between surface electromyography (sEMG) signals and FES to generate the desired muscle force. Zhou et al. (2016) used the wrist torque during isometric contraction as an intermediate variable to the transformation from sEMG to the pulse width (PW) and frequency of FES for flexor carpi radialis (FCR) or extensor carpi ulnaris (ECU). They also used static force during grasp as an intermediate variable to determine the transfer relationship between sEMG features and FES parameters for flexor digitorum superficialis (FDS) (Zhou et al., 2020). In these studies, force generated during static isometric contraction was used as the intermediate variables due to that the sEMG–force relationship was easily affected by joint motion. However, the actual FES control was executed during dynamic tasks. The sEMG–FES parameter relationship obtained during static contractions was different from that in dynamic contractions. Therefore, to improve FES control for dynamic tasks, it is necessary to establish the sEMG–FES parameter relationship during dynamic tasks.

Joint torque is a dynamic information that can reflect motion intentions and forces (Huang et al., 2020). Joint torques calculated based on optical motion capture devices are considered to be the most accurate, but it is impossible to use optical capture devices in practical application. Therefore, some studies estimated joint torque through the musculoskeletal model (Hou et al., 2016; Chen et al., 2017). However, the musculoskeletal model contains many physiological parameters that are difficult to measure. Huang et al. (2020) estimated joint torque from sEMG and joint angle based on backpropagation neural networks and found that joint angles also played a role in the estimation process. It proved that joint angle, as an index to describe joint motion, can improve the accuracy of prediction of joint torque based on sEMG. Therefore, combining kinematic information and sEMG can better realize dynamic movement estimation. It may also be applicable to the estimation of FES parameters.

On the other hand, at present, most practical FES applications only stimulate one muscle (Xiao et al., 2018; Zhou et al., 2020), which is inconsistent with the neural strategies of human motor control, that humans recruit multiple muscles rather than a single muscle when performing movements. It has been largely suggested that our central nervous system (CNS) recruits a group of muscles in a fixed pattern to reduce the dimension of information processing, which is defined as muscle synergies (Bernstein, 1966; d'Avella et al., 2003; Ison and Artemiadis, 2014). Stimulating a group of muscles in this fixed pattern can mimic this physiological property. Additionally, biomimetic multi-channel FES systems have been proved to be beneficial for recovery (Ambrosini et al., 2011; Ferrante et al., 2016), and they could reduce muscle fatigue compared with single-channel FES (Happak et al., 1989; Wang et al., 2021). Moreover, it was found that the multi-channel FES could improve muscle coordination for patients (Ferrante et al., 2016; Niu et al., 2019).

The aim of this study was to develop a dynamic multi-channel mapping strategy from voluntary sEMG and joint motion to FES parameters. This strategy was used to achieve high symmetrical movements of bilateral hands. Compared with the previous studies, this strategy achieved a dynamic prediction during movement instead of during static contractions. To dynamically reproduce the target joint torque, the joint angle and mean absolute value (MAV) of sEMG were used to modulate the PW of FES through a proposed direct transfer function (DTF). This strategy was also applied to a real-time FES system to verify its online accuracy. We hypothesized that this strategy would improve the accuracy of FES-induced movement.

MATERIALS AND METHODS

Subjects

A total of six healthy right-handed subjects (4 men and 2 women; aged: 21–25; referenced as S1–S6) were selected and invited to participate in the experiment. Any participant with a history of wrist injuries and wrist extension elicited by FES with pain was excluded from the study. All the subjects gave their written informed consent before the experiment. The study was approved by the Ethics Committee of Tianjin University.

Experiment

Preliminary Experiment

Before the formal experiment, there were two preliminary experiments for each subject. The first one was performed to calculate the muscle synergy of each subject. The subjects were asked to sat naturally in the chair with their upper arms putting on the table in front of them. Then, two wireless sEMG sensors (Trigno^{TM} Avanti Platform, DELSYS, United States), sampled at 2000 Hz, were placed in the direction of the muscle fibers of ECU and extensor carpi radialis (ECR) of right hand. Then, they were asked to keep wrist extension for 20 s and the sEMG data were recorded. The muscle synergy matrix W was calculated to set the ratio of each FES channel for each subject, which was described in section "Surface Electromyography Processing."

The second preliminary experiment was performed to measure the threshold of the FES PW for each subject. The FES device was the RehaStim2 (HASOMED GmbH, Magdeburg, Germany) and the pulse can be controlled through the ScienceMode2 communication protocol (Kuberski, 2012). The value of PW of multi-channel FES was set based on muscle synergy. Then, two pairs of stimulating electrodes (3 cm × 3 cm) were placed on the muscle belly of ECU and ECR of left arm. The proportion of PW of each channel was based on the proportion of muscle synergy matrix W for each subject. The stimulation pulse waveform used for FES was a biphasic square-wave waveform with the amplitude of 15 mA and the frequency of 40 Hz for 2 s. The lower threshold of the PW, PW_{min}, was determined by increasing the PW from 10 μs (frequency = 40 Hz, amplitude = 15 mA) with 10-μs increments until the subject's wrist moved. The upper threshold of the PW, PW_{max}, was determined by increasing the PW from 10 μs (frequency = 40 Hz, amplitude = 15 mA) with 10-μs increments until the subject had pain. The thresholds of PW of ECR and the ratio between PW of ECR and ECU for each subject are shown in **Table 1**.

TABLE 1 | The thresholds of PW and the ratio between PW of ECR and ECU for subjects.

Subject	Frequency = 40 Hz, amplitude = 15 mA		Ratio
	PW_{min} (μs)	PW_{max} (μs)	
S1	120	290	0.698
S2	120	250	0.679
S3	170	270	0.815
S4	120	260	0.918
S5	150	300	0.779
S6	160	300	0.642

Formal Experiment

In the formal experiment, there were three parts for each subject. A total of five reflective spherical markers were attached on bilateral hands and arms of each participant. The position of markers is shown in **Figure 1**. Kinematic data of the wrist movements were obtained simultaneously with EMG acquisition system from Vicon optical motion capture system (VICON VERO, OML (Oxford Metrics Limited), United Kingdom), sampled at 100 Hz. The marker data were filtered using a fourth-order Butterworth low-pass filter with the cutoff frequency of 10 Hz. Subjects sat comfortably in the chair and put both arms on the table in front of them. The first one was performed to build the transfer functions to map sEMG and joint torque. In this part, only one sEMG sensor was placed in the direction of the muscle fibers of ECR of right hand. The sEMG from ECR was widely used to estimate the motion intention of wrist (Khokhar et al., 2010; Song et al., 2013). They were asked to perform seven sessions of wrist extension using their right hand at random speed (the wrist extension time was fixed to 2 s) with sEMG from ECR and kinematic data were recorded simultaneously. Each session included five trails of wrist extension, and there was 1-min rest between each session. Each subject performed 35 trails of wrist extension movements in total. The first six sessions of data were used to establish the transfer function mapping the joint angle and MAV to the joint torque. The inputs of the transfer function were the MAV and the joint angle and the output was the joint torque, which was described in section "Polynomial Fitting." The last session of data was used to verify the accuracy of the transfer function.

The second part was performed to build the transfer functions to map FES and joint torque. In this part, two pairs of stimulating electrodes (3 cm × 3 cm) were placed on the muscle belly of ECU and ECR of left arm. The FES PW of ECR increased from PW_{min} (frequency = 40 Hz, amplitude = 15 mA) with 10-μs increments was used to stimulate the subjects to perform wrist extension until PW was equaled to PW_{max}. During the stimulation, the subjects did not perform voluntary contractions. The kinematic data were recorded simultaneously, and there was a 1-min rest between stimulations to avoid the effects of muscle fatigue. The kinematic data and the value of PW were used to establish the transfer function mapping the joint angle and joint torque to PW. The inputs of the transfer function were the joint torque and angle and the output was the PW, which was described in section "Polynomial Fitting."

The third part was performed to verify the accuracy of the DTF. Based on the data of the above two parts, the DTF of

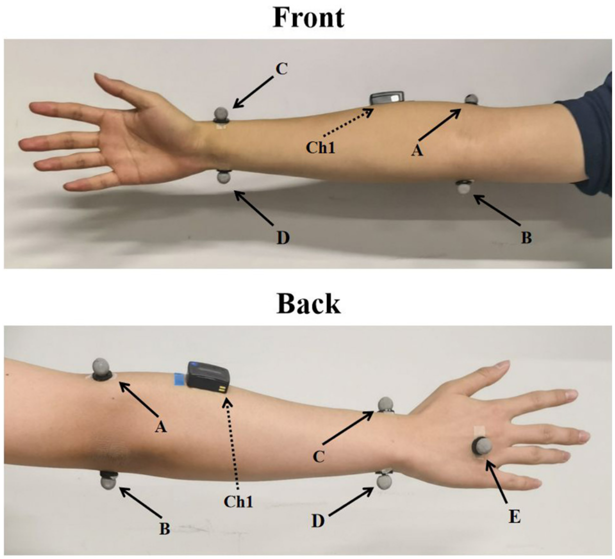

FIGURE 1 | The placement of markers and sEMG sensor. A–E indicates the corresponding five markers and Ch1 indicates sEMG sensor placed at ECR.

the subjects can be established. The last session of sEMG and kinematic data from the voluntary movement was inputted into the DTF, and the estimated PW was the output. The estimated PW was used to stimulate the left arms of subjects with kinematic data recorded simultaneously. The FES-induced joint torque was compared with the voluntary joint torque to analyze the accuracy of the FES-induced joint torque of the transfer functions. The joint torque was calculated from the kinematic data based on the inverse dynamics, and the method was described in section "Joint Angle." It should be noted that only the wrist extension movement phase was intercepted for training and analysis, because only extensor muscles were recorded and stimulated. The wrist extension movement phase was intercepted between the start of movement and 110° wrist angle. The start of movement was the crossing time when the angular velocity of the wrist joint crossed the threshold $mean(\omega_{rest}) + 3^{*}sd(\omega_{rest})$ from bottom to top and maintained over the threshold for more than 30 ms, where ω_{rest} indicated the wrist angular velocity at rest, and $mean(\omega_{rest})$ and $sd(\omega_{rest})$ indicated the mean and standard deviation of ω_{rest}.

Surface Electromyography Processing

The sEMG signal data were filtered using a fourth-order Butterworth band pass filter between 20 and 300 Hz and a notch filter with 50 Hz and its frequency multiplication. Then, the feature MAV was calculated from sEMG the signal by Equation 1.

$$MAV_i = \frac{1}{N}\sum_{k=0}^{N-1}\left|E_{i-k}\right| \tag{1}$$

where MAV_i is the MAV at the ith point of the sEMG data, E_{i-k} is the sEMG data after preprocessing at the $i - kth$ point, and N is the length of the window. In this paper, the length of the window was 200 samples (100 ms) and the MAV was calculated with a sliding window of 20 samples (10 ms) to make sure that the MAV and the kinematic data can correspond one-to-one according to time.

The non-negative matrix factorization (NMF) algorithm was used to extract the features of muscle synergy. Muscle activation pattern can be calculated as follows:

$$E = W_1 \cdot H_1 + W_2 \cdot H_2 + \cdots + W_k \cdot H_k + erro \tag{2}$$

where E is the m × n sEMG data set matrix (the number channels of sEMG signals, n is the signal length), W_k is the kth m × 1 matrix of synergy, H_k is the kth 1 × n matrix of time-varying synergy activation coefficient, and k is the number of synergies. W represents the activation degree of each muscle. In this paper, the number of synergies was 1 and W is normalized by dividing by the maximum value of element in W. Due to the number of muscles involved in wrist extension is limited and the difficulty to determine the FES PW when the number of muscle synergies increased, only two sEMG channels and one muscle synergy were used in this study.

Kinematic and Kinetic Data Processing

Joint Angle

We built a simplified model of the wrist joint. In the Vicon coordinate system, we defined the direction of the vector p_1 along the line connecting the midpoint of point A and point B and the midpoint of point C and point D, the direction of the vector p_2 along the line connecting point C and point D and the direction of the vector p_3 along the line connecting point E and the midpoint of point C and point D as shown in **Figure 2A**. The vector p_1 and the vector p_2 determined the plane of the forearm and the vector p_2 and the vector p_3 determined the plane of the hand.

Taking the vector p_2 as the x-axis, the local coordinate system of the forearm ($R_f = [e_{fx}, e_{fy}, e_{fz}]$) and hand ($R_h = [e_{hx}, e_{hy}, e_{hz}]$) can be established as follows:

$$\begin{cases} e_{fx} = e_{hx} = \dfrac{p_2}{|p_2|} \\ e_{fz} = \dfrac{p_1 \times p_2}{|p_1 \times p_2|} \\ e_{fy} = e_{fx} \times e_{fy} \\ e_{hz} = \dfrac{p_2 \times p_3}{|p_2 \times p_3|} \\ e_{hy} = e_{hx} \times e_{hz} \end{cases} \tag{3}$$

where × is the vector product.

The rotation matrix R_{hf} between the forearm's local coordinate system and the hand's coordinate system can be calculated as follows:

$$R_{hf} = (R_h)^{-1} R_f \tag{4}$$

The joint angle θ_w, the joint angular velocity ω_w, and the joint angular acceleration α_w between the hand and the forearm in

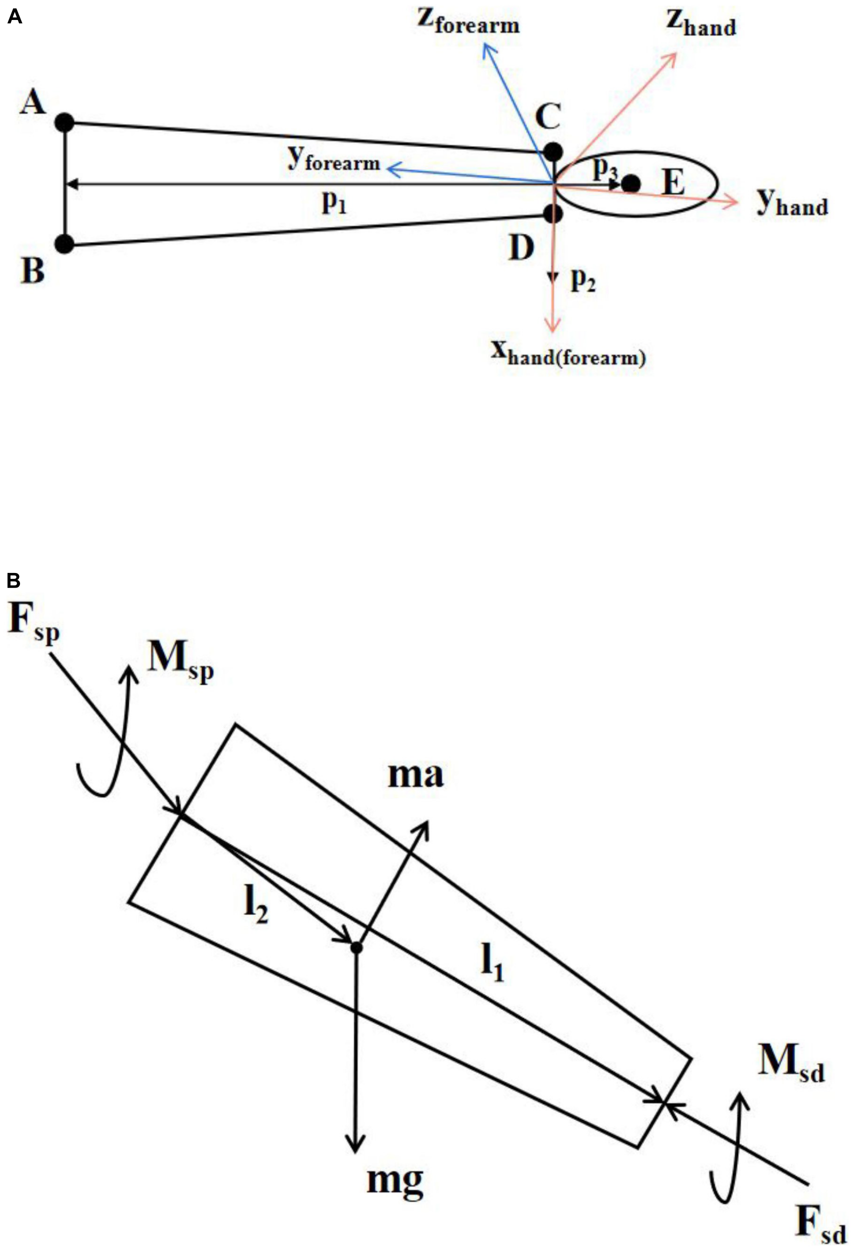

FIGURE 2 | (A) Simplified model of hand and forearm. A–E indicates the corresponding five markers. The orange coordinate system is the hand coordinate system and the blue coordinate system is the forearm coordinate system. The *x*-axis of the hand coordinate system and the forearm coordinate system are the same. **(B)** Schematic diagram of inverse kinetics.

the direction of wrist flexion and extension can be calculated as follows:

$$\begin{cases} \theta_w = tanh^{-1}\left(-\dfrac{R_{hf}\,(2,3)}{R_{hf}\,(3,3)}\right) \\ \omega_w = \dfrac{d\theta_w}{dt} \\ \alpha_w = \dfrac{d\omega_w}{dt} \end{cases} \tag{5}$$

Joint Torque

Inverse dynamic is a common method for kinetic analysis of human motion (Hatze, 2002; Riemer et al., 2008; Arteaga et al., 2020). It calculates the resultant forces and torques at both ends of the body segment from the inertia and kinematic information. The forces and motion parameters on the body segment are shown in **Figure 2B**, where m is the mass of the body segment, a is the acceleration of the body segment, g is the acceleration of gravity, F_{sd} and M_{sd} are the force and torque at the distal end of the body segment, F_{sp} and M_{sp} are the force and torque at the proximal end of the body segment, and l_1 and l_2 are the distance vector from the rotation center of the proximal joint of the body segment to the rotation center of the distal joint of the body segment and the distance vector from the center of rotation of the proximal joint of the body segment to the center of mass.

According to Newton–Euler equations, the dynamic equation of the body segment can be established as follows:

$$\begin{cases} F_{sp} + F_{sd} + mg = ma \\ M_{sp} + M_{sd} - l_2 \times F_{sp} + (l_1 - l_2) \times F_{sd} = I\alpha + \omega \times I\omega \end{cases} \tag{6}$$

where α is the angular acceleration of body segment, ω is the angular velocity of body segment, *I* is the moment of inertia of the body segment, and × is the vector product. The force on the distal end of the hand is zero during wrist extension. The mass, center of mass, and moment of inertia of the hand can be estimated from the human body parameters (De Leva, 1996; Dumas et al., 2004). **Table 2** lists the subjects' physiological data. Therefore, the joint torque M_w of the wrist during wrist extension can be calculated as follows:

$$M_w = l_2 \times \left(m_h\, a_h - m_h\, g\right) + I_h\, \alpha_w + \omega_w \times I_h\, \omega_w \tag{7}$$

where m_h is the mass of the hand, a_h is the acceleration at the center of mass of the hand, I_h is the moment of inertia of the hand, and × is the vector product.

Polynomial Fitting

We built a DTF of EMG, joint angle, and FES through polynomial fitting (PF) as shown in **Figure 3**. The transfer function is subject-specific due to the factors such as resistance between skin and electrode, electrode location, and fat thickness.

It has been proved that the wrist position affects sEMG signal (Roman-Liu and Bartuzi, 2013; Jochumsen et al., 2018) and FES may also be affected. A polynomial transfer function was established to map MAV, joint torque, and PW at each integer angle firstly, which could be considered to describe the relationship at isometric contraction. The joint angle was approximated to an integer to ensure that there were enough samples for each angle to fit. Dozens of polynomial transfer functions for wrist extension were obtained. **Figure 4A** shows an example of the fitting of MAV and joint torque at different fitting orders at 135°. The polynomial transfer function mapping MAV

TABLE 2 | Physiological data of subjects.

Subject	S1	S2	S3	S4	S5	S6
Gender	**m**	**m**	**m**	**f**	**f**	**m**
Mass of body/kg	77.6	70.2	73.0	53.5	51.8	77.8
Length of hand/m	0.174	0.172	0.165	0.152	0.156	0.179
I (1,1) of hand/kg × m^2	0.0023	0.0020	0.0019	0.0014	0.0012	0.0024
I (2,2) of hand/kg × m^2	0.0038	0.0033	0.0032	0.0023	0.0020	0.0040
I (3,3) of hand/kg × m^2	0.0057	0.0050	0.0048	0.0035	0.0030	0.0060
Center of mass of hand/m (distance from wrist)	0.0637	0.0630	0.0604	0.0576	0.0544	0.0655

I (1,1), I (2,2), and I (3,3) are the values of the elements on the diagonal line of the moment of inertia of the body segment (I).

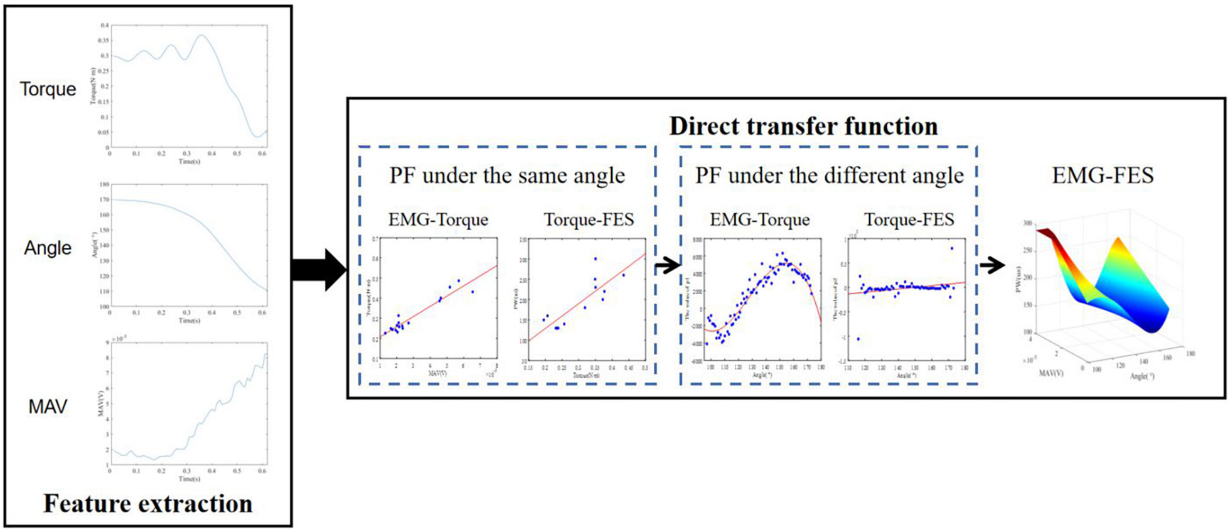

FIGURE 3 | The FES estimation procedure.

to the estimated joint torque and that mapping the actual joint torque at each integral angle were listed as Equation 8.

$$\begin{cases} T_i = p_{1,i}MAV_i{}^{n} + p_{2,i}MAV_i{}^{n-1} + \cdots + p_{n,i}MAV_i + p_{n+1,i} \\ PW_i = q_{1,i}T_i{}^{n} + q_{2,i}T_i{}^{n-1} + \cdots + q_{n,i}T_i + q_{n+1,i} \end{cases} \tag{8}$$

where MAV_i, PW_i, and T_i are the estimated joint torque, the value of MAV, the PW of FES, and the actual joint torque at i° and n is the fitting orders of MAV_i and T_i. $p_{n,i}$ and $q_{n,i}$ are the coefficients of the two polynomial functions at i°, respectively. At different wrist positions, polynomial functions had different coefficients. Therefore, joint angles and coefficients at different angles were fitted. To ensure enough data for fitting, we consider all the angles × around the integer angle A ($A - 0.5 \leq \times < A + 0.5$) to be the same isometric contraction state, which can be used to establish the fitting function at A. The range of angles to establish the polynomial transfer functions depended on the angular range of wrist extension for each subject. **Figure 4B** shows an example of the fitting of $p_{1,\theta}$ and joint angle at one order of T_i. The coefficients at different angles can be calculated by Equations 9, 10.

$$\begin{cases} p_{1,\theta} = f_1(\theta) = a_{1,1}\theta^{m} + a_{2,1}\theta^{m-1} + \cdots \\ \quad + a_{m,1}\theta + a_{m+1,1} \\ \qquad \vdots \\ p_{n+1,\theta} = f_{n+1}(\theta) = a_{1,n+1}\theta^{m} + a_{2,n+1}\theta^{m-1} + \cdots \\ \quad + a_{m,n+1}\theta + a_{m+1,n+1} \end{cases} \tag{9}$$

$$\begin{cases} q_{1,\theta} = g_1(\theta) = b_{1,1}\theta^{m} + b_{2,1}\theta^{m-1} + \cdots + b_{m,1}\theta \\ \quad + b_{m+1,1} \\ \qquad \vdots \\ q_{n+1,\theta} = g_{n+1}(\theta) = b_{1,n+1}\theta^{m} + b_{2,n+1}\theta^{m-1} + \cdots \\ \quad + b_{m,n+1}\theta + b_{m+1,n+1} \end{cases} \tag{10}$$

where θ is the joint angle and m is the fitting orders of θ. $a_{m,n}$ and $b_{m,n}$ are the coefficients of the two polynomial functions, respectively.

The DTF of PW, MAV, and joint angle can be obtained by combining the polynomials obtained by fitting as follows:

$$\begin{cases} PW_{\theta} = g_1(\theta)\left(T(MAV_{\theta})\right)^{n} + g_2(\theta)\left(T(MAV_{\theta})\right)^{n-1} + \cdots \\ \quad + g_n(\theta)\,T(MAV_{\theta}) + g_{n+1}(\theta) \\ T(MAV_{\theta}) = f_1(\theta)\,MAV_{\theta}{}^{n} + f_2(\theta)\,MAV_{\theta}{}^{n-1} + \cdots \\ \quad + f_n(\theta)\,MAV_{\theta} + f_{n+1}(\theta) \end{cases} \tag{11}$$

Experiment of Real-Time Functional Electrical Stimulation

To understand how this strategy performed in a real-time FES system, an online experiment of FES combined with the DTF was designed. S1 and S4 took part in the experiment. The real-time FES-BM system in the study of Zhao et al. (2021) was used in this study. The wrist joint angle was calculated by two inertial measurement units (IMUs) (Trigno$^{\text{TM}}$ Avanti Platform, DELSYS, United States), which were placed at the right hand and forearm, respectively. Each subject was asked to put both their arms on the table in front of them with the same initial wrist angle. They were asked to perform five wrist extensions in one session, and there were three sessions in total. During the extension, FES parameters were generated according to the collected EMG and kinematic data of the right hand and used to stimulate the left hand to induce movement. The real-time status was shown and recorded by a GUI designed by LabVIEW (National Instruments, Inc.). The kinematic data were recorded by Vicon to verify the accuracy in real time.

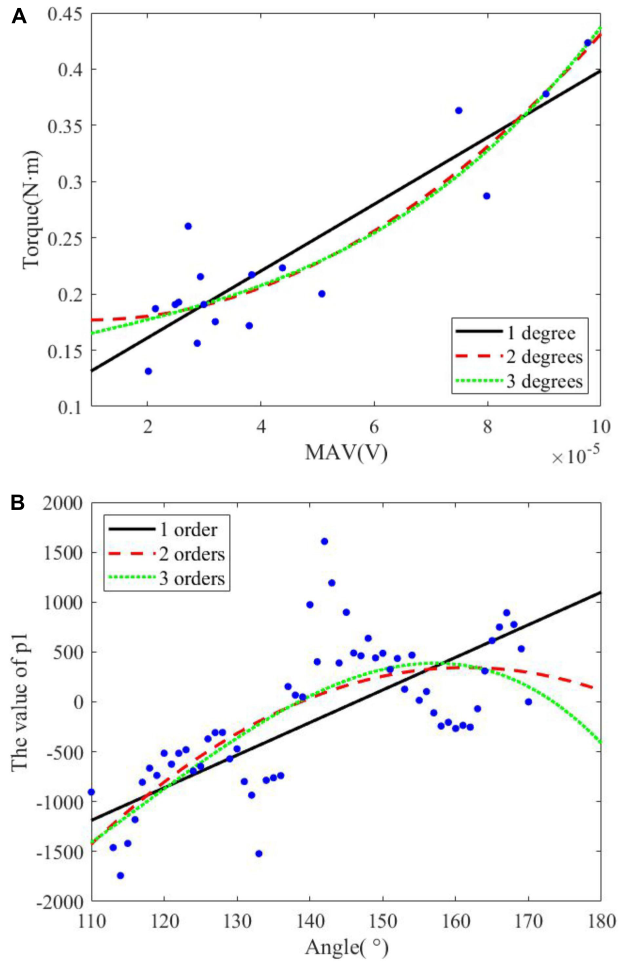

FIGURE 4 | Polynomial fitting at different degrees. **(A)** Example of the fitting of MAV and joint torque. **(B)** Example of the fitting of $p_{1,\theta}$ and joint angle.

Evaluation

The orders of MAV or T and the orders of θ for PF were investigated to get the optimal fitting. They were developed from one to three orders. Therefore, there were nine combinations for transfer functions. The coefficient of determination (R^2) of estimated joint torque and true joint torque was used as

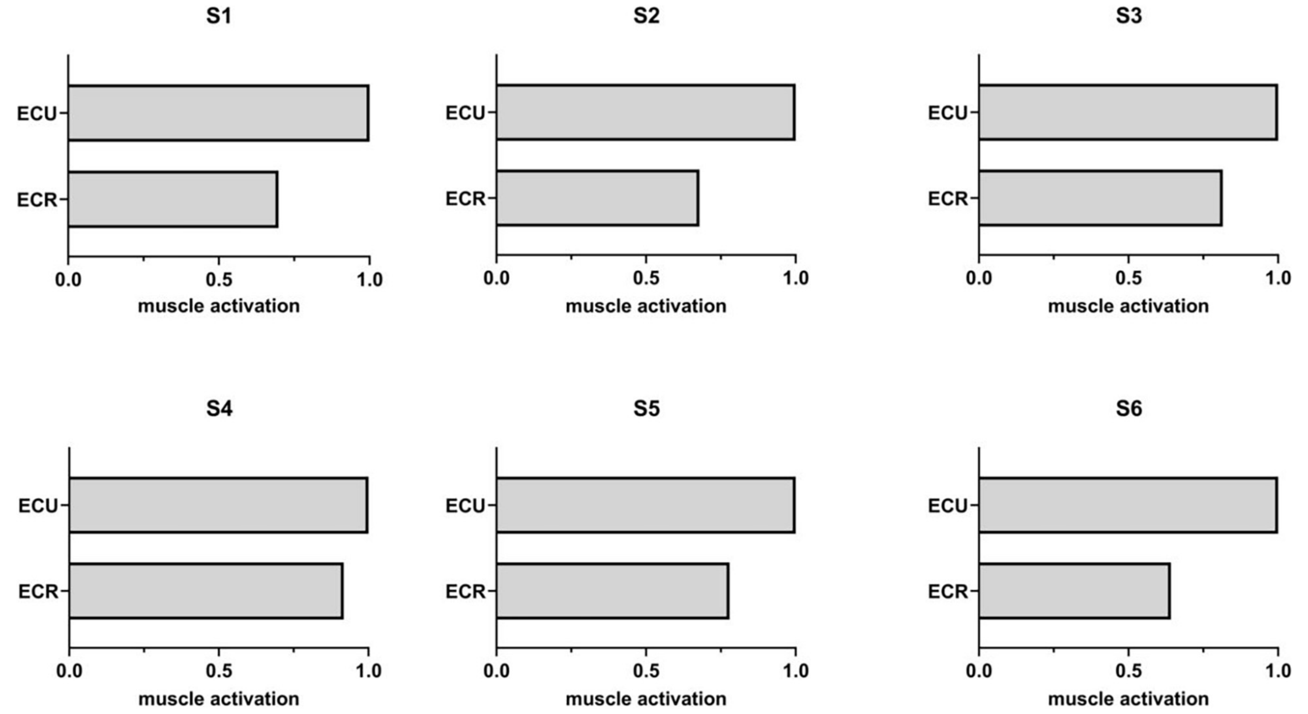

FIGURE 5 | The synergy matrix for all subjects during wrist extension.

an indicator for comparison of the transfer functions fitting MAV and joint angle to joint torque of each combination. The R^2 of estimated PW and true PW was used as an indicator for comparison of the transfer functions fitting joint torque and joint angle to PW of each combination. A one-way repeated measures analysis of variance (ANOVA) was applied to investigate the effect of the degrees of MAV/T and the degrees of θ for PF.

The accuracy of joint torque estimation affected the accuracy of PW estimation and the accuracy between the FES-included joint torque and the voluntary joint torque reflected the effectiveness of the strategy. Therefore, R^2 and the normalized root mean square error (NRMSE) of joint torque and estimated joint torque were used as an indicator to verify the accuracy of estimation. Moreover, R^2 and NRMSE of FES-included joint torque/angle and the voluntary joint torque/angle were used as an indicator to verify the accuracy of DTF.

RESULTS

Muscle Synergy

Figure 5 shows the synergy matrix of all subjects during wrist extension. It can be seen that the synergy matrix was similar for all subjects, which revealed the reliability of synergy theory. When the number of synergies was 1, $R^2 = 0.773 \pm 0.068$ and variance accounted for (VAF) (Israely et al., 2018) was 0.792 ± 0.093. It showed that the factorization was accurate, although the number of synergies was 1.

Fitting Order Selection for Polynomial Fitting

Figure 6A shows the R^2 for PF of all subjects between the joint toque, MAV and joint angle. R^2 of one-order PF for MAV was significantly higher than that of two-order PF for MAV ($p < 0.001$) and three-order PF for MAV ($p < 0.001$). For the one-order PF for MAV, R^2 of three-order PF for θ was significantly higher than that of one-order ($p = 0.004$) and two-order ($p < 0.001$) PF for θ. Therefore, the combination of one-order PF for MAV and three-order PF for θ were selected as the model of PF to build the relationship between the joint toque, MAV, and joint angle. The combination of one-order PF for MAV and three-order PF for θ had the best accuracy ($R^2 = 0.952 \pm 0.092$).

Similarly, **Figure 6B** shows the R^2 for PF of all subjects between the PW, joint torque, and joint angle. The ANOVA analysis revealed that no significant difference appeared between the one-order, the two-order, and the three-order PF for T, but the combination of one-order PF for joint torque and one-order PF for joint angle has less variability and a higher R^2 ($R^2 = 0.681 \pm 0.075$). Therefore, the combination of one-order PF for joint torque and one-order PF for joint angle was selected as the model of PF to build the relationship between the PW, joint torque, and joint angle.

The Accuracy of Joint Torque Estimation

R^2 and NRMSE of joint torque estimation of all subjects are shown in **Figure 7**. The coefficient of determination was 0.949 ± 0.033 (max: S4: $R^2 = 0.954 \pm 0.050$, min: S6:

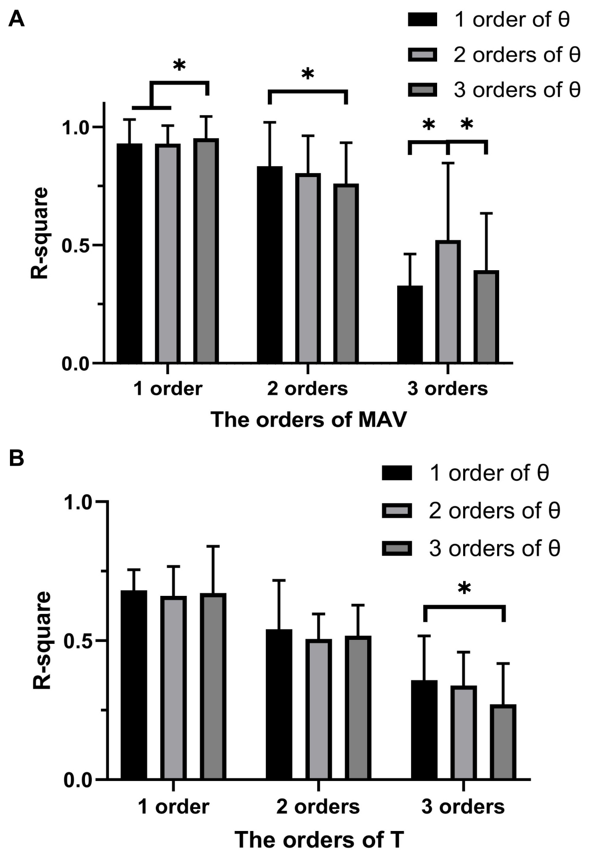

FIGURE 6 | **(A)** The average accuracy for PF of MAV and joint angle at different degrees. **(B)** The average accuracy for PF of joint torque and joint angle at different degrees. The symbol "*" indicates a significant difference ($p < 0.05$).

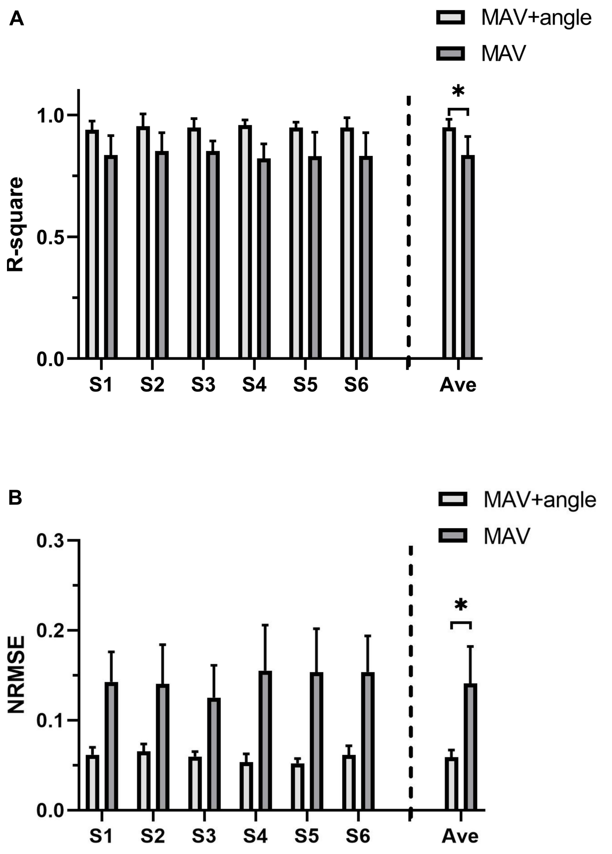

FIGURE 7 | The joint torque estimation accuracy of all subjects. **(A)** R^2 of joint torque estimation based on MAV and joint angle and joint torque estimation based on MAV only. **(B)** NRMSE of joint torque estimation based on MAV and joint angle and joint torque estimation based on MAV only. The symbol "*" indicates a significant difference ($p < 0.05$).

$R^2 = 0.939 \pm 0.036$) and the NRMSE was 0.059 ± 0.008 (max: S2: NRMSE $= 0.065 \pm 0.008$, min: S5: NRMSE $= 0.052 \pm 0.005$). **Figure 8A** shows true and predicted joint torque based on MAV and joint torque for all subjects and **Figure 8B** shows a representative trial of predicted joint torque of S1, where the time of each wrist extension was normalized. We also built a three-order polynomial transfer function mapping MAV to joint torque to demonstrate the importance of joint angle. R^2 and NRMSE of joint torque estimation based on MAV only were 0.836 ± 0.106 and 0.141 ± 0.041, respectively, as shown in **Figure 7**, which was significantly lower ($p < 0.001$) than the function combined with MAV and joint angle.

The Accuracy of Functional Electrical Stimulation-Included Joint Torque/Angle

The last session of sEMG and kinematic data was used to verify the accuracy of the transfer function for each subject. Due to the presence of the PW threshold for each subject, the estimated value beyond the threshold was set to the lower or upper threshold. At the same time, the minimum interval of PW in Rehastim2 FES device was 10 μs and the frequency of FES was 40 Hz. Therefore, the PW was changed every 25 ms and the PW value used for stimulation was a 10-digit integer that rounded the mean of the estimated PW values 25 ms before.

The same length data was intercepted from the moment when the wrist extension started to compare the similarity between the FES-included movement and the voluntary movement. **Table 3** shows the mean R^2 and NRMSE of PF mapping the joint angle to the joint torque of each subject between the FES-induced and the voluntary wrist extension. The coefficient of determination and NRMSE for joint torque fitting were 0.701 ± 0.220 and 0.241 ± 0.080. The R^2 and NRMSE of joint angle were 0.966 ± 0.042 and 0.047 ± 0.005. **Figure 9A** shows the true and FES-induced joint torque and joint angle of all subjects and **Figure 9B** shows a representative trial of FES-included movement of S1, where the time of each wrist extension was normalized.

The Effect of Speed on Accuracy

As the extension speed may affect the estimation accuracy, according to the t_{110} which represented the time from the start to wrist extension to joint angle of 110°, we divided

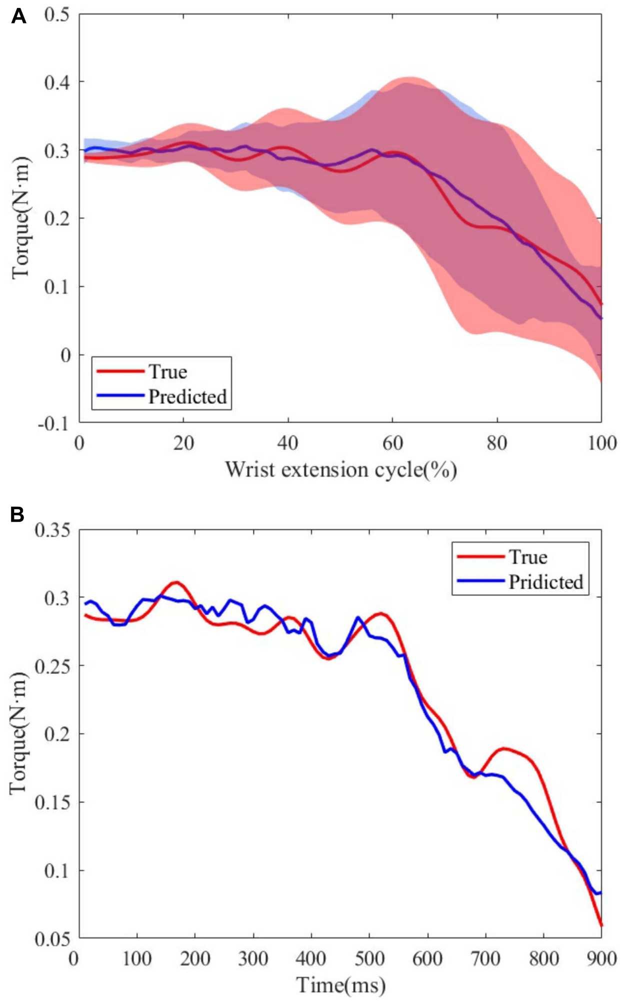

FIGURE 8 | **(A)** True and predicted joint torque based on MAV and joint torque for all subjects. The shadow regions represent the standard deviations and the lines represent the average joint torque for all subjects. **(B)** A representative trial of predicted joint torque of S1.

the trials into three groups: fast ($t_{110} < 400$ ms), medium (400 ms $< t_{110} <$ 800 ms), and slow ($t_{110} >$ 800 ms). **Figure 10** shows the R^2 of joint torque and FES-induced joint torque of three groups. The R^2 of joint torque estimation of fast, medium, and slow groups was 0.695 ± 0.206, 0.711 ± 0.224, and 0.707 ± 0.231, respectively. The R^2 of FES-induced joint torque of fast, medium, and slow groups was 0.947 ± 0.041, 0.947 ± 0.033, and 0.954 ± 0.037, respectively. However, there was no significant difference between the R^2 of joint torque estimation and FES-induced joint torque of three groups.

The Accuracy of Functional Electrical Stimulation-Included Joint Torque/Angle in Real Time

Figure 11 shows the process of the real-time FES system combined with the DTF. The ratio of PW of two FES channels was set based on the ratio obtained from muscle synergy, and the FES was triggered when a wrist extension was recognized. **Figure 12** shows a representative session of S4. The latency of this system was between 30 and 200 ms. The R^2 and NRMSE of FES-induced joint angle and joint torque were $R^2 = 0.940 \pm 0.038$ and NRMSE $= 0.071 \pm 0.014$ and $R^2 = 0.607 \pm 0.294$ and NRMSE $= 0.303 \pm 0.119$, respectively.

DISCUSSION

This study developed a dynamic multi-channel mapping strategy to improve the accuracy of desired force and the symmetry of bilateral movements during FES-BM, which has been proved to improve the rehabilitation effect of FES. The main contribution was that this study succeeded in estimating FES parameters based on joint angle and sEMG during dynamic tasks. Real-time estimation of FES parameters was realized with joint torque as the intermediate variable. This strategy not only reduced the influence of the joint angle on the EMG signal, but also avoided the influence of the movements. First, the contractions around each integer joint angle were regarded as the same isometric state, and the corresponding PF transfer function was calculated. Then, the PF transfer function mapping joint angle to each polynomial coefficient was established. The DTF realized the transformation from the MAV and joint angle to PW directly. Estimation of FES parameters based on transfer functions can reduce the computational complexity of the system and thus reduce the delay.

TABLE 3 | The coefficient of determination and NRMSE of the FES-induced and voluntary wrist extension.

Subject	Joint torque		Joint angle	
	R^2	NRMSE	R^2	NRMSE
S1	0.72088 ± 0.21260	0.22045 ± 0.06755	0.97606 ± 0.01851	0.04351 ± 0.00413
S2	0.81741 ± 0.07079	0.17548 ± 0.06259	0.99041 ± 0.00581	0.01220 ± 0.00133
S3	0.58755 ± 0.31304	0.30479 ± 0.10263	0.95180 ± 0.03253	0.05492 ± 0.00529
S4	0.74325 ± 0.10946	0.21252 ± 0.05987	0.97031 ± 0.04859	0.05027 ± 0.00547
S5	0.66418 ± 0.35803	0.27560 ± 0.09624	0.95793 ± 0.03974	0.06017 ± 0.00441
S6	0.67327 ± 0.15849	0.25647 ± 0.07432	0.94823 ± 0.07493	0.06373 ± 0.00692
Mean	0.70109 ± 0.22031	0.24089 ± 0.07963	0.96579 ± 0.04171	0.04747 ± 0.00473

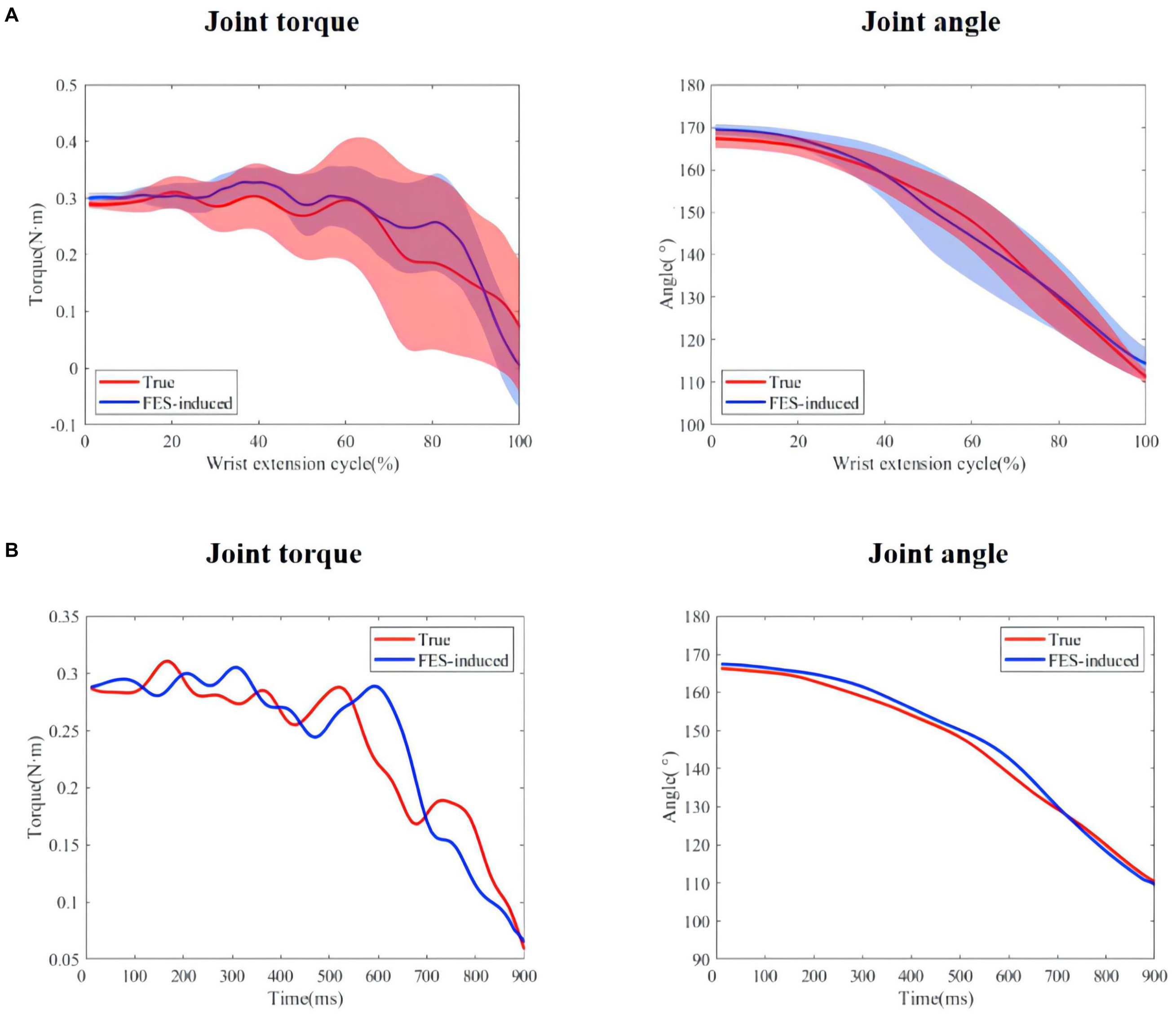

FIGURE 9 | (A) True and predicted FES-included movement of S1. The shadow regions represent the standard deviations and the lines represent the average joint torque/angle during the five stimulation trials. **(B)** A representative trial of FES-included movement of S1.

Muscle synergy has been used to control multi-channel FES in many studies. Previous studies show the similarities in muscle synergy between individuals (Overduin et al., 2008). Therefore, it is also feasible for FES control based on other people's muscle synergy patterns (Niu et al., 2019). To improve the accuracy of FES-induced movement, Zhuang et al. (2015) applied muscle synergies to the virtual arm model to test a synergy based NMES strategy, and the results showed close resemblance to the original elbow trajectory of normal movements. Razavian et al. (2018) designed a muscle synergy-based FES controller which employed direct relations between the muscle synergies and the produced hand forces and achieved a final hand position error of 2 cm for a 2-D point-to-point reaching task. The previous studies usually used the muscle synergies W, which reflect the muscle pattern, as the FES pattern and the activation coefficients H, which reflected the sEMG activation, as the FES activation. Therefore, we used the muscle synergy to determine the ratio of the PW of two stimulation channels. With the use of muscle synergy, we controlled multi-channel FES based on only one sEMG channel. Unlike previous studies, our study replaced the activation coefficients H by the DTF, which can better fit voluntary movement and FES-induced movement. However, it was difficult to establish the DTF when the number of muscle synergies was not one. The number of muscle synergy was fixed one in our study. Our study proved that multi-channel FES based on muscle synergy could be used to control FES-induced torque.

For the estimation of joint torque, it was found that the combination of 1° PF for MAV and 3° PF for θ had the best fit.

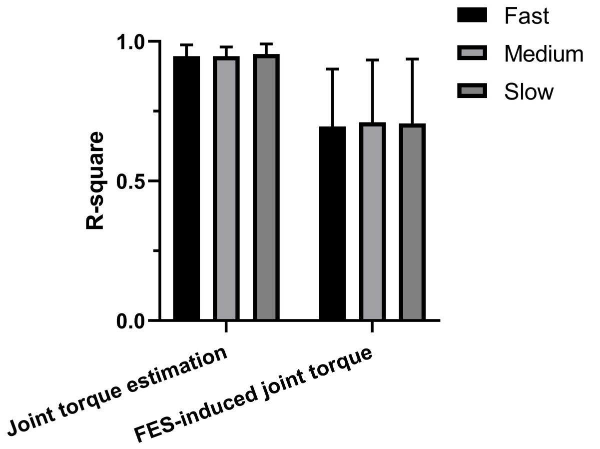

FIGURE 10 | The accuracy of joint torque estimation with sEMG and joint torque production with FES at different speeds.

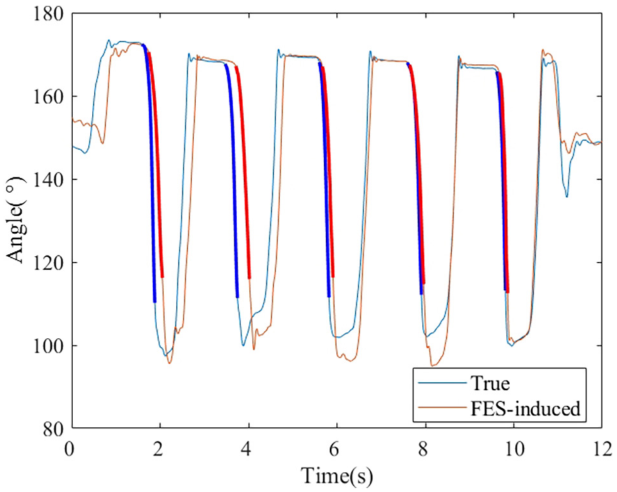

FIGURE 12 | A representative session of S4. The bold lines indicate the wrist extension and FES-induced parts that were used to calculate the accuracy.

The accuracy of joint torque estimation for the transfer function based on joint angle and MAV ($R^2 = 0.949$ and NRMSE = 0.059) was significantly higher than the transfer function based on MAV only ($R^2 = 0.836$ and NRMSE = 0.141), which further demonstrated the advantages of combining sEMG and joint angle. Compared to the previous studies (Kamavuako et al., 2013; Yu et al., 2021), this study achieved a higher accuracy of wrist joint torque estimation with less sEMG electrodes by the combination of sEMG and kinematic information. Gregory found that there was a relationship between FES-induced torque and total charge (Gregory et al., 2007), which was also demonstrated in this paper. But few studies established the transfer function between the joint torque and PW. Similar to establishing the transfer relationship between joint torque and MAV, this study used PF to build the model. The combination of 1° PF for joint torque and 1° PF for θ had the best fit. However, the accuracy of PW estimation for PF model was only 0.681. It can be seen that the non-linear degree of PW and joint torque was not easy to be fitted by PF.

In terms of joint angle reproduction, this study achieved a high accuracy ($R^2 = 0.965$ and NRMSE = 0.047). Rossi et al. (2020) proposed an average threshold crossing (ATC) FES control strategy, and the correlation coefficient of joint angle during elbow flexion was 0.87 ± 0.07. Bi et al. (2020) designed a multiple-gesture FES system, and the correlation coefficient of joint angle during wrist extension was 0.89 ± 0.04. The accuracy of FES-induced joint angle for this study was much

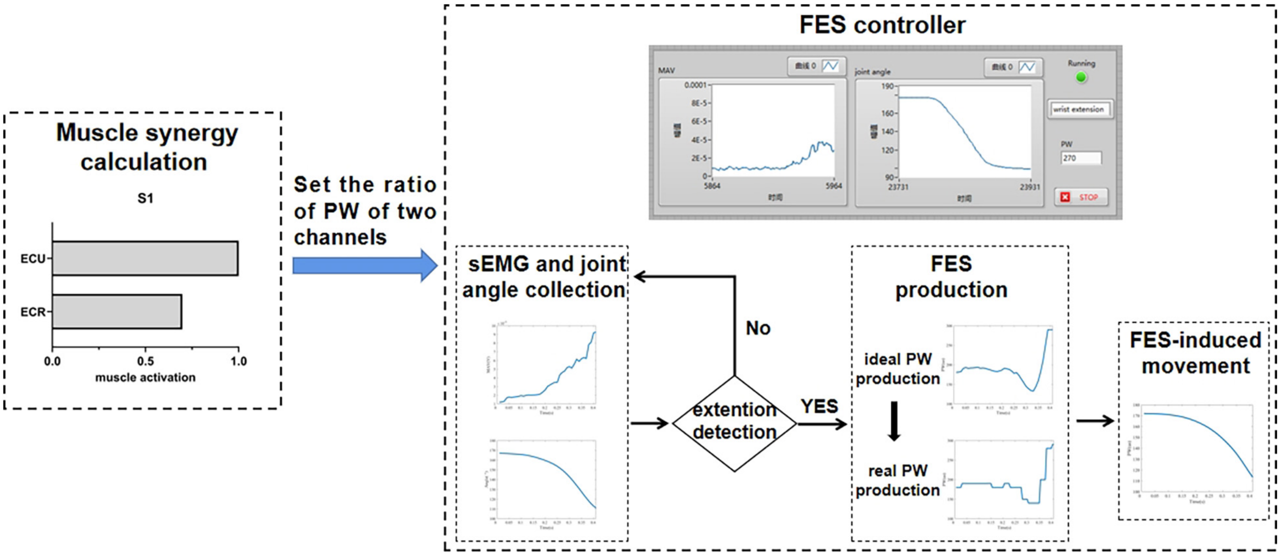

FIGURE 11 | The design of the real-time FES system combined with the DTF.

better than previous studies. However, it was more difficult to generate desired joint torque. The accuracy of FES-induced joint torque was $R^2 = 0.701$ and NRMSE $= 0.241$, which was lower than the FES-induced static force at isometric contraction in previous studies (the correlation coefficient, $R = 0.912 \pm 0.055$ and $R = 0.91 \pm 0.04$) (Zhou et al., 2016, 2020). Using FES to generate desired joint torque during movement is difficult, due to the effect of speed and position.

Building an accurate mapping relationship from desired force to FES is significant, especially in dynamic movement. Razavian et al. (2018) proposed a feedback controller for FES to control hand movements in a 2-D task space based on force. To our knowledge, our study is the first to propose a strategy for dynamic prediction of FES based on joint torque. The combination of sEMG and kinematic information can effectively reduce the influence of wrist position on sEMG signals. Moreover, it seems that the speed will not affect the accuracy of joint torque estimation and FES-induced joint torque during wrist extension.

When the control strategy was realized with a real-time system, the accuracy of FES-induced joint angle and joint torque was $R^2 = 0.940 \pm 0.038$ and NRMSE $= 0.071 \pm 0.014$ and $R^2 = 0.607 \pm 0.294$ and NRMSE $= 0.303 \pm 0.119$. The reason why the accuracy was lower than that of the offline method may be that the delay of the FES control system led to the inconsistency of the both wrist angles. Therefore, it is necessary to reduce the latency of gesture recognition and system communication to improve the accuracy of the real-time FES system combined with the DTF.

In this study, an estimation model of PW was established based on wrist extension, which are common in the rehabilitation of patients with stroke. High accuracy of joint angle and torque reproduction makes sure that the patients with stroke can simulate the force pattern of healthy muscles by themselves (Chan et al., 2009; Knutson et al., 2016) or experienced rehabilitation physicians (Huang et al., 2014; Zhou et al., 2016). In practical application, joint angles can be acquired using IMUs, data gloves, and bend sensors, etc.

However, the main purpose of this study was to evaluate the feasibility of building a relationship between joint angle, sEMG, and FES based on joint torque, and there are some limitations. First, the muscle fatigue and the discomfort from continuous movement have not been studied. Zhou et al. (2016) proposed that real-time controlled FES will reduce muscle fatigue produced by FES and the increasing of PW produced less discomfort than the increasing of FES amplitude. Therefore, PW was used as the FES parameters adjusted in this study. The muscle fatigue might affect the accuracy of joint torque reproduction. We will study the changes in accuracy and discomfort of movement during a continuous use in the future. Second, only healthy subjects were studied in this study. Although this strategy was established from the actual FES-induced joint torque which may reduce the effect of muscle atrophy of patients with stroke, the performance of this strategy still needs to be verified.

CONCLUSION

In previous studies, the relationship between sEMG signal and FES control parameters was established during static isometric contraction. However, it is not appropriate to use the static relationship for FES control during movement. This study proposed a dynamic mapping strategy based on sEMG and kinematic information *via* joint torque. The coefficient of determination and NRMSE for FES-induced joint angle fitting were 0.965 and 0.047 and those for FES-induced joint torque fitting were 0.701 and 0.241. The DTF also had a good performance in real-time FES system, with $R^2 = 0.940$ and 0.607 and NRMSE $= 0.071$ and 0.303 for the joint angle and torque fitting, respectively. It was concluded that the transfer function established under dynamic tasks *via* joint torque could achieve a good movement output for FES-BM. This FES control strategy estimated PW directly with a small amount of calculation and a short delay. Future work is still needed to test this strategy in patients with stroke and study the influence of muscle fatigue.

DATA AVAILABILITY STATEMENT

The raw data supporting the conclusions of this article will be made available by the authors, without undue reservation.

ETHICS STATEMENT

The studies involving human participants were reviewed and approved by the Ethics Committee of Tianjin University. The patients/participants provided their written informed consent to participate in this study. Written informed consent was obtained from the individual(s) for the publication of any potentially identifiable images or data included in this article.

AUTHOR CONTRIBUTIONS

RX, XZ, ZW, and LM contributed to conception and design of the study. RX and XZ organized the database. RX, XZ, and ZW performed the statistical analysis. XZ wrote the first draft of the manuscript. RX, ZW, LM, and DM wrote sections of the manuscript. All authors contributed to manuscript revision, read, and approved the submitted version.

FUNDING

This work was supported by the National Key Research and Development Program of China (Nos. 2020YFC2004300 and 2020YFC2004302) and National Natural Science Foundation of China (Nos. 81901860, 81925020, and 82101448).

REFERENCES

Ambrosini, E., Ferrante, S., Pedrocchi, A., Ferrigno, G., and Molteni, F. (2011). Cycling induced by electrical stimulation improves motor recovery in postacute hemiparetic patients: a randomized controlled trial. *Stroke* 42, 1068–1073.

Arteaga, M. V., Castiblanco, J. C., Mondragon, I. F., Colorado, J. D., and Alvarado-Rojas, C. (2020). EMG-driven hand model based on the classification of individual finger movements. *Biomed. Signal Process. Control* 58:101834.

Barsi, G. I., Popovic, D. B., Tarkka, I. M., Sinkjaer, T., and Grey, M. J. (2008). Cortical excitability changes following grasping exercise augmented with electrical stimulation. *Exp. Brain Res.* 191, 57–66. doi: 10.1007/s00221-008-1495-5

Bernstein, N. (1966). *The Co-Ordination And Regulation Of Movements*. Oxford: Pergamon Press.

Bi, Z., Wang, Y., Wang, H., Zhou, Y., Xie, C., Zhu, L., et al. (2020). Wearable EMG bridge—a multiple-gesture reconstruction system using electrical stimulation controlled by the volitional surface electromyogram of a healthy forearm. *IEEE Access* 8, 137330–137341.

Chan, M. K.-L., Tong, R. K.-Y., and Chung, K. Y.-K. (2009). Bilateral upper limb training with functional electric stimulation in patients with chronic stroke. *Neurorehabil. Neural Repair.* 23, 357–365.

Chen, J., Zhang, X., Gu, L., and Nelson, C. (2017). Estimating muscle forces and knee joint torque using surface electromyography: a musculoskeletal biomechanical model. *J. Mech. Med. Biol.* 17:1750069.

d'Avella, A., Saltiel, P., and Bizzi, E. (2003). Combinations of muscle synergies in the construction of a natural motor behavior. *Nat. Neurosci.* 6, 300–308.

De Leva, P. (1996). Adjustments to Zatsiorsky-Seluyanov's segment inertia parameters. *J. Biomech.* 29, 1223–1230.

Dumas, R., Aissaoui, R., and De Guise, J. A. (2004). A 3D generic inverse dynamic method using wrench notation and quaternion algebra. *Comput. Methods Biomech. Biomed. Eng.* 7, 159–166. doi: 10.1080/10255840410001727805

Ferrante, S., Chia Bejarano, N., Ambrosini, E., Nardone, A., Turcato, A. M., Monticone, M., et al. (2016). A personalized multi-channel FES controller based on muscle synergies to support gait rehabilitation after stroke. *Front. Neurosci.* 10:425. doi: 10.3389/fnins.2016.00425

Fu, M. J., Curby, A., Suder, R., Katholi, B., and Knutson, J. S. (2020). Home-based functional electrical stimulation-assisted hand therapy video games for children with hemiplegia: development and proof-of-concept. *IEEE Trans. Neural Syst. Rehabil. Eng.* 28, 1461–1470. doi: 10.1109/TNSRE.2020.2992036

Glanz, M., Klawansky, S., Stason, W., Berkey, C., and Chalmers, T. C. (1996). Functional electrostimulation in poststroke rehabilitation: a meta-analysis of the randomized controlled trials. *Arch. Phys. Med. Rehabil.* 77, 549–553.

Gregory, C. M., Dixon, W., and Bickel, C. S. (2007). Impact of varying pulse frequency and duration on muscle torque production and fatigue. *Muscle Nerve* 35, 504–509.

Happak, W., Gruber, H., Holle, J., Mayr, W., Schmutterer, C., Windberger, U., et al. (1989). "Multi-channel indirect stimulation reduces muscle fatigue. Images of the twenty-first century," in *Proceedings of the Annual International Engineering in Medicine and Biology Society*, (Piscataway, NJ: IEEE), 240–241.

Hatze, H. (2002). The fundamental problem of myoskeletal inverse dynamics and its implications. *J. Biomech.* 35, 109–115. doi: 10.1016/s0021-9290(01)00158-0

Hodkin, E. F., Lei, Y., Humby, J., Glover, I. S., Choudhury, S., Kumar, H., et al. (2018). Automated FES for upper limb rehabilitation following stroke and spinal cord injury. *IEEE Trans. Neural Syst. Rehabil. Eng.* 26, 1067–1074. doi: 10.1109/TNSRE.2018.2816238

Hou, J., Sun, Y., Sun, L., Pan, B., Huang, Z., Wu, J., et al. (2016). A pilot study of individual muscle force prediction during elbow flexion and extension in the neurorehabilitation field. *Sensors* 16:2018. doi: 10.3390/s16122018

Huang, Y., Chen, K., Zhang, X., Wang, K., and Ota, J. (2020). Joint torque estimation for the human arm from sEMG using backpropagation neural networks and autoencoders. *Biomed. Signal Process. Control* 62:102051.

Huang, Z., Wang, Z., Lv, X., Zhou, Y., Wang, H., and Zone, S. (2014). A novel functional electrical stimulation-control system for restoring motor function of post-stroke hemiplegic patients. *Neural Regener. Res.* 9, 2102–2110. doi: 10.4103/1673-5374.147938

Ison, M., and Artemiadis, P. (2014). The role of muscle synergies in myoelectric control: trends and challenges for simultaneous multifunction control. *J. Neural Eng.* 11:051001. doi: 10.1088/1741-2560/11/5/051001

Israely, S., Leisman, G., Machluf, C. C., and Carmeli, E. (2018). Muscle synergies control during hand-reaching tasks in multiple directions post-stroke. *Front. Comput. Neurosci.* 12:10. doi: 10.3389/fncom.2018.00010

Jochumsen, M., Waris, A., and Kamavuako, E. N. (2018). The effect of arm position on classification of hand gestures with intramuscular EMG. *Biomed. Signal Process. Control* 43, 1–8.

Kamavuako, E. N., Scheme, E. J., and Englehart, K. B. (2013). Wrist torque estimation during simultaneous and continuously changing movements: surface vs. untargeted intramuscular EMG. *J. Neurophysiol.* 109, 2658–2665. doi: 10.1152/jn.00086.2013

Kelso, J. S. (1995). *Dynamic Patterns: The Self-Organization Of Brain And Behavior*. Cambridge, MA: MIT press.

Khokhar, Z. O., Xiao, Z. G., and Menon, C. (2010). Surface EMG pattern recognition for real-time control of a wrist exoskeleton. *Biomed. Eng. Online* 9, 1–17. doi: 10.1186/1475-925X-9-41

Kimberley, T. J., Lewis, S. M., Auerbach, E. J., Dorsey, L. L., Lojovich, J. M., and Carey, J. R. (2004). Electrical stimulation driving functional improvements and cortical changes in subjects with stroke. *Exp. Brain Res.* 154, 450–460. doi: 10.1007/s00221-003-1695-y

Knutson, J. S., Gunzler, D. D., Wilson, R. D., and Chae, J. (2016). Contralaterally controlled functional electrical stimulation improves hand dexterity in chronic hemiparesis a randomized trial. *Stroke* 47, 2596–2602.

Knutson, J. S., Harley, M. Y., Hisel, T. Z., and Chae, J. (2007). Improving hand function in stroke survivors: a pilot study of contralaterally controlled functional electric stimulation in chronic hemiplegia. *Arch. Phys. Med. Rehabil.* 88, 513–520. doi: 10.1016/j.apmr.2007.01.003

Knutson, J. S., Harley, M. Y., Hisel, T. Z., Makowski, N. S., and Chae, J. (2014). Contralaterally controlled functional electrical stimulation for recovery of elbow extension and hand opening after stroke a pilot case series study. *Am. J. Phys. Med. Rehabil.* 93, 528–539. doi: 10.1097/PHM.0000000000000066

Kuberski, B. (2012). *ScienceMode2—Description And Protocol*. Available online at: https://hasomed.de/ [Accessed December 12, 2012].

Lynch, C. L., and Popovic, M. R. (2008). Functional electrical stimulation. *IEEE Control Syst. Mag.* 28, 40–50.

Malesevic, J., Konstantinovic, L., Bijelic, G., and Malesevic, N. (2021). Smart protocols for physical therapy of foot drop based on functional electrical stimulation: a case study. *Healthcare* 9:502. doi: 10.3390/healthcare9050502

Niu, C. M., Bao, Y., Zhuang, C., Li, S., Wang, T., Cui, L., et al. (2019). Synergy-based FES for post-stroke rehabilitation of upper-limb motor functions. *IEEE Trans. Neural Syst. Rehabil. Eng.* 27, 256–264.

Overduin, S. A., D'Avella, A., Roh, J., and Bizzi, E. (2008). Modulation of muscle synergy recruitment in primate grasping. *J. Neurosci.* 28, 880–892.

Quandt, F., and Hummel, F. C. (2014). The influence of functional electrical stimulation on hand motor recovery in stroke patients: a review. *Exp. Transl. Stroke Med.* 6:9.

Razavian, R. S., Ghannadi, B., Mehrabi, N., Charlet, M., and Mcphee, J. (2018). Feedback control of functional electrical stimulation for 2-D arm reaching movements. *IEEE Trans. Neural Syst. Rehabil. Eng.* 26, 2033–2043. doi: 10.1109/TNSRE.2018.2853573

Riemer, R., Hsiao-Wecksler, E. T., and Zhang, X. (2008). Uncertainties in inverse dynamics solutions: a comprehensive analysis and an application to gait. *Gait Posture* 27, 578–588. doi: 10.1016/j.gaitpost.2007.07.012

Roman-Liu, D., and Bartuzi, P. (2013). The influence of wrist posture on the time and frequency EMG signal measures of forearm muscles. *Gait Posture* 37, 340–344. doi: 10.1016/j.gaitpost.2012.07.027

Rossi, F., Ros, P. M., Rosales, R. M., and Demarchi, D. (2020). Embedded bio-mimetic system for functional electrical stimulation controlled by event-driven sEMG. *Sensors* 20:1535. doi: 10.3390/s20051535

Ruiz-Olaya, A. F., Lopez-Delis, A., and Da Rocha, A. F. (2019). "Using orientation sensors to control a fes system for upper-limb motor rehabilitation," in *Bioinformatics and Biomedical Engineering*, eds I. Rojas and F. Ortuno (Cham: Springer).

Schick, T., Schlake, H.-P., Kallusky, J., Hohlfeld, G., Steinmetz, M., Tripp, F., et al. (2017). Synergy effects of combined multichannel EMG-triggered electrical stimulation and mirror therapy in subacute stroke patients with severe or very severe arm/hand paresis. *Restor. Neurol. Neurosci.* 35, 319–332.

Song, R., Tong, K.-Y., Hu, X., and Zhou, W. (2013). Myoelectrically controlled wrist robot for stroke rehabilitation. *J. Neuroeng. Rehabilit.* 10, 1–8. doi: 10.1186/1743-0003-10-52

Summers, J., Garry, M., Kagerer, F., Hiraga, C., and Loftus, A. (2004). "Bilateral training and recovery of upper arm function after stroke," in *Proceedings of the Xth International Symposium on Motor Control*, Sofia.

Wang, H., Bi, Z., Zhou, Y., Li, F., Wang, K., Lu, X.-Y., et al. (2021). Wearable and wireless distributed multi-site fes prototype for selective stimulation and fatigue reduction: a case study. *Radioengineering* 30:227.

Xiao, L., Yu, Z., and Mao, M. (2018). Contralaterally controlled functional electrical stimulation improves wrist dorsiflexion and upper limb function in patients with early-phase stroke: a randomized controlled trial. *Ann. Phys. Rehabil. Med.* 61:e36.

Yu, Y., Chen, C., Zhao, J., Sheng, X., and Zhu, X. (2021). Surface electromyography image-driven torque estimation of multi-dof wrist movements. *IEEE Trans. Ind. Electron.* 69, 795–804.

Zhao, X., Wang, Z., Xu, R., and Ming, D. (2021). "A real-time sEMG-based control strategy and system for contralaterally controlled functional electrical stimulation," in *Proceedings of the 2021 IEEE International Conference on Robotics and Biomimetics (ROBIO)*, (Piscataway, NJ: IEEE), 785–789.

Zhou, Y. X., Wang, H. P., Bao, X. L., Lu, X. Y., and Wang, Z. G. (2016). A frequency and pulse-width co-modulation strategy for transcutaneous neuromuscular electrical stimulation based on sEMG time-domain features. *J. Neural Eng.* 13:016004. doi: 10.1088/1741-2560/13/1/016004

Zhou, Y., Zeng, J., Li, K., Hargrove, L. J., and Liu, H. (2020). sEMG-driven functional electrical stimulation tuning *via* muscle force. *IEEE Trans. Ind. Electron.* 68, 10068–10077.

Zhuang, C., Marquez, J. C., Qu, H., He, X., and Lan, N. (2015). "A neuromuscular electrical stimulation strategy based on muscle synergy for stroke rehabilitation," in *Proceedings of the 2015 7th International IEEE/EMBS Conference on Neural Engineering (NER)*, (Piscataway, NJ: IEEE), 816–819. doi: 10.1109/RBME.2018.2874132

Conflict of Interest: The authors declare that the research was conducted in the absence of any commercial or financial relationships that could be construed as a potential conflict of interest.

frontiers | Frontiers in Neuroscience

TYPE Original Research
PUBLISHED 24 August 2022
DOI 10.3389/fnins.2022.944291

OPEN ACCESS

EDITED BY
Yao-Chuan Chang,
Feinstein Institute for Medical Research, United States

REVIEWED BY
Hao Wang,
Shenzhen Institutes of Advanced Technology (CAS), China
Heng Li,
Shanghai Jiao Tong University, China

*CORRESPONDENCE
Lin Meng
linmeng@tju.edu.cn
Dong Ming
richardming@tju.edu.cn

†These authors have contributed equally to this work

SPECIALTY SECTION
This article was submitted to Neural Technology, a section of the journal Frontiers in Neuroscience

RECEIVED 15 May 2022
ACCEPTED 26 July 2022
PUBLISHED 24 August 2022

CITATION
Dong H, Hou J, Song Z, Xu R, Meng L and Ming D (2022) An adaptive reflexive control strategy for walking assistance system based on functional electrical stimulation.
Front. Neurosci. 16:944291.
doi: 10.3389/fnins.2022.944291

An adaptive reflexive control strategy for walking assistance system based on functional electrical stimulation

Hongtao Dong[1†], Jie Hou[1†], Zhaoxi Song[1], Rui Xu[1,2], Lin Meng[1]* and Dong Ming[1,2]*

[1]Academy of Medical Engineering and Translational Medicine, Tianjin University, Tianjin, China, [2]Department of Biomedical Engineering, College of Precision Instruments and Optoelectronics Engineering, Tianjin University, Tianjin, China

Functional electrical stimulation (FES) neuroprostheses have been regarded as an effective approach for gait rehabilitation and assisting patients with stroke or spinal cord injuries. A multiple-channel FES system was developed to improve the assistance and restoration of lower limbs. However, most neuroprostheses need to be manually adjusted and cannot adapt to individual needs. This study aimed to integrate the purely reflexive FES controller with an iterative learning algorithm while a multiple-channel FES walking assistance system based on an adaptive reflexive control strategy has been established. A real-time gait phase detection system was developed for accurate gait phase detection and stimulation feedback. The reflexive controller generated stimulation sequences induced by the gait events. These stimulation sequences were updated for the next gait cycle through the difference between the current and previous five gait cycles. Ten healthy young adults were enrolled to validate the multiple-channel FES system by comparing participants' gait performance to those with no FES controller and purely reflexive controller. The results showed that the proposed adaptive FES controller enabled the adaption to generate fitted stimulation sequences for each participant during various treadmill walking speeds. The maximum, minimum, and range of motion (ROM) of the hip, knee, and ankle joints were furtherly improved for most participants, especially for the hip and knee flexion and ankle dorsiflexion compared with the purely reflexive FES control strategy. The presented system has the potential to enhance motor relearning and promote neural plasticity.

KEYWORDS

functional electrical stimulation (FES), lower limbs, neurorehabilitation, gait assistance, adaptive reflexive control strategy

Introduction

Stroke is a neurological disorder with the world's highest prevalence. The number of patients with stroke in 2017 was over 100 million, which has almost doubled compared with 1990 (Arnao et al., 2016; Avan et al., 2019). About 80–90% of patients with stroke suffer from gait disorders, affecting their life quality and bringing heavy economic burdens to the patient's families and society (Schaechter, 2004; Hara, 2013; Shmuel et al., 2013; Mountain et al., 2020). Functional electrical stimulation (FES) is a technology that applies low-energy electrical pulses to the muscle resulting in active muscle contraction and further functional limb movements (Lynch and Popovic, 2008a). Electrical stimulation has been proven to increase muscle force, promote neuroplasticity, and enhance rehabilitation outcomes and is regarded as an effective rehabilitation treatment for gait disorders (Shin et al., 2022). However, most FES systems employ an open-loop control strategy with a constant stimulation mode in the market (Krishnamoorthy et al., 2008; Bulea et al., 2013; Chang et al., 2017). The open-loop control method has a simple computation and quick response advantage, but the constant stimulation mode cannot be adjusted for patients' assistance requirements in real-time. It may cause inadequate muscle activations and poor limb coordination.

The close-loop FES control strategy integrates feedback information, such as joint angles, electromyography (EMG), and human-machine interactive moment to adjust stimulation parameters based on the desired joint angle or moment trajectories. Seel et al. (2016) applied an iterative learning control (ILC) method to adjust the FES parameters based on inertial data to reduce muscle fatigue effectively. Jailani et al. (2010) proposed a knee biomechanical model that combined the joint trajectory control and fuzzy logic control, where the electrical pulse width was adjusted with the feedback of angle difference. However, as the human neuromuscular system is highly nonlinear (Dietz, 1992; Nielsen, 2002), the pure trajectory control model may not be readily applied to a real-time FES assistance system under various scenarios (Shiavi et al., 1987; Perry et al., 1995; Chen et al., 2018).

Some studies adopted biological-inspired control mechanisms in FES control strategies. Zhang et al. proposed a novel central pattern generator (CPG) based model to generate primary bipedal gaits in an FES walking system (Zhang et al., 2015). A long short-term memory (LSTM) neural network, proposed by Li et al. (2021), was used for predicting synchronous tibialis anterior (TA) EMG based on real-time angular velocity where the TA stimulation intensity was further modulated. Meng et al. proposed a purely reflexive control model to generate multiple electrical stimulation sequences (Meng et al., 2017). The gait events were mapped to muscle activity output during human walking. The model was realized to smooth limb coordination for walking assistance and reduce computational burden, making it straightforward to implement in practice. However, the stimulation parameters must be set before use and cannot be adjusted in real-time.

To further enhance the effectiveness of FES walking assistance, especially for meeting individuals' assistance needs under various walking speeds, we proposed a multiple-channel FES walking assistance system with an adaptive reflexive control method where the electrical stimulation parameters can be adjusted to temporal gait parameters and sagittal shank angle. A validation experiment was conducted by recruiting ten healthy young participants to walk on a treadmill at various speeds wearing the FES system. The gait performance under different stimulation control strategies (purely reflexive controller vs. adaptive reflexive controller) was compared and investigated.

Methods

Hardware design

As shown in Figure 1, the FES system consists of a self-designed real-time gait phase detection system, an 8-channel programmable electrical stimulation device (RehaStim 2, HASOMED GmbH, Germany), and a host computer (Intel 6 Core i7-8750H, 2.20 GHz, and Windows 10 system).

The wearable real-time gait phase detection system includes force-sensitive resistors (FSR) embedded in shoe insoles and an inertial measurement unit (IMU; JY901, Witmotion, Shenzhen, China), as shown in Figure 1. The 6-axis IMU consists of an accelerometer and a gyroscope measuring acceleration and angular rate along three orthogonal axes. The STM32 chip (STM32F103C8T6, Witmotion, Shenzhen, China) is used for data acquisition, gait event detection, and communication with the host computer *via* Bluetooth 2.0.

The algorithms described in the following sections have been implemented in a C++ program and Qt software. The RehaStim 2 consists of eight electrical stimulation channels based on two separately controlled modules and is connected to the host computer through a USB 3.1. The electrical stimulation parameters, such as stimulation frequency, pulse width (PW), and pulse amplitude, can be controlled by the host computer *via* the ScienceMode2 communication protocol in real-time.

FES reflexive control strategy

Four muscles were selected for each leg, namely, tibialis anterior (TA), lateral gastrocnemius (LG), biceps femoris (BF), and rectus femoris (RF). The muscles are associated with the flexion/extension of the hip, knee, and ankle during walking. The reflexive control strategy generates stimulation sequences of eight muscles based on the event impulses from the gait phase detection system. A hierarchical FES controller is shown in Figure 2. The top level employs a finite state control model where the state function S switches on and off the stimulation of muscles for movement coordination. In the low level, the transfer function H generates the impulse responses for stimulation amplitude by convolving with an event impulse.

The transfer function H is a second-order low-pass Bessel filter, as shown below.

$$H(t) = \left(g \frac{1}{\tau} e^{\frac{-1.5t}{\tau}} \sin\left(\frac{\sqrt{3}t}{2\tau} \right) \right)$$

The τ is the time coefficient derived from the filter cut-off frequency and determines the profile of the impulse response. The g is the gain coefficient, normalizing the impulse response to 0 and 1.

The state functions are responsible for switching on/off the electrical stimulation according to five detected gait phases: load response (LR), stance (ST), pre-swing (PS), swing (SW), and terminal swing (TSW).

$$S_{TA} = \begin{cases} 1, & state = SW \text{ } or \text{ } TSW \\ 0, & otherwise \end{cases}$$

$$S_{BF} = \begin{cases} 1, & state = SW \text{ } or \text{ } TSW \\ 0, & otherwise \end{cases}$$

$$S_{LG,LR} = \begin{cases} 1, & state = LR \\ 0, & otherwise \end{cases}$$

$$S_{LG,PS} = \begin{cases} 1, & state = PS \\ 0, & otherwise \end{cases}$$

$$S_{RF,LR} = \begin{cases} 1, & state = LR \\ 0, & otherwise \end{cases}$$

$$S_{RF,TSW} = \begin{cases} 1, & state = TSW \\ 0, & otherwise \end{cases}$$

The FES sequences of eight muscles generated by the reflexive controller during treadmill walking are shown in Figure 3. The generation of electrical stimulation patterns elicited by impulse signals for each muscle is expressed as follows:

$$\begin{aligned} C_{TA} &= \left(H_{TA,LR} * I_{SW} \cdot \Delta_{cTA} + C_{TA,\min}\right) \cdot S_{TA} \\ C_{LG} &= \left(H_{LG,LR} * I_{LR} \cdot \Delta_{cLG} + C_{LG,\min}\right) \cdot S_{LG,LR} \\ &\quad + \left(H_{LG,PS} * I_{PS} \cdot \Delta_{cLG} + C_{LG,\min}\right) \cdot S_{LG,PS} \\ C_{BF} &= \left(H_{BF,SW} * I_{SW} \cdot \Delta_{cBF} + C_{BF,\min}\right) \cdot S_{BF} \\ C_{RF} &= \left(H_{RF,LR} * I_{LR} \cdot \Delta_{cRF} + C_{RF,\min}\right) \cdot S_{RF,LR} \\ &\quad + \left(H_{RF,TSW} * I_{TSW} \cdot \Delta_{cRF} + C_{RF,\min}\right) \cdot S_{RF,TSW} \end{aligned}$$

where, I is the gait event impulse generated from gait phase transitions, *and* H is the transfer function that generates the response output by convolving with the impulse input I. The Δ_c is the difference between $C_{\max}$ and $C_{\min}$ where $C_{\max}$ is the maximum threshold current amplitude that can produce a maximal muscle contraction without any discomfort, and $C_{\min}$ is the minimum threshold current amplitude that can elicit a visible muscle contraction. The values of $C_{\max}$ and $C_{\min}$ for each muscle were measured in a preparation experiment for every participant, detailed in Appendix 1 document.

Gait phase detection

An IF-THEN type finite state machine was employed to detect five gait events, namely, heel strike (HS), foot flat (FF), heel off (HO), toe off (TO), and sagittal threshold angle (STA). These gait events are furtherly used to define gait phases, such as LR, ST, PS, SW, and TSW. The sensory signals include foot contact signals from FSRs and angle signals from the IMU attached to the shank. An adaptive threshold method is used to convert the inputs to binary signals. The S_H and S_T are binary signals representing the heel and toe contact states where the logic value of 1 indicates that the heel or toe is in contact with the ground, and 0 indicates that it is off the ground. The binary signal S_ϕ represents the state of sagittal shank angle (ϕ_S) during the swing phase ($S_H = S_T = 0$). It determines the initiation of TSW when a participant extends the knee to prepare to strike the foot on the floor. Four types of gait impulses, I_{LR}, I_{PS}, I_{SW}, and I_{TSW} are generated for the FES controller based on gait phase transitions, as shown in Figure 2.

I_{LR}: the impulse indicates the initial foot contact with the ground. In normal gait, the heel usually strikes the ground first. However, individuals with a pathological walk may establish foot contact with the forefoot. Therefore, the transition is detected if any foot part touches the ground after the swing phase (last state: $S_H = 0, S_T = 0$; and current state: $S_H = 1$ or $S_T = 1$).

I_{PS} : the transition occurs when the FSR underneath the heel is not pressed, and the forefoot is still in contact with the ground. This event indicates a transition from the stance phase to the pre-swing phase (last state: $S_H = S_T = 1$; and current state: $S_H = 0, S_T = 1$).

I_{SW} : the impulse indicates the transition from the stance or pre-swing phase to the swing phase, where the swing phase is when the foot is lifted entirely off the ground so that no FSRs are pressed (last state: $S_H = 1$ or $S_T = 1$; and current state: $S_H = S_T = 0$).

I_{TSW} : the impulse indicates the transition from the swing phase to the terminal swing phase when the hip flexes forward and the measured ϕ_S reaches its threshold (last state: $S_H = S_T = 0, S_\phi = 0$; and current state: $S_H = S_T = 0, S_\phi = 1$).

Adaptive parameters update

An adaptive method is proposed where the muscle stimulation time t_s and sagittal shank angle at TO (ϕ_{TO}) are used as real-time feedback signals to meet the assistance needs of various gait speeds. The adaptive model updates the time coefficient parameter τ of eight muscles and PW of both LG muscles. The time constant determines the stimulation amplitude profile while the PW of LG muscles modulates the ankle push-off at various speeds (Brockett and Chapman, 2016). These parameters are updated based on the muscle stimulation time and sagittal shank angle of the previous five gait cycles. One

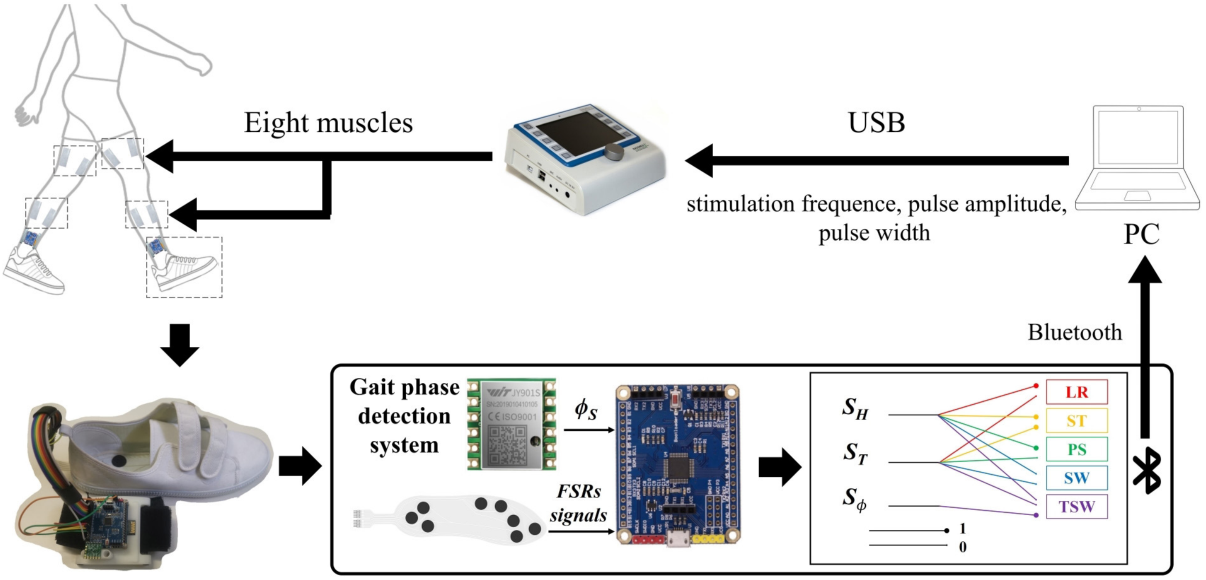

FIGURE 1
The structure of the functional electrical stimulation (FES) walking assistance system. The system consists of three main parts: a programmable electrical stimulator, a real-time gait phase detection device, and a host computer. The FSR-embedded insole and an inertial measurement unit (IMU) chip were connected to an STM32 microcontroller that detected gait phases by an IF-THEN type finite state machine during walking. The sensory signals, including gait phase detection result and shank angle, were transmitted to the host PC *via* Bluetooth. At the same time, the adaptive FES controller generated electrical stimulation sequences for the muscles. The stimulation parameters were adapted and applied to eight muscles by the programmable electrical stimulator RehaStim through a USB 3.1 port.

gait cycle is regarded as the interval between consecutive heel strikes of the same foot (S_H =1, $S_T = 0$).

According to the difference in the stimulation duration time between the previous five gait cycles and the current gait cycle, the closed-loop control model adjusts the corresponding τ to change the muscle stimulation time for the next gait cycle. Take τ_{TA} as an example.

The stimulation of TA is activated during the SW and TSW, as shown in Figure 3. If the stimulation time of TA in the current gait cycle is $t_{TA}\,(n)$, the average stimulation time of the previous five gait cycles can be calculated as $\bar{t}_{TA}$:

$$\bar{t}_{TA} = \frac{1}{5}\sum_{i=1}^{5} t_{TA}\,(n-i)$$

The difference between the t_{TA} and $\bar{t}_{TA}$ can be calculated as $\Delta t_{TA} = t_{TA}\,(n) - \bar{t}_{TA}$. If $|\Delta t_{TA}| > 0.04$ s, the time coefficient τ_{TA} is updated as follows:

$$\tau_{TA}\,(n+1) = \begin{cases} \tau_{TA}\,(n) + L\,\Delta t_{TA} < -0.04s \\ \tau_{TA}\,(n) - L\,\Delta t_{TA} > 0.04s \end{cases}$$

where, $\tau_{TA}\,(n+1)$ is the transfer function time coefficient of the next gait cycle and $\tau_{TA}\,(n)$ is the transfer function time coefficient of the current gait cycle. As the response time of the transfer function fitted by a second-order low-pass Bessel filter is about one-fourth of the overall activation time, the update threshold is set as 0.04 with an iterative learning step L of 0.01. In addition, the value of τ is limited between 0.01 and 1 due to the requirement of muscle response time for movement coordination during human walking.

According to the second-order low-pass Bessel filter properties of the transfer function $H_{TA,TO}$, the cut-off frequency f_c can be calculated based on the time coefficient:

$$f_c = \frac{1}{2\pi * \tau}$$

Eventually, the cut-off frequency $f_{c,TA,TO}$ is updated to the adaptive reflexive controller for adjusting the amplitude stimulation profile of C_{TA}. The same procedure is applied to all muscles. The update progress is shown in Figure 4A.

Similarly, according to the $\overline{\phi}_{TO}$ of previous five gait cycles and the ϕ_{TO} of the current gait cycle, the PW values of both LG of the next gait are interactively updated:

$$PW_{LG}\,(n+1) = \begin{cases} PW_{LG}\,(n) + L_{PW} \quad \Delta\phi_{TO} < -2^{\circ} \\ PW_{LG}\,(n) - L_{PW} \quad \Delta\phi_{TO} > 2^{\circ} \end{cases}$$

where, $PW_{LG}\,(n+1)$ is the PW of LG muscle for the next gait cycle, $PW_{LG}\,(n)$ is the stimulation pulse width at the current gait. $\Delta\phi_{TO} = \phi_{TO}(n) - \overline{\phi}_{TO}$. The step L_{PW} of iterative learning is set to 20 μs. Additionally, the limited range of PW_{LG} is set between 250 and 500 μs. The update process is shown in Figure 4B.

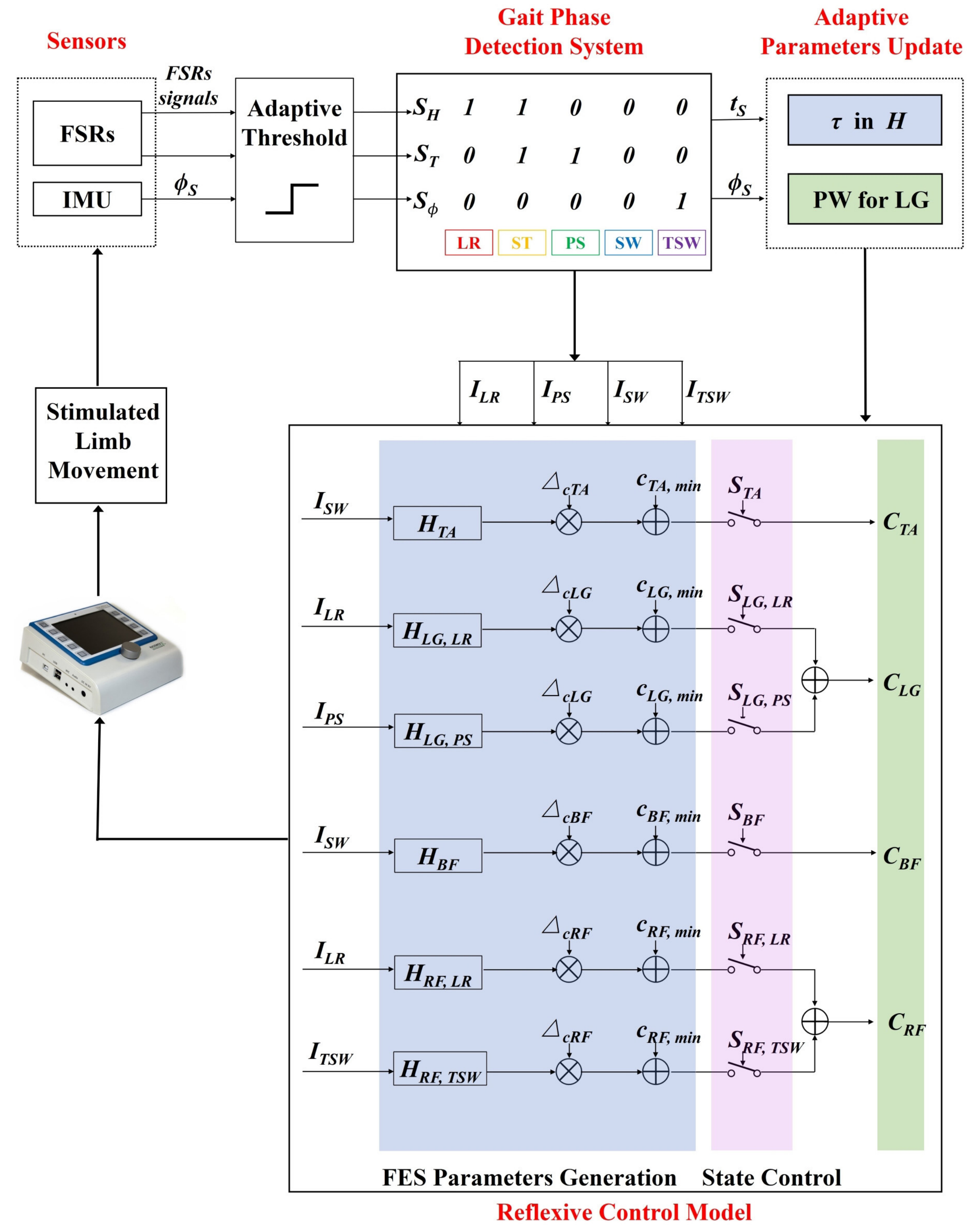

FIGURE 2

The adaptive reflexive FES control diagram. Input signals are first translated into binary signals by an adaptive threshold. Gait phases are identified based on a rule-based machine learning algorithm. Gait event impulses are generated when specific gait transitions between gait phases occur. A hierarchical FES control model consists of two levels of control where the top level switches the stimulation state of muscles, and the low level generates the stimulation sequences. The time constant parameter τ and stimulation pulse width are adaptively updated with an iterative learning method in the low level controller based on the real-time feedback of muscle stimulation time t_s and sagittal shank angle ϕ_{TO}, respectively. LR, load response; ST, stance; PS, pre-swing; SW, swing; TSW, terminal swing.

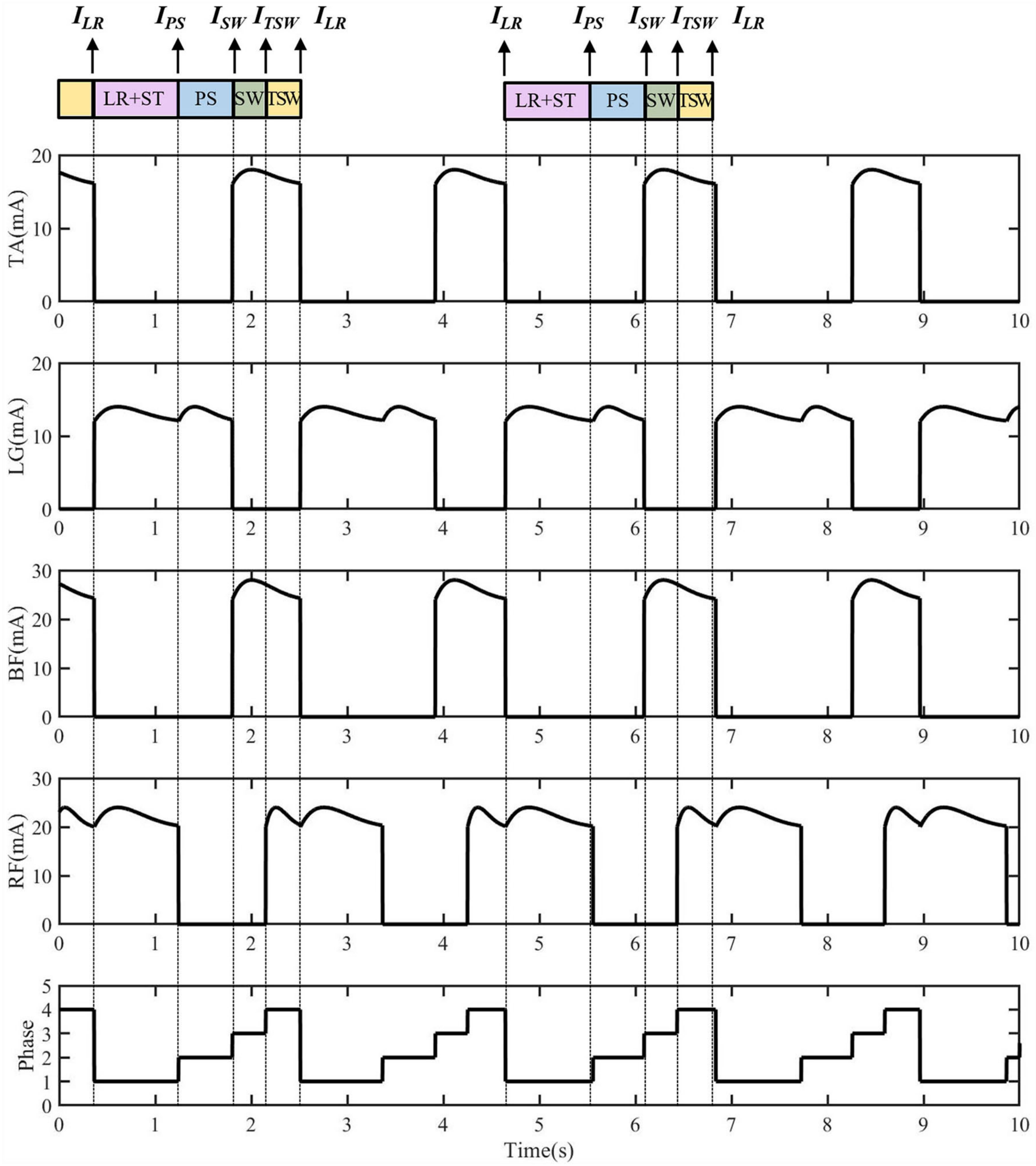

FIGURE 3
The electrical stimulation sequences for four muscles of one side generated from the reflexive FES controller. The I_{LR} triggered the lateral gastrocnemius (LG) and rectus femoris (RF) muscle activations for the knee extension and hip flexion. The I_{PS} triggered the LG muscle for ankle plantarflexion. The I_{SW} triggered the tibialis anterior (TA) and biceps femoris (BF) muscles for the ankle dorsiflexion, knee flexion, and hip extension at early swing. The I_{TSW} triggers TA, RF, and BF muscles for the preparation of load response.

Experiment

Experimental set-up

For this experiment, ten healthy young adults (ten men) were recruited. The mean [±standard deviation (SD)] age was 25.1 (±1.6) years, and the mean (±SD) height was 177.3 (±5.83) cm, as shown in Table 1. The participants were fully informed of the procedure and gave written consent before the experiment. The study was approved by the Ethics Committee of Tianjin University and was conducted in the Motion Rehabilitation Laboratory of Tianjin University.

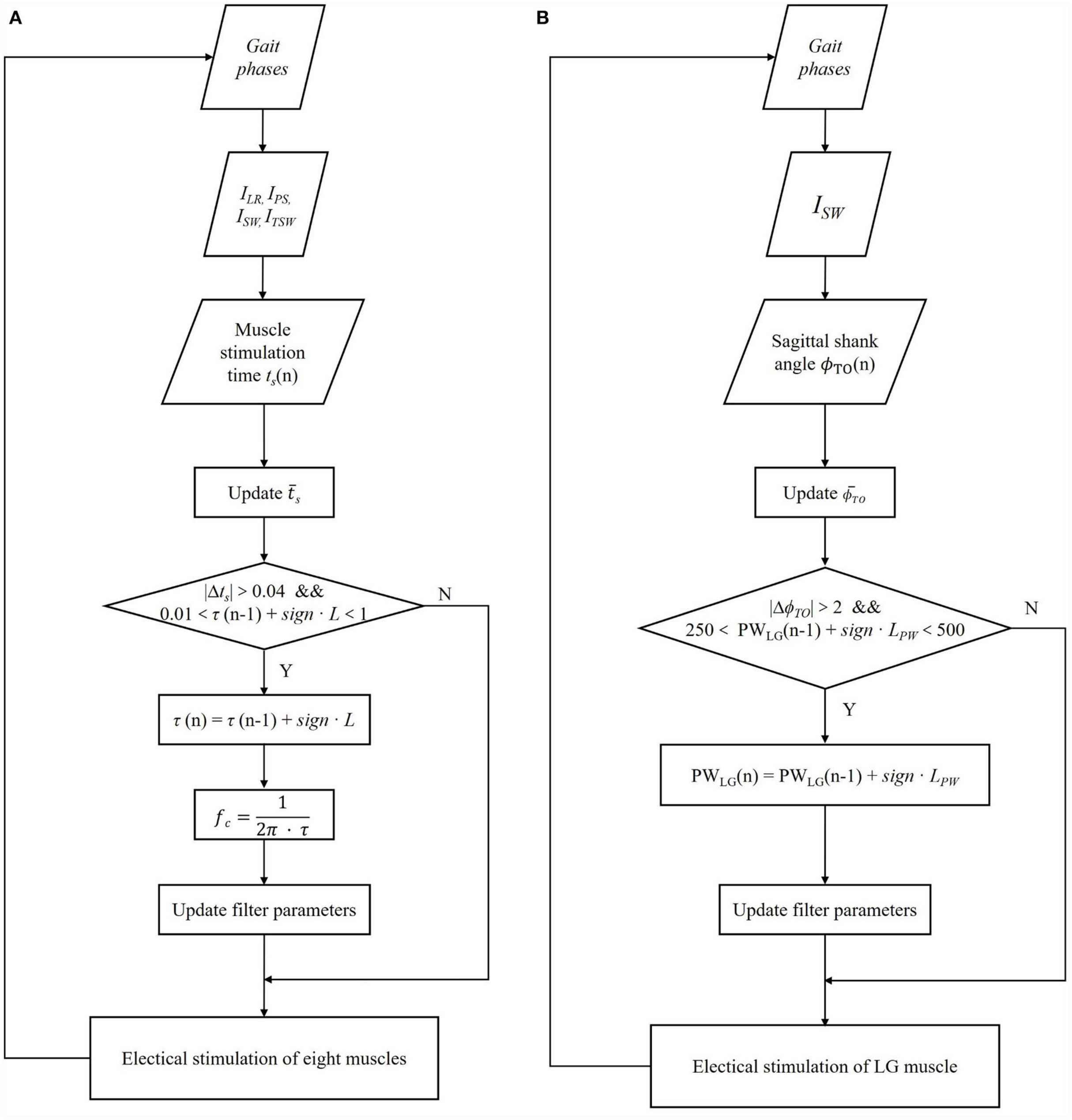

FIGURE 4
Block diagram of the iterative learning control algorithm for transfer function time constant coefficient τ of all eight muscles **(A)** and pulse width parameter of two lateral gastrocnemius muscles (LG) **(B)** based on each gait cycle.

Eight muscles were selected in the experiment: RF, BF, LG, and TA of both legs, to augment hip, knee, and ankle flexion/extension, respectively. Electrical stimulation electrodes were placed on the muscles, and the $C_{\max}$ and $C_{\min}$ of every muscle were measured in the preparation session. The measurement procedure and results are shown in Appendix 1 document. Participants wore shorts and gait detection devices. The Vicon Plug-in-Gait (PiG) model was used to evaluate the gait performance of the participants where retroreflective markers were attached to the anterior superior iliac spine, the posterior superior iliac spine, thigh, knee, ankle, tibial wand, heel, and toe of both sides, as shown in Figure 5.

The participants were instructed to walk on a treadmill under three different conditions: (1) without FES controller (NFC); (2) with a purely reflexive FES controller (RFC); and (3) with an adaptive reflexive FES controller (ARFC). In each

TABLE 1 Participants' demographic information.

Subjects	Gender	Age (years)	Height (cm)	Weight (kg)
A	M	26	174	80
B	M	27	175	78
C	M	26	176	76
D	M	25	181	67
E	M	25	170	69
F	M	25	181	60
G	M	24	188	78
H	M	26	185	85
I	M	26	172	70
J	M	21	171	62

M, male.

session, the treadmill walking speed increased from 1.0 to 2.0 km/h and then decreased to 1.0 km/h with an incrementation step of 0.2 km/h. The participants needed to complete at least 15 gait cycles at each speed. The host computer collected stimulation parameters, detected gait phases, and shank angle information while the Vicon Nexus software captured marker trajectories with a sampling rate of 100 Hz. The Vicon Lock Sync device was used to synchronize the collected data.

Data analysis

Joint kinematic data of the hip, knee, and ankle were obtained using the PiG model. One gait cycle data were time-normalized to 0–100% with 101 samples. A total of 165 gait cycles were extracted for each participant. The maximum and minimum of the hip, knee, and ankle were calculated based on gait cycles and investigated using a one-way analysis of variance (ANOVA) with stimulation pattern as the main factor. A paired t-test was performed to evaluate the difference in gait kinematics under three stimulation conditions. All statistical analyses were performed using the MATLAB Statics Toolbox (MATLAB2020a, The MathWorks, USA). Statistical significance was set as $p < 0.05$.

Results

Table 2 showed that the real-time gait event detection algorithm obtained an accuracy rate of 100% to identify all five gait phases, and the average delay time was less than 20 ms. The FES sequences for eight muscles were generated from the transfer functions triggered by the gait event impulses during treadmill walking, as shown in Figure 3. Figure 6 shows that the time coefficient $\tau_{TA,TO}$ and pulse width of LG muscles were adaptively adjusted with various walking speeds during one participant's trial. We can see that the rise time of the stimulation pattern responded more quickly at 2.0 km/h speed compared with those at slower speeds indicating that the ARFC can efficiently adjust the stimulation pattern according to the change in walking speeds.

Joint kinematics were compared under three stimulation conditions for all participants, as shown in Figure 7. Results showed that both stimulation control strategies (RFC and ARFC) did not hinder normal gait patterns (Figure 7) and significantly promoted the joint movement, as shown in Figure 7 and Table 3. The participants achieved larger flexion and extension of the hip and knee as the electrical stimulation applied to the RF and BF muscles helped in promoting the joint movement (Table 3). The electrical stimulation on the TA muscle led to a higher ankle maximum angle than that without FES assistance. It can also be observed that the ARFC has a better promoting effect than the RFC in all joint kinematic parameters. The participants obtained a larger ROM of the hip (RFC: 35.16 ± 3.92; ARFC: 37.85 ± 4.99), knee (RFC: 54.34 ± 8.05; ARFC: 59.54 ± 8.20), and ankle (RFC: 22.44 ± 6.52; ARFC: 25.07 ± 6.36) with the ARFC compared with the RFC. The ankle push-off at the terminal stance was also increased during the ARFC trial (RFC: −10.81 ± 7.76; ARFC: −13.92 ± 7.95). The results indicated that the proposed ARFC method could provide better gait assistance at different speeds.

Discussion

The FES is an effective technique to restore gait functions for patients with motor disorders (Lynch and Popovic, 2008b; Popovic, 2014). Due to the disturbances from internal time-varying muscle characteristics with electrical stimulation and external environmental uncertainties, most current FES systems used pre-set stimulation patterns and parameters and mainly focused on the drop foot correction. Patients may not achieve satisfactory gait performances due to the low adaptability of FES control strategies (Krishnamoorthy et al., 2008; Bulea et al., 2013; Chang et al., 2017). Therefore, accurate gait phase detection and adaptive control strategy are the critical parts of high adaptability to provide efficient walking assistance and rehabilitation.

A wearable real-time gait phase detection device integrating the FSRs-embedded shoe insole and IMU was developed. The reliability and feasibility of the combination of the FSRs and IMU in gait phase detection have been proved in previous studies (Prasanth et al., 2021). The FSRs can provide the most reliable information about foot contact conditions (Hanlon and Anderson, 2009), and the data from the inertial sensor added the information during the swing. Therefore, the combination of FSRs and IMU enables the identification of multiple gait phases during a gait cycle. Pappas et al. (2001) reported above 96% detection accuracy of HS, FF, HO,

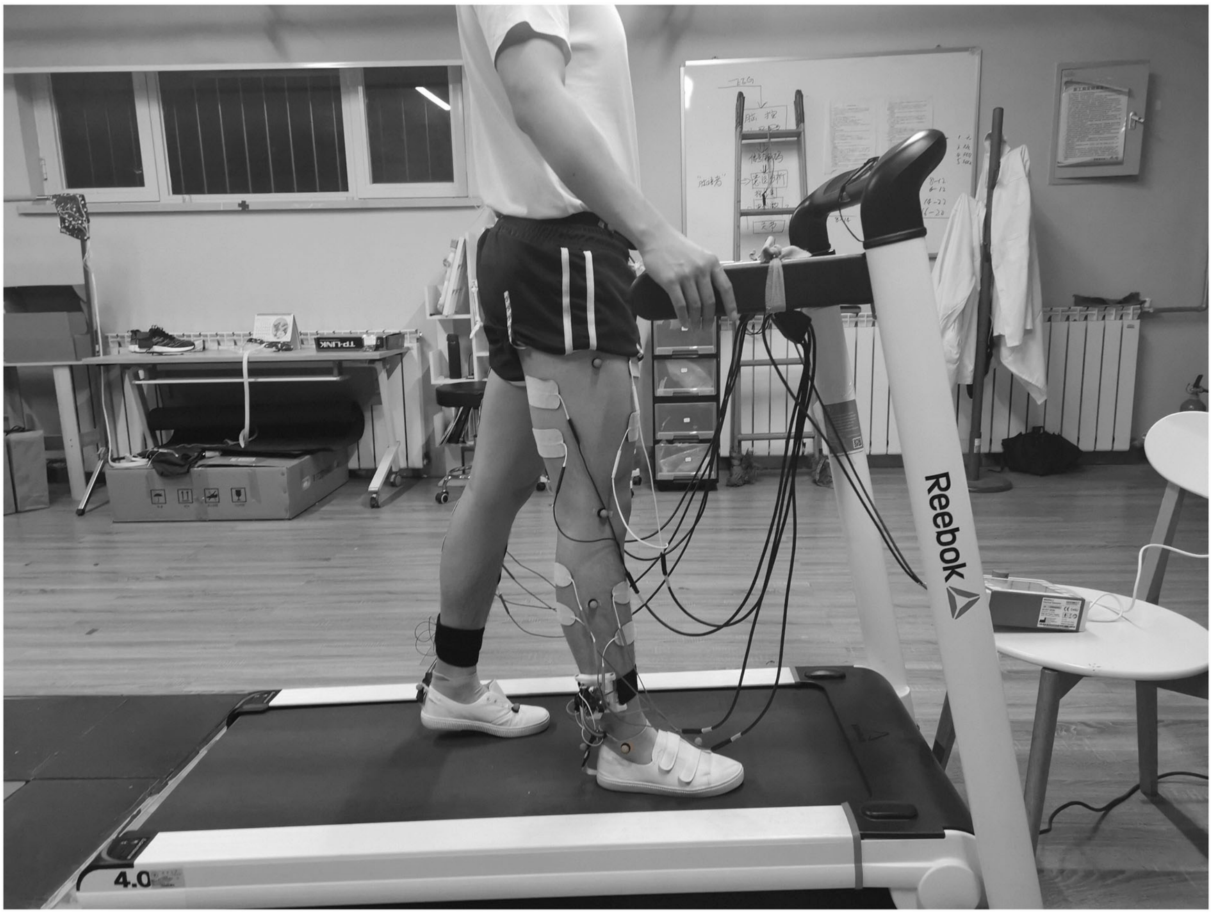

FIGURE 5
Schematic of the experimental setup: a participant walked on the treadmill wearing real-time gait detection devices. Electrical stimulation electrodes were attached to the eight muscles, and the retroreflective markers were placed on the lower limbs.

TABLE 2 Accuracy and time latency for gait event detection during various speeds.

Speed (km/h)	Total stride number	Gait events	Accuracy (%)	Average latency (ms)
1.0 ∼ 1.4	900	HS	100	9.6
		HO	100	14.4
		TO	100	13.9
		STA	100	10.5
1.6 ∼ 2.0	750	HS	100	10.1
		HO	100	21.4
		TO	100	15.0
		STA	100	17.3

HS, heel strike; HO, heel off; TO, toe off; STA, the shank angle ϕ_S reached its threshold during the swing.

and TO for both unimpaired and pathological gait with a detection delay of less than 90 ms using a threshold-based method. Sui et al. (2020) proposed a Convolutional Neural Network (CNN)-based gait detection algorithm, which achieved an average error of 8.86 ms for the TO detection and 9.12 ms for the HS, and a gait phase detection accuracy of 96.44% on healthy subjects. Our study proposed a rule-based machine learning algorithm for identifying five gait phases: HS, FF, HO, TO, and STA. The real-time performance achieved an accuracy rate of 100% and an average delay of less than 20 ms.

Multiple-channel FES systems with adaptive control methods were proposed in previous studies (Ladouceur and Barbeau, 2000; Johnston et al., 2003; Kesar et al., 2011; Street et al., 2015; Miller et al., 2016; da Cunha et al., 2021). Mueller et al. (2020) proposed an FES system-based ILC in which individual fitted stimulation patterns of the antagonistic muscle pairs for the knee and ankle joints were generated by warping healthy subjects' physiological joint angles trajectories. The experimental results showed slight improvements in the peak joint angles in the range of 4 degrees on three of four spinal cord injured subjects. Jiang et al. (2020) proposed an adaptive

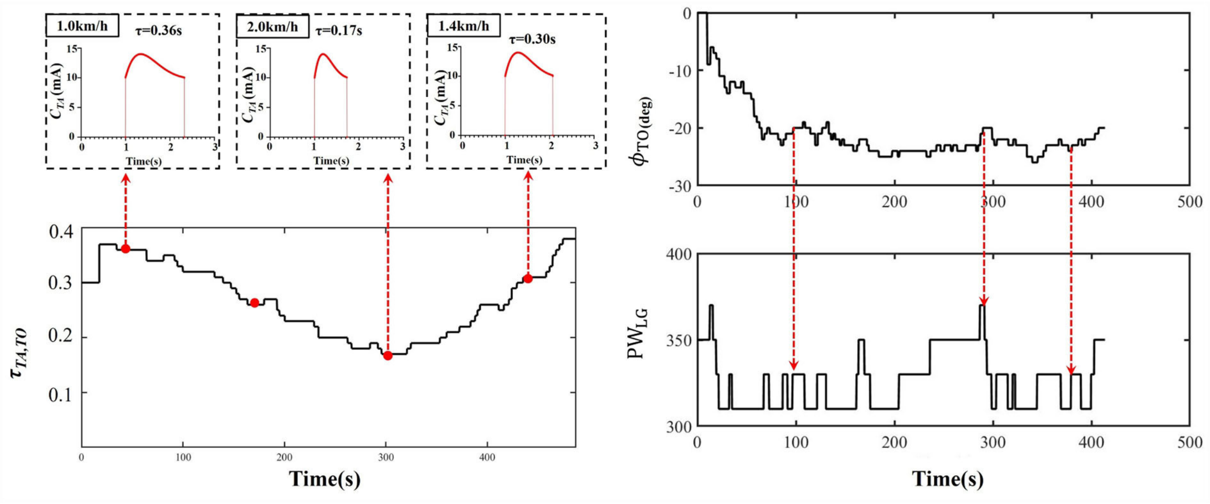

FIGURE 6

An example of the time constant coefficient $\tau_{TA,TO}$ of TA muscle and pulse width (PW) of LG muscle over in a trial of one participant with walking speed varying from 1.0 to 2.0 km/h.

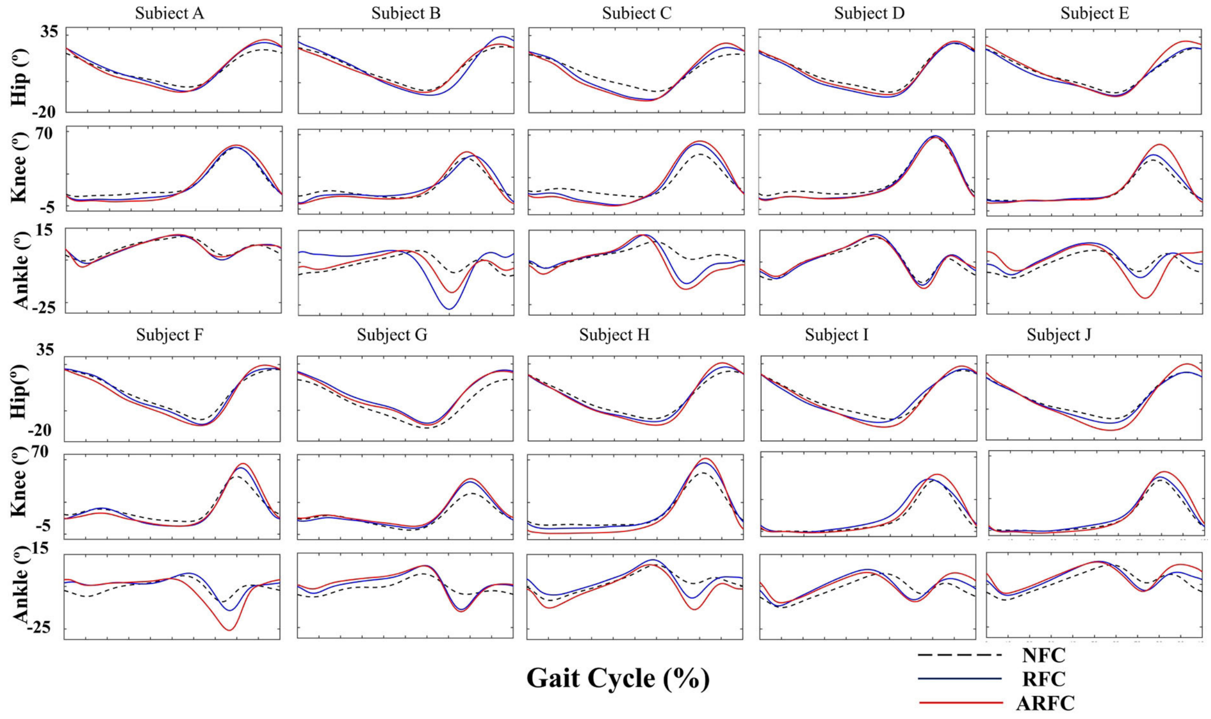

FIGURE 7

Joint kinematics of the hip, knee, and ankle joints under three different stimulation conditions for individual participants.

FES control method that employed a linear model with ILC to adjust the stimulation timing and intensity according to the average walking speed and the error between the actual maximum ankle dorsiflexion and target angle. Their proposed control method obtained a better orthotic effect for foot drop correction than the performance with constant pre-set stimulation parameters. However, these FES control strategies required complex calibration procedures and complicated

TABLE 3 Effects of stimulation condition on joint kinematic parameters using one-way analysis of variance (ANOVA).

Kinematic parameters (°)	NFC	RFC	ARFC	F-value	*P*-value
Hip maximum	23.69 ± 3.40	26.26 ± 3.24	27.87 ± 3.17	679.4	<0.0001
Hip minimum	−6.60 ± 2.78	−8.87 ± 2.501	−10.04 ± 3.19	620.5	<0.0001
Hip ROM	30.28 ± 4.07	35.16 ± 3.92	37.85 ± 4.99	1264	<0.0001
Knee maximum	53.23 ± 9.27	58.44 ± 8.59	62.62 ± 7.55	502.8	<0.0001
Knee minimum	6.59 ± 5.11	4.14 ± 3.82	3.16 ± 4.30	258.4	<0.0001
Knee ROM	46.64 ± 8.46	54.34 ± 8.05	59.54 ± 8.20	1016	<0.0001
Ankle maximum	8.47 ± 2.73	10.74 ± 2.78	10.40 ± 3.38	275.1	<0.0001
Ankle minimum	−7.45 ± 3.82	−11.69 ± 6.89	−14.55 ± 7.15	549.7	<0.0001
Ankle ROM	15.93 ± 4.00	22.44 ± 6.52	25.07 ± 6.36	1088	<0.0001
Ankle minimum during TS	−2.35 ± 5.22	−10.81 ± 7.76	−13.92 ± 7.95	1165	<0.0001

NFC, no FES controller; RFC, reflexive FES controller; ARFC, adaptive reflexive FES controller.

mathematical models. Compared with these complicated models, the biological-inspired FES strategies have shown their advantages in motor relearning and simplicity in modeling (Meng et al., 2017). However, the purely RFC cannot adjust the stimulation pattern for participants' individual needs during various walking speeds. This study was the first attempt to integrate the purely RFC and iterative learning algorithm and develop a multiple-channel FES walking assistance system based on an adaptive reflexive control strategy. An adaptive algorithm based on the iterative learning method was proposed to adjust the electrical stimulation parameters corresponding to muscle stimulation time and sagittal shank angle. A multiple-channel FES system was established, and the validation experiment was performed by recruiting healthy young adults. The results showed that the ARFC method achieved a better promoting effect on joint kinematics during treadmill walking than the pure RFC controller at various speed conditions.

The functionality of the ARFC was evaluated in a validation experiment involving ten healthy young male participants compared with their gait performance under the NFC and RFC stimulation conditions. The participants did not report any discomfort or disturbance during treadmill walking with the stimulation applied. The FES control strategy provided a correct muscle activation sequence consistent with the participant's voluntary movements. The ARFC significantly improved the maximum, minimum, and ROM for most participants compared with the RFC. The ankle plantarflexion angle using the ARFC was significantly larger than the RFC, indicating that the adaptive change of time constant coefficient τ and PW increased the ankle push-off and further promoted walking speed. The ankle plantarflexion and knee flexion play a critical role in generating forward propulsion (Neptune et al., 2001; Anderson et al., 2004), and the patients often exhibited a reduction in the ankle and knee movements (Bhadra et al., 2001; Kesar et al., 2010). The ARFC also achieved a larger knee and hip flexion angle in early swing, which would help improve foot clearance and leg swing. It may provide more appropriate training assistance for patients with a neurological disease with individual stimulation pattern adjustment and potentially enhance motor learning and promote neural plasticity.

There are still some limitations in this study. The experiment only recruited healthy young men, and the subject size was relatively small. The enrolled healthy young subjects have intact motor units and good muscle responses to electrical stimulation compared to patients with stroke who usually have muscular atrophy combined with a damaged perception level (Arasaki et al., 2009; Shin et al., 2022). The affected muscular properties might have a potential influence on the modulation of the stimulation parameters and hinder the performance of the FES assistance (Ambrosini et al., 2014). Moreover, we did not observe effective PW parameter adjustment for LG muscles during treadmill walking. It might be because healthy participants can meet the propulsion need of ankle plantarflexion by voluntary LG muscle contraction, and the scenario of treadmill walking limits the participants' walking variation. The proposed multiple-channel FES needs further validation with stroke patients, and the overground walking experiment should be considered in future studies.

Conclusion

This article proposed a multiple-channel FES walking assistance system with an adaptive reflexive FES control strategy. The validation experiment was performed by recruiting ten healthy young men. Walking performance under three stimulation conditions was investigated and compared. The results showed that the system generates accurate stimulation patterns for each muscle group while the stimulation parameters were successfully further adapted to various walking speeds. The ARFC method significantly improved the maximum, minimum, and ROM of the hip, knee, and ankle joints, especially for the hip and knee flexion and ankle dorsiflexion, compared with the purely RFC strategy. The presented system has the potential to provide efficient gait assistance for patients and promote motor relearning and neural plasticity. Future studies will carry out a clinical experiment to prove the system effect's on patients with stroke.

Data availability statement

The datasets presented in this article are not readily available as the study is still ongoing. Requests to access the datasets should be directed to linmeng@tju.edu.cn.

Ethics statement

The studies involving human participants were reviewed and approved by the Ethics Committee of Tianjin University. The patients/participants provided their written informed consent to participate in this study. Written informed consent was obtained from the individual(s) for the publication of any potentially identifiable images or data included in this article.

Author contributions

LM and DM: conception and design of the study. HD, JH, and ZS: system development and experiments. HD and JH: analysis and interpretation of data and drafting the manuscript. LM: project supervision and manuscript revision. RX: revising the article critically for important intellectual content. DM: project administration. All authors approved the final version to be submitted.

Funding

The work was funded by the National Key R&D Program of China (2020YFC2004300 and 2020YFC2004302), the National Natural Science Foundation of China (82001921), and the Natural Science Foundation of Tianjin (20JCZDC0080).

Conflict of interest

The authors declare that the research was conducted in the absence of any commercial or financial relationships that could be construed as a potential conflict of interest.

Publisher's note

Supplementary material

The Supplementary Material for this article can be found online at: https://www.frontiersin.org/articles/10.3389/fnins.2022.944291/full#supplementary-material

References

Ambrosini, E., Ferrante, S., Schauer, T., Ferrigno, G., Molteni, F., and Pedrocchi, A. (2014). An automatic identification procedure to promote the use of FES-cycling training for hemiparetic patients. *J. Healthc. Eng.* 5, 275–291. doi: 10.1260/2040-2295.5.3.275

Anderson, F. C., Goldberg, S. R., Pandy, M. G., and Delp, S. L. (2004). Contributions of muscle forces and toe-off kinematics to peak knee flexion during the swing phase of normal gait: an induced position analysis. *J. Biomech.* 37, 731–737. doi: 10.1016/j.jbiomech.2003.09.018

Arasaki, K., Igarashi, O., Machida, T., Hyodo, A., and Ushijima, R. (2009). Reduction in the motor unit number estimate (MUNE) after cerebral infarction. *Suppl. Clin. Neurophysiol.* 60, 189–195. doi: 10.1016/S1567-424X(08)00019-6

Arnao, V., Acciarresi, M., Cittadini, E., and Caso, V. (2016). Stroke incidence, prevalence and mortality in women worldwide. *Int. J. Stroke* 11, 287–301. doi: 10.1177/1747493016632245

Avan, A., Digaleh, H., Napoli, M. D., Stranges, S., and Azarpazhooh, M. R. (2019). Socioeconomic status and stroke incidence, prevalence, mortality, and worldwide burden: an ecological analysis from the global burden of disease study 2017. *BMC Med.* 17, 1–30. doi: 10.1186/s12916-019-1397-3

Bhadra, N., Kilgore, K. L., and Peckham, P. H. (2001). Implanted stimulators for restoration of function in spinal cord injury. *Med. Eng. Phys.* 23, 19–28. doi: 10.1016/S1350-4533(01)00012-1

Brockett, C. L., and Chapman, G. J. (2016). Biomechanics of the ankle. *Orthop. Trauma* 30, 232–238. doi: 10.1016/j.mporth.2016.04.015

Bulea, T. C., Kobetic, R., Audu, M. L., Schnellenberger, J. R., and Triolo, R. J. (2013). Finite state control of a variable impedance hybrid neuroprosthesis for locomotion after paralysis. *IEEE Trans. Neural Syst. Rehabil. Eng.* 21, 141–151. doi: 10.1109/TNSRE.2012.2227124

Chang, S. R., Nandor, M. J., Li, L., Kobetic, R., Foglyano, K. M., Schnellenberger, J. R., et al. (2017). A muscle-driven approach to restore stepping with an exoskeleton for individuals with paraplegia. *J. Neuroeng. Rehabil.* 14, 1–12. doi: 10.1186/s12984-017-0258-6

Chen, G., Ma, L., Song, R., Li, L., Wang, X., and Tong, K. (2018). Speed-adaptive control of functional electrical stimulation for dropfoot correction. *J. Neuroeng. Rehabil.* 15, 1–11. doi: 10.1186/s12984-018-0448-x

da Cunha, M. J., Rech, K. D., Salazar, A. P., and Pagnussat, A. S.(2021). Functional electrical stimulation of the peroneal nerve improves poststroke gait speed when combined with physiotherapy. A systematic review and meta-analysis. *Ann. Phys. Rehabil. Med.* 64, 1–11. doi: 10.1016/j.rehab.2020.03.012

Dietz, V. (1992). Human neuronal control of automatic functional movements: interaction between central programs and afferent input. *Physiol. Rev.* 72, 33–69. doi: 10.1152/physrev.1992.72.1.33

Hanlon, M., and Anderson, R. (2009). Real-time gait event detection using wearable sensors. *Gait Posture* 30, 523–527. doi: 10.1016/j.gaitpost.2009.07.128

Hara, Y. (2013). Rehabilitation with functional electrical stimulation in stroke patients. *Int. J. Phys. Med. Rehabil.* 01, 1–6. doi: 10.4172/2329-9096.1000147

Jailani, R., Tokhi, M. O., and Gharooni, S.C. (2010). "Spring brake orthosis for fes-assisted walking with wheel walker," in *International Conference of Modelling and Simulation in Engineering, Economics and Management* (Barcelona), 677–685.

Jiang, C., Zheng, M., Li, Y., Wang, X., Li, L., and Song, R. (2020). Iterative adjustment of stimulation timing and intensity during FES-assisted treadmill walking for patients after stroke. *IEEE Trans. Neural Syst. Rehabil. Eng.* 28, 1292–1298. doi: 10.1109/TNSRE.2020.2986295

Johnston, T. E., Finson, R. L., Smith, B. T., Bonaroti, D. M., Betz, R. R., and Mulcahey, M. J. (2003). Functional electrical stimulation for augmented walking in adolescents with incomplete spinal cord injury. *J. Spinal Cord Med.* 26, 390–400. doi: 10.1080/10790268.2003.11753711

Kesar, T. M., Perumal, R., Jancosko, A., Reisman, D. S., Rudolph, K. S., Higginson, J. S., et al. (2010). Novel patterns of functional electrical stimulation have an immediate effect on dorsiflexor muscle function during gait for people poststroke. *Phys. Ther.* 90, 55–66. doi: 10.2522/ptj.20090140

Kesar, T. M., Reisman, D. S., Perumal, R., Jancosko, A. M., Higginson, J. S., Rudolph, K. S., et al. (2011). Combined effects of fast treadmill walking and functional electrical stimulation on post-stroke gait. *Gait Posture* 33, 309–313. doi: 10.1016/j.gaitpost.2010.11.019

Krishnamoorthy, V., Hsu, W., Scholz, J., Benoit, D., Kesar, T., Perumal, R., et al. (2008). Gait training after stroke: a pilot study combining a gravity-balanced orthosis, functional electrical stimulation, and visual feedback. *J. Neurol. Phys. Ther.* 32, 192–202. doi: 10.1097/NPT.0b013e31818e8fc2

Ladouceur, M., and Barbeau, H. (2000). Functional electrical stimulation-assisted walking for persons with incomplete spinal injuries: changes in the kinematics and physiological cost of overground walking. *Scand. J. Rehabil. Med.* 32, 72–79. doi: 10.1080/003655000750045587

Li, Y., Yang, X., Zhou, Y., Chen, J., Du, M., and Yang, Y. (2021). Adaptive stimulation profiles modulation for foot drop correction using functional electrical stimulation: a proof of concept study. *IEEE J. Biomed. Health Inf.* 25, 59–68. doi: 10.1109/JBHI.2020.2989747

Lynch, C. L., and Popovic, M. R. (2008a). Functional electrical stimulation. *IEEE Control Syst. Mag.* 28, 40–50. doi: 10.1109/MCS.2007.914689

Lynch, C. L., and Popovic, M. R. (2008b). "Functional electrical stimulation: closed-loop control of induced muscle contractions," in *Agu Fall Meeting*.

Meng, L., Porr, B., Macleod, C. A., and Gollee, H. (2017). A functional electrical stimulation system for human walking inspired by reflexive control principles. *Proc. Inst. Mech. Eng. Part H J. Eng. Med.* 231, 315–325. doi: 10.1177/0954411917693879

Miller, L., Rafferty, D., Paul, L., and Mattison, P. (2016). The impact of walking speed on the effects of functional electrical stimulation for foot drop in people with multiple sclerosis. *Disabil. Rehabil. Assist. Technol.* 11, 478–483. doi: 10.3109/17483107.2015.1027296

Mountain, A., Lindsay, M. P., Teasell, R., Salbach, N. M., de Jong, A., Foley, N., et al. (2020). Canadian stroke best practice recommendations: rehabilitation, recovery, and community participation following stroke. Part two: transitions and community participation following stroke. *Int. J. Stroke* 15, 789–806. doi: 10.1177/1747493019897847

Mueller, P., del Ama, A. J., Moreno, J. C., and Schauer, T. (2020). Adaptive multichannel FES neuroprosthesis with learning control and automatic gait assessment. *J. Neuroeng. Rehabil.* 17, 1–20. doi: 10.1186/s12984-020-0640-7

Neptune, R. R., Kautz, S. A., and Zajac, F. E. (2001). Contributions of the individual ankle plantar flexors to support, forward progression and swing initiation during walking. *J. Biomech.* 34, 1387–1398. doi: 10.1016/S0021-9290(01)00105-1

Nielsen, J. B. (2002). Motoneuronal drive during human walking. *Brain Res. Rev.* 40, 192–201. doi: 10.1016/S0165-0173(02)00201-1

Pappas, I. P. I., Popovic, M. R., Keller, T., Dietz, V., and Morari, M. (2001). A reliable gait phase detection system. *IEEE Trans. Neural Syst. Rehabil. Eng.* 9, 113–125. doi: 10.1109/7333.928571

Perry, J., Garrett, M., Gronley, J. K., and Mulroy, S. J. (1995). Classification of walking handicap in the stroke population. *Stroke* 26, 982–989. doi: 10.1161/01.STR.26.6.982

Popovic, D. B. (2014). Advances in functional electrical stimulation (FES). *J. Electromyogr. Kinesiol.* 24, 795–802. doi: 10.1016/j.jelekin.2014.09.008

Prasanth, H., Caban, M., Keller, U., Courtine, G., Ijspeert, A., Vallery, H., et al. (2021). Wearable sensor-based real-time gait detection: a systematic review. *Sensors* 21, 1–28. doi: 10.3390/s21082727

Schaechter, J. D. (2004). Motor rehabilitation and brain plasticity after hemiparetic stroke. *Prog. Neurobiol.* 73, 61–72. doi: 10.1016/j.pneurobio.2004.04.001

Seel, T., Werner, C., Raisch, J., and Schauer, T. (2016). Iterative learning control of a drop foot neuroprosthesis—generating physiological foot motion in paretic gait by automatic feedback control. *Control Eng. Pract.* 48, 87–97. doi: 10.1016/j.conengprac.2015.11.007

Shiavi, R., Bugle, H. J., and Limbird, T. (1987). Electromyographic gait assessment, Part 1: adult EMG profiles and walking speed. *J. Rehabil. Res. Dev.* 24, 13–23.

Shin, H. E., Kim, M., Lee, D., Jang, J. Y., Soh, Y., Yun, D. H., et al. (2022). Therapeutic effects of functional electrical stimulation on physical performance and muscle strength in post-stroke older adults: a review. *Ann. Geriatr. Med. Res.* 26, 16–24. doi: 10.4235/agmr.22.0006

Shmuel, S., Yocheved, L., Becher, M., and Vatine, J.-J. (2013). Dual-channel functional electrical stimulation improvements in speed-based gait classifications. *Clin. Interv. Aging* 8, 271–277. doi: 10.2147/CIA.S41141

Street, T., Taylor, P., and Swain, I. (2015). Effectiveness of functional electrical stimulation on walking speed, functional walking category, and clinically meaningful changes for people with multiple sclerosis. *Arch. Phys. Med. Rehabil.* 96, 667–672. doi: 10.1016/j.apmr.2014.11.017

Sui, J. D., Chen, W. H., Shiang, T. Y., Chang, T. S., and IEEE (2020). "Real-time wearable gait phase segmentation for running and walking," in *IEEE International Symposium on Circuits and Systems (ISCAS)*.

Zhang, D., Zhang, Q., and Zhu, X. (2015). Exploring a type of central pattern generator based on hindmarsh-rose model: from theory to application. *Int. J. Neural Syst.* 25, 1–15. doi: 10.1142/S0129065714500282

frontiers | Frontiers in Neuroscience

TYPE Hypothesis and Theory
PUBLISHED 26 September 2022
DOI 10.3389/fnins.2022.951942

EDITED BY
Jessica O. Winter,
The Ohio State University,
United States

REVIEWED BY
Heng Li,
Shanghai Jiao Tong University, China
Jian K. Liu,
University of Leeds, United Kingdom

*CORRESPONDENCE
Hao Wang
hao.wang@siat.ac.cn
Tianzhun Wu
tz.wu@siat.ac.cn

SPECIALTY SECTION
This article was submitted to
Neural Technology,
a section of the journal
Frontiers in Neuroscience

RECEIVED 24 May 2022
ACCEPTED 05 September 2022
PUBLISHED 26 September 2022

CITATION
Liu Y, Yue W, Yu S, Zhou T, Zhang Y, Zhu R, Song B, Guo T, Liu F, Huang Y, Wu T and Wang H (2022) A physical perspective to understand myelin. I. A physical answer to Peter's quadrant mystery.
Front. Neurosci. 16:951942.
doi: 10.3389/fnins.2022.951942

A physical perspective to understand myelin. I. A physical answer to Peter's quadrant mystery

Yonghong Liu[1], Wenji Yue[1], Shoujun Yu[1], Tian Zhou[1], Yapeng Zhang[1], Ran Zhu[1], Bing Song[1], Tianruo Guo[2], Fenglin Liu[1], Yubin Huang[1], Tianzhun Wu[1,3]* and Hao Wang[1,3]*

[1]Institute of Biomedical and Health Engineering, Shenzhen Institutes of Advanced Technology (SIAT), Chinese Academy of Sciences (CAS), Shenzhen, China, [2]Graduate School of Biomedical Engineering, University of New South Wales, Sydney, NSW, Australia, [3]Key Laboratory of Health Bioinformatics, Chinese Academy of Sciences (CAS), Shenzhen, China

In the development of oligodendrocytes in the central nervous systems, the inner and outer tongue of the myelin sheath tend to be located within the same quadrant, which was named as Peters quadrant mystery. In this study, we conduct *in silico* investigations to explore the possible mechanisms underlying the Peters quadrant mystery. A biophysically detailed model of oligodendrocytes was used to simulate the effect of the actional potential-induced electric field across the myelin sheath. Our simulation suggests that the paranodal channel connecting the inner and outer tongue forms a low impedance route, inducing two high-current zones at the area around the inner and outer tongue. When the inner tongue and outer tongue are located within the same quadrant, the interaction of these two high-current-zones will induce a maximum amplitude and a polarity reverse of the voltage upon the inner tongue, resulting in the same quadrant phenomenon. This model indicates that the growth of myelin follows a simple principle: an external negative or positive E-field can promote or inhibit the growth of the inner tongue, respectively.

KEYWORDS

Peter's quadrant mystery, oligodendrocyte, E-field, modeling, electrical stimulation

Introduction

Since the pioneering electron microscope (SE) observations of the spiral structure of myelin sheath were conducted between the 1950s and 1980s (BEN GEREN, 1954; Bunge et al., 1989), the ultrastructure and function of the myelin sheath have been paid more attention in neuroscience (Chang et al., 2016; Monje, 2018). The myelin sheath was initially reported as a pure electrical insulator, enabling a "saltatory" impulse propagation (Boullerne, 2016). However, this hypothesis cannot explain many experimental observations in myelin ultrastructures. For example, myelin in the superficial layers of the cortex has diversified longitudinal distribution (Tomassy et al., 2014); myelin sheaths in the peripheral nervous system (PNS) spiral oppositely and the same to its neighbor on the same (Uzman and Nogueira-Graf, 1957; Armati and Mathey, 2013) and adjacent axon, respectively (Richards et al., 1983); and in particular, Peters quadrant mystery (Peters, 1964; Webster, 1971; Fraher, 1972; Waxman and Swadlow, 1976; Berthold and Carlstedt, 1982; Bertram and Schröder, 1993; Schröder, 1996; Traill, 2005) (a mysterious experimental observation showing that the inner and outer tongues of oligodendrocytes tend to locate within the same quadrant) has been observed in many myelin sheaths. These non-trivial ultrastructures imply that the function of the myelin is more than an insulating layer.

An anatomically accurate and biophysically detailed model can improve our understanding of myelin ultrastructures and functions. For example, a coil inductor model of the spiraling structure was used to understand the unique spiraling directions between adjacent myelin sheaths. (Wang et al., 2021) To achieve a positive mutual inductance, the neighboring myelin on the same axon shall have opposite spiraling directions, while the neighboring myelin on the adjacent axons shall have the same spiraling direction. This simulation has been confirmed by SEM (scanning electron microscope) observations (Waxman and Swadlow, 1976).

This study follows the same research paradigm to explore the possible mechanisms underlying the Peters quadrant mystery. In particular, the myelin sheath is modeled as a distributed parameter circuit, and the electric field (E-field) distribution induced by neural electric activities is investigated *in silico*. The simulated E-field was used to explain why the inner tongue and outer tongue of the myelin sheath tend to locate in the same quadrant, a repeatedly observed intriguing phenomenon (Peters, 1964; Webster, 1971; Fraher, 1972; Waxman and Swadlow, 1976; Berthold and Carlstedt, 1982; Bertram and Schröder, 1993; Schröder, 1996; Traill, 2005). The new knowledge gained in this study provides new insights into the relationships between neural electrical activity and myelin growth.

Peter's quadrant mystery

During axon growth, the myelin wraps around it as a spiral "bandage." However, there is an interesting tendency for this spiral's initial and endpoints to occur close together, as if the myelin were insisting on running only complete laps of the arena (Webster, 1971; Traill, 2005). This is analogous to winding rope into a film spool until the rope spills at the angle where the initial "lump" occurs. Initial and endpoints will tend to occur within the same "quadrant" (**Figure 1A**). Peters first observed this phenomenon in the optic nerves of rodent models in 1964 (Peters, 1964), then further confirmed by multiple studies in visual callosal (Waxman and Swadlow, 1976), dorsal and anterior root axon (Fraher, 1972; Berthold and Carlstedt, 1982), and sural nerves (Bertram and Schröder, 1993; Schröder, 1996). Interestingly, Schwann cell myelination in PNS demonstrated quadrant tendency diminishing gradually with the thickening of myelin (Fraher, 1972). In contrast, myelination of oligodendrocytes in the CNS exhibits a stronger tendency with the thickening of myelin (Peters, 1964).

The actual experimental result of Peter's quadrant mystery is illustrated in **Figures 1A,B** with the reproduced data from Peter's observation (**Figure 1B**; Peters, 1964). The angle between the outer tongue and the inner tongue is defined as β. As seen in **Figure 1B**, the occurrence probability of the case when β is within the first quadrant (each quadrant is 45°) is 52.2%, which is much higher than other quadrants. There is an abrupt change of the probability when the inner tongue grows from the last quadrant to the first quadrant.

Peter's quadrant mystery indicates two points:

1. The outer tongue exerts an effect upon the growth rate of the inner tongue;
2. This effect has an abrupt change when the inner tongue goes through the radial quadrant where the outer tongue is located.

How can the outer tongue affect the growth rate of the inner tongue? This is still an open question that does not seem to have a biological answer (like protein, molecule, and gene) (Traill, 2005). Thus, a physical hypothesis is proposed to build the connection between the growth rate of the inner tongue and the position of the outer tongue. We assume that the electric field (E-field) upon the inner tongue can modulate the inner tongue's growth rate. A distributed parameter circuit modeling the cross-section of the myelin sheath is built to analyze this E-field.

Methods

The circuit simulation

In this study, a cross-section of a myelinated axon is modeled as a distributed parameter circuit, as shown in **Figure 1E**. The transmembrane parts can be modeled as an RC circuit, while the non-transmembrane parts are modeled as resistors. It is emphasized that the inner tongue and outer tongue are connected with a paranodal channel (**Figure 1D**), which is a path filled with cytoplasmic liquid and forms a low impedance route. The details of the connection between the inner/outer tongues and the cytoplasmic channels is shown in **Figure 1C**, showing an unwrapped myelin sheath with the axon. Therefore, in terms of the circuit, the outer tongue and inner

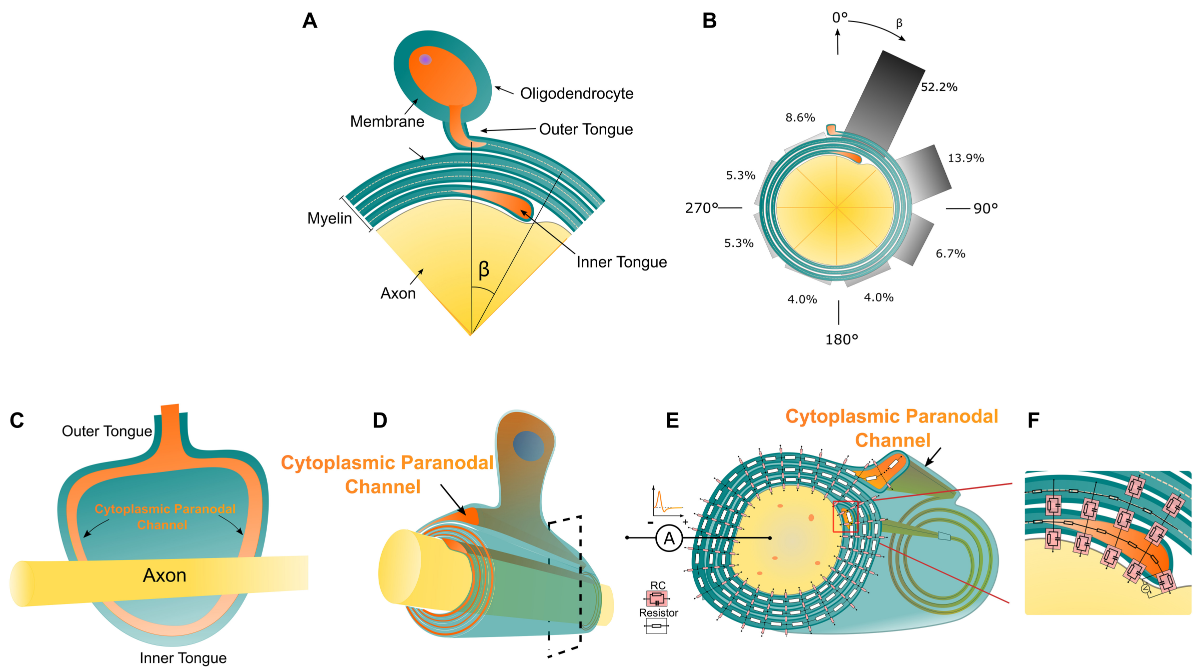

FIGURE 1
(A) The illustration of the Peters quadrant mystery in Oligodendrocytes: there is a relative angle β between the inner and outer tongue. When β is lower than 50°, the inner and outer tongues are considered in the same quadrant. **(B)** The frequency of β within each 45° octant [reproduced from Peter's observation (Peters, 1964)]. **(C)** The unwrapped myelin sheath with axon showing the connection between the inner/outer tongues and the cytoplasmic paranodal channels. **(D)** An illustrative drawing of an axon myelinated by an oligodendrocyte, the orange part indicates the cytoplasmic paranodal channel connecting the inner and outer tongue; **(D)** The equivalently distributed circuit network model of the cross-section of a myelinated axon. Two kinds of circuit components representing different local electrical properties of the myelin sheath are shown. **(E,F)** The transmembrane capacitance of the growth terminal of the inner tongue.

tongue are connected with a resistor, whose impedance is low. This low impedance route is critical for the simulation. Since the inner tongue is the growing terminal, the transmembrane voltage of the inner tongue is measured in the simulation, as shown in Figure 1F. The inside terminal of the inner tongue is set as the reference during the measurement.

The origin of the current source

The origin of the current source implemented in the circuit simulation is the action potential. The explanation of the waveform and polarity of the current source is illustrated in Figure 2. Figure 2A shows a typical waveform of the action potential. Since we only consider the absolute voltage change (start from 0 mV rather than −70 mV), the action potential is very similar to a positive monophasic voltage waveform (take the inside terminal of the axon as the reference point in Figure 1E). When an inward ionic current happens at the Ranvier node (the depolarization phase with inward Na^+ ionic current of the action potential), based on Kirchhoff's circuit laws, it can be inferred that there will an electric current to form a current circle shown in Figure 2B. Therefore, the E-field across the myelin has a dominant positive component, which is equivalent to a current from the inside to the outside. So the current source applied in Figure 1E has a positive monophasic current waveform with its positive terminal connected with the inside terminal of the axon.

Results

The current is more concentrated in the inner-tongue-zone and outer-tongue-zone

The detailed circuit configuration of the modeling is shown in Figure 3. The actual parameters of each unit are based on the histological characteristics and measured properties of myelin (Gentet et al., 2000; Liang et al., 2017). The outer tongue is always located at Layer 1. There are 40 nodes for each layer. Then the growth progress of the myelin can be modeled by changing the position of the inner tongue. Thus, for the modeling of dynamic progress of myelin growth, we move the position of the inner tongue. As shown in Figure 3, the inner tongue is located at Layer 6-Node 1, meaning the inner tongue overlaps with the outer tongue at this status, and it is the first unit of Layer 6. At the same time, it was grown from Layer

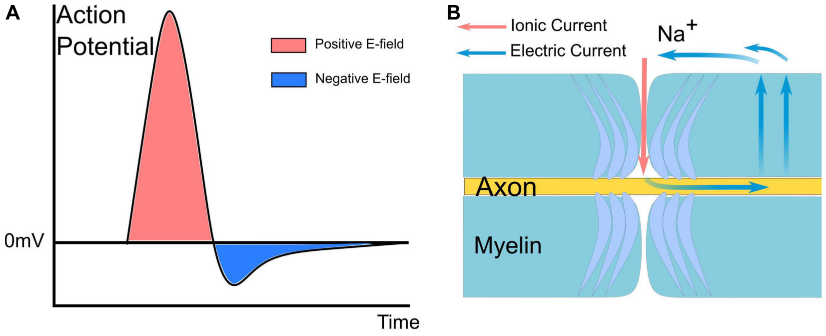

FIGURE 2
A typical waveform of the action potential and current path between the node of Ranvier and the internode of myelin. **(A)** The action potential is mainly a monophasic positive voltage pulse. **(B)** Based on Kirchhoff's circuit laws, it can be inferred that there will be an electric current to form a current circle during the inward Na ionic current.

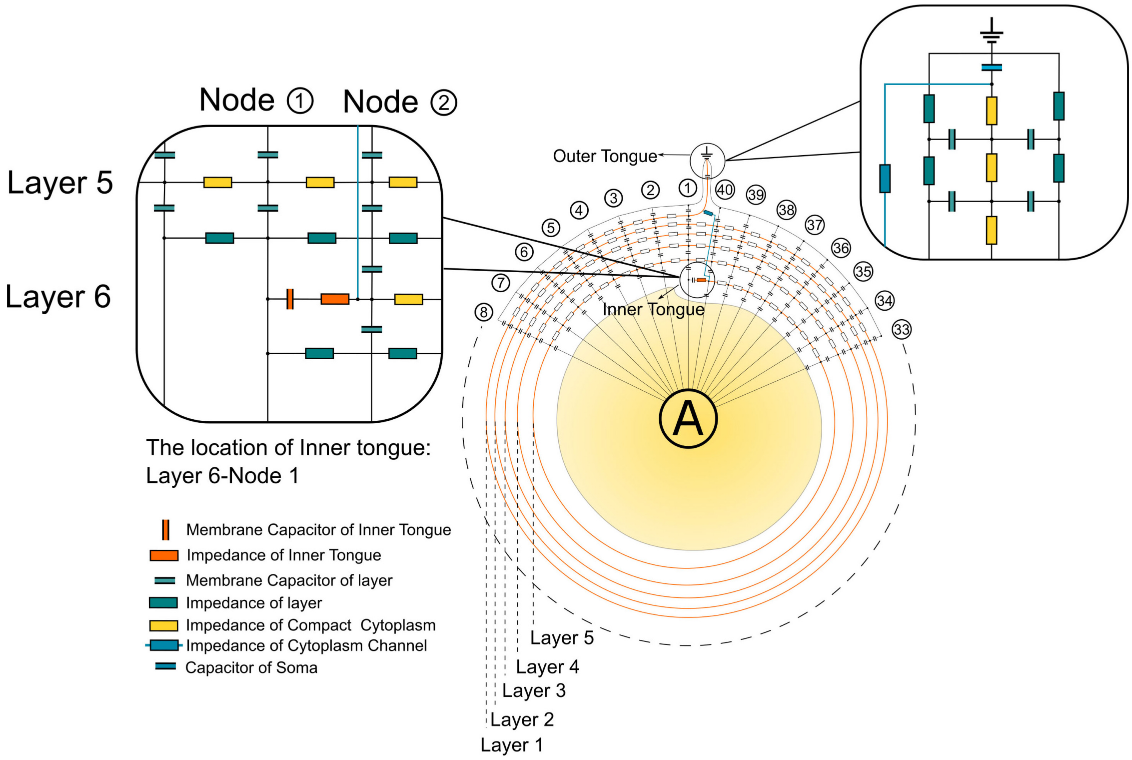

FIGURE 3
The detailed circuit configuration for modeling.

5-Node 40, the previous state, and will grow to Layer 6-Node 2 in the next state. The voltage change of inner tongue's membrane capacitor is simulated by all different states of myelin growth progress, from layer 2 to layer 6. All model parameter are described in Table 1.

The amplitude of the current across each transmembrane capacitor in Figure 1E is recorded and re-distributed into the round shape analogous to the circle of the myelin sheath, as shown in Figure 4A. The current emitted from the axon is not distributed radially identical. Instead, the current is preferentially concentrated at the area close to the inner tongue and outer tongue, called inner-tongue-zone and outer-tongue-zone, respectively (Figure 4A). As shown in Figure 4B, these high current zones move with the position of the inner tongue and outer tongue, showing that these two high current zones are directly induced by the existence of the inner and outer tongues. The cause of these two high current zones is qualitatively explained in Figure 4C.

TABLE 1 Electrical parameters of elements used in modeling.

Membrane Capacitor of Inner Tongue	50 nF
Impedance of Inner Tongue	4 Ω
Membrane Capacitor of Layer	1 nF
Impedance of Layer	1 kΩ
Impedance of Compact Cytoplasm	4 kΩ
Impedance of Cytoplasm Channel	10 Ω
Capacitor of Soma	100 nF

Since the current source is connected with the inner terminal and outer terminal, it can be considered that the current is emitted from the axon to the outer space of the myelin sheath. The current emission follows a specific distribution, as shown in Figure 4C-i. This distribution can be understood by a two-step analysis shown in Figures 4C-ii,iii. Firstly, due to the existence of the low impedance route, the inner and outer tongue can concentrate more current, shown in Figure 4C-ii:

$I_{inner} \gg I_{radial}$ and $I_{outer} \gg I_{radial}$

The current into the inner tongue is shared between the radial path and the channel path, shown in Figure 4C-iii:

$$I_{inner} = I_{inner-radial} + I_{inner-channel}$$

It is the same for the current into the outer tongue:

$$I_{outer} = I_{outer-radial} + I_{outer-channel}$$

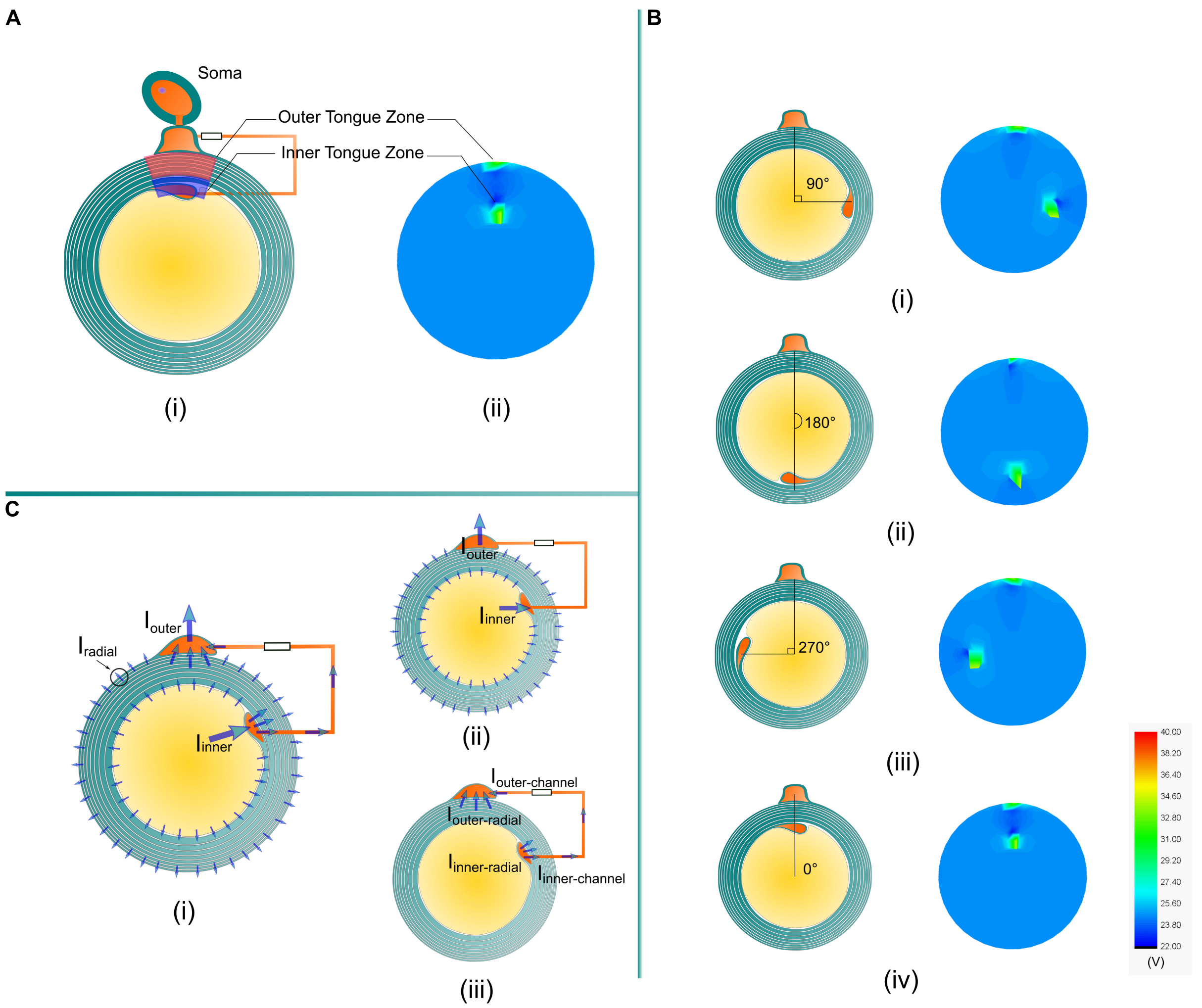

FIGURE 4
(A) The high current zones related to the position of the inner tongue and the outer tongue in the simulation are named the inner tongue zone and outer tongue zone. **(B)** The inner tongue zone moves with the position of the inner tongue when the angles between the inner and outer tongues are **(i)** 90°, **(ii)** 180°, **(iii)** 270°, and **(iv)** 0°. **(C)** A brief illustration of the reason for the two high current zones. **(i)** An illustrative plot of all possible current. **(ii)** The current through the cytoplasmic channel *via* inner and outer tongues is much higher than the radial current in all directions. **(iv)** The current in the cytoplasmic channel will generate a high E-field, making the radial current at the inner and outer tongues more concentrated to form the two high current zones.

Although $I_{inner-radial}$ is just part of the total current into the inner tongue, due to the current concentration effect, it still can be concluded that:

$$I_{inner-radial} > I_{radial}$$

In general, due to the current concentration effect by the low impedance route connecting the inner and outer tongues, the radial current at the area close to the inner and outer tongue will be higher than that of the other position, resulting in the two high current zones. This is an intuitive and qualitative explanation.

We also validated that the high current zone is a stable modeling result by changing the impedance of the cytoplasmic paranodal channel, as shown in **Figure 5**. The resistance represents the cytoplasmic channel is connected to Layer 5-Node 1. Then the current on the capacitors of the peripheral region (Layer 5-Node 38, 39, 40, 1, 2, 3, 4) is measured by changing the resistance of the cytoplasmic channel. As seen, no matter how high the channel impedance is, as long as it exists, the capacitor closer to the channel always has higher current than the peripheral region.

The radial angle influences the electric voltage on the inner tongue

Since the inner tongue is the growing terminal, we will focus on how the voltage changes on the inner tongue, which is the voltage measured on the specific capacitor representing the tip membrane of the inner tongue shown in **Figure 1F**. As explained in **Figure 2**, the action potential can be approximately considered as a monophasic positive current pulse. The actual applied current waveform in the simulation is also a monophasic current pulse shown in **Figure 6A**. During the growth of the inner tongue, the voltage amplitude on the inner tongue will have a periodical maximum when the inner-tongue-zone is radially overlapped with the outer-tongue zone (located at the same quadrant in **Figure 6B**). When the inner tongue is located at position 1 (**Figure 6B-i**), the voltage waveform as a maximum positive peak. When it is located at position 2 (**Figure 6B-ii**), the voltage waveform has a maximum negative peak. As seen, the voltage upon the inner tongue has a polarity reverse when it grows from position 1 to position 2. A continuous change of the maximum voltage with the inner tongue growth is shown in **Figure 6C**, showing a periodic polarity reverse. As seen, the transmembrane voltage of the inner tongue is affected by the relative position between the inner tongue and outer tongue (or the radial angle between the inner and outer tongue). Meanwhile, it has an abrupt change when the inner and outer tongues are in the same quadrant. If the growth rate of the inner tongue is modulated by the polarity and amplitude of this voltage, the same quadrant mystery can have a simple answer, as explained below.

The voltage polarity reverse

An illustrative drawing to explain the polarity reverse is shown in **Figure 7**. When the inner tongue and the outer tongue are located in the same quadrant, the two high-current zones will have interaction, forming a directional current flow from the inner tongue toward the outer tongue (**Figure 7A**). When the inner tongue is located at position 1, the radial current of the inner tongue, $I_{inner-radial}$, toward the position of the outer tongue will form a transmembrane current upon the inner tongue with an outward direction shown in **Figure 7B-i**, which is equivalent to an externally applied negative E-field. When the inner tongue is located at position 2, this transmembrane current has an inward direction, which is opposite to the situation of position 1 (**Figure 7B-ii**) and is equivalent to an externally applied positive E-field. This is the reason for the polarity reversed in **Figure 6**.

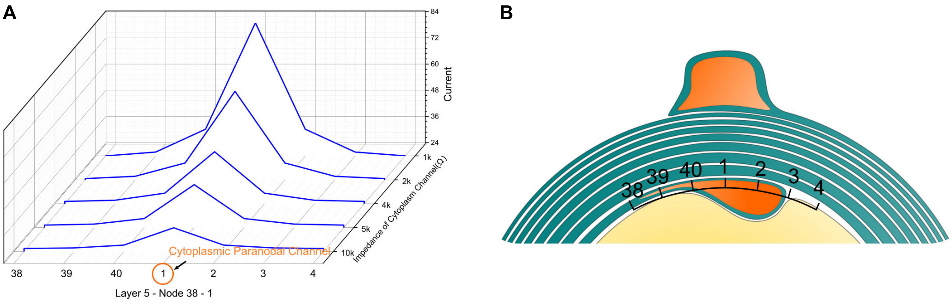

FIGURE 5
(A) The current concentration effect of the cytoplasmic paranodal channel. The resistance represents the cytoplasmic channel connected to Layer 5-Node 1. Then the current on the capacitors of the peripheral region [Layer 5-Node 38, 39, 40, 1, 2, 3, 4 **(B)**] is measured by changing the resistance of the cytoplasmic channel. No matter how high the impedance of the channel is, as long as it exists, the capacitor closer to the channel always has a higher current than the peripheral region.

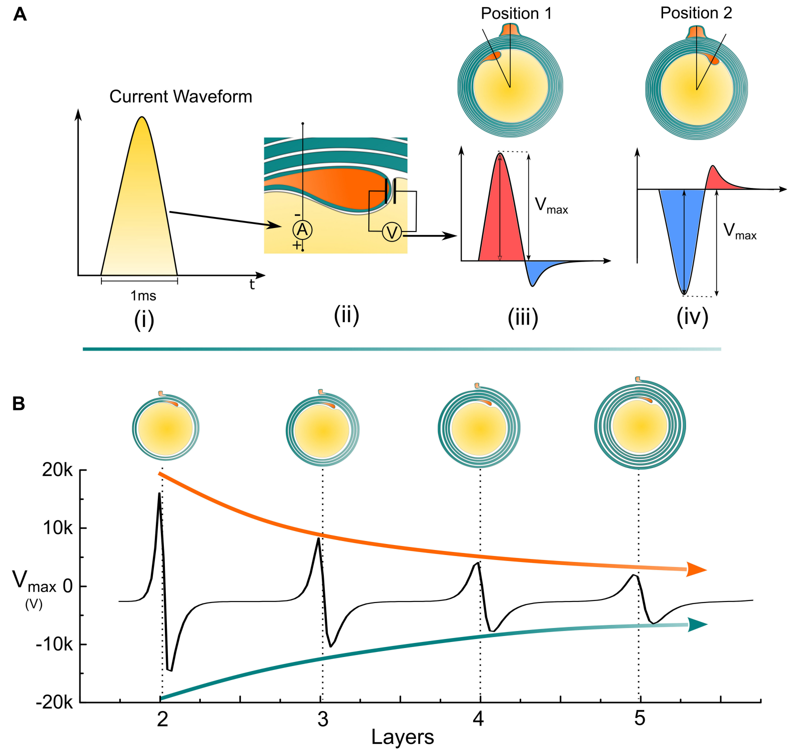

FIGURE 6
Simulation details and the measured voltage amplitude of the inner tongue. **(A) (i)** A monophasic positive current pulse is used to model the action potential; **(ii)** The detailed configuration of the applied current source and how the voltage on the inner tongue is measured; **(iii)** The illustrative voltage waveform on the inner tongue when the inner tongue is at position 1; **(iv)** The illustrative voltage waveform on the inner tongue when the inner tongue is at position 2; **(B)** The amplitude of the measured voltage amplitude (Vmax) by increasing the number of myelin layers.

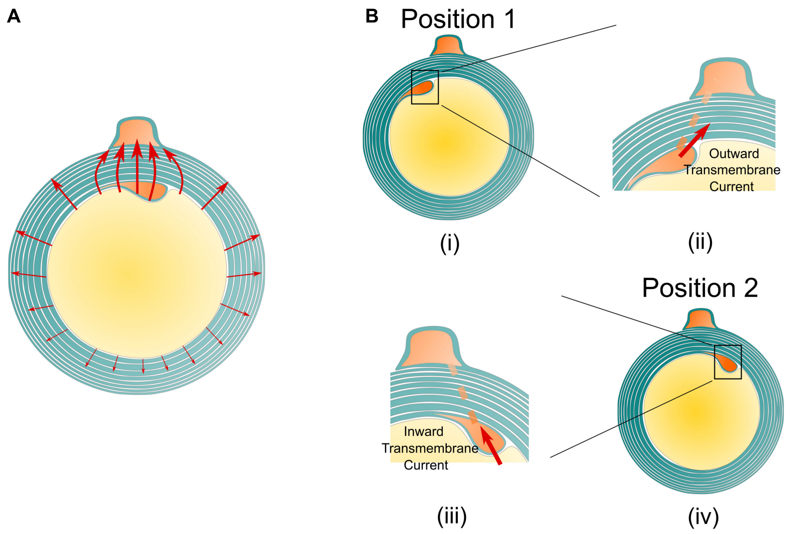

FIGURE 7
The illustrative current flow on the cross section of the myelin sheath. **(A)** The current from the inner tends to flow toward the outer tongue. **(B)** An illustrative drawing explains the reason for the polarity reverse. When the inner tongue is at position 1 **(i)**, the current from the inner tongue to the outer tongue forms an outward transmembrane current on the inner tongue **(ii)**; when the inner tongue is at position 2 **(iii)**, the current from the inner tongue to the outer tongue forms an inward transmembrane current on the inner tongue **(iv)**.

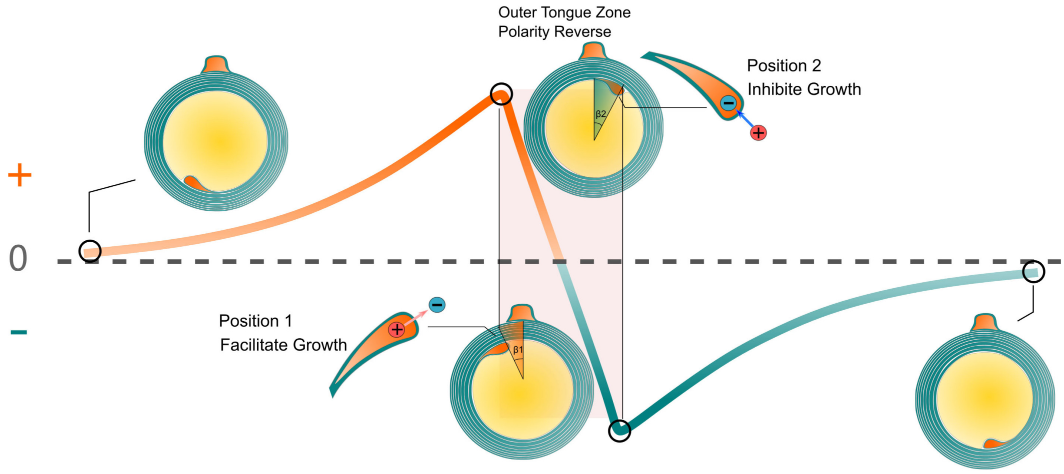

FIGURE 8
The relationship between the transmembrane voltage of the inner tongue and its radial position. The growth rate is correlated with the polarity (direction) and amplitude of the transmembrane E-field.

The explanation to Peter quadrant mystery

The relationship between the transmembrane voltage of the inner tongue and its radial position is illustrated in **Figure 8**. It is emphasized that the curve in **Figure 8** is an illustrative drawing, not an accurate duplication from the simulation results. When the inner tongue locates in position 1 (entering the outer-tongue-zone), the transmembrane E-field of the inner tongue reaches the maximum outward value. In Peter's observations, position 1 showed the lowest occurrence frequency (Peters, 1964), indicating the fastest growth rate. With further growth, the inner tongue will reach position 2 (leaving the outer-tongue-zone). The transmembrane E-field of the inner tongue reaches the maximum inward value. The occurrence frequency at this position is the highest, indicating the slowest growth rate. Therefore, we can conclude that the growth rate is correlated with the polarity (direction) and amplitude of the transmembrane E-field. An outward E-field can facilitate growth, while an inward E-field can inhibit growth. In other words, an extracellular negative E-field can promote myelin growth, while an extracellular positive E-field can inhibit myelin growth.

Our simulations suggested that the existence of the paranodal channel connecting the inner and outer tongue forms two high-current zones. When these two high-current-zones are getting close, which happens when the inner and outer tongues are located within the same quadrant, the voltage upon the inner tongue will have a maximum amplitude and a polarity reverse, resulting in a minimum growth rate at position 2. So the inner tongue tends to stay at position 2, observed as the same quadrant phenomenon. Interestingly, this phenomenon does not only appear in Oligodendrocytes (Peters, 1964; Waxman and Swadlow, 1976) but also exists in the early stage of the myelination by Schwann cells in PNS (Fraher, 1972). A comparison of the difference between Oligodendrocytes and Schwann cells is shown in **Figure 9** to explain this experimental observation. For oligodendrocytes, the inner tongue and outer tongue are connected with paranodal channels. For Schwann cells, apart from the paranodal channels, there are also other cytoplasmic channels, called Schmidt–Lanterman incisures (SLI), located along the whole internode span. All these cytoplasmic channels connect the inner and outer tongues of the Schwann cells, providing low impedance routes. Thus, the same quadrant phenomenon also happens during the growth of Schwann cells. However, it is known that for a mature Schwann cell, its inner tongue and outer tongue form two radial circles shown in **Figure 9**, rather than just occupying a certain radial angle, which is the situation of Oligodendrocytes. Therefore, the same quadrant tendency will diminish for a mature Schwann cell (Gomez-Sanchez et al., 2017).

A possible explanation for g-ratio

The g-ratio is the ratio of the inner axonal diameter to the total outer diameter, including the myelin sheath (Chomiak and Hu, 2009). The g-ratio ranged from 0.72 to 0.81 in CNS, and 0.46 to 0.8 in PNS. However, if the axon diameter is less than 0.4 μm, it will fail to form the myelin sheath (Waxman and Bennett, 1972), indicating the key role of the axonal physical properties in terminating the growth of myelin. Although there are still controversies (Smith and Koles, 1970; Waxman and Bennett, 1972), earlier studies suggested the contribution of g-ratio in modulating conduction velocity (Sukhorukov et al., 1993). However, this theory fails to build

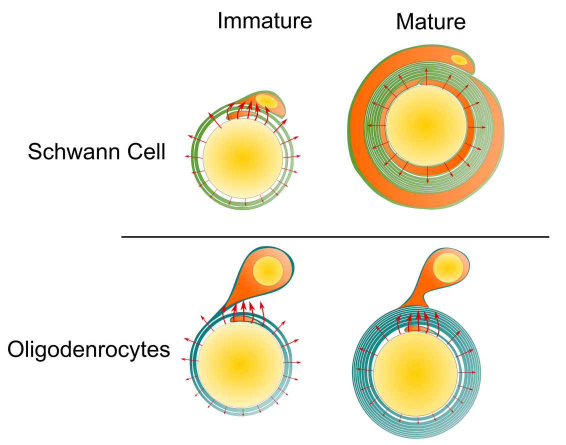

FIGURE 9
The same quadrant phenomenon for Schwann cell and Oligodendrocyte. For the Schwann cell, at its mature state, its inner tongue and outer tongue form two circles, eliminating the occurrence of the two high-current zones. So the same quadrant phenomenon tends to disappear with growth.

the connection between the signal propagation and the inner tongue, which is the growth terminal of the myelin. In this study, the modeled E-field tends to decrease by increasing the layers of myelin layers. Thus, when the E-field is lower than a certain threshold, the growth of the inner tongue will be automatically terminated. Thus, this theory indicates the potential correlation between the g-ratio and the E-field on the inner tongue. In our next study, a more detailed model is proposed to explain the g-ratio phenomenon (Liu et al., 2021).

Discussion

The same quadrant phenomenon does not happen at the early stage of myelination

There is another evidence to support our theory that the same quadrant phenomenon is deeply linked with cytoplasmic channels. During the myelination, the myelin will have a compaction process to form these cytoplasmic channels connecting the inner and outer tongues. Therefore, the same quadrant phenomenon shall not happen at the early stage of myelination since the myelin is not compact yet. This agrees with the experimental observation (Peters, 1964). The same quadrant phenomenon is not observed for optical nerves of 7 days postnatal rats when the number of myelin lamellae is not higher than 3. While for optical nerves of postnatal rats older than 14 days, when the number of myelin lamellae is higher than 4, the same quadrant phenomenon can be clearly observed.

The same quadrant phenomenon also does not only happen in the section of the same quadrant

As depicted in **Figure 1B**, the occurrence of the inner tongue's position is the maximum at about 1 o'clock direction and gradually decreases in the clockwise direction. From the analysis in **Figure 6**, the voltage upon the inner tongue also reaches the negative maximum at about 1 o'clock direction. Then, it gradually increases to the positive maximum in the clockwise direction. So our model can explain the same quadrant phenomenon and the clockwise changing trend, duplicating all minor details of the experimental observation.

Comparison with previous studies on explaining the same quadrant phenomenon

The same quadrant phenomenon has long been considered a mystery (Chang et al., 2016). Although it has been observed and validated by many studies (Peters, 1964; Webster, 1971; Fraher, 1972; Waxman and Swadlow, 1976; Berthold and Carlstedt, 1982; Bertram and Schröder, 1993; Schröder, 1996; Traill, 2005), only two previous works tried proposing possible mechanisms (Traill, 2011; Fabbri, 2015). One is proposed by I. M. Fabbri (2015). In his work, the myelinated nerve is modeled as a spiral coaxial cable to transmit the neural signal as an electromagnetic wave. Suppose the inner and outer tongues are located very close to each other. In that case, the myelin sheath will be more like a spiral geometry, which is preferred for better handling power throughout the nervous system. Another is proposed by Robert R. Traill (2011), who considers the myelinated nerve an optical fiber to transmit IR radiation. If the number of myelin lamellae is integral, the myelin sheath can form a perfect circle, which is beneficial for IR radiation as a standing wave to propagate. But in Robert R. Traill's model, the outer tongue is the growing terminal, which is biologically incorrect. Both of these two models fail in several aspects.

1. The same quadrant phenomenon does not mean myelin lamellae should be an integral number. The integral number means the inner tongue should stop its growth at position 1 in **Figure 6**, which these two models presume. However, it is clearly mentioned in the original experimental observation that the inner tongue stops at position 2, which is a bit over the outer tongue. Our model explains that the inner tongue should stop at position 2 due to the minimum growth rate.
2. As mentioned in section "The same quadrant phenomenon does not happen at the early stage of myelination", in our model, the same quadrant phenomenon does

not happen in the early stage of myelination when the myelin sheath is not compact, which agrees with the experimental observation. However, both of these models do not account for it.

3. The gradual change along the clockwise direction, as explained in section "The same quadrant phenomenon also does not only happen in the section of the same quadrant," is not accounted for in these two models.
4. Both models try to explain the phenomenon in terms of function rather than reason. An observed phenomenon always has a reason to happen but does not necessarily serve a specific function. Explaining a phenomenon in terms of function is not so reliable since the assumed function may not really exist. Our model gives the origin of the same quadrant phenomenon, explaining how this same quadrant phenomenon is formed.

The physical perspective to study the myelin development

The conventional research paradigm from biological and chemical perspectives is quite limited for neuroscience, especially for the myelin study. Now we know quite a lot of ultrastructures of myelin sheaths, such as the non-random spiraling directions between neighboring myelin sheaths (Uzman and Nogueira-Graf, 1957; Richards et al., 1983; Bunge et al., 1989; Armati and Mathey, 2013), the same quadrant phenomenon (Peters, 1964), g-ratio (Stikov et al., 2015) and radial sorting (Pereira et al., 2009). All these ultrastructures were repeatedly observed and validated by many studies and yet have reasonable explanations. A possible reason is that these ultrastructures imply an effect of action at a distance, whose explanations are beyond biology and chemistry. The effect of action at a distance is a term in physics, meaning that one object can exert an effect upon another object without physical contact. Normally, this effect of action at a distance is realized by a field. Let's take the same quadrant phenomenon in this study as an example. There are so many compact myelin lamellae between the inner and outer tongues. But the position of the outer tongue determines where the inner tongue should stop its growth without physical contact. It is difficult to imagine any protein or receptor can induce this result. But the electric field can easily build the logical connection between the positions of inner and outer tongues. Another successful case is the explanation of the non-random spiraling directions between neighboring myelin sheaths by the electromagnetic field (Wang et al., 2021). It is known that on the same axon, if one myelin sheath spiraling direction, from inner tongue to outer tongue, is clockwise, then the neighboring myelin sheath will have the opposite spiraling direction, which is anti-clockwise (Uzman and Nogueira-Graf, 1957). Again, it is almost impossible to imagine a protein or a receptor on one myelin sheath that can sense the spiraling direction of the neighboring myelin sheath and then determine the spiraling direction of itself. In our previous model, the spiraling of the cytoplasmic channel in the myelin sheath is considered a coil inductor to generate a magnetic field from the current of action potential activation. Due to the mutual inductance between the cytoplasmic channels in adjacent myelin sheaths as coil inductors, the current in one myelin sheath will generate an induced current in the neighboring myelin sheath by electromagnetic induction. Since a positive mutual inductance is beneficial for neural signal propagation, the spiraling directions between adjacent myelin sheaths should always be opposite, as observed in the experiments. But this explanation in terms of function is incomplete since it does not give the reason for the formation. However, by knowing the effect of electric field modulation on the myelin growth proposed in this study, it can be inferred that the electric field also induces this non-random spiraling. The current induced by the adjacent myelin sheath can affect the myelin growth when the first lamella is formed. One terminal grows faster due to the induced current and then becomes the inner tongue, thus determining the spiraling direction. In our next study, we will further show how this model is further extended to account for other ultrastructures such as g-ratio and radial sorting.

The relationship between neural activity and myelin development

It is known that myelin forms the white matter, a major portion of our brain. It plays a critical role in neural signal propagation and memory (Fields and Bukalo, 2020). Meanwhile, most degenerative neural diseases are accompanied by demyelination or myelin degeneration. Therefore, investigating the development mechanism and regeneration method of myelin is an important topic in neuroscience and treating degenerative neural diseases. Currently, one of the most promising directions to decode the development mechanism of myelin is neural activity-dependent myelination (Fields, 2015). Many studies show that both myelination and demyelination are deeply linked with action potentials. But the detailed interaction mechanism between the action potential and the myelin growth is yet to be elucidated. However, this study proposes a definite principle of E-field modulated myelin growth, showing that the electric field can exert both promoting and inhibitory effects. Considering that neural activity is mainly a changing E-field, our theory provides the clue to unveil the secret of myelin development. Moreover, our model may also explain the direct cause of some degenerative neural diseases, such as Parkinson's disease, as abnormal neural activities. We will make a more detailed discussion about this part in our next work (Liu et al., 2021).

The limitation of our model

The major limitation of our model is that, in the current stage, the model is qualitative rather than quantitative. The qualitative modeling result is determined by the circuit structure, which is a circular capacitor network with a low impedance route connecting the positions of inner and outer tongues, as shown in **Figure 3**. As long as this circuit structure is the same, the qualitative modeling result shown in **Figure 6B** and **Figure 8** is not affected by the actual circuit parameters. Although our model can derive the principle of electrical modulation on myelin growth, the actual amplitude of the voltage/E-field required to affect the myelin growth remains unknown. But it is also quite difficult to further improve the model due to several factors.

1. The first one is the parameter rescale issue. A myelin sheath is a 3D structure with a certain longitudinal length, while our circuit model is 2D. How to rescale the parameter of an electrical component representing a 3D object is always a question. Therefore, it is difficult to precisely determine the actual value of each component in the circuit.
2. The active properties of the myelin sheath are neglected. Our model only considered the passive properties of the myelin structure (that is, the RC properties) without including active ionic mechanisms such as potassium ion channels (Wilson and Chiu, 1990) and radial components (Peters, 1961). However, the contribution of active conductance in the voltage generation upon the inner tongue is still an open question without experimental details of potassium channel density distributed in myelin.

Conclusion

The physical origin of the same quadrant mystery is the preferential E-field distribution on the cross-section of the myelin. Since actional potentials induce E-field, it explains the relation between neural electric activity and the ultrastructure of myelin. Furthermore, the preferential E-field distribution resulting from the breaking of the central symmetry by the outer tongue explains the difference of the "same quadrant" observation between Oligodendrocytes in CNS and Schwann cells in PNS. Meanwhile, this study also reveals the physical factor that modulates myelin growth: an extracellular negative or positive E-field can promote or inhibit myelin growth, respectively. Finally, the computational approach can probe neuronal ultrastructures at a resolution far beyond the current state-of-the-art biological experiments, providing a promising tool to explore neuroscience from a physical perspective.

Data availability statement

The original contributions presented in this study are included in the article, further inquiries can be directed to the corresponding author/s.

Author contributions

HW proposed the theory. YL carried out the modeling process. TG helped refine the theory and improve the writing. WY, TZ, YZ, RZ, BS, FL, YH, and TW contributed to the reference collection, idea discussion, and early state of the theory establishment. SY helped plot figures and search for the references for manuscript revision. All authors contributed to the article and approved the submitted version.

Funding

This work was supported by the grant from Guangdong Research Program (2019A1515110843 and 2019A1515110948), Shenzhen Research Program (JCYJ20170818152810899 and GJHZ20200731095206018), Chinese Academy of Sciences Research Program (2011DP173015 and 172644KYSB20190077), and National Natural Science Foundation of China grants (31900684 and 32000727).

Acknowledgments

A preprint has previously been published (Stikov et al., 2015).

Conflict of interest

The authors declare that the research was conducted in the absence of any commercial or financial relationships that could be construed as a potential conflict of interest.

Publisher's note

References

Armati, P. J., and Mathey, E. K. (2013). An update on schwann cell biology—immunomodulation, neural regulation and other surprises. *J. Neurol. Sci.* 333, 68–72. doi: 10.1016/j.jns.2013.01.018

BEN GEREN, B. (1954). The formation from the Schwann cell surface of myelin in the peripheral nerves of chick embryos. *Exp. Cell Res.* 7, 558–562. doi: 10.1016/s0014-4827(54)80098-x

Berthold, C. H., and Carlstedt, T. (1982). Myelination of S1 dorsal root axons in the cat. *J. Comp. Neurol.* 209, 225–232. doi: 10.1002/cne.902090302

Bertram, M., and Schröder, J. M. (1993). Developmental changes at the node and paranode in human sural nerves: Morphometric and fine-structural evaluation. *Cell Tissue Res.* 273, 499–509. doi: 10.1007/BF00333704

Boullerne, A. I. (2016). The history of myelin. *Exp. Neurol.* 283(Pt B), 431–445. doi: 10.1016/j.expneurol.2016.06.005

Bunge, R. P., Bunge, M. B., and Bates, M. (1989). Movements of the Schwann cell nucleus implicate progression of the inner (axon-related) Schwann cell process during myelination. *J. Cell Biol.* 109, 273–284. doi: 10.1083/jcb.109.1.273

Chang, K. J., Redmond, S. A., and Chan, J. R. (2016). Remodeling myelination: Implications for mechanisms of neural plasticity. *Nat. Neurosci.* 19, 190–197. doi: 10.1038/nn.4200

Chomiak, T., and Hu, B. (2009). What is the optimal value of the g-ratio for myelinated fibers in the rat CNS? A theoretical approach. *PLoS One* 4:e7754. doi: 10.1371/journal.pone.0007754

Fabbri, I. M. (2015). The spiral coaxial cable. *Int. J. Microwave Sci. Technol.* 2015, 1–18. doi: 10.1155/2015/630131

Fields, R. D. (2015). A new mechanism of nervous system plasticity: Activity-dependent myelination. *Nat. Rev. Neurosci.* 16, 756–767. doi: 10.1038/nrn4023

Fields, R. D., and Bukalo, O. (2020). Myelin makes memories. *Nat. Neurosci.* 23, 469–470. doi: 10.1038/s41593-020-0606-x

Fraher, J. P. (1972). A quantitative study of anterior root fibres during early myelination. *J. Anat.* 112, 99.

Gentet, L. J., Stuart, G. J., and Clements, J. D. (2000). Direct measurement of specific membrane capacitance in neurons. *Biophys. J.* 79, 314–320. doi: 10.1016/S0006-3495(00)76293-X

Gomez-Sanchez, J. A., Pilch, K. S., van der Lans, M., Fazal, S. V., Benito, C., Wagstaff, L. J., et al. (2017). After nerve injury, lineage tracing shows that myelin and Remak Schwann cells elongate extensively and branch to form repair Schwann cells, which shorten radically on remyelination. *J. Neurosci.* 37, 9086–9099. doi: 10.1523/JNEUROSCI.1453-17.2017

Liang, W., Zhao, Y., Liu, L., Wang, Y., Li, W. J., and Lee, G. B. (2017). Determination of cell membrane capacitance and conductance via optically induced electrokinetics. *Biophys. J.* 113, 1531–1539. doi: 10.1016/j.bpj.2017.08.006

Liu, Y., Zhang, Y., Yue, W., Zhu, R., Guo, T., Liu, F., et al. (2021). A Physical perspective to understand the mechanism of myelin development. *arXiv* Preprint. arXiv:2111.13689.

Monje, M. (2018). Myelin plasticity and nervous system function. *Annu. Rev. Neurosci.* 41, 61–76. doi: 10.1146/annurev-neuro-080317-061853

Pereira, J. A., Benninger, Y., Baumann, R., Gonçalves, A. F., Özçelik, M., Thurnherr, T., et al. (2009). Integrin-linked kinase is required for radial sorting of axons and Schwann cell remyelination in the peripheral nervous system. *J. Cell Biol.* 185, 147–161. doi: 10.1083/jcb.200809008

Peters, A. (1961). A radial component of central myelin sheaths. *J. Biophys. Biochem. Cytol.* 11:733. doi: 10.1083/jcb.11.3.733

Peters, A. (1964). Further observations on the structure of myelin sheaths in the central nervous system. *J. Cell Biol.* 20, 281–296. doi: 10.1083/jcb.20.2.281

Richards, W., Kalil, R., and Moore, C. L. (1983). An observation about myelination. *Exp. Brain Res.* 52, 219–225. doi: 10.1007/BF00236630

Schröder, J. M. (1996). Developmental and pathological changes at the node and paranode in human sural nerves. *Microsc. Res. Tech.* 34, 422–435. doi: 10.1002/(SICI)1097-0029(19960801)34:5<422::AID-JEMT2<3.0.CO;2-O

Smith, R. S., and Koles, Z. J. (1970). Myelinated nerve fibers: Computed effect of myelin thickness on conduction velocity. *Am. J. Physiol.* 219, 1256–1258. doi: 10.1152/ajplegacy.1970.219.5.1256

Stikov, N., Campbell, J. S., Stroh, T., Lavelée, M., Frey, S., Novek, J., et al. (2015). In vivo histology of the myelin g-ratio with magnetic resonance imaging. *Neuroimage* 118, 397–405. doi: 10.1016/j.neuroimage.2015.05.023

Sukhorukov, V. L., Arnold, W. M., and Zimmermann, U. (1993). Hypotonically induced changes in the plasma membrane of cultured mammalian cells. *J. Membr. Biol.* 132, 27–40. doi: 10.1007/BF00233049

Tomassy, G. S., Berger, D. R., Chen, H. H., Kasthuri, N., Hayworth, K. J., Vercelli, A., et al. (2014). Distinct profiles of myelin distribution along single axons of pyramidal neurons in the neocortex. *Science* 344, 319–324. doi: 10.1126/science.1249766

Traill, R. (2011). Coherent Infra-Red as logically necessary to explain Piagetian psychology and neuro-microanatomy—two independent corroborations for Gurwitsch's findings, and the importance of self-consistent theory. *J. Phys. Conf. Ser.* 329:012018. doi: 10.1088/1742-6596/329/1/012018

Traill, R. R. (2005). Strange regularities in the geometry of myelin nerve-insulation—a possible single cause. *Ondwelle Short Monogr.* 1, 1–9.

Uzman, B. G., and Nogueira-Graf, G. (1957). Electron microscope studies of the formation of nodes of Ranvier in mouse sciatic nerves. *J. Cell Biol.* 3, 589–598. doi: 10.1083/jcb.3.4.589

Wang, H., Wang, J., Cai, G., Liu, Y., Qu, Y., and Wu, T. (2021). A physical perspective to the inductive function of myelin—a missing piece of neuroscience. *Front. Neural Circuits* 14:86. doi: 10.3389/fncir.2020.562005

Waxman, S. G., and Bennett, M. V. (1972). Relative conduction velocities of small myelinated and non-myelinated fibres in the central nervous system. *Nat. New Biol.* 238, 217–219. doi: 10.1038/newbio238217a0

Waxman, S. G., and Swadlow, H. A. (1976). Ultrastructure of visual callosal axons in the rabbit. *Exp. Neurol.* 53, 115–127. doi: 10.1016/0014-4886(76)90287-9

Webster, H. D. (1971). The geometry of peripheral myelin sheaths during their formation and growth in rat sciatic nerves. *J. Cell Biol.* 48, 348–367. doi: 10.1083/jcb.48.2.348

Wilson, G. F., and Chiu, S. Y. (1990). Ion channels in axon and Schwann cell membranes at paranodes of mammalian myelinated fibers studied with patch clamp. *J. Neurosci.* 10, 3263–3274. doi: 10.1523/JNEUROSCI.10-10-03263.1990

frontiers | Frontiers in Neuroscience

TYPE Hypothesis and Theory
PUBLISHED 03 October 2022
DOI 10.3389/fnins.2022.951998

A physical perspective to understand myelin II: The physical origin of myelin development

Yonghong Liu[1], Wenji Yue[1], Shoujun Yu[1], Tian Zhou[1], Yapeng Zhang[1], Ran Zhu[1], Bing Song[1], Tianruo Guo[2], Fenglin Liu[1], Yubin Huang[1], Tianzhun Wu[1,3]* and Hao Wang[1,3]*

[1]Institute of Biomedical and Health Engineering, Shenzhen Institutes of Advanced Technology (SIAT), Chinese Academy of Sciences (CAS), Shenzhen, China, [2]Key Laboratory of Health Bioinformatics, Chinese Academy of Sciences, Shenzhen, China, [3]Graduate School of Biomedical Engineering, University of New South Wales, Sydney, NSW, Australia

OPEN ACCESS

EDITED BY
Jessica O. Winter,
The Ohio State University,
United States

REVIEWED BY
Heng Li,
Shanghai Jiao Tong University, China
Jian K. Liu,
University of Leeds, United Kingdom

*CORRESPONDENCE
Tianzhun Wu
tz.wu@siat.ac.cn
Hao Wang
hao.wang@siat.ac.cn

SPECIALTY SECTION
This article was submitted to
Neural Technology,
a section of the journal
Frontiers in Neuroscience

RECEIVED 24 May 2022
ACCEPTED 05 September 2022
PUBLISHED 03 October 2022

CITATION
Liu Y, Yue W, Yu S, Zhou T, Zhang Y, Zhu R, Song B, Guo T, Liu F, Huang Y, Wu T and Wang H (2022) A physical perspective to understand myelin II: The physical origin of myelin development.
Front. Neurosci. 16:951998.
doi: 10.3389/fnins.2022.951998

The physical principle of myelin development is obtained from our previous study by explaining Peter's quadrant mystery: an externally applied negative and positive E-field can promote and inhibit the growth of the inner tongue of the myelin sheath, respectively. In this study, this principle is considered as a fundamental hypothesis, named Hypothesis-E, to explain more phenomena about myelin development systematically. Specifically, the g-ratio and the fate of the Schwann cell's differentiation are explained in terms of the E-field. Moreover, an experiment is proposed to validate this theory.

KEYWORDS

myelin development, g-ratio, electrical stimulation, neural degenerative disorder, E-field

Introduction

Myelin is an insulating sheath forming around axons. Its biological function in neural systems and the growing mechanism have attracted increasing attention in the field of neuroscience (Lemke, 1988; Colognato and Franklin, 2004; Dutta et al., 2018; Stadelmann et al., 2019; Fields and Bukalo, 2020; Liu et al., 2021a). Previous studies reported a series of experimental observations about the micro-structures of myelin. For example, (1) The spiraling directions of neighboring myelin sheaths has a certain pattern. That is, the neighboring myelin sheaths on the same axon have the opposite spiraling direction (Richards et al., 1983), while the neighboring myelin sheaths on the adjacent axons have the same spiraling directions (Uzman and Nogueira-Graf, 1957; Bunge et al., 1989; Armati and Mathey, 2013); (2) For oligodendrocytes (OLs), the inner and outer tongues tend to be located within the same radial quadrant (Peters, 1961, 1964; Hildebrand, 1971; Webster, 1971; Fraher, 1972); (3) The axons of varying calibers tend to have myelin sheaths of the same thickness, resulting in the g-ratio phenomenon (FitzGibbon and Nestorovski, 2013; Stikov et al., 2015; Andersson et al., 2020); (4) Only the axon with sufficient caliber can be myelinated, resulting in the radial sorting phenomenon (Feltri et al., 2016; Harty et al., 2019; Ommer et al., 2019); and

(5) For Schwann cells (SCs), one SC can only myelinate one axon. If the SC forms the remak bundle, it can never form the myelination, even if a large axon is ensheathed (Harty et al., 2019). These experimental observations indicate a multifaceted mechanism underlying myelin growth. For example, (1) the non-random spiraling phenomenon suggests that myelin growth can be influenced by the interaction between spatially closed myelin sheaths. (2) The same quadrant phenomenon indicates that myelin growth can be influenced by the relationship between the inner and outer tongues. (3) The g-ratio phenomenon indicates a possible correlation between inner tongue growth and the number of myelin lamellae. (4) The radial sorting phenomenon indicates a possible correlation between the myelin growth and the curvature of axons. (5) The characteristic SC properties in myelination and the remak bundle indicate the effect of the surrounding environment in formulating the growth of the inner tongue. Previous studies about mechanisms underlying myelin growth mainly focused on studying contributions from different molecules or proteins (Höke et al., 2003; Colognato and Franklin, 2004; Zheng et al., 2008; Orita et al., 2013; Hines et al., 2015; Feltri et al., 2016; Harty and Monk, 2017; Harty et al., 2019) without providing reasonable explanations for these phenomena. All these phenomena indicate an action at a distance, which is a kind of physical field, is dominating the formation of myelin growth. Thus, a study from a physical perspective can provide a substantial body of new knowledge yet to be discovered. In our previous study, the non-random spiraling phenomenon and the same quadrant phenomenon were explained from the perspective of the electromagnetic field (Wang et al., 2021) and electric field (Liu et al., 2021a). The former reveals the function of cytoplasmic channels in myelin sheath as a coil inductor and the role of the magnetic field in the neural signal. The latter reveals that the electric field modulates the growth of myelin. In this study, we further extend the hypothesis in our previous work, named as Hypothesis-E, to conduct *in silico* investigations of the physical origins of the unexplained myelin observations mentioned above. We name it Hypothesis-E, "E" refers to "electric." In Hypothesis-E, an external negative E-field promotes myelin growth, while an external positive E-field inhibits myelin growth (**Figure 1A**). This study proposed three new hypotheses based on Hypothesis-E to further explain the physical origins of a series of morphological characteristics (**Figures 1B–D**) of the myelin.

Hypothesis-E$_N$ to explain g-ratio

g-ratio

The myelin g-ratio, defined as the ratio between the inner and the outer diameter of the myelin sheath, has been reported in many experimental studies (FitzGibbon and Nestorovski, 2013; Stikov et al., 2015; Andersson et al., 2020). This precise relationship between axonal diameter and myelin sheath thickness has been reported is one of the most enigmatic questions: how is the myelinating glial cell instructed to make precisely the correct number of wraps? Transplantation of oligodendrocytes into nerve tracts containing axons of different sizes demonstrates that the number of wraps is determined by the axon but not by the glial cell because the transplanted glial cells elaborate myelin sheaths appropriate for their new location (Fanarraga et al., 1998). A key axonal signal for regulating myelin sheath thickness, the growth factor neuregulin (Ngr1), is now identified by Zuckerkandl and Pauling (1965). However, the detailed mechanisms of controlling the myelin wrapping by the axonal signal remain unclear.

Hypothesis-E$_N$

The cross-section of a myelinated axon in the resting state (no action potential is activated) is shown in **Figure 2A**. The intracellular potential is more negative than the extracellular potential, resulting in a negative E-field on the inner tongue. This negative E-field is the driven force making the inner tongue grow and wrap around the axon to form myelination. Then the Hypothesis-E$_N$ ("N" refers to "negative") is described as follows:

> *The inner tongue of myelin is driven by a negative E-field from the axon in the resting state. The strength of the E-field on the inner tongue is proportional to its growth rate. When the E-field is lower than a threshold, the growth of the inner tongue terminates.*

Modeling the relationship between g-ratio and the E-field

Figure 2B shows a mature myelinated axon with the number of myelin lamellae as ***N***. The axonal radius is ***a,*** and the thickness of a single myelin lamella is ***b***. Then the total myelin thickness, ***D***, is **b** × **N**. We assume that the axonal cross-section is centrally symmetric. So we only simulate the local axon with a radial angle as θ, as shown in **Figure 2B**. The capacitance, ***C***, of each layer is proportional to its area. Since the longitudinal length of each layer is identical, the capacitance of each layer is proportional to the arc length ***l***:

$$C \propto Area \propto l$$

Then for the $\boldsymbol{n^{th}}$ layer, the capacitance, $\boldsymbol{C_n}$, is proportional to its arc length $\boldsymbol{l_n}$:

$$C_n \propto l_n = \theta \times (a + (n-1)b)$$

The voltage, $\boldsymbol{V_n}$, on the $\boldsymbol{n^{th}}$ layer is $V_n = \frac{Q_n}{C_n}$.

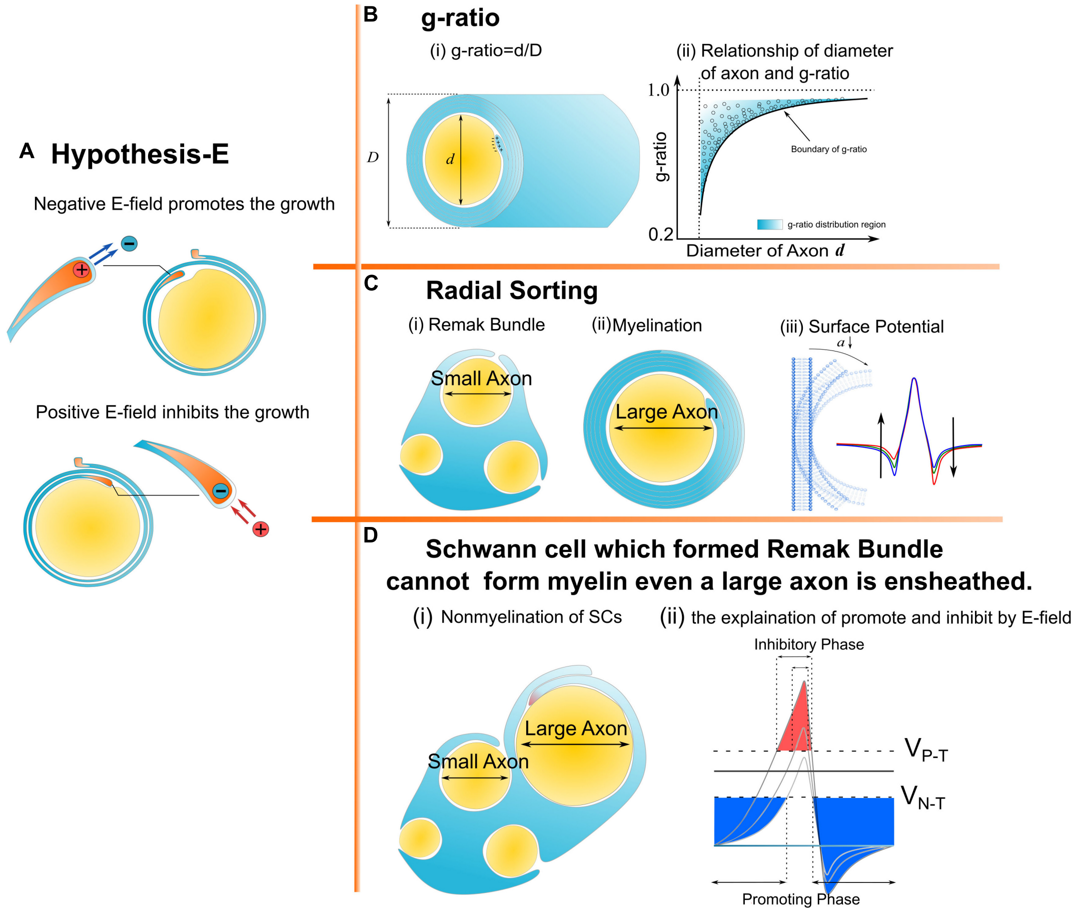

FIGURE 1

A series of morphological characteristics of myelin explained a mathematical and physical perspective. **(A)** Hypothesis-E: The effect of E-field on myelin growth; **(B,C)** phenomena explained by Hypothesis-E: **(B)** g-ratio: The thickness of myelin sheath has a specific relationship with the diameter of the axon. **(C)** Radial Sorting: Myelin selectively myelinated axon based on axonal diameter; **(D)** SC of remak bundle cannot form myelin even when a large axon is ensheathed.

Here $\boldsymbol{Q_n}$ is the charge on the capacitor. So the voltage, $\boldsymbol{V_1}$, on the first layer is $V_1 = \frac{Q_1}{C_1}$.

Since all capacitors are connected in series, as shown in Figure 2C, the two boundary conditions are:

(1). The charge on each capacitor is the same, assigned with the value of $\boldsymbol{Q}$:

$$Q = Q_1 = Q_2 = Q_3 = \cdots = Q_N$$

(2). The resting potential, $\boldsymbol{V_R}$, is equivalent to a voltage source connected with these series-connected capacitors, as shown in Figure 2C, so $\boldsymbol{V_R}$ is the sum of the voltage on all capacitors:

$$V_R = \sum_{n=1}^{N} V_n = \sum_{n=1}^{N} \frac{Q_n}{C_n} = Q \times \sum_{n=1}^{N} \frac{1}{C_n}$$

The charge, $\boldsymbol{Q}$, on each capacitor is:

$$Q = \frac{V_R}{\sum_{n=1}^{N} \frac{1}{C_n}}$$

The voltage, $\boldsymbol{V_1}$, on the first layer, which is the inner tongue, is as shown below:

$$V_1 = \frac{Q}{C_1} = \frac{V_R}{C_1 \times \sum_{n=1}^{N} \frac{1}{C_n}} = \frac{V_R}{a \times \sum_{n=1}^{N} \frac{1}{(a+(n-1)b)}} \tag{1}$$

when the voltage potential, $\boldsymbol{V_R}$, and the thickness of a single myelin lamella, $\boldsymbol{b}$ are constants, the voltage on the inner tongue, $\boldsymbol{V_1}$, is only a function of the number of layers $\boldsymbol{N}$, axonal radius $\boldsymbol{a}$, and monotonically decreases with the number of layers, $\boldsymbol{N}$. Here the threshold E-field proposed in Hypothesis-E$_N$ is defined as $\boldsymbol{V_{N-T}}$ ("N" refers to "negative" and "T" refers to "threshold").

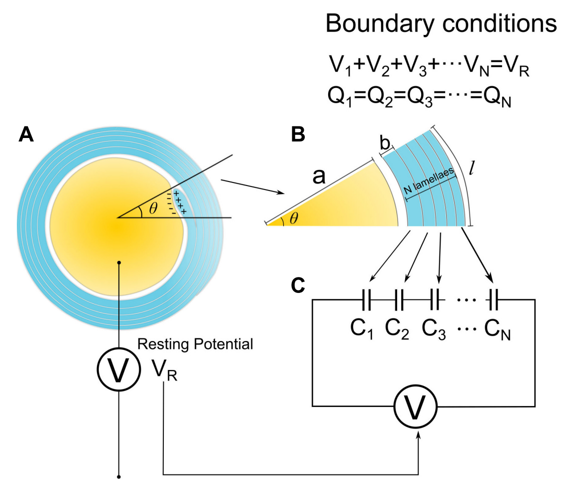

FIGURE 2
The model to explain g-ratio. **(A)** The cross-section of a myelinated axon in the static condition, the resting potential is equivalent to a voltage source; **(B)** a section of myelin cross-section with a radial angle of θ; **(C)** the equivalent circuit modeling the myelin cross-section.

And the ratio between $\boldsymbol{V_{N-T}}$ and $\boldsymbol{V_R}$ is defined as η_{N-T}:

$$\eta_{N-T} = \frac{V_{N-T}}{V_R} \tag{2}$$

Then the criteria for the max number of myelin lamellae $\boldsymbol{N_{max}}$ is:

$$\begin{cases} V_1 \geq V_{N-T} \text{ when } N = N_{max} \\ V_1 \leq V_{N-T} \text{ when } N = N_{max}+1 \end{cases} \tag{3}$$

Substitute (1) and (2) into (3) and get:

$$\begin{cases} \frac{1}{a \times \sum_{n=1}^{N_{max}} \frac{1}{(a+(n-1)b)}} \geq \eta_{N-T} \\ \frac{1}{a \times \sum_{n=1}^{N_{max}+1} \frac{1}{(a+(n-1)b)}} \leq \eta_{N-T} \end{cases} \tag{4}$$

(4) can be further simplified as follow:

$$\frac{1}{a \times \sum_{n=1}^{N_{max}} \frac{1}{(a+(n-1)b)}} \approx \eta_{N-T} \tag{5}$$

As seen, the value $\boldsymbol{N_{max}}$ is a function of $\boldsymbol{a}$ and η_{N-T}, while $\boldsymbol{b}$ is constant:

$$N_{max} = f_1(a, \eta_{N-T})$$

Then *g-ratio* is also a function of $\boldsymbol{a}$ and η_{N-T}:

$$g_{ratio} = \frac{a}{a+D} = \frac{a}{a+b \times N_{max}} = \frac{a}{a+b \times f_1(a, \eta_{N-T})} = f_2(a, \eta_{N-T})$$

To enable calculating these two functions, we need to obtain the constant of $\boldsymbol{b}$. Based on previous studies, we set $\boldsymbol{b}$ = 17 nm as a typical value (Nave and Werner, 2014). The g-ratio and $\boldsymbol{N_{max}}$ simulation is shown in **Figures 3A,B**.

Results

In **Figure 3A**, the g-ratio curve monotonically increases with axonal radius $\boldsymbol{a}$. The curve of $\boldsymbol{N_{max}}$ has a decreasing slope with $\boldsymbol{a}$, approaching a constant value determined by η_{N-T}. It is emphasized that $\boldsymbol{N_{max}}$ is an axon's maximum number of myelin lamellae. The actual measured number of myelin lamellae $\boldsymbol{N}$ should be no more than $\boldsymbol{N_{max}}$ shown in **Figure 3B**, $N \leq N_{max}$. Thus, g-ratio curves shown in **Figure 3A** are a minimum value, which is a lower limit. As illustrated in **Figure 3D**, all measured data points of the g-ratio shall be higher than the g-ratio curve in **Figure 3A**. By fitting the curve of this lower edge, the actual η_{N-T} can be obtained. In **Figure 3E**, we validate our simulations with the experimental data from previously published studies of myelinated axons (Sanders and Whitteridge, 1946; Zhao et al., 1995; Michailov et al., 2004; Chomiak and Hu, 2009; Paus and Toro, 2009; Ikeda and Oka, 2012; FitzGibbon and Nestorovski, 2013; Barbizan et al., 2014; Bercury et al., 2014; Ronchi et al., 2014; Xie et al., 2014; Lee et al., 2017; Klok et al., 2018; Dimas et al., 2019; Marro et al., 2019; Ferreira et al., 2021). We found a clear edge can be formed (the red fitting curves are plotted by ourselves for an indicator of boundary). As mentioned above, by fitting this lower edge, the threshold voltage, which is an important characteristic of the target nervous system, can be obtained. This characteristic is not recognized yet in conventional theories and models. Noticeably, $\boldsymbol{N_{max}}$ goes infinite when $\boldsymbol{a}$ approaches zero, indicating that the axon with a very small diameter can have infinitely thick myelin. However, the axons with a radius within the divergence region in **Figure 3B** are unmyelinated. We will make a more detailed discussion in the next section.

Discussion

Why does the divergence happen?

The condition to achieve $\boldsymbol{N_{max}}$ is to meet the condition of Equation (5), as written again here:

$$\frac{1}{a \times \sum_{n=1}^{N_{max}} \frac{1}{(a+(n-1)b)}} \approx \eta_{N-T} \tag{5}$$

However, the limit of η_{N-T} when $\boldsymbol{N_{max}}$ approaches infinite is as follows:

$$\lim_{N_{max}\to\infty} \eta_{N-T} = \lim_{N_{max}\to} \frac{1}{a \times \sum_{n=1}^{N_{max}} \frac{1}{(a+(n-1)b)}} = \frac{b}{a}$$

where $\boldsymbol{b/a}$ is the lower limit of η_{N-T}. If the actual η_{N-T} is above this lower limit, $\boldsymbol{V_1}$ can reach $\boldsymbol{V_{N-T}}$ when $\boldsymbol{N_{max}}$ is a finite number; then, the myelin growth stops (Eq. 6). However, if the actual is η_{N-T} lower than this lower limit, $\boldsymbol{V_1}$ can never be

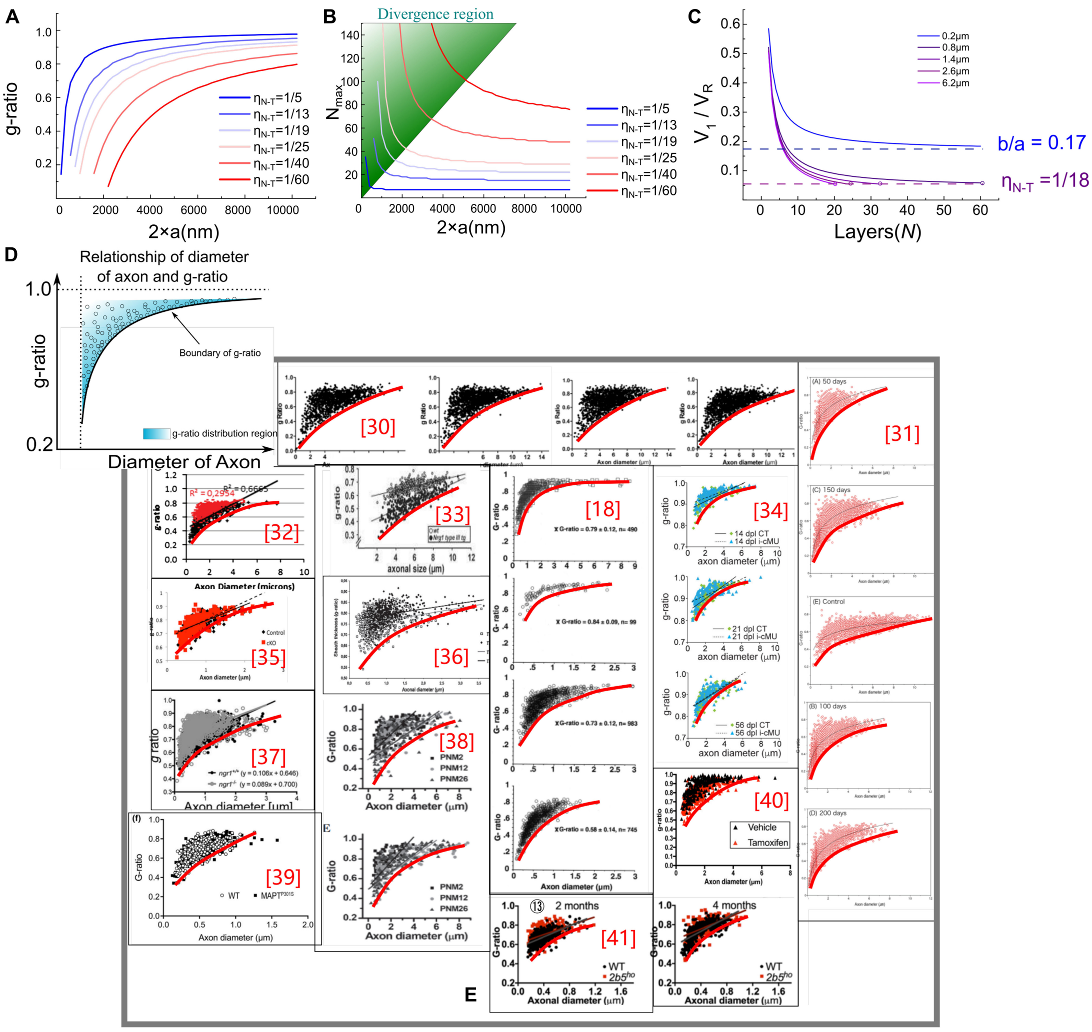

FIGURE 3

(A,B) g-ratio values and the maximum number of myelin lamellae, N_{max} values, given different η_{N-T}. **(C)** The relationship between $\boldsymbol{N}_{max}$ and $\boldsymbol{V}_1/\boldsymbol{V}_R$. When b/a < η_{N-T}, $\boldsymbol{N}_{max}$ is a finite number, otherwise $\boldsymbol{N}_{max}$ is infinite. **(D)** Illustration of the claim: the measured statistical data of g-ratio shall locate above the g-ratio curve; **(E)** the measured statistical data of g-ratio in publications (Michailov et al., 2004; Paus and Toro, 2009; Ikeda and Oka, 2012; FitzGibbon and Nestorovski, 2013; Barbizan et al., 2014; Bercury et al., 2014; Nave and Werner, 2014; Ronchi et al., 2014; Xie et al., 2014; Lee et al., 2017; Dimas et al., 2019; Marro et al., 2019; Ferreira et al., 2021).

reduced to V_{N-T}, whatever N_{max} is; the myelin growth never stops (Eq. 7).

$$when\ \frac{b}{a} < \eta_{N-T};\ N = finite\ number \tag{6}$$

$$when\ \frac{b}{a} \geq \eta_{N-T};\ N \to \infty \tag{7}$$

where the occurrence of divergence is determined by the ratio between the thickness of single-layer myelin, $\boldsymbol{b}$, and the axonal radius, $\boldsymbol{a}$. When $\boldsymbol{a}$ is large enough to meet Eq. (6), the calculation of N_{max} is convergent. Otherwise, the divergence happens when $\boldsymbol{a}$ is a small number, which is the case of unmyelinated axons. A more intuitive modeling result is shown in **Figure 3C**. Since V_1 decreases with the growth of myelin lamellae, the ratio of $\boldsymbol{V}_1/\boldsymbol{V}_R$ will decrease with $\boldsymbol{N}$. Then this ratio reaches the value of η_{N-T}, the curve stops at the value of $\boldsymbol{N}_{max}$. As seen, the curve of the axonal diameter of 0.8, 1.4, 2.6, and 6.2 μm can have a finite value of $\boldsymbol{N}_{max}$. However, when axon diameter is 0.2 μm, the curve of $\boldsymbol{V}_1/\boldsymbol{V}_R$ approaches $\frac{b}{a} = 0.17$ ($\boldsymbol{b}$ = 17 nm and axonal radius $\boldsymbol{a}$ = 100 nm), which is higher than η_{N-T} = 1/18≈0.056, the growth cannot be stopped.

The relation between the divergence region and unmyelinated axons

Since the modeling result can closely predict the biological observations of the g-ratio and myelin thickness at different axonal diameters, we tend to explore the

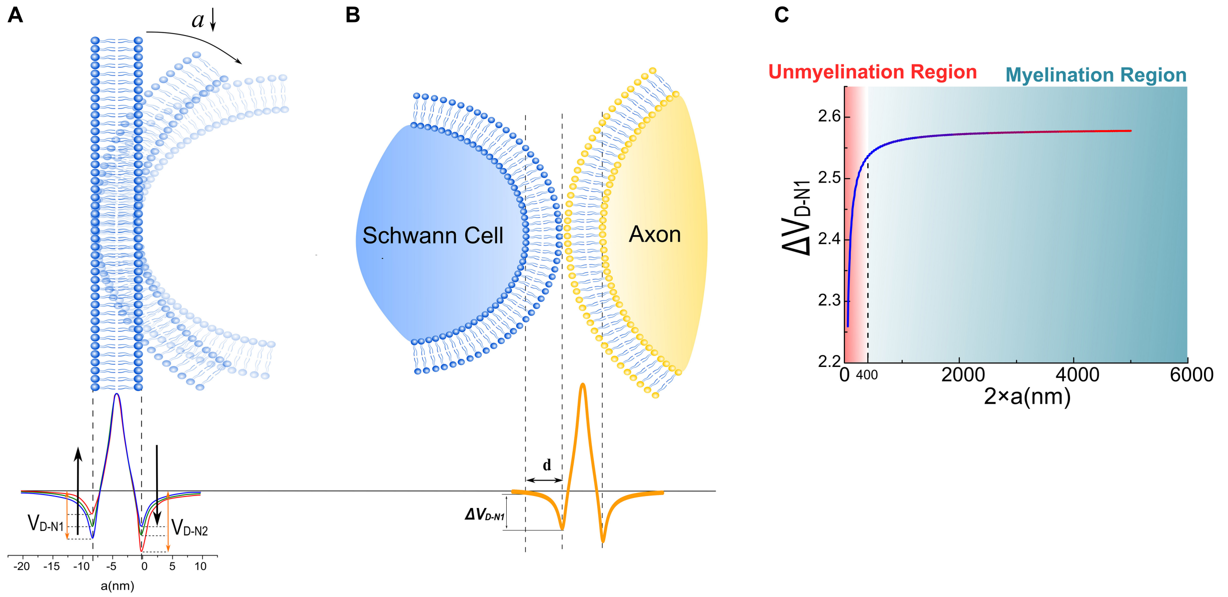

FIGURE 4
(A) The dipole potential generated by the bending of the cell membrane; **(B)** when a Schwann cell contact with the cell membrane of an axon, a portion of the surface potential, V_{D-N1}, will be exerted upon Schwann cell's membrane, labeled as ΔV_{D-N1}; **(C)** the simulation result of ΔV_{D-N1} is a function of axonal diameters.

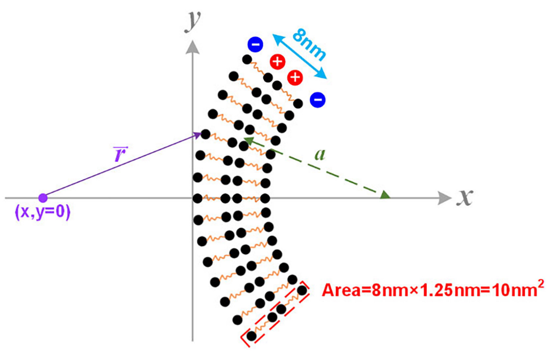

FIGURE 5
The modeling details of the calculation of the cell membrane's dipole potential.

biological meaning hidden behind the divergence region. It is observed that the number of myelin lamellae suddenly decreases to zero when the axonal diameter is lower than a threshold, indicating that some unknown factors dominate the growth of smaller myelin and forbid the process of myelination.

Interestingly, Hypothesis-E$_N$ suggests that the axon of very small diameter can have infinitely thick myelin, which disagrees with biology. Therefore, some unknown factor that inhibits myelin growth during myelin development is introduced when the axonal diameter is lower than a certain value. We will discuss this unknown factor in section "A revision of the g-ratio model."

An introspection of this model

The origin of the g-ratio is the myelin's growth rate inversely proportional to its layers. That is, the promoting factor of myelin growth decays with its layers. Meanwhile, the inner tongue is the growing terminal of the myelin, indicating this promoting factor exerts its function on the inner tongue. In our model, the voltage, V_1, on the inner tongue meets these boundary conditions. Any alternative theories shall also meet the above-mentioned boundary conditions. Since this V_1 is obtained from Hypothesis-E$_N$, so it is renamed as V_{EN} in this article to avoid confusion.

Hypothesis-E$_D$ to explain radial sorting

Radial sorting

Radial sorting is the process by which Schwann cells choose larger axons to myelinate during development (Monk et al., 2015). During this process, SCs proliferate and expand cellular extensions into bundles of unsorted axons to detach individual axons and establish the 1:1 relationship (one SC can only myelinated one axon) required for myelination (Webster et al., 1973). Axons with a diameter of < 1 µm remain in bundles, and SCs in contact with these axons differentiate into unmyelinated SCs, called remak bundles (Griffin and Thompson, 2008). This radial sorting process is reported to be tightly regulated and depends on signals from axons as well as the extracellular matrix (Ghidinelli et al., 2017).

Hypothesis-E$_D$

With the radial sorting process, SCs can recognize functionally identified axons just by their calibers. Axons of large caliber possess a promoting factor, while the axons of small caliber possess an inhibiting factor to the myelin growth. Based on Hypothesis-E, we can predict that larger axons can possess a more negative voltage than that of smaller axons. Then Hypothesis-E$_D$ ("D" refers to "dipole") refers to:

> *When SCs get close to the surfaces of axons, axons of larger caliber will exert a special "E-field," which is more negative than that of the axons of smaller caliber, to the cell membrane of SCs. Thus, SCs tend to grow and wrap on larger axons. When the caliber of axons is lower than a threshold, the amplitude of the negative E-filed is too low to enable the growth of SCs on their surfaces.*

Modeling the relationships between the radial sorting and the dipole potential

In **Figure 4A**, the axon membrane lipid bilayer consists of two layers of amphiphilic molecules. The positively charged hydrophobic tails of these lipids are directed toward the membrane center, while the negatively charged hydrophilic heads are directed toward the extra- and intracellular fluid (Monje, 2018). Each amphiphilic molecule is an electric dipole, a group of separated charges with opposite polarities. Thus, by arranging the position of each polar, the potential of a point as a function of the distance to the membrane can be calculated as shown in **Figure 5**. The arrangement of each polar is determined by the thickness of the bilayer and the diameter of the axon. Here axon radius, $\boldsymbol{a}$, is a variable. The total thickness of the lipid bilayer is 8 nm, a typical value of a cell membrane. The length of the dipole of each amphiphilic molecule is 3.6 nm, while the distance between the two positively charged polar is 0.8 nm. The cross-sectional area of each group of molecules is 10 nm^2. The charge quantity of the n$_{th}$ polar is q_n. The route from n$_{th}$ polar to the specific point (x, y = 0) on the x-axis is $\vec{\mathbf{r}}_n$. The total electric potential at the position (x, y = 0) is the sum of the potential from each polar, as below:

$$\varphi = \frac{1}{4\pi\varepsilon_0} \sum \frac{q_n}{\left|\vec{\mathbf{r}}_n\right|}$$

Here q_n is a value with a sign corresponding to the polarity of the charge. Considering the value of each q_n is identical, so

$$\varphi = \frac{1}{4\pi\varepsilon_0} \sum \frac{q_n}{\left|\vec{\mathbf{r}}_n\right|} \propto \sum \frac{1}{\left|\vec{\mathbf{r}}_n\right|}$$

So

$$\triangle V_{N1} = \varphi|_{x=0\ nm} - \varphi|_{x=-8\ nm}$$

The potential, also called the dipole potential, generated by this lipid bilayer is shown in **Figure 4A**. Such dipole potential has two negative peaks at the extra- and intracellular surface and one positive peak at the membrane center (McLaughlin, 1989; Langner et al., 1990; McLaughlin and Murray, 2005; Leventis and Grinstein, 2010). The bending of the cell membrane will break the centrosymmetry of the bilayer structure and change the amplitude of those two negative peaks, called the flexoelectric effect (Petrov, 2002). In particular, the amplitude of the left negative peak located at the extracellular surface, named $\boldsymbol{V}_{D-N1}$ ("D" refers to "dipole" and "N" refers to "negative"), decreases with bending, while the amplitude of the right negative peak located at the intracellular surface, named $\boldsymbol{V}_{D-N2}$, increases with bending. When the SC membrane contacts with the axon surface, a portion of $\boldsymbol{V}_{D-N1}$, labeled as $\Delta\ \boldsymbol{V}_{D-N1}$ in **Figure 4B**, is applied across SC's membrane. This $\Delta\ \boldsymbol{V}_{D-N1}$ meets the criteria of growth promotion, which is an external negative E-field. Meanwhile, the amplitude of this $\Delta\ \boldsymbol{V}_{D-N1}$ increases with the axon caliber and saturates at a certain value (**Figure 4C**). Interestingly, in this modeling, $\Delta\ \boldsymbol{V}_{D-N1}$ has a sudden decline from a specific position at about 400 nm.

The surface potential of the cell membrane can influence the binding affinity of the peptide to lipid bilayers (Zhan and Lazaridis, 2012). So it is conjectured that the binding affinity between the polarized protein molecules on the SC membrane and axons, which are responsible for the interface adhesion, is positively correlated with the surface dipole potential of the axon $\Delta\ \boldsymbol{V}_{D-N1}$. When the axon caliber is large, $\Delta\ \boldsymbol{V}_{D-N1}$ is strong enough for the molecules to form the bound; thus, SCs can grow and wrap on these axons to form myelin. However, when the axon caliber is lower than a certain value, e.g., 400 nm in **Figure 4C**, $\Delta\ \boldsymbol{V}_{D-N1}$ is insufficient to provide the binding affinity, leading to the failure of SC in adhering to the axon. It indicates that there is a threshold of axonal diameter to be myelinated, which is the observation of radial sorting of SCs. This threshold is about 1 μm is the actual observation. Considering that the modeling in this study is simplified and qualitative, it only indicates the existence of the threshold diameter rather than giving a precise value to it. Nevertheless, these simulation results suggest that the dipole potential from the axon surface can be one of the factors influencing myeline developments.

An introspection of this model

In radial sorting, SCs can robustly identify the axons by their physical calibers. It means that the surface curvature is an important factor to be experienced by SCs. So it can be inferred that this physical identification signal is related to the surface curvature. The dipole potential is one of the candidates determined by the axon caliber and whose changing trend is consistent with Hypothesis-E. Since this $\Delta\ \boldsymbol{V}_{D-N1}$ is obtained from Hypothesis-E_D, it is renamed as $\boldsymbol{V}_{ED}$ to avoid confusion with other variables. Meanwhile, it is well-known that Nrg1 type III plays a crucial role in the myelination of SCs. A complete theory/model should account for this protein. We will have a detailed discussion in section "A more complete understanding of radial sorting."

Hypothesis-E_P to explain behaviors of Schwann cells

Different behaviors of Schwann cells in myelination and remak bundle

The SCs behave differently in myelination and remak bundles (Feltri et al., 2016). In the scenario of myelination, an SC will wrap around a large axon with a 1:1 relationship. In the scenario of a remak bundle, an SC can never form myelination, even if a large axon is ensheathed.

Hypothesis-E_P

Hypothesis-E_P (P refers to "Positive") is proposed to reveal the myelination criteria and explain the mechanism underlying differential SC activities:

> *The growth of the inner tongue of myelin is inhibited by a positive E-field induced by action potentials. The strength of the E-field on the inner tongue is proportional to its capability of growth-inhibiting. When the E-field is lower than a threshold, it does not exert its inhibition function.*

In **Figure 6A**, a new perspective about how myelin growth is modulated by E-field is shown. $\boldsymbol{V}_P$ and $\boldsymbol{V}_N$ refer to the amplitude of resting potential and the positive peak voltage of the action potential, respectively. The threshold voltage $\boldsymbol{V}_{P-T}$ is the threshold voltage to inhibit myelin growth, while $\boldsymbol{V}_{N-T}$ is the threshold voltage to promote myelin growth. The ratio between $\boldsymbol{V}_{P-T}$ and $\boldsymbol{V}_P$ is $\eta\ _{P-T}$, and the ratio between $\boldsymbol{V}_{N-T}$ and $\boldsymbol{V}_N$ is $\eta\ _{N-T}$. The area higher than $\boldsymbol{V}_{P-T}$ is the inhibition phase (red area in **Figure 6A**), while the area lower than $\boldsymbol{V}_{P-T}$ is the promotion phase of myelin growth (blue area in **Figure 6A**).

In **Figures 6Bi,ii**, the total voltage $\boldsymbol{V}$ (this voltage can be either the resting potential $\boldsymbol{V}_R$ or the action potential $\boldsymbol{V}_A$, "***A***" refers to "action") across a single-layer myelin is applied on $\boldsymbol{C}_{1-A}$ and $\boldsymbol{C}_{2-A}$ ("A" refers to the capacitor of case A in **Figure 6B**):

$$C_{1-A} \propto a;$$

$$C_{2-A} \propto 2\ \times\ (a+b);$$

$$Q_{1-A}\ =\ C_{1-A}\ \times\ V_{1-A}\ =\ Q_{2-A}\ =\ C_{2-A}\ \times\ V_{2-A}\ =\ Q;$$

$$V_{1-A} + V_{2-A}\ =\ V;$$

Since $\boldsymbol{C}_{2-A}$ only has a single layer of the cell membrane, the equivalent capacitance shall be doubled compared with the one with double layers of the cell membrane.

Then the ratio between the voltage on $\boldsymbol{C}_{1-A}$ and $\boldsymbol{V}$ is:

$$\eta_A\ =\ \frac{V_{1-A}}{V}\ =\ \frac{1}{1+\frac{a}{2a+2b}}\ =\ \frac{1}{1+\frac{1}{2+2\ \times\ \frac{b}{a}}};$$

In **Figures 6Biii,iv**, the total voltage $\boldsymbol{V}$ across a double-layer myelin is applied on $\boldsymbol{C}_{1-B}$, $\boldsymbol{C}_{2-B}$, and $\boldsymbol{C}_{3-B}$ ("B" refers to the capacitor of case B in **Figure 6B**):

$$C_{1-B} \propto a;$$

$$C_{2-B} \propto a+b;$$

$$C_{3-B} \propto 2\ \times\ (a+b+b');$$

$$Q_{1-B}\ =\ C_{1-B}\ \times\ V_{1-B}\ =\ Q_{2-B}\ =\ C_{2-B}\ \times\ V_{2-B}\ = \\ Q_{3-B}\ =\ C_{3-B}\ \times\ V_{3-B}\ =\ Q;$$

$$V_1 + V_2 + V_3\ =\ V;$$

Here we set the thickness of the second layer is $\boldsymbol{b}'$, which is different from that of the first layer $\boldsymbol{b}$. Since $\boldsymbol{C}_{3-B}$ only has a single layer of the cell membrane, its equivalent capacitance shall be doubled.

Then the ratio between the voltage on $\boldsymbol{C}_{1-B}$ and $\boldsymbol{V}$ is:

$$\eta_B\ =\ \frac{V_{1-B}}{V}\ =\ \frac{1}{1+\frac{a}{a+b}+\frac{a}{2(a+b+b')}};$$

Since the myelin lamellae are not compact yet at the initial myelination process, $\boldsymbol{b}$ is a value comparable with $\boldsymbol{a}$. So here we set the ratio of $\boldsymbol{b}/\boldsymbol{a}$ is 0.1, which is a typical value and a reasonable approximation, to further simplify the equation of $\eta\ _A$ and $\eta\ _B$ as below:

$$\eta_A\ =\ \frac{1}{1+\frac{1}{2+2\ \times\ \frac{b}{a}}}\ \approx\ 0.88;$$

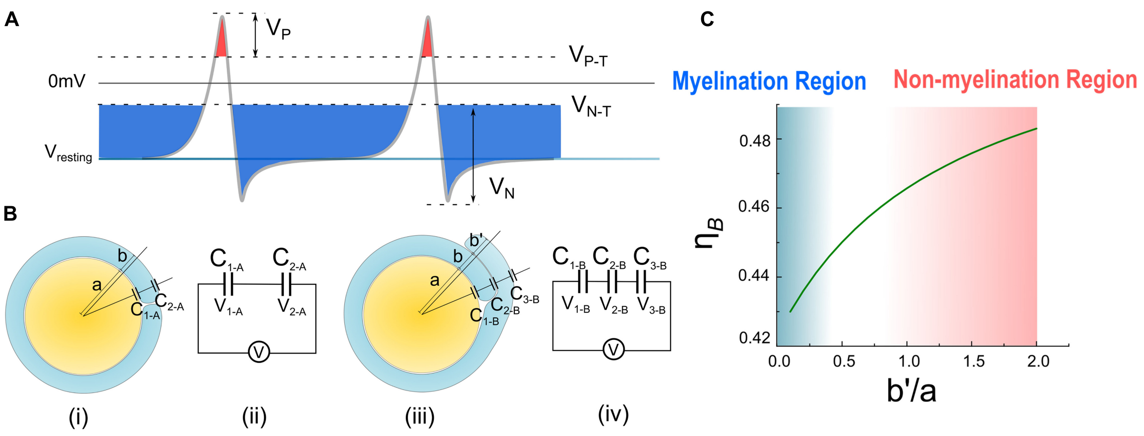

FIGURE 6
(A) The illustration of Hypothesis combining E_N and E_P; **(B)** (i), (ii) the condition of case A with one layer of myelin and its equivalent circuit. (iii), (iv) The condition of case B with double- layer myelin and its equivalent circuit. **(C)** Calculate result of η_B curve changes with $\frac{b'}{a}$.

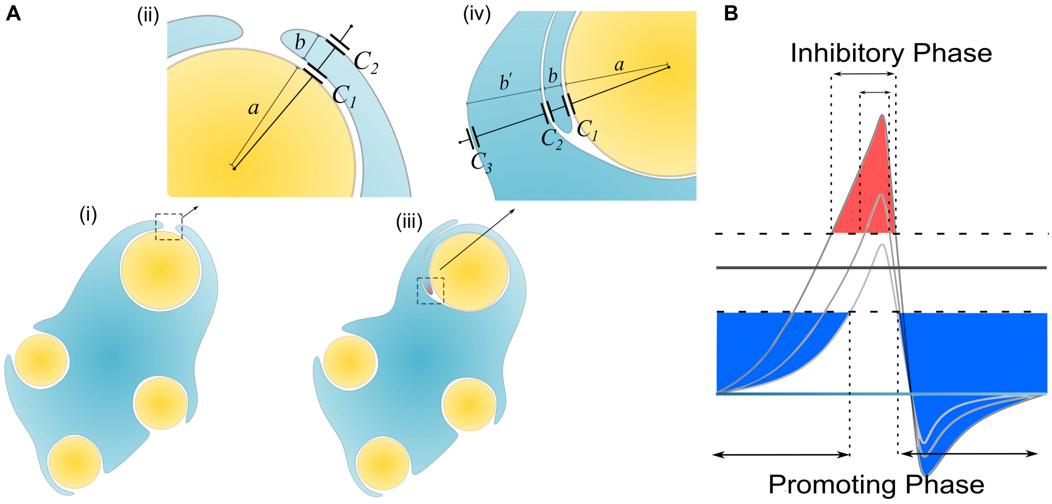

FIGURE 7
(A) The scenario when an SC of remak bundle ensheathes a large axon: (i, ii) Only one layer of SC is wrapped; (iii, iv) when the SC tries to wrap the second layer; **(B)** A more decayed action potential induces a shorter inhibitory phase (red region).

$$\eta_B = \frac{1}{1 + \frac{a}{a+b} + \frac{a}{2(a+b+b')}} = \frac{1}{1.909 + \frac{1}{2(1.1+\frac{b'}{a})}};$$

As seen, η_A is a constant, meaning that about 88% of the transmembrane voltage, which can be either $\boldsymbol{V_R}$ or $\boldsymbol{V_A}$, will be applied onto the adaxonal layer of the myelin. Meanwhile, η_B is a function of $\frac{b'}{a}$, which is calculated as shown in Figure 6C. η_B increases with $\frac{b'}{a}$.

Then let's consider the situations of the wrapping of the second myelin lamella on a large axon by both a normal SC and a remak SC, as shown in Figures 6B, 7A, respectively. For an SC forming myelination, the condition is similar to Figure 6B when a/b'. So its η_B is located within the blue region in Figure 6C, labeled with myelination region. For a remak SC, the condition is similar to Figure 6A. When a large axon is ensheathed by a remak bundle, initially the axon is wrapped by a SC as shown in Figures 7Ai,ii. When one of the SC terminal tends to further grow and wrap the large axon to form myelin, it inevitably faces the situation shown in Figures 7Aiii,iv when $\boldsymbol{b'}$ is comparative or even larger than $\boldsymbol{a}$. Thus its η_B is located within a pink region in Figure 6C, labeled with the non-myelination region.

In Hypothesis-E_P, a positive voltage $\boldsymbol{V_P}$ in the action potential can inhibit myelin growth. Therefore, for a normal SC myelinating a large axon, the inhibiting voltage exerted upon the inner tongue is lower. The promoting factor induced by the negative voltage (mainly comes from the resting potential) dominates the myelin growth (see Figure 7B). However, for a remak SC, the inhibiting voltage upon the inner tongue is higher. Thus the inhibiting factor dominates the myelin growth, stopping the wrapping of the second layer. Since this inhibitory voltage on the inner tongue, $\boldsymbol{V_P} \times \eta_B$, is obtained from Hypothesis-E$_P$, it is renamed as $\boldsymbol{V_{EP}}$ to avoid confusion with other variables. This simulation under Hypothesis-E$_P$ supports the experimental observation of the radial sorting (Monk et al., 2015), that is, (1) An SC can merely myelinate one axon. (2) Remak SC cannot myelinate. Moreover, we can also make a rough estimation of η_{P-T}. It is a value located close to the myelination and non-myelination region interface 0.43~0.46 shown in **Figure 6C**.

The modeling process shown in **Figure 6** is an oversimplified model since the non-compact myelin sheath cannot be simplified as pure capacitors. We propose it just for consistency with the method in **Figure 2**. A More reasonable model with a circuit network by considering the cytoplasm in non-compact myelin sheath is shown in **Figure 8A**. The inner, middle, and outer layers are modeled as capacitors, respectively, C1, C2, and C3. The cytoplasmic fluid within the cell is modeled as resistors connecting the inner, middle, and outer layers. The modeling parameter is shown as follows:

$$C_1 = 5pF;$$

Considering that the middle layer consists of two layers of cell membrane, thus:

$$C_2 = 6pF||6pF = 12pF;$$

Since we need to model the increasing of the outer layer, thus C3 should change within a range as follows:

$$C_3 = 7pF \sim 70pF;$$

The resistor modeling the cytoplasmic fluid is:

$$R = 1\Omega;$$

Then we connect a voltage source, which models the action potential, with the intracellular and extracellular terminals. The voltage on one of the capacitors on the inner layer, which is C1, is measured by changing the value of C3. The simulation is performed in Simulink of MATLAB. The modeling results are shown in **Figure 8B**. As seen, the general trend of the voltage on the inner layer by increasing the outer layer is consistent with the result in **Figure 6C**. The exact numerical value is different. This is because by considering the conductive cytoplasmic channel connecting the inner and outer layers, the capacitors modeling the middle layer are short-circuited. Thus, all the voltage is shared only by the inner and outer layers, amplifying the voltage tuning effect by increasing the outer layer. Considering that all models here are for qualitative rather than quantitative study, we only focus on the general changing trend rather than the exact numerical value.

Discussion

This model also indicates potential explanations for other experimental observations, as discussed below. Firstly, it is contradictory to the conventional understanding of the correlation between neural activities and myelin development. It was widely believed that the action potential is a positive factor in the myelination process (Monje, 2018), while in our model, it is a negative factor. If our model is correct, it can be predicted that by eliminating the action potential during myelin development, the myelin can grow thicker. Mayoral et al. (2018) have confirmed this hypermyelination phenomenon of oligodendrocytes by muting the action potential, which is supporting evidence of our model. It can be foreseen that the same phenomenon can be observed in the experiment of SCs. Secondly, the frequency of the action potential is also a factor affecting the fate of myelination. When the action potential is activated more frequently, which is the case of sensory fibers, the inhibiting factor tends to dominate, and the axons tend to be unmyelinated. Conversely, when the action potential is activated more rarely, which is the case of motor fibers, the promoting factor tends to dominate, and the axons tend to be myelinated. This may partially explain that the majority of the sensory fibers are unmyelinated while the counterparts of the motor fibers are myelinated (Schmalbruch, 1986). This model also indicates a positive correlation between neural hyperactivity and the degeneration of myelin. It may provide a clue for neurodegenerative disorders such as Parkinson's disease, whose early stage symptoms, such as hand tremors and muscle stiffness, are the results of uncontrollable hyper-activation of some neurons, while the accompanying symptoms include the demyelination of neurons. At least, these phenomena are not contradictory to our model.

A recap of the g-ratio phenomenon

The observation of the hypermyelination of oligodendrocytes by muting the action potential (Mayoral et al., 2018) reveals the relationship between myelination and neural activities. This observation indicates that an axon with fewer action potentials tends to have thicker myelin, while an axon with more action potentials tends to have thinner myelin. So the action potential is an inhibitory factor to the myelin growth, which agrees with our theory. Meanwhile, it also indicates a quantitative relationship between the frequency of action potential and the myelin thickness. An illustrative drawing of this quantitative relationship is shown in **Figure 9A**. For an axon with a very high frequency of action potential (**Figure 9A1**), it tends to be unmyelinated, which refers to the unmyelinated region (Region 1 in **Figure 9A1**). For an axon with a very low frequency of action potential, its myelin can grow to the maximum thickness, which refers to the lower

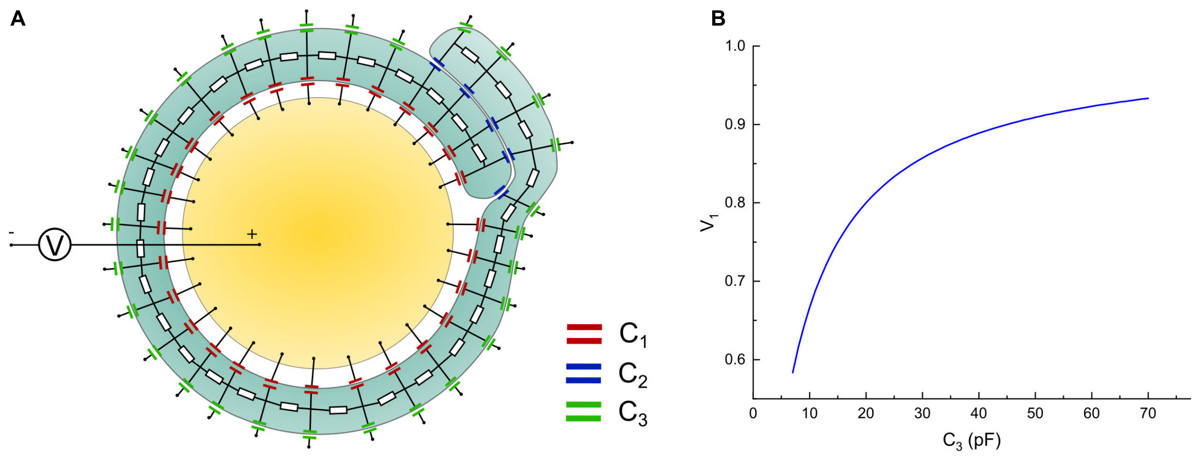

FIGURE 8
(A) A more detailed circuit model; **(B)** the voltage on the inner layer capacitor, C1, by increasing the capacitance of the outer layer, C3.

edge (Region 3 in **Figure 9A2**). For the axon with a medium frequency of action potential, its myelin cannot grow to the maximum thickness, even at its mature state. This scenario refers to Region 2 in **Figure 9A2**. Then based on our theory, a complete explanation of the g-ratio phenomenon, including the non-myelination region, the lower edge, and the scattering data distribution, is proposed in **Figure 9A**. Moreover, our theory also makes another very interesting prediction. If unmyelinated axons tend to have a lower diameter and higher frequency of action potentials, it indicates a relationship between the action potential and the axonal diameter. In other words, the action potential is also an inhibitory factor to the radial growth of the axon.

An introspection of this model

Currently, we cannot claim this is the exclusively correct model. But it is highly consistent with the whole theory. The behavior of SCs is determined by whether the inner tongue can further grow to form the second layer, which is still a growth issue. Since the inner tongue growth is affect by E-field in this theory, by leveraging the same circuit model and Hypothesis-E, we can easily acquire the explanatory model shown in **Figure 7** without adding any new hypotheses.

Discussion: A rethinking of the complete model

The influence of the total voltage

At the beginning of this study, we have proposed the Hypothesis-E, which conjectures that the development of myelin is guided by an E-field applied upon the inner tongue. By explaining different phenomena of myelin development, it is concluded that this E-field consists of three components, as summarized below.

(1) The component, $\boldsymbol{V_{EN}}$, from $\boldsymbol{V_R}$. Although $\boldsymbol{V_R}$ is almost an identical value for axons of different calibers, its component, $\boldsymbol{V_{EN}}$, applied to the inner tongue changes with both the axon caliber and the number of myelin lamellae, explained in **Figure 2**. Therefore, $\boldsymbol{V_{EN}}$ is a function of both the axon caliber, $\boldsymbol{a}$, and the number of myelin lamellae, $\boldsymbol{N}$:

$$V_{EN} = f_{EN}(a, N);$$

(2) The component, $\boldsymbol{V_{EP}}$ from $\boldsymbol{V_A}$. This $\boldsymbol{V_{EP}}$ functions the same as $\boldsymbol{V_{EN}}$ in the circuit, just with a different waveform. So it is also a function of $\boldsymbol{a}$ and $\boldsymbol{N}$ and changes with the same trend as $\boldsymbol{V_{EN}}$:

$$V_{EP} = f_{EP}(a, N);$$

(3) The component, $\boldsymbol{V_{ED}}$, is from the dipole potential of the cell membrane. This component does not change with the number of myelin lamellae, $\boldsymbol{N}$. So it is just a function of $\boldsymbol{a}$:

$$V_{ED} = f_{ED}(a);$$

The voltage upon the inner tongue, $\boldsymbol{V_I}$, is the sum of these three components:

$$V_I = f_{EN}(a, N) + f_{EP}(a, N) + f_{ED}(a); \tag{8}$$

The detailed waveform is shown in **Figure 9B**.

Since the major target of this study is to establish a new theoretical framework for the mechanism of myelin development, we do not intend to involve an accurately quantitative comparison of the importance of each component.

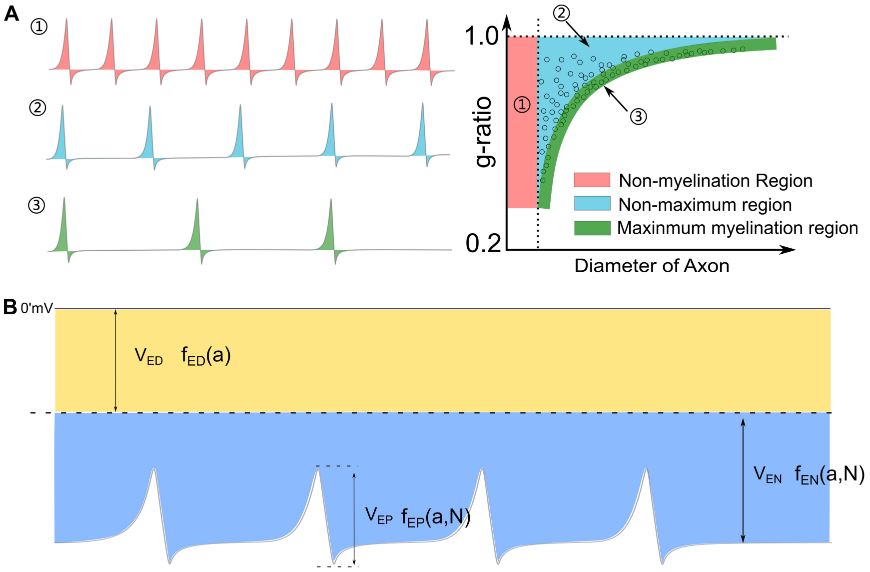

FIGURE 9

(A) The relationship between the frequency of action potential and the thickness of myelin: (1) An axon with a very high frequency of action potentials tends to be unmyelinated; (2) An axon with a medium frequency of action potentials cannot have maximum myelin thickness; (3) An axon with a very low frequency of action potentials tends to have maximum myelin thickness, forming the lower edge of the g-ratio data. **(B)** A complete perspective of Hypothesis-E: the total voltage consists of three major components: V_{ED},V_{EN}, and $\boldsymbol{V}_{\mathrm{EP}}$.

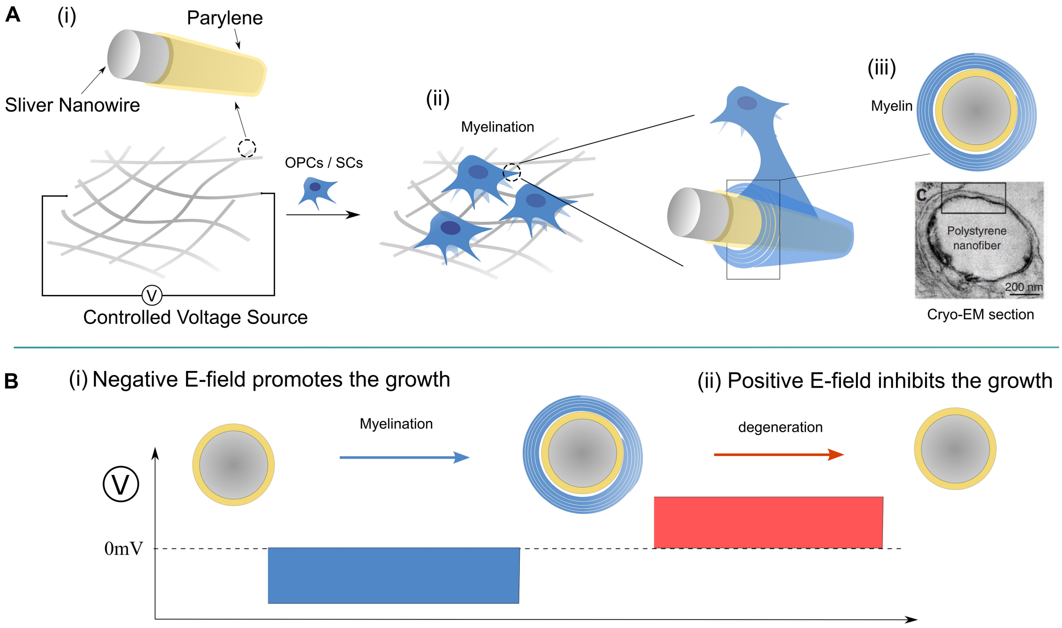

FIGURE 10

A designed experiment for validation of Hypothesis-E: **(A)** The experimental setup; **(B)** modulate the myelination process by controlling the E-field of the nano-wire.

However, a very rough and qualitative analysis can still help us have a better understanding. The amplitude of the dipole potential of the lipid membrane, whose measurement is not an easy task, is estimated within the range of 200∼1,000 mV (Brockman, 1994; Wang et al., 2006; Yang et al., 2008). It means $\boldsymbol{V}_{ED}$, which is just a small portion of the dipole potential, as shown in **Figure 4**, may possess an amplitude of tens of mV, which is a comparative value to $\boldsymbol{V}_R$ and $\boldsymbol{V}_A$. Meanwhile, $\boldsymbol{V}_{EN}$

and V_{EP} take a small ratio of V_R and V_A, respectively. Thus, V_{ED} may take the major portion of V_I. In this scenario, V_I has no substantial positive part. So a complete Hypothesis-E, which is a corrected version of Hypothesis-E_P in **Figure 6A**, is described below:

> *The growth of the myelin is promoted by the negative E-field when it exceeds a threshold, represented by the potential V_{N1-T}, and inhibited by the negative E-field when it is lowered than another threshold, represented by the potential V_{N2-T}, respectively.*

Meanwhile, the conclusion about the g-ratio explanation in **Figure 2** should also be corrected from two perspectives. Firstly, actual myelin growth is modulated by V_I, the sum of three components, rather than just one component assumed in **Figure 2**. Meanwhile, V_{EN} and V_{ED} have their own changing trends with the axonal diameter, and it is unclear how V_I changes with axonal diameter. Therefore, the actual lower limit curve may deviate from the calculated one in **Figure 3**. The second correction comes from the different observations of myelin thickness. Some studies reported that the axon caliber is weakly correlated with the myelin thickness (Paus and Toro, 2009; FitzGibbon and Nestorovski, 2013; Stikov et al., 2015; Andersson et al., 2020). The number of myelin lamellae is normally lower than 50. However, we also notice that in some studies, it is reported that the myelin can have a perpetual growth, which makes the number of myelin lamellae more than 100 (Berthold et al., 1983; Fields, 2014). Meanwhile, in this scenario, a larger axon tends to have thicker myelin. It seems the divergence in **Figure 3B** can happen in some conditions. As explained in **Figure 3C**, it is because the voltage on the inner tongue (V_{ED}+V_{EN}) is always higher than the threshold voltage. Considering that V_{ED} does not decay with the increasing number of myelin lamellae, it is highly possible that V_{ED} can solely provide the voltage to promote myelin growth. The myelin can grow perpetually with a constant growth rate, which agrees with the description in a previous study (Berthold et al., 1983), quoted here:

> *It is, moreover, concluded that myelin production on the average seems to be a perpetual process which, in the fully mature cat, operates at the same rate regardless of axon size.*

A possible experiment for the validation of this theory is proposed in **Figure 10**, in which the applied E-field controls the myelination of non-axon fibers. It has been validated that axonal cues are not necessary for the myelin wrapping of oligodendrocytes, though they are still necessary for myelin compaction (Armati and Mathey, 2013). It is highly possible that SCs follow the same principle. So we can design an experiment shown in **Figure 10** to validate the contribution of the E-field in myelin development. A mesh of silver micro/nano-wires, 0.2–10 μm in diameter, coated with 1 μm thick parylene as an insulating layer is used as a substitute for the axons with varying calibers. When it is partially immersed in the culture medium, the surface potential can be controlled by the applied voltage, as shown. The oligodendrocytes or SCs can both be cultured with nano-wire in the medium, and the myelination process can be observed by varying the applied voltage. Based on our theory, several phenomena can be predicted as follow:

1. The minimum diameter of the myelinated wire decreases with the increasing amplitude of the negative voltage.
2. When the positive voltage is applied, the myelination process will be inhibited for all wires.
3. If a negative voltage is applied to induce the myelination first, the post-applied positive voltage can induce demyelination (**Figure 10B**).
4. There will be a threshold voltage, ***VN1-T′***, to initiate the myelination process.
5. There will be another threshold voltage, ***VN2-T′***, to initiate the demyelination.

The paradox of neural-activity-dependent myelination

The paradox of this neural-activity-dependent (Foster et al., 2019) can be summarized as follow:

> *Some studies observed that the action potential is a positive regulator for myelin growth, while in others, the action potential is a negative regulator.*

This paradox can be easily solved by extending our theory, as shown in the **Figure 11**.

As shown in **Figure 11A**, the axon's cell membrane is charged by E-field from either resting potential or action potential. As well-known, in the resting state, the extracellular is more positive than intracellular for an axon. So for resting potential, the extracellular is positive. Meanwhile, the action potential will flip the potential, making the extracellular negative. So, generally speaking, the extracellular is positive for the resting potential and is negative for the action potential.

This extracellular potential, or E-field, can modulate the myelin growth before the myelin cell (let's say this is an oligodendrocyte) attach to the axon, as shown in **Figure 11B1**. Then according to our theory, the resting potential will inhibit the myelin attachment due to the positive E-field, while the action potential will promote the myelin attachment due to the negative E-field. So in this scenario, the action potential is a positive regulator for myelination.

However, the result will be the opposite once the myelin is attached to the axon, as shown in **Figure 11B2**. This is because

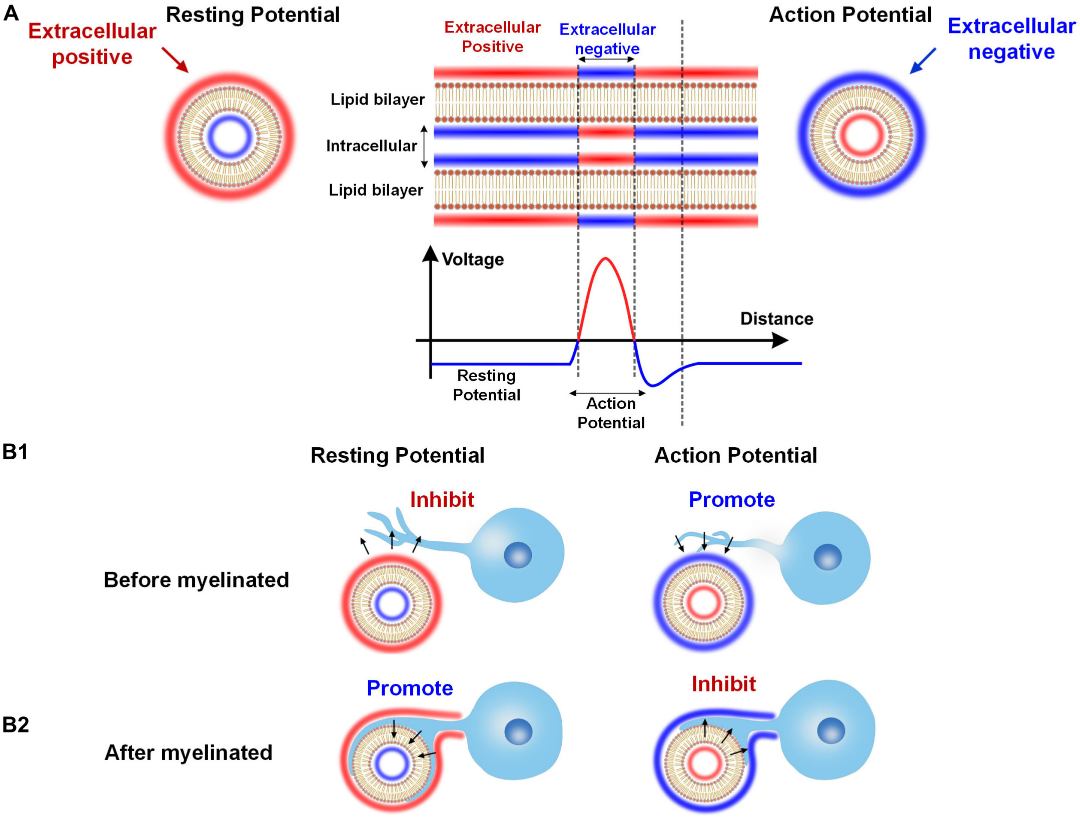

FIGURE 11

The dual effect of neural activity on myelination. **(A)** The extracellular E-field of neural activity on an axon: The resting potential induces a positive extracellular E-field, while the action potential induces a negative extracellular E-field. **(B1)** When the myelin cell has not attached to the axon, the positive extracellular E-field by the resting potential inhibits myelin growth, and the negative extracellular E-field by the action potential promotes myelin growth. **(B2)** When the myelin cell is attached to the axon, the resting and action potential effect will reserve.

once the myelin cell contacts the axon, the direction of the E-field will be opposite. The cell membrane of the myelin cell attached to the axon can experience the intracellular E-field. So for the resting potential, the intracellular negative E-field will promote the inner tongue growth. But for the action potential, the intracellular positive E-field will inhibit the inner tongue growth. So in this scenario, the action potential is a negative regulator for myelination.

According to the above explanation, we can conclude that:

(1) The action potential is a promoting factor for forming new myelin sheaths. So if we only investigate the number of myelin sheaths, the action potential is a positive regulator. This is the phenomenon observed by a majority group of neural-activity-dependent myelination (Fields, 2015). The rat was trained for several hours each day, and the motor cortex will have more myelin (Kleim et al., 2002; Sampaio-Baptista et al., 2013). In this study, both action and resting potential exert their functions on myelination. During the training, the action potential can initiate the new myelination wrapping. But the training only lasts several hours each day. It means that for the rest 20 h each day, the resting potential increases the thickness of the myelin sheaths. So in this study, both the increment of new myelin and sheath thickening can be observed. However, people did not recognize the function of resting potential to myelin growth. Therefore, the initiation of myelin wrapping and the further myelin thickening are all attributed to the role of action potentials.

(2) The action potential is an inhibiting factor for inner tongue growth after the myelin sheath is formed. So if we only investigate the thickness of a formed myelin sheath, the action potential is a negative regulator. Jonah Chan's group observed this phenomenon in the experiment on optic fibers (Mayoral et al., 2018). In Jonah Chan's study, the action potentials of the optic fibers are entirely removed. As a result, the myelin sheaths grow thicker, called hypermyelination. This experiment perfectly shows the promoting effect of resting potential on myelin growth. Meanwhile, it also indicates that the action potential is an inhibitory factor to myelin growth.

A revision of the g-ratio model

The fitting curves in **Figure 3E** are manually plotted to indicate the existence of the lower limit. They are not based on specific modeling parameters. An accurate data fitting is impossible according to the g-ratio model in section "Modeling the relationship between g-ratio and the E-field." The primary reason is that the model is not complete in section "Modeling the relationship between g-ratio and the E-field." As we mentioned in section "The influence of the total voltage," a more comprehensive model should also consider the voltage V_{ED} from dipole potential.

Now three voltage components need to be considered in the g-ratio calculation:

(1) V_{EN} is the voltage component from the resting potential. Since this component decays with the increasing lamellae layers, the growth of the inner tongue tends to terminate at a particular layer. So V_{EN} is the factor that determines the myelin sheath will have a maximum layer, meaning that the g-ratio shall have a lower limit.

(2) V_{ED} is the component from the dipole potential. This component does not decay with the increasing lamellae layers. Since it is also part of the total voltage to induce the myelin growth, this V_{ED} will change the actual shape of the lower limit of the g-ratio.

(3) V_T is the threshold voltage required for myelin growth. Section "Modeling the relationship between g-ratio and the E-field" considers this voltage as a ratio, η_{N-T}, to the resting potential, which is a constant. But now, we need to add the dipole potential, a function of axonal diameter. Therefore, this V_T cannot be simplified as a ratio but be considered as an actual voltage.

When all these three parameters, V_{EN}, V_{ED}, and V_T, are given, a g-ratio curve can be calculated. V_{EN} is a parameter that a given number of layers can calculate. V_{ED} is a parameter whose actual value is unknown. We only know its general changing trend shown in **Figure 4C**. V_T is also an unkown parameter. Therefore, we cannot generate all the possible g-ratio just by changing V_T.

But we still can give a proper V_{ED} and demonstrate a more corrected g-ratio modeling result. We rescale the curve in **Figure 4C** to the same amplitude of the resting potential, which is 70 mV, which means the maximum value of the dipole potential is 70 mV. So now, V_{ED} is a known parameter. Then we change V_T from 70.49 to 91.23 mV to generate the g-ratio curve. A comparison of the g-ratio modeling results before and after the correction is shown in **Figure 12**. Before the correction (**Figure 12A**), those g-ratio curves do not converge to the origin point. But after the correction, all g-ratio curves converge to the origin point (**Figure 12B**). According to a detailed observation of those g-ratio data in **Figure 3E**, the lower limit curves converge to the origin point, which agrees with our correction.

Then we try fitting some g-ratio data with our corrected g-ratio curve, as shown in **Figure 13**. Since we do not have the original data published in other studies (Begolly et al., 2016; Lee et al., 2017; Piscopo et al., 2018; Elazar et al., 2019), we can only overlap our modeling curves with the data figures to show how good the fitting is. The most fitting curves are plotted as thicker lines. The corresponding V_T is also shown in each figure. These four cases show that our modeling results can better fit the lower limit.

Here we need to emphasize several points.

(1) Our modeling results show that by adding V_{ED}, the calculated curves are closer to the experimental results. So this correction is quite necessary.

(2) A good fitting does not necessarily mean our modeling parameter is correct. Since there are infinite combinations of V_{ED} and V_T, we cannot know the actual value of these two parameters just by modeling. In other studies, there are also many experimental data that the parameters in **Figure 3B** cannot fit. The deviation mainly comes from the slope and curvature, which can be tuned by both V_{ED} and V_T.

(3) Our theory provides a framework to understand these phenomena rather than predicting the actual parameters. Therefore, pursuing the modeling accuracy at the current stage is meaningless and impossible.

Now we also can explain the unknown factor mentioned in section "The relation between the divergence region and unmyelinated axons" that can eliminate the divergence in **Figure 3B**. As shown in **Figure 12B**, we correct the modeling of the lower edge of g-ratio by considering the influence of the dipole potential. The major difference is that all curves are converged to zero point, which means the lower limit of g-ratio is zero only when the axonal diameter is also zero. The divergence in **Figure 3B** means that the curve of the g-ratio's lower edge goes to zero. Before the correction, which is shown in **Figure 12A**, the curves go to zero when the axonal diameter is a non-zero value. This is the reason for the divergence region. However, after the correction in **Figure 12B**, all curves reach zero only when the axonal diameter is a zero value. An axon with a diameter of zero is biologically impossible. Thus the divergence is eliminated.

A more complete understanding of radial sorting

It is known that the Nrg1 type III plays a critical role in myelination (Nave and Salzer, 2006). However, Nrg1 type III is not the sole factor for myelination. It is confirmed that the CHO

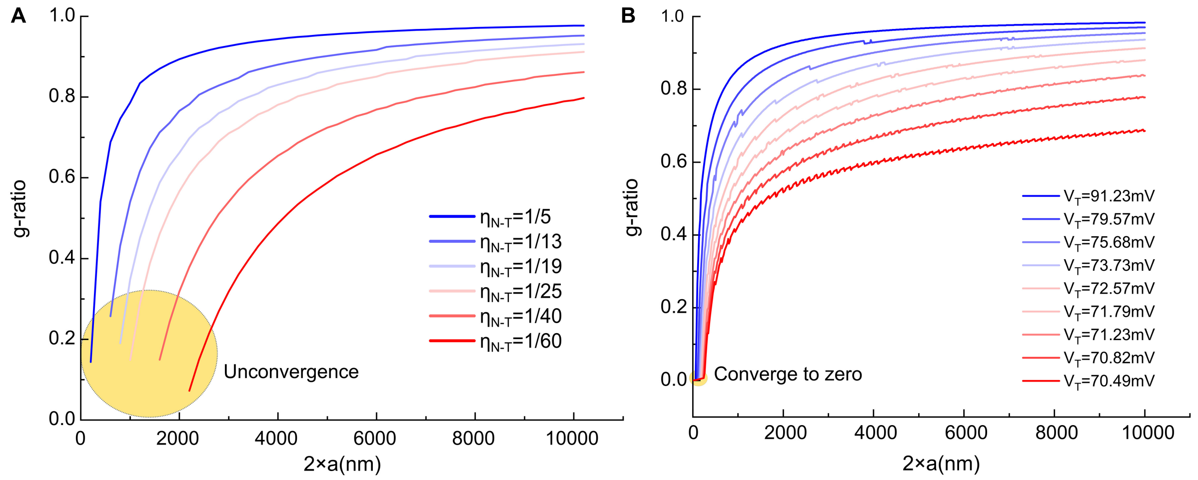

FIGURE 12
The comparison of the g-ratio curves before and after the correction. **(A)** The g-ratio curves before the correction, these curves are not converged to zero point; **(B)** the g-ratio curves after the correction, all curves are converged to zero point.

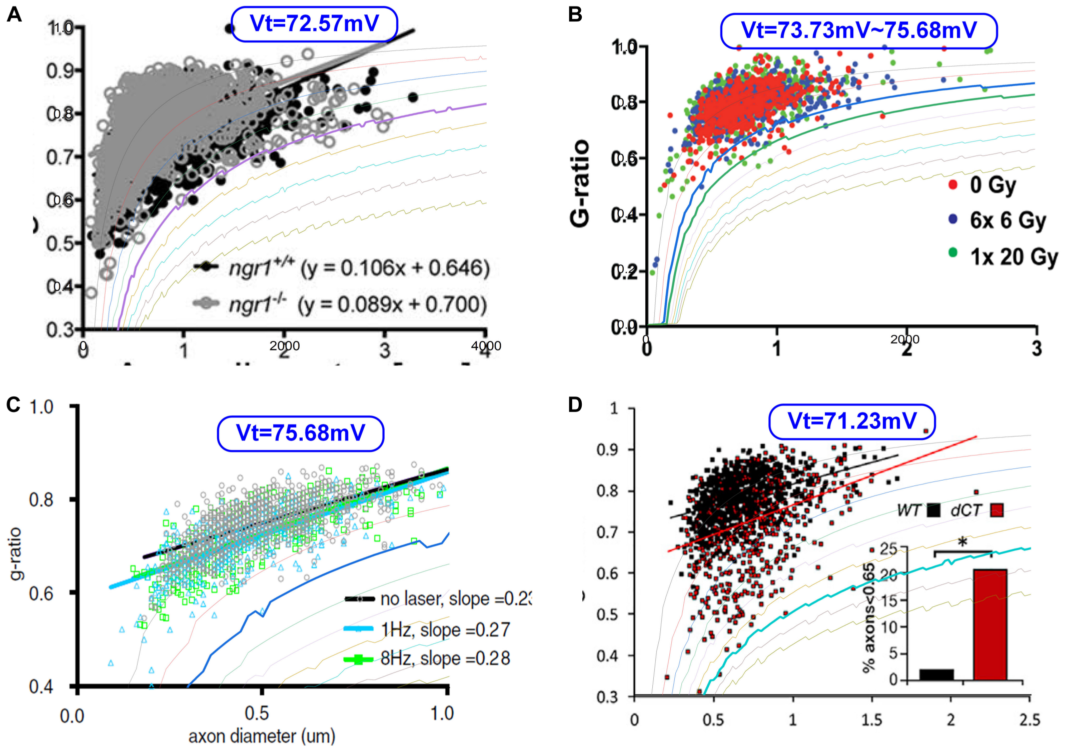

FIGURE 13
The fitting of the lower limits of g-ratio data. **(A)** Lee et al. (2017); **(B)** Begolly et al. (2016); **(C)** Piscopo et al. (2018); **(D)** Elazar et al. (2019).

cell with Nrg1 expression cannot be myelinated by SCs (Taveggia et al., 2005). So apart from the Nrg1, there is still a missing factor to control the fate of SCs. In our theory, this factor is E-field, the sum of voltages from resting, action, and dipole potentials. It is known that for oligodendrocytes, Nrg1 is not required. Thus our theory can perfectly be applied. However, Nrg1 is necessary for SCs. So it can be inferred that there is a protein that can sense the E-field to control the growth of SCs, on the SC surface. The E-field sensing function is activated when it is bonded with the Nrg1 on the axonal surface. This is the reason that CHO cells with Nrg1 expression, which has a much lower resting potential (∼-10 mv) and no action potential, cannot be myelinated. So generally, our theory still remains the same. But for SCs, the theory should be extended to include the effect of Nrg1.

Conclusion

Our simulation suggests that myelin development can be modulated by E-field. This E-field is induced by three origins: the resting potential, the action potential, and the dipole potential. Each has its unique changing patterns with the axonal caliber and the number of myelin lamellae. Our model can be used to explain a series of observed phenomena during myelin development, such as radial sorting and g-ratio. Furthermore, our model reveals that the myelination process can be controlled by physical factors, bridging neural electrical activities and neural development.

Data availability statement

The original contributions presented in this study are included in the article, further inquiries can be directed to the corresponding author/s.

Author contributions

HW proposed the theory. YL carried out the modeling process. TG helped refine the theory and improve the writing. WY, TZ, YZ, RZ, BS, FL, YH, and TW contributed to the reference collection, idea discussion, and early state of the theory establishment. SY helped plot figures and search for the references for manuscript revision. All authors contributed to the article and approved the submitted version.

Funding

This work was supported by the grant from the Guangdong Research Program (2019A1515110843 and 2019A1515110948), Shenzhen Research Program (JCYJ20170818152810899 and GJHZ20200731095206018), Chinese Academy of Sciences Research Program (2011DP173015 and 172644KYSB20190077), and National Natural Science Foundation of China grants (31900684 and 32000727).

Acknowledgments

A preprint has previously been published (Liu et al., 2021b).

Conflict of interest

The authors declare that the research was conducted in the absence of any commercial or financial relationships that could be construed as a potential conflict of interest.

Publisher's note

References

Andersson, M., Kjer, H. M., Rafael-Patino, J., Pacureanu, A., Pakkenberg, B., Thiran, J. P., et al. (2020). Axon morphology is modulated by the local environment and impacts the noninvasive investigation of its structure–function relationship. *Proc. Natl. Acad. Sci. U.S.A.* 117, 33649–33659. doi: 10.1073/pnas.2012533117

Armati, P. J., and Mathey, E. K. (2013). An update on Schwann cell biology—immunomodulation, neural regulation and other surprises. *J. Neurol. Sci.* 333, 68–72. doi: 10.1016/j.jns.2013.01.018

Barbizan, R., Castro, M. V., Ferreira, R. S., Barraviera, B., and Oliveira, A. L. (2014). Long-term spinal ventral root reimplantation, but not bone marrow mononuclear cell treatment, positively influences ultrastructural synapse recovery and motor axonal regrowth. *Int. J. Mol. Sci.* 15, 19535–19551. doi: 10.3390/ijms151119535

Begolly, S., Shrager, P. G., Olschowka, J. A., Williams, J. P., and O'Banion, M. K. (2016). Fractionation spares mice from radiation-induced. *Int. J. Radiat. Oncol. Biol. Phys.* 96, 449–457. doi: 10.1016/j.ijrobp.2016.05.005

Bercury, K. K., Dai, J., Sachs, H. H., Ahrendsen, J. T., Wood, T. L., and Macklin, W. B. (2014). Conditional ablation of raptor or rictor has differential impact on oligodendrocyte differentiation and CNS myelination. *J. Neurosci.* 34, 4466–4480. doi: 10.1523/JNEUROSCI.4314-13.2014

Berthold, C. H., Nilsson, I., and Rydmark, M. (1983). Axon diameter and myelin sheath thickness in nerve fibres of the ventral spinal root of the seventh lumbar nerve of the adult and developing cat. *J. Anat.* 136(Pt 3), 483–508.

Brockman, H. (1994). Dipole potential of lipid membranes. *Chem. Phys. Lipids* 73, 57–79. doi: 10.1016/0009-3084(94)90174-0

Bunge, R. P., Bunge, M. B., and Bates, M. (1989). Movements of the Schwann cell nucleus implicate progression of the inner (axon-related) Schwann cell process during myelination. *J. Cell Biol.* 109, 273–284. doi: 10.1083/jcb.109.1.273

Chomiak, T., and Hu, B. (2009). What is the optimal value of the g-ratio for myelinated fibers in the rat CNS? A theoretical approach. *PLoS One* 4:e7754. doi: 10.1371/journal.pone.0007754

Colognato, H., and Franklin, R. J. (2004). The mysteries of myelin unwrapped. *Science* 304, 688–689. doi: 10.1126/science.1097851

Dimas, P., Montani, L., Pereira, J. A., Moreno, D., Trötzmüller, M., Gerber, J., et al. (2019). CNS myelination and remyelination depend on fatty acid synthesis by oligodendrocytes. *Elife* 8:e44702. doi: 10.7554/eLife.44702.030

Dutta, D. J., Woo, D. H., Lee, P. R., Pajevic, S., Bukalo, O., Huffman, W. C., et al. (2018). Regulation of myelin structure and conduction velocity by perinodal astrocytes. *Proc. Natl. Acad. Sci. U.S.A.* 115, 11832–11837. doi: 10.1073/pnas.1811013115

Elazar, N., Vainshtein, A., Golan, N., Vijayaragavan, B., Schaeren-Wiemers, N., Eshed-Eisenbach, Y., et al. (2019). Axoglial adhesion by Cadm4 regulates CNS myelination. *Neuron* 101, 224–231. doi: 10.1016/j.neuron.2018.11.032

Fanarraga, M. L., Griffiths, I. R., Zhao, M., and Duncan, I. D. (1998). Oligodendrocytes are not inherently programmed to myelinate a specific size of axon. *J. Comp. Neurol.* 399, 94–100. doi: 10.1002/(SICI)1096-9861(19980914)399:1<94::AID-CNE7>3.0.CO;2-5

Feltri, M. L., Poitelon, Y., and Previtali, S. C. (2016). How Schwann cells sort axons: New concepts. *Neuroscientist* 22, 252–265. doi: 10.1177/1073858415572361

Ferreira, S., Pitman, K. A., Summers, B. S., Wang, S., Young, K. M., and Cullen, C. L. (2021). Oligodendrogenesis increases in hippocampal grey and white matter prior to locomotor or memory impairment in an adult mouse model of tauopathy. *Eur. J. Neurosci.* 54, 5762–5784. doi: 10.1111/ejn.14726

Fields, R. D. (2014). Myelin formation and remodeling. *Cell* 156, 15–17. doi: 10.1016/j.cell.2013.12.038

Fields, R. D. (2015). A new mechanism of nervous system plasticity: Activity-dependent myelination. *Nat. Rev. Neurosci.* 16, 756–767. doi: 10.1038/nrn4023

Fields, R. D., and Bukalo, O. (2020). Myelin makes memories. *Nat. Neurosci.* 23, 469–470. doi: 10.1038/s41593-020-0606-x

FitzGibbon, T., and Nestorovski, Z. (2013). Human intraretinal myelination: Axon diameters and axon/myelin thickness ratios. *Indian J. Ophthalmol.* 61:567. doi: 10.4103/0301-4738.121075

Foster, A. Y., Bujalka, H., and Emery, B. (2019). Axoglial interactions in myelin plasticity: Evaluating the relationship between neuronal activity and oligodendrocyte dynamics. *Glia* 67, 2038–2049. doi: 10.1002/glia.23629

Fraher, J. P. (1972). A quantitative study of anterior root fibres during early myelination. *J. Anat.* 112(Pt 1), 99–124.

Ghidinelli, M., Poitelon, Y., Shin, Y. K., Ameroso, D., Williamson, C., Ferri, C., et al. (2017). Laminin 211 inhibits protein kinase a in Schwann cells to modulate neuregulin 1 type III-driven myelination. *PLoS Biol.* 15:e2001408. doi: 10.1371/journal.pbio.2001408

Griffin, J. W., and Thompson, W. J. (2008). Biology and pathology of nonmyelinating Schwann cells. *Glia* 56, 1518–1531. doi: 10.1002/glia.20778

Harty, B. L., and Monk, K. R. (2017). Unwrapping the unappreciated: Recent progress in Remak Schwann cell biology. *Curr. Opin. Neurobiol.* 47, 131–137. doi: 10.1016/j.conb.2017.10.003

Harty, B. L., Coelho, F., Pease-Raissi, S. E., Mogha, A., Ackerman, S. D., Herbert, A. L., et al. (2019). Myelinating Schwann cells ensheath multiple axons in the absence of E3 ligase component Fbxw7. *Nat. Commun.* 10, 1–12. doi: 10.1038/s41467-019-10881-y

Hildebrand, C. (1971). Ultrastructural and light-microscopic studies of the nodal region in large myelinated fibres of the adult feline spinal cord white matter. *Acta Physiol. Scand.* 364, 43–79. doi: 10.1111/j.1365-201X.1971.tb10978.x

Hines, J. H., Ravanelli, A. M., Schwindt, R., Scott, E. K., and Appel, B. (2015). Neuronal activity biases axon selection for myelination in vivo. *Nat. Neurosci.* 18, 683–689. doi: 10.1038/nn.3992

Höke, A., Ho, T., Crawford, T. O., LeBel, C., Hilt, D., and Griffin, J. W. (2003). Glial cell line-derived neurotrophic factor alters axon schwann cell units and promotes myelination in unmyelinated nerve fibers. *J. Neurosci.* 23, 561–567. doi: 10.1523/JNEUROSCI.23-02-00561.2003

Ikeda, M., and Oka, Y. (2012). The relationship between nerve conduction velocity and fiber morphology during peripheral nerve regeneration. *Brain Behav.* 2, 382–390. doi: 10.1002/brb3.61

Kleim, J. A., Barbay, S., Cooper, N. R., Hogg, T. M., Reidel, C. N., Remple, M. S., et al. (2002). Motor learning-dependent synaptogenesis is localized to functionally reorganized motor cortex. *Neurobiol. Learn. Mem.* 77, 63–77. doi: 10.1006/nlme.2000.4004

Klok, M. D., Bugiani, M., de Vries, S. I., Gerritsen, W., Breur, M., van der Sluis, S., et al. (2018). Axonal abnormalities in vanishing white matter. *Ann. Clin. Transl. Neurol.* 5, 429–444. doi: 10.1002/acn3.540

Langner, M., Cafiso, D., Marcelja, S., and McLaughlin, S. (1990). Electrostatics of phosphoinositide bilayer membranes. Theoretical and experimental results. *Biophys. J.* 57, 335–349. doi: 10.1016/S0006-3495(90)82535-2

Lee, J. Y., Kim, M. J., Li, L., Velumian, A. A., Aui, P. M., Fehlings, M. G., et al. (2017). Nogo receptor 1 regulates Caspr distribution at axo-glial units in the central nervous system. *Sci. Rep.* 7:8958. doi: 10.1038/s41598-017-09405-9

Lemke, G. (1988). Unwrapping the genes of myelin. *Neuron* 1, 535–543. doi: 10.1016/0896-6273(88)90103-1

Leventis, P. A., and Grinstein, S. (2010). The distribution and function of phosphatidylserine in cellular membranes. *Ann. Rev. Biophys.* 39, 407–427. doi: 10.1146/annurev.biophys.093008.131234

Liu, Y., Zhang, Y., Yue, W., Zhu, R., Guo, T., Liu, F., et al. (2021a). A physical answer to Peters quadrant mystery: A modeling study. *arXiv* [Preprint]. arXiv:2111.11690

Liu, Y., Zhang, Y., Yue, W., Zhu, R., Guo, T., Liu, F., et al. (2021b). A Physical perspective to understand the mechanism of myelin development. *arXiv* [Preprint]. arXiv:2111.13689

Marro, B. S., Skinner, D. D., Cheng, Y., Grist, J. J., Dickey, L. L., Eckman, E., et al. (2019). Disrupted CXCR2 signaling in oligodendroglia lineage cells enhances myelin repair in a viral model of multiple sclerosis. *J. Virol.* 93, e240–e219. doi: 10.1128/JVI.00240-19

Mayoral, S. R., Etxeberria, A., Shen, Y. A. A., and Chan, J. R. (2018). Initiation of CNS myelination in the optic nerve is dependent on axon caliber. *Cell Rep.* 25, 544–550. doi: 10.1016/j.celrep.2018.09.052

McLaughlin, S. (1989). The electrostatic properties of membranes. *Ann. Rev. Biophys. Biophys. Chem.* 18, 113–136. doi: 10.1146/annurev.bb.18.060189.000553

McLaughlin, S., and Murray, D. (2005). Plasma membrane phosphoinositide organization by protein electrostatics. *Nature* 438, 605–611. doi: 10.1038/nature04398

Michailov, G. V., Sereda, M. W., Brinkmann, B. G., Fischer, T. M., Haug, B., Birchmeier, C., et al. (2004). Axonal neuregulin-1 regulates myelin sheath thickness. *Science* 304, 700–703. doi: 10.1126/science.1095862

Monje, M. (2018). Myelin plasticity and nervous system function. *Ann. Rev. Neurosci.* 41, 61–76. doi: 10.1146/annurev-neuro-080317-061853

Monk, K. R., Feltri, M. L., and Taveggia, C. (2015). New insights on Schwann cell development. *Glia* 63, 1376–1393. doi: 10.1002/glia.22852

Nave, K. A., and Salzer, J. L. (2006). Axonal regulation of myelination by neuregulin 1. *Curr. Opin. Neurobiol.* 16, 492–500. doi: 10.1016/j.conb.2006.08.008

Nave, K. A., and Werner, H. B. (2014). Myelination of the nervous system: Mechanisms and functions. *Ann. Rev. Cell Dev. Biol.* 30, 503–533. doi: 10.1146/annurev-cellbio-100913-013101

Ommer, A., Figlia, G., Pereira, J. A., Datwyler, A. L., Gerber, J., DeGeer, J., et al. (2019). Ral GTPases in Schwann cells promote radial axonal sorting in the peripheral nervous system. *J. Cell Biol.* 218, 2350–2369. doi: 10.1083/jcb.201811150

Orita, S., Henry, K., Mantuano, E., Yamauchi, K., De Corato, A., Ishikawa, T., et al. (2013). Schwann cell LRP1 regulates remak bundle ultrastructure and axonal interactions to prevent neuropathic pain. *J. Neurosci.* 33, 5590–5602. doi: 10.1523/JNEUROSCI.3342-12.2013

Paus, T., and Toro, R. (2009). Could sex differences in white matter be explained by g ratio? *Front. Neuroanat.* 3:14. doi: 10.3389/neuro.05.014.2009

Peters, A. (1961). A radial component of central myelin sheaths. *J. Cell Biol.* 11, 733–735. doi: 10.1083/jcb.11.3.733

Peters, A. (1964). Further observations on the structure of myelin sheaths in the central nervous system. *J. Cell Biol.* 20, 281–296. doi: 10.1083/jcb.20.2.281

Petrov, A. G. (2002). Flexoelectricity of model and living membranes. *Biochim. Biophys. Acta* 1561, 1–25. doi: 10.1016/S0304-4157(01)00007-7

Piscopo, D. M., Weible, A. P., Rothbart, M. K., Posner, M. I., and Niell, C. M. (2018). Changes in white matter in mice resulting from low-frequency brain stimulation. *Proc. Natl. Acad. Sci. U.S.A.* 115, E6339–E6346. doi: 10.1073/pnas.1802160115

Richards, W., Kalil, R., and Moore, C. L. (1983). An observation about myelination. *Exp. Brain Res.* 52, 219–225. doi: 10.1007/BF00236630

Ronchi, G., Jager, S. B., Vaegter, C. B., Raimondo, S., Giacobini-Robecchi, M. G., and Geuna, S. (2014). Discrepancies in quantitative assessment of normal and regenerated peripheral nerve fibers between light and electron microscopy. *J. Peripher. Nerv. Syst.* 19, 224–233. doi: 10.1111/jns.12090

Sampaio-Baptista, C., Khrapitchev, A. A., Foxley, S., Schlagheck, T., Scholz, J., Jbabdi, S., et al. (2013). Motor skill learning induces changes in white matter microstructure and myelination. *J. Neurosci.* 33, 19499–19503. doi: 10.1523/JNEUROSCI.3048-13.2013

Sanders, F. K., and Whitteridge, D. (1946). Conduction velocity and myelin thickness in regenerating nerve fibres. *J. Physiol.* 105, 152–174. doi: 10.1113/jphysiol.1946.sp004160

Schmalbruch, H. (1986). Fiber composition of the rat sciatic nerve. *Anat. Rec.* 215, 71–81. doi: 10.1002/ar.1092150111

Stadelmann, C., Timmler, S., Barrantes-Freer, A., and Simons, M. (2019). Myelin in the central nervous system: Structure, function, and pathology. *Physiol. Rev.* 99, 1381–1431. doi: 10.1152/physrev.00031.2018

Stikov, N., Campbell, J. S., Stroh, T., Lavelée, M., Frey, S., Novek, J., et al. (2015). Quantitative analysis of the myelin g-ratio from electron microscopy images of the macaque corpus callosum. *Data Brief* 4, 368–373. doi: 10.1016/j.dib.2015.05.019

Taveggia, C., Zanazzi, G., Petrylak, A., Yano, H., Rosenbluth, J., Einheber, S., et al. (2005). Neuregulin-1 type III determines the ensheathment fate of axons. *Neuron* 47, 681–694. doi: 10.1016/j.neuron.2005.08.017

Uzman, B. G., and Nogueira-Graf, G. (1957). Electron microscope studies of the formation of nodes of Ranvier in mouse sciatic nerves. *J. Cell Biol.* 3, 589–598. doi: 10.1083/jcb.3.4.589

Wang, H., Wang, J., Cai, G., Liu, Y., Qu, Y., and Wu, T. (2021). A physical perspective to the inductive function of myelin—a missing piece of neuroscience. *Front. Neural Circuits* 14:562005. doi: 10.3389/fncir.2020.562005

Wang, L., Bose, P. S., and Sigworth, F. J. (2006). Using cryo-EM to measure the dipole potential of a lipid membrane. *Proc. Natl. Acad. Sci. U.S.A.* 103, 18528–18533. doi: 10.1073/pnas.0608714103

Webster, H. D. (1971). The geometry of peripheral myelin sheaths during their formation and growth in rat sciatic nerves. *J. Cell Biol.* 48, 348–367. doi: 10.1083/jcb.48.2.348

Webster, H. D., Martin, J. R., and O'Connell, M. F. (1973). The relationships between interphase Schwann cells and axons before myelination: A quantitative electron microscopic study. *Dev. Biol.* 32, 401–416. doi: 10.1016/0012-1606(73)90250-9

Xie, F., Liang, P., Fu, H., Zhang, J. C., and Chen, J. (2014). Effects of normal aging on myelin sheath ultrastructures in the somatic sensorimotor system of rats. *Mol. Med. Rep.* 10, 459–466. doi: 10.3892/mmr.2014.2228

Yang, Y., Mayer, K. M., Wickremasinghe, N. S., and Hafner, J. H. (2008). Probing the lipid membrane dipole potential by atomic force microscopy. *Biophys. J.* 95, 5193–5199. doi: 10.1529/biophysj.108.136507

Zhan, H., and Lazaridis, T. (2012). Influence of the membrane dipole potential on peptide binding to lipid bilayers. *Biophys. Chem.* 161, 1–7. doi: 10.1016/j.bpc.2011.10.002

Zhao, J. X., Ohnishi, A., Itakura, C., Mizutani, M., Yamamoto, T., Hojo, T., et al. (1995). Smaller axon and unaltered numbers of microtubules per axon in relation to number of myelin lamellae of myelinated fibers in the mutant quail deficient in neurofilaments. *Acta Neuropathol.* 89, 305–312. doi: 10.1007/BF00309623

Zheng, H., Chang, L., Patel, N., Yang, J., Lowe, L., Burns, D. K., et al. (2008). Induction of abnormal proliferation by nonmyelinating schwann cells triggers neurofibroma formation. *Cancer Cell* 13, 117–128. doi: 10.1016/j.ccr.2008.01.002

Zuckerkandl, E., and Pauling, L. (1965). "Evolutionary divergence and convergence in proteins", in *Evolving genes and proteins*, eds B. Vernon, and J. V. Henry (Cambridge: Academic Press), 97–166. doi: 10.1016/B978-1-4832-2734-4.50017-6

frontiers | Frontiers in Neuroscience

TYPE Original Research
PUBLISHED 20 October 2022
DOI 10.3389/fnins.2022.1029683

OPEN ACCESS

EDITED BY
Liming Li,
Shanghai Jiao Tong University, China

REVIEWED BY
Yao-Chuan Chang,
Feinstein Institute for Medical Research, United States
Shuang Liu,
Tianjin University, China

*CORRESPONDENCE
J. Douglas Steele
dsteele@dundee.ac.uk

SPECIALTY SECTION
This article was submitted to Neural Technology, a section of the journal Frontiers in Neuroscience

RECEIVED 27 August 2022
ACCEPTED 03 October 2022
PUBLISHED 20 October 2022

CITATION
Steele JD, Farnan T, Semple DM and Bai S (2022) Fronto-medial electrode placement for electroconvulsive treatment of depression.
Front. Neurosci. 16:1029683.
doi: 10.3389/fnins.2022.1029683

Fronto-medial electrode placement for electroconvulsive treatment of depression

J. Douglas Steele[1]*, Tom Farnan[1], David M. Semple[2] and Siwei Bai[3]

[1]School of Medicine, University of Dundee, Dundee, United Kingdom, [2]University Hospital Hairmyres, NHS Lanarkshire, Glasgow, United Kingdom, [3]Department of Electrical and Computer Engineering, Technical University of Munich, Munich, Germany

Electroconvulsive therapy (ECT) is the most effective treatment for severe treatment-resistant depression but concern about cognitive side-effects, particularly memory loss, limits its use. Recent observational studies on large groups of patients who have received ECT report that cognitive side-effects were associated with electric field (EF) induced increases in hippocampal volume, whereas therapeutic efficacy was associated with EF induced increases in sagittal brain structures. The aim in the present study was to determine whether a novel fronto-medial (FM) ECT electrode placement would minimize electric fields in bilateral hippocampi (HIP) whilst maximizing electric fields in dorsal sagittal cortical regions. An anatomically detailed computational head model was used with finite element analysis, to calculate ECT-induced electric fields in specific brain regions identified by translational neuroimaging studies of treatment-resistant depressive illness, for a range of electrode placements. As hypothesized, compared to traditional bitemporal (BT) electrode placement, a specific FM electrode placement reduced bilateral hippocampal electric fields two-to-three-fold, whilst the electric fields in the dorsal anterior cingulate (dAC) were increased by approximately the same amount. We highlight the clinical relevance of this specific FM electrode placement for ECT, which may significantly reduce cognitive and non-cognitive side-effects and suggest a clinical trial is indicated.

KEYWORDS
ECT, side-effects, electric fields, depression, computational modeling

Introduction

Psychiatric illnesses are the leading cause of long term disability world-wide with depression the commonest cause (Whiteford et al., 2013; WHO, 2018). Better treatments, with improved efficacy and reduced side-effects, are needed. Electroconvulsive therapy (ECT) is the most effective treatment for severe treatment-resistant depression, typically used when patients have not responded to multiple treatments or need a rapid response with faster action than other treatments (Pagnin et al., 2004; Wade et al., 2020).

A recent report from the Scottish ECT Accreditation Network (SEAN) national audit (SEAN, 2021), covering a decade of treatments from 2009 to 2018, with ∼4000 treatments per year, found the majority of patients receiving ECT were in the 50–79 years old age range, the most common diagnosis was depression with or without psychotic symptoms, ∼15% of treatment episodes were recorded as emergency lifesaving treatments, and 75% of patients were "much improved" or "very much improved" after a course of ECT. The commonest reported side-effects in the SEAN reports were memory problems, headache and muscle aches and brief disorientation.

Side-effects on memory are among the most important factors limiting acceptance, prescription and use of ECT and may contribute to premature discontinuation of treatment, or a lack of use of ECT when it could be effective (Finnegan and McLoughlin, 2019). Whilst there is little evidence for anterograde memory impairment persisting for longer than a few weeks after the last treatment, the duration of retrograde amnesia is more controversial. In practice, minimization of cognitive side-effects is by identification of patients at higher risk and modifying treatment delivery: e.g., stimulus dose, frequency of treatments, pulse-width, and electrode placement. Bitemporal (BT) placement of electrodes has the greatest therapeutic efficacy but most cognitive side-effects; high dose right unilateral (RUL) electrode placement has fewer side-effects (Finnegan and McLoughlin, 2019) but is generally regarded as less effective.

In health, the hippocampus is crucial for human episodic memory encoding (Squire, 1986; Lisman et al., 2017) with the anterior region also implicated in emotional experience (Gray and McNaughton, 2000; Phelps, 2004). Adverse memory side-effects of ECT are thought to be predominately related to stimulation of the hippocampus, although other regions including the inferior and middle frontal gyri are important for memory retrieval, with all regions stimulated to a variable extent by a wide-variety of ECT electrode placements (Bai et al., 2019). However, for patients who have not received ECT, depressive illness is itself associated with cognitive, including memory impairment (Anderson et al., 2021), and there is robust evidence for hippocampal volume reduction in unipolar and bipolar illnesses (Hibar et al., 2016; Schmaal et al., 2016).

Recently, a series of publications from the Global ECT-MRI Research Collaboration (GEMRIC) have reported important findings. First, a longitudinal neuroimaging study of brain structure in a large number of patients reported that the number of ECT sessions and electrode placement impacts the extent and laterality of ECT-induced hippocampal enlargement, but there was no relationship between hippocampal volume enlargement and clinical outcome (Oltedal et al., 2018). A second study calculated the electric field (EF) induced by ECT in different brain regions, reporting a strong relationship between EF intensity and brain volume increase, but that neither structural volume increase nor EF intensity were associated with antidepressant response (Argyelan et al., 2019) although a relationship has also been reported (Deng et al., 2021). These were univariate studies and an alternative multivariate approach can be helpful (Steele and Paulus, 2019). A third GEMRIC study tested for associations between 80 different brain regions and clinical outcome using a multivariate approach, reporting that structural brain increases in cortical mid-line structures, such as the dorsal anterior cingulate (dAC) and precuneus posterior cingulate (PPC), predicted individual patient response but not medial temporal regions, such as the amygdala and hippocampus, which have been the focus of ECT research thus far (Mulders et al., 2020). Its long been established that induction of a generalized seizure is required for efficacy, and these recent studies suggest that an ECT electrode configuration specifically designed to maximize the induced EF in dorsal sagittal structures, simultaneously minimizing the induced EF in bilateral HIP, could be optimally therapeutic and minimize cognitive side-effects.

Electric field is typically maximal in brain regions immediately deep to the ECT electrodes. This means an electrode placement rotated through 90 degrees from the ubiquitous (in the UK) BT orientation, with the anterior electrode near the dAC and posterior electrode near the PPC in a fronto-medial (FM) configuration (Lee et al., 2016), should maximize the induced EF in these structures, also maximizing the distance from the electrodes to bilateral HIP. However, the precise EF in specific brain sub-regions identified as important in clinical neuroimaging studies of treatment-resistant depression is unclear. Also, different FM electrode placements are possible. Therefore, we used a computational model (Bai et al., 2019) to test the hypothesis that an optimal FM placement would maximize the EF in specific sagittal brain regions whilst minimizing the EF in subregions of bilateral HIP, identified by neuroimaging studies of patients with treatment-resistant depression who had not received ECT.

Materials and methods

Head computational model and analyses

A finite element head model was constructed from a 3T MRI T1-weighted 1 mm isotropic resolution brain scan provided by the NIH Human Connectome Project (MGH1010, gender: female, age: 25–29) (Fan et al., 2016). Briefly, head tissue compartments were analyzed using Brainsuite[1] to segment skin and subcutaneous tissue (fat and muscle), skull, cerebrospinal fluid, gray matter, and white matter. Segmented

---

[1] http://brainsuite.org/

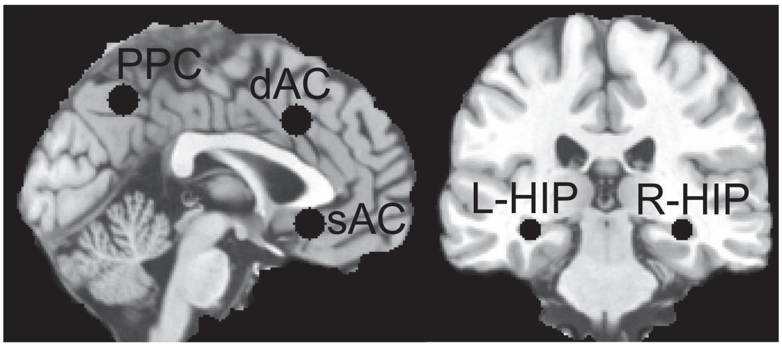

FIGURE 1
Regions of Interest (ROI) used for sampling the electric field (EF) distributions; left hippocampus (L-HIP), right hippocampus (R-HIP) and for other abbreviations see main text.

tissue compartments were then imported into 3D Slicer[2] for manual correction of voxels as required (Bai et al., 2019; Bakir et al., 2019). The tissue compartments were assumed to be homogeneous with conductivities assigned from the mean values from multiple studies (Bai et al., 2019). Modeling was done using COMSOL Multiphysics (v5.0) finite element analysis software (COMSOL AB, Stockholm, Sweden) with a direct linear solver. Mean and standard deviation of the EFs were calculated from 100 points selected randomly within anatomically defined regions of interest (ROI).

Regions of interest for electric field and current density calculations

We calculated EFs in specific sagittal brain regions and bilateral HIP for different electrode configurations. *A priori* defined spherical ROI were defined using Montreal Neurological Institute (MNI) standard brain anatomy selected from the translational neuroimaging studies discussed later: dAC (0,19,37) 15 mm (Steele et al., 2008; Tolomeo et al., 2016), subgenual AC (sAC) (0,25,−9) 15 mm (Drevets et al., 1997), precuneus posterior cingulate (PPC) (0,−58,46) 15 mm (Johnston et al., 2015) hippocampi (HIP) (−32,−28,−10) 10 mm, (34,−26,−10) 10 mm (Johnston et al., 2015), where the coordinate is the location of the center of the sphere and diameter is in mm. These ROIs are shown in **Figure 1**. The head model segmentation, manual editing, and configuration of COMSOL for electrode placements and solving was done using the scan in its original non-MNI patient anatomical space. To determine MNI equivalent locations, the T1 scan was spatially normalized using SPM12[3], then the resultant deformation field used to calculate the inverse transformation (Ashburner, 2016), from MNI back to original patient scan anatomical space.

Electroconvulsive therapy electrode placements

A total of 7 bipolar ECT electrode placements, including 4 alternative FM placements, were investigated: (i) BT–center of each electrode was 3 cm superior to the midpoint of a line from the lateral canthus of the eye to the external ear canal, (ii) bifrontal (BF)–center of each electrode was 5 cm superior to the lateral canthus of the eyes, (iii) RUL–anterior electrode 5 cm superior to the lateral canthus of the right eye with posterior electrode just right of the vertex, (iv) mid-frontal-occipital (MFO)–anterior electrode just above nasion and the posterior electrode over the occiput (15), (v) mid-frontal-vertex (MFV1)–anterior electrode just above nasion (as MFO) but with posterior electrode at the vertex, (vi) MFV2–anterior electrode higher at 2.5 cm above nasion and the posterior electrode at the vertex, and (vii) MFV3–anterior electrode highest at 5 cm above the nasion and the posterior electrode at the vertex. MFV3 is the most dorsal of the 4 sagittal FM electrode configurations. These electrode placements are shown in **Figure 2** and modeling for each assumed an ECT current of 800 mA delivered to the scalp from a pair of circular electrodes with 5 cm diameter (Bai et al., 2019).

Results

Figure 2 shows sagittal and coronal views of the EF magnitudes for the 7 electrode configurations with the coronal views chosen to intersect the hippocampi ROIs. As expected, the EFs were highest in brain regions under the electrodes. Mean and standard deviation EFs for selected ROI are shown in **Table 1**.

---

[2] www.slicer.org

[3] https://www.fil.ion.ucl.ac.uk/spm/software/spm12/

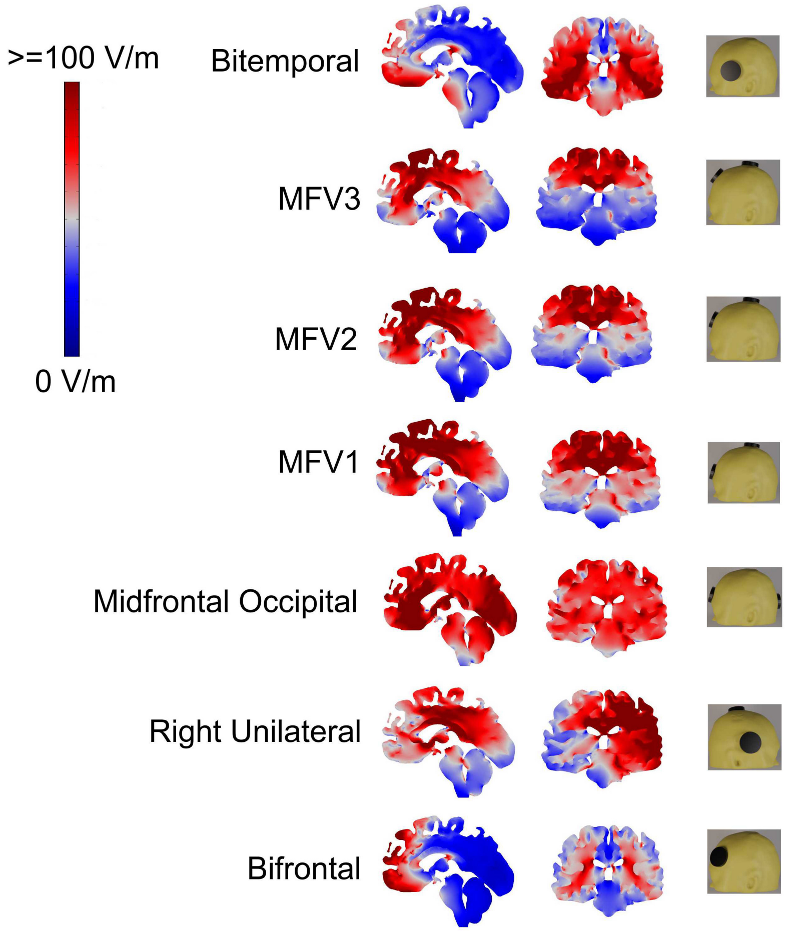

FIGURE 2
Electric field (EF) distributions and electroconvulsive therapy (ECT) electrode placements; for the latter anterior is to the left except for the right unilateral (RUL) placement, see main text for abbreviations. High EF (red) and low EF (blue) with color bar showing EF in V/m.

TABLE 1 Electroconvulsive therapy (ECT)-induced electric fields in V/m (standard deviation) for different electrode placements sampled within specific regions of interest (ROI).

	Left hippocampus	Right hippocampus	dAC	sAC	PPC	dAC/Left hippocampus	dAC/Right hippocampus
BT	99 (16)	84 (19)	33 (12)	53 (7)	26 (2)	0.3	0.4
RUL	59 (8)	82 (10)	75 (19)	72 (18)	76 (8)	1.3	0.9
BF	62 (12)	55 (14)	43 (13)	51 (7)	19 (2)	0.7	0.8
MFO	69 (7)	75 (6)	87 (6)	118 (13)	88 (5)	1.2	1.2
MFV1	56 (6)	59 (7)	113 (17)	101 (14)	80 (8)	2.0	1.9
MFV2	47 (5)	50 (6)	114 (16)	91 (14)	72 (6)	2.4	2.3
MFV3	38 (4)	41 (4)	97 (11)	71 (11)	62 (6)	2.6	2.4

Electrode placements commonly used in clinical practice

The BT placement resulted in the highest bilateral hippocampal ROI EFs, with high EFs throughout both temporal lobes and particularly high EFs in bilateral temporal lobe white matter. The right hippocampal ROI EF for RUL placement was comparable to that obtained for the BT placement. With a longer distance between the electrodes and hippocampi, BF resulted in lower hippocampal ROI EFs than BT, and significant EFs only in the most anterior medial frontal brain regions. BT resulted in the lowest EF in the dAC ROI, compared to RUL and BF configurations. In contrast, RUL resulted in a high dAC ROI EF because with RUL, the posterior electrode is close to the vertex.

Table 1 also shows the ratio of EFs for dorsal AC ROI to each hippocampal ROI: BT had the lowest and RUL the highest ratios.

Alternative novel sagittal electrode placements

Mid-frontal-occipital had the electrodes placed lowest in the sagittal plane and resulted in the highest bilateral hippocampal EFs for all sagittal placements with significant EFs throughout most of the brain. Moving the posterior electrode from the occipital region to the vertex (MFV1) resulted in a reduction in hippocampal ROI EFs and the EFs throughout both temporal lobes. Then, moving the anterior electrode more superior (MFV2) resulted in a further reduction in hippocampal ROI EFs due to increased distance from the electrodes to both HIP. Hippocampal EFs were minimized by moving the anterior electrode still more superior (MFV3) but this resulted in only a small reduction in the dAC ROI EF, compared with the MFV2 placement. The highest dAC ROI to hippocampal EF ROI ratios were obtained using the most superior MFV3 placement but the increase was marginal in comparison to the MFV2 placement.

It is important that the minimum distance between the two electrodes is not extremely low, to avoid superficial shunting of current between the electrodes due to the electrically resistant skull. BF electrode placement is a long-established method for delivering ECT. Traditional BF electrode placement is 5 cm superior to the outer canthus of the eye, making the distance between the centers of the electrodes about 18 cm or less depending on head size. Deducting 2–3 cm from each of the electrodes due to their size makes the closest edge to edge electrode distance 12–14 cm for BF.

With regard to MFV2 placement and assuming standard EEG positions, then nasion to inion is measured for each patient and percentages are used. By definition Fp1 is 10% from nasion to inion, and the vertex is 50% from nasion to inion. With most patients the nasion to Fp1 distance is about 5 cm, so as Fp1 to vertex is 40% of the distance, the Fp1 to vertex distance is about 20 cm. If we assume the center of the anterior MFV2 electrode is *at Fp1 or no higher than 1 cm above this*, with the posterior electrode at the *vertex*, then allowing for 5 cm diameter electrodes, this makes the minimum MFV2 electrode edge distance 14–15 cm, which compares favorably with BF placement.

Therefore, from the perspective of maximizing the dAC/hippocampus ratios and ensuring an inter-electrode edge distance no less than BF, the optimal FM electrode placement is MFV2.

Discussion

Electroconvulsive therapy is the most effective treatment for severe and treatment-resistant depression but use is limited because of concern about side-effects (Finnegan and McLoughlin, 2019). ECT causes increases in the volume of brain structures (Argyelan et al., 2019) and ECT-induced increases in the volume of the dentate gyri of the HIP are associated with increased memory impairment (Gbyl et al., 2021). Volume increases in the HIP are not associated with clinical response (Oltedal et al., 2018; Mulders et al., 2020), but increases in the volume of sagittal cortical regions, such as the dorsal anterior and posterior cingulate are associated with clinical response (Mulders et al., 2020). We therefore tested the hypothesis that one of the FM electrode configurations, but not alternative electrode placements such as BT, would minimize the induced EF in the bilateral HIP and maximize the EFs in the dAC and PPC. Detailed computational modeling confirmed this hypothesis.

A large systematic review and meta-analysis of studies of healthy subjects concluded that a sub-region of the dorsal medial cortex, the dAC, integrates subjective experience of negative affect and pain and is important for cognitive control (Shackman et al., 2011). Clinically, anterior cingulotomy, which comprises small bilateral lesions in the dAC, has long been used as a treatment of last resort for severe treatment-resistant depressive illness, when all other treatments including ECT have been tried and failed, the patient wants the operation and can provide sustained informed consent (Steele et al., 2008). In an observational study of patients who had received cingulotomy, we reported the dAC has a causal role in negative affect so lesions in this region could be therapeutic for patients with otherwise intractable mood, anxiety and pain syndromes (Tolomeo et al., 2016). These findings for cingulotomy may be consistent with a study on different patients who had received ECT and not surgery, where we reported ECT decreases the connectivity between the dAC and other brain regions (Perrin et al., 2012). An unexpected result was that smaller dAC lesions were associated with better clinical response (Steele et al., 2008), suggesting the therapeutic effect may be due to smaller lesions inducing connectivity and plasticity change. Consistent with this, ECT increases plasticity (Dukart et al., 2014) and changes in the dAC predicted clinical response (Mulders et al., 2020).

Depressive illness has been associated with abnormal function of other cingulate regions. We and others reported that the sAC and rostral AC have a blunted reward response using fMRI (Johnston et al., 2015; Rupprechter et al., 2020) with reduced connectivity from the sAC-rostral AC to the basal ganglia (Rupprechter et al., 2020). Others have reported sAC functional abnormalities using PET (Drevets et al., 1997; Mayberg et al., 1999) with a small deep brain stimulation trial reporting beneficial effect (Mayberg et al., 2005) but a larger blinded study did not report efficacy (Holtzheimer et al., 2017). Using fMRI, we also reported blunting of the reward response of the PPC of patients with treatment resistant depression (Johnston et al., 2015), and abnormally increased connectivity between the PPC and the lateral orbitofrontal cortex has been reported (Cheng et al., 2018). Notably, the MF electrode configuration also increases ECT-induced EFs in the sAC and PPC regions compared to alternative configurations such as BT, implying it could induce gray matter increase and plasticity also in these regions.

There is robust evidence from two large ENIGMA consortium studies for hippocampal volume reductions in unipolar (Schmaal et al., 2016) and bipolar (Hibar et al., 2016) illnesses. An influential review of preclinical studies predicted that depression is associated with hippocampal abnormalities linked to ruminations (Deakin and Graeff, 1991; Deakin, 2013) and our fMRI study on patients with treatment-resistant depression reported consistent hippocampal abnormalities (Johnston et al., 2015). Cognitive abnormalities in patients with depression who have not received ECT may be linked to abnormal hippocampal function (Johnston et al., 2015). However, whilst ECT is associated with hippocampal volume increases, reversing depression-associated hippocampal decreases, there is clinical evidence that this change does not represent a causal therapeutic effect (Oltedal et al., 2018; Argyelan et al., 2019) although a relationship has also been reported (Deng et al., 2021). Antidepressants also cause neurogenesis and hippocampal volume increase (Malberg et al., 2021) but without adverse effects on memory (BNF, 2016) and some effective treatments (Steele et al., 2008) have no direct effect on the hippocampus. In contrast to uncertainty about ECT therapeutic mechanisms, evidence for ECT-induced memory problems is relatively robust, particularly for BT (Finnegan and McLoughlin, 2019) which we show is associated with the highest bilateral hippocampal ECT-induced EFs. Alternative electrode placements such as RUL have been proposed to minimize effects on one hippocampus, with RUL treatment efficacy comparable to BT by administering RUL ECT at six times the threshold dose (Finnegan and McLoughlin, 2019). Notably though, we found the induced EF in the stimulated hemisphere with RUL is as high as BT assuming the same stimulation parameters. This implies that in clinical practice the right temporal lobe and hippocampus receives a higher EF with RUL placement than with BT, but the left hemisphere a low EF presumably accounting for reduced cognitive side-effects overall.

Previous studies have used EF modeling to investigate different electrode placements, including BT, BF, RUL, and other configurations including MFO, which all are associated with significant ECT-induced hippocampal EFs (Bai et al., 2019). EF calculations for different electrode placements which included a version of FM have also been reported, which are consistent with our findings. However, the aims of these earlier studies were different: determination of minimum current to induce a seizure in rhesus macaque monkeys using ECT and magnetic seizure therapy using a variety of electrode placements (Peterchev et al., 2015), determination of the spatial extent of brain stimulation necessary to produce a seizure in macaque monkeys using a variety of electrode placements (Lee et al., 2017), and a study that concluded that differences in EF strength from different electrode placements may be linked to cognitive side-effects (Lee et al., 2016). Regarding patients who have actually received a version of FM ECT, to our knowledge there is only a conference abstract published a decade ago reporting a single patient (Rosa et al., 2012); a 40 years old woman with manic phase treatment-resistant schizoaffective disorder, who received as an open label trial, 10 sessions of low current amplitude ECT. The authors reported motor and EEG seizures were qualitatively like conventional ECT, the patient had no significant memory complaints although formal testing was not performed, she had resolution of psychotic and euphoric symptoms, and the authors concluded further investigation of FM placement was indicated.

Our work is novel because (i) it additionally builds on recent GEMRIC (Oltedal et al., 2018; Argyelan et al., 2019; Mulders et al., 2020) studies of patients who have received ECT, (ii) it uses for quantification MNI defined regions reported from neuroimaging studies of patients with severe treatment-resistant depression who have not received ECT (Steele et al., 2008; Johnston et al., 2015; Tolomeo et al., 2016), (iii) we compared four alternative FM electrode placements, and (iv) we highlight the particular clinical relevance of the MFV2 FM electrode placement for actual treatment. This FM electrode placement may have additional clinical advantages over BT electrode placement, by reducing the likelihood of non-cognitive side-effects caused by direct electrical stimulation over temporalis muscle with supraphysiological bite induction, which can cause damage of the tongue, teeth and dental implants, jaw pain and headache (Haghighi et al., 2016; Mulder and Grootens, 2020). Consequently, we suggest a randomized blinded clinical trial is indicated, to compare the therapeutic efficacy and side-effects of MFV2 vs. other placements. Limitations of EF modeling for ECT research have been discussed (Sartorius, 2022), which imply that EFs to brain structures distant from electrodes may be less than calculated, supporting the rationale for the FM orientation avoiding bilateral hippocampal EF effects.

In conclusion, ECT is the most effective treatment for severe treatment-resistant depression yet concern about cognitive side-effects, particularly memory loss, limits prescription and use of ECT (Finnegan and McLoughlin, 2019). We have modeled the induced EF from a range of electrode placements in specific brain regions informed by a range of translational neuroimaging studies, including four alternative FM placements, and highlight the MFV2 placement as being particularly important from a clinical perspective. We predict this electrode placement will minimize cognitive side-effects such as memory loss and may reduce non-cognitive side-effects such as oral cavity damage and headache, whilst maintaining or increasing therapeutic efficacy.

Data availability statement

Publicly available datasets were analyzed in this study. This data can be found here: NIH Human Connectome Project (MGH1010).

Ethics statement

Ethical review and approval were not required for the study on human participants in accordance with the local legislation and institutional requirements. Written informed consent was not required for the study on human participants in accordance with the local legislation and institutional requirements.

Author contributions

JS, TF, and SB conceived the project. SB and TF did the computational modeling. JS wrote the initial draft. All authors discussed the results and contributed to the final manuscript.

Acknowledgments

We thank our institutions for non-specific support.

Conflict of interest

The authors declare that the research was conducted in the absence of any commercial or financial relationships that could be construed as a potential conflict of interest.

Publisher's note

References

Anderson, I. M., McAllister-Williams, R. H., Downey, D., Elliott, R., and Loo, C. (2021). Cognitive function after electroconvulsive therapy for depression: Relationship to clinical response. *Psychol. Med.* 51, 1647–1656. doi: 10.1017/S0033291720000379

Argyelan, M., Oltedal, L., Deng, Z. D., Wade, B., Bikson, M., Joanlanne, A., et al. (2019). Electric field causes volumetric changes in the human brain. *Elife* 8:e49115. doi: 10.7554/eLife.49115

Ashburner, J. (2016). *How. to get the individual coordinate from MNI space.* Available online at: https://www.jiscmail.ac.uk/cgi-bin/webadmin?A2=spm;8005badf.1606 (accessed March 2, 2022).

Bai, S., Martin, D., Guo, T., Dokos, S., and Loo, C. (2019). Computational comparison of conventional and novel electroconvulsive therapy electrode placements for the treatment of depression. *Eur. Psychiatry* 60, 71–78. doi: 10.1016/j.eurpsy.2019.05.006

Bakir, A., Bai, S., Lovell, N., Martin, D., Loo, C., and Dokos, S. (2019). "Finite element modelling framework for electroconvulsive therapy and other transcranial stimulations," in *Brain and human body modeling*, eds S. Makarov, M. Horner, and G. Noetscher (Cham: Springer).

BNF (2016). *British national formulary (online).* London: BMJ Group and Pharmaceutical Press.

Cheng, W., Rolls, E. T., Qiu, J., Yang, D., Ruan, H., Wei, D., et al. (2018). Functional connectivity of the precuneus in unmedicated patients with depression. *Biol. Psychiatry Cogn. Neurosci. Neuroimaging* 3, 1040–1049. doi: 10.1016/j.bpsc.2018.07.008

Deakin, J. (2013). The origins of '5-HT and mechanisms of defence' by Deakin and Graeff: A personal perspective. *J. Psychopharmacol.* 27, 1084–1089. doi: 10.1177/0269881113503508

Deakin, J. F. W., and Graeff, F. G. (1991). 5-HT and the mechanisms of defence. *J. Psychopharmacol.* 5, 305–315. doi: 10.1177/026988119100500414

Deng, Z. D., Argyelan, M., Miller, J., Quinn, D. K., Lloyd, M., Jones, T. R., et al. (2021). Electroconvulsive therapy, electric field, neuroplasticity, and clinical outcomes. *Mol. Psychiatry* 27, 1676–1682. doi: 10.1038/s41380-021-01380-y

Drevets, W. C., Price, J. L., Simpson, J. R. Jr., Todd, R. D., Reich, T., Vannier, M., et al. (1997). Subgenual prefrontal cortex abnormalities in mood disorders. *Nature* 386, 824–827. doi: 10.1038/386824a0

Dukart, J., Regen, F., Kherif, F., Colla, M., Bajbouj, M., Heuser, I., et al. (2014). Electroconvulsive therapy-induced brain plasticity determines therapeutic outcome in mood disorders. *Proc. Natl. Acad. Sci. U.S.A.* 111, 1156–1161. doi: 10.1073/pnas.1321399111

Fan, Q., Witzel, T., Nummenmaa, A., Van Dijk, K. R. A., Van Horn, J. D., Drews, M. K., et al. (2016). MGH-USC human connectome project datasets with ultra-high b-value diffusion MRI. *Neuroimage* 124(Pt B), 1108–1114. doi: 10.1016/j.neuroimage.2015.08.075

Finnegan, M., and McLoughlin, D. M. (2019). "Cognitive side-effects of ECT," in *The ECT handbook*, 4th Edn, eds I. N. Ferrier and J. Waite (Cambridge: Cambridge University Press), 109–120. doi: 10.1017/9781911623175.013

Gbyl, K., Stottrup, M. M., Mitta Raghava, J., Xue Jie, S., and Videbech, P. (2021). Hippocampal volume and memory impairment after electroconvulsive therapy in patients with depression. *Acta Psychiatr. Scand.* 143, 238–252. doi: 10.1111/acps.13259

Gray, J. A., and McNaughton, N. (2000). *The neuropsychology of anxiety: An enquiry into the functions of the septo-hippocampal system.* Oxford: Oxford University Press.

Haghighi, M., Sedighinejad, A., Naderi Nabi, B., Emiralavi, C., Biazar, G., Mirmozaffari, K., et al. (2016). The incidence and predictors of headache and myalgia in patients after electroconvulsive therapy (ECT). *Anesthesiol. Pain Med.* 6:e33724. doi: 10.5812/aapm.33724

Hibar, D. P., Westlye, L. T., van Erp, T. G., Rasmussen, J., Leonardo, C. D., Faskowitz, J., et al. (2016). Subcortical volumetric abnormalities in bipolar disorder. *Mol. Psychiatry* 21, 1710–1716. doi: 10.1038/mp.2015.227

Holtzheimer, P. E., Husain, M. M., Lisanby, S. H., Taylor, S. F., Whitworth, L. A., McClintock, S., et al. (2017). Subcallosal cingulate deep brain stimulation for treatment-resistant depression: A multisite, randomised, sham-controlled trial. *Lancet Psychiatry* 4, 839–849. doi: 10.1016/S2215-0366(17)30371-1

Johnston, B. A., Tolomeo, S., Gradin, V., Christmas, D., Matthews, K., and Steele, J. D. (2015). Failure of hippocampal deactivation during loss events in treatment-resistant depression. *Brain* 138(Pt 9), 2766–2776. doi: 10.1093/brain/awv177

Lee, W. H., Lisanby, S. H., Laine, A. F., and Peterchev, A. V. (2016). Comparison of electric field strength and spatial distribution of electroconvulsive therapy and magnetic seizure therapy in a realistic human head model. *Eur. Psychiatry* 36, 55–64. doi: 10.1016/j.eurpsy.2016.03.003

Lee, W. H., Lisanby, S. H., Laine, A. F., and Peterchev, A. V. (2017). Minimum electric field exposure for seizure induction with electroconvulsive therapy and magnetic seizure therapy. *Neuropsychopharmacology* 42, 1192–1200. doi: 10.1038/npp.2016.276

Lisman, J., Buzsaki, G., Eichenbaum, H., Nadel, L., Ranganath, C., and Redish, A. D. (2017). Viewpoints: How the hippocampus contributes to memory, navigation and cognition. *Nat. Neurosci.* 20, 1434–1447. doi: 10.1038/nn.4661

Malberg, J. E., Hen, R., and Madsen, T. M. (2021). Adult neurogenesis and antidepressant treatment: The surprise finding by Ron Duman and the field 20 years later. *Biol. Psychiatry* 90, 96–101. doi: 10.1016/j.biopsych.2021.01.010

Mayberg, H. S., Liotti, M., Brannan, S. K., McGinnis, S., Mahurin, R. K., Jerabek, P. A., et al. (1999). Reciprocal limbic-cortical function and negative mood: Converging PET findings in depression and normal sadness. *Am. J. Psychiatry* 156, 675–682. doi: 10.1176/ajp.156.5.675

Mayberg, H. S., Lozano, A. M., Voon, V., McNeely, H. E., Seminowicz, D., Hamani, C., et al. (2005). Deep brain stimulation for treatment-resistant depression. *Neuron* 45, 651–660. doi: 10.1016/j.neuron.2005.02.014

Mulder, L. A. C., and Grootens, K. P. (2020). The incidence of post-electroconvulsive therapy headache: A systematic review. *J. ECT* 36, e22–e28. doi: 10.1097/YCT.0000000000000677

Mulders, P. C. R., Llera, A., Beckmann, C. F., Vandenbulcke, M., Stek, M., Sienaert, P., et al. (2020). Structural changes induced by electroconvulsive therapy are associated with clinical outcome. *Brain Stimul.* 13, 696–704. doi: 10.1016/j.brs.2020.02.020

Oltedal, L., Narr, K. L., Abbott, C., Anand, A., Argyelan, M., Bartsch, H., et al. (2018). Volume of the human hippocampus and clinical response following electroconvulsive therapy. *Biol. Psychiatry* 84, 574–581. doi: 10.1016/j.biopsych.2018.05.017

Pagnin, D., de Queiroz, V., Pini, S., and Cassano, G. B. (2004). Efficacy of ECT in depression: A meta-analytic review. *J. ECT* 20, 13–20. doi: 10.1097/00124509-200403000-00004

Perrin, J. S., Merz, S., Bennett, D. M., Currie, J., Steele, D. J., Reid, I. C., et al. (2012). Electroconvulsive therapy reduces frontal cortical connectivity in severe depressive disorder. *Proc. Natl. Acad. Sci. U.S.A.* 109, 5464–5468. doi: 10.1073/pnas.1117206109

Peterchev, A. V., Krystal, A. D., Rosa, M. A., and Lisanby, S. H. (2015). Individualized low-amplitude seizure therapy: Minimizing current for electroconvulsive therapy and magnetic seizure therapy. *Neuropsychopharmacology* 40, 2076–2084. doi: 10.1038/npp.2015.122

Phelps, E. A. (2004). Human emotion and memory: Interactions of the amygdala and hippocampal complex. *Curr. Opin. Neurobiol.* 14, 198–202. doi: 10.1016/j.conb.2004.03.015

Rosa, M. A., Abdo, G. L., Rosa, M. O., LLisanby, S. H., and Peterchev, A. V. (2012). Frontomedial electrode placement with low current amplitude: a case report (abstract from the 22nd annual meeting of the international society of electroconvulsive therapy and neurostimulation). *J. ECT* 28:146.

Rupprechter, S., Romaniuk, L., Series, P., Hirose, Y., Hawkins, E., Sandu, A. L., et al. (2020). Blunted medial prefrontal cortico-limbic reward-related effective connectivity and depression. *Brain* 143, 1946–1956. doi: 10.1093/brain/awaa106

Sartorius, A. (2022). Electric field distribution models in ECT research. *Mol. Psychiatry*. doi: 10.1038/s41380-022-01516-8

Schmaal, L., Veltman, D. J., van Erp, T. G., Samann, P. G., Frodl, T., Jahanshad, N., et al. (2016). Subcortical brain alterations in major depressive disorder: findings from the ENIGMA major depressive disorder working group. *Mol. Psychiatry* 21, 806–812. doi: 10.1038/mp.2015.69

SEAN (2021). *SEAN Annual Report 2019: A summary of ECT in Scotland for 2009-2018.* Available online at: https://www.sean.org.uk/AuditReport/Main.html (accessed March 2, 2022).

Shackman, A. J., Salomons, T. V., Slagter, H. A., Fox, A. S., Winter, J. J., and Davidson, R. J. (2011). The integration of negative affect, pain and cognitive control in the cingulate cortex. *Nat. Rev. Neurosci.* 12, 154–167. doi: 10.1038/nrn2994

Squire, L. R. (1986). Mechanisms of memory. *Science* 232, 1612–1619. doi: 10.1126/science.3086978

Steele, J. D., and Paulus, M. P. (2019). Pragmatic neuroscience for clinical psychiatry. *Br. J. Psychiatry* 215, 404–408. doi: 10.1192/bjp.2019.88

Steele, J. D., Christmas, D., Eljamel, M. S., and Matthews, K. (2008). Anterior cingulotomy for major depression: Clinical outcome and relationship to lesion characteristics. *Biol. Psychiatry.* 63, 670–677. doi: 10.1016/j.biopsych.2007.07.019

Tolomeo, S., Christmas, D., Jentzsch, I., Johnston, B. A., Sprenglemeyer, R., Matthews, K., et al. (2016). A causal role for the anterior mid-cingulate cortex in negative affect and cognitive control. *Brain* 139, 1844–1854.

Wade, B. S. C., Hellemann, G., Espinoza, R. T., Woods, R. P., Joshi, S. H., Redlich, R., et al. (2020). Depressive symptom dimensions in treatment-resistant major depression and their modulation with electroconvulsive therapy. *J. ECT* 36, 123–129. doi: 10.1097/YCT.0000000000000623

Whiteford, H. A., Degenhardt, L., Rehm, J., Baxter, A. J., Ferrari, A. J., Erskine, H. E., et al. (2013). Global burden of disease attributable to mental and substance use disorders: findings from the Global Burden of Disease Study 2010. *Lancet* 382, 1575–1586. doi: 10.1016/S0140-6736(13)61611-6

WHO (2018). *Depression: Fact sheet*. Geneva: WHO.

Frontiers in Neuroscience

Provides a holistic understanding of brain function from genes to behavior

Part of the most cited neuroscience journal series which explores the brain - from the new eras of causation and anatomical neurosciences to neuroeconomics and neuroenergetics.

Discover the latest Research Topics

See more →

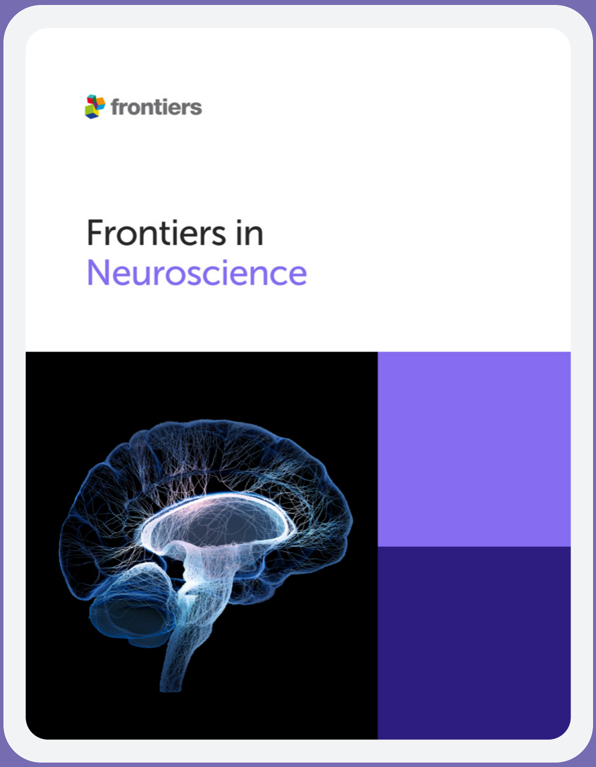
frontiers

Frontiers in
Neuroscience

Frontiers

Avenue du Tribunal-Fédéral 34
1005 Lausanne, Switzerland
frontiersin.org

Contact us

+41 (0)21 510 17 00
frontiersin.org/about/contact